

Dissertation

Submitted to the

Combined Faculty of Mathematics, Engineering and Natural Sciences

of the Ruprecht-Karls University of Heidelberg, Germany

For the degree of

Doctor of Engineering

Presented by

Master of Science (M.Sc.)

Nina Felicia Conzelmann

Born in Albstadt, Germany

Oral examination: April 7th, 2025

Bottom-Up Assembly of Modular Systems for Trapping and Near-Infrared Light-Triggered Killing of Bacteria

Referees:

Prof. Dr. Joachim P. Spatz

Institute for Molecular Systems Engineering
and Advanced Materials
Ruprecht-Karls University, Heidelberg
Max-Planck-Institute for Medical Research,
Heidelberg

Prof. Dr. Peer Fischer

Institute for Molecular Systems Engineering
and Advanced Materials
Ruprecht-Karls University, Heidelberg
Max-Planck-Institute for Medical Research,
Heidelberg

“If you only do what you can do, you will never be more than you are now.”

- Kung Fu Panda-

– Für meine Familie –

Contents

CONTENTS	I
DANKSAGUNG	VII
ABSTRACT	IX
DEUTSCHE ZUSAMMENFASSUNG	XI
ACRONYMS	XIII
1 INTRODUCTION	3
1.1 Bacteria - Background	3
1.1.1 Bacterial Structure	3
1.1.1.1 <i>Gram-Positive Bacteria</i>	4
1.1.1.2 <i>Gram-Negative Bacteria</i>	4
1.1.2 Bacterial Mobility	5
1.1.2.1 <i>Motile versus Non-Motile Bacteria</i>	5
1.1.3 Bacterial Biofilm-Formation.....	5
1.2 Antibiotics, Antibiotic-Resistances and Antibiotic-Alternatives	6
1.2.1 Antimicrobial Peptides (AMPs).....	7
1.2.2 Bacteriophages and Phage Therapy	8
1.2.2.1 <i>Bacteriophages and Their Specific Adhesion</i>	9
1.3 Nosocomial and Implant-Associated Infections	10
1.4 Biomaterials	11
1.4.1 Antibacterial Coatings	11
1.4.1.1 <i>Anti-Adhesion/Protein-Repellent Coatings</i>	12
1.4.1.2 <i>Contact-Killing Coatings</i>	13
1.4.1.3 <i>Agent-Release Coatings</i>	14
1.5 Poly(Lactide-Co-Glycolide) Acid (PLGA)	16
1.6 Poloxamer (Pluronic®)	18
1.7 Polyethylene Glycol (PEG)	19
1.8 Polymer Particle Production	19

1.8.1	Particle Preparation Techniques.....	19
1.8.2	Pore-Forming Agents – Porogens	21
1.9	Thermodynamic Spreading Coefficient.....	22
1.10	Synthetic Lipid Vesicles – Liposomes.....	23
1.10.1	Synthetic Vesicles – Formation Techniques.....	24
1.10.2	Particle Endocytosis by Liposomes	26
1.11	Plasmonic Nanoparticles – Gold Nanorods (AuNRs).....	28
1.11.1	Properties	28
1.11.2	Biomedical Applications Applying AuNRs	30
2	MOTIVATION	35
3	MATERIALS & METHODS.....	41
3.1	Modular Porous Polymer-Based Microcapsules for Trapping and Near-Infrared Light-Triggered Killing of Bacteria.....	41
3.1.1	Materials	41
3.1.1.1	<i>Polymer-Based Microcapsules.....</i>	<i>41</i>
3.1.1.2	<i>Calcium Carbonate Particles</i>	<i>42</i>
3.1.1.3	<i>Gold Nanorods (AuNRs).....</i>	<i>42</i>
3.1.1.4	<i>Bacteria Culturing</i>	<i>43</i>
3.1.2	Methods.....	44
3.1.2.1	<i>(Cryogenic-)Scanning Electron Microscopy (cryo-SEM).....</i>	<i>44</i>
3.1.2.2	<i>Confocal Laser Scanning Microscope (CLSM) Imaging.....</i>	<i>44</i>
3.1.2.3	<i>UV-Vis Spectroscopy.....</i>	<i>45</i>
3.1.2.4	<i>Zeta Potential Measurements.....</i>	<i>45</i>
3.1.2.5	<i>Polymer-Based Microcapsules Production Procedure.....</i>	<i>45</i>
3.1.2.6	<i>Calcium Carbonate Particle Production and Layer-by-Layer Coating</i>	<i>46</i>
3.1.2.7	<i>Microcapsule Post-Production Etching Procedure</i>	<i>47</i>
3.1.2.8	<i>Bacteria Capturing Performance of Microcapsules.....</i>	<i>47</i>
3.1.2.9	<i>Gold Nanorod Synthesis.....</i>	<i>47</i>
3.1.2.10	<i>Gold Nanorod Concentration Calculations.....</i>	<i>49</i>
3.1.2.11	<i>Gold Nanorod PLGA-Functionalization.....</i>	<i>49</i>
3.1.2.12	<i>Cell Viability Tests with Microcapsules</i>	<i>50</i>
3.1.2.13	<i>Bacteria Viability Tests with Microcapsules</i>	<i>51</i>

3.1.2.14	<i>Live/Dead Bacteria Quantification</i>	51
3.1.2.15	<i>Near Infrared (NIR)-Laser (808 nm) Setup</i>	52
3.1.2.16	<i>NIR-Laser Treatment of Single Bacteria Loaded Microcapsules</i>	52
3.1.2.17	<i>NIR Light-Emitting Diode (LED)-Setup</i>	53
3.1.2.18	<i>Agar-Plate Bacteria Viability Tests with Microcapsules</i>	54
3.2	Adhesion-Mediated Engulfment and Killing of Bacteria by Synthetic	
	Vesicles	55
3.2.1	Materials	55
3.2.1.1	<i>Giant Unilamellar Vesicles (GUVs) Formation</i>	55
3.2.1.2	<i>Gold Nanorods (AuNR)</i>	56
3.2.1.3	<i>Gold Nanorod Functionalization</i>	57
3.2.1.4	<i>Bacteria Culturing</i>	58
3.2.2	Methods.....	58
3.2.2.1	<i>Formation Techniques of Giant Unilamellar Vesicles</i>	58
3.2.2.2	<i>Adhesion Protein (gp37) Isolation and Purification</i>	60
3.2.2.3	<i>Bacteria Adhesion and Engulfment Studies</i>	61
3.2.2.4	<i>Gold Nanorod Synthesis</i>	61
3.2.2.5	<i>Gold Nanorod Functionalization</i>	62
4	RESULTS & DISCUSSIONS	65
4.1	Modular Porous Polymer-Based Microcapsule System for Trapping and	
	Light-Triggered Killing of Bacteria	65
4.1.1	Demanded Design of Polymer-Based Microcapsules.....	66
4.1.2	Polymer-Based Microcapsules Production and Formation Procedure	68
4.1.2.1	<i>Polymer Particle Formation – The Emulsion Evaporation Process</i>	69
4.1.2.2	<i>Solid Particle Formation</i>	70
4.1.2.3	<i>Hollow Core Generation</i>	72
4.1.2.4	<i>Microcapsules Size Variation</i>	75
4.1.2.5	<i>Importance of DCM-to-Water Volume Ratio</i>	79
4.1.2.6	<i>Effect of Polyvinylpyrrolidone (PVP)</i>	80
4.1.2.7	<i>Pore Generation via Porogens</i>	81
4.1.2.8	<i>Pore Generation via Solid Templates</i>	92
4.1.2.9	<i>Bacteria-Microcapsule Penetration Tests and Post-Production Etching</i> <i>Process</i>	94

4.1.2.10	<i>Microcapsule Uptake Efficiency: Motile vs. Non-Motile Bacteria..</i>	100
4.1.3	Gold Nanorods (AuNRs)	102
4.1.3.1	<i>AuNR Synthesis</i>	102
4.1.3.2	<i>AuNR Functionalization by PLGA-SH</i>	103
4.1.4	Functionalization of Microcapsules by PLGA-Coated AuNRs	105
4.1.5	Cell Viability Tests with Microcapsules	106
4.1.6	Bacteria Viability Tests with Microcapsules.....	107
4.1.7	Killing Performance of Single AuNR-Functionalized Microcapsules.....	109
4.1.8	Killing Performance of AuNR-Functionalized Microcapsules in Bulk Solutions	113
4.1.9	Effect of NIR-Laser-Treatment on Skin Model Tissue.....	115
4.2	Adhesion Mediated Engulfment and Killing of Bacteria by Synthetic Vesicles.....	116
4.2.1	Requirements, Formation and Composition of Giant Unilamellar Vesicles..	117
4.2.2	Adhesion Protein (gp37) Mediated Binding of Bacteria	121
4.2.3	AuNR-Decorated Synthetic Vesicles as Active Bacteria Killing System	127
5	SUMMARY & CONCLUSIONS.....	133
5.1	Modular Porous Polymer-Based Microcapsule System for Trapping and Light-Triggered Killing of Bacteria.....	134
5.2	Adhesion Mediated Engulfment and Killing of Bacteria by Synthetic Vesicles.....	135
6	OUTLOOK.....	139
6.1	Modular Porous Polymer-Based Microcapsule System for Trapping and Light-Triggered Killing of Bacteria.....	139
6.2	Adhesion Mediated Engulfment and Killing of Bacteria by Synthetic Vesicles.....	140
7	APPENDIX.....	145
7.1	Supporting Information	145
7.1.1	Modular Porous Polymer-Based Microcapsule System	145
7.1.2	Synthetic Vesicles	155

7.2	Publications	156
7.3	Bibliography	157

Danksagung

Viele besondere Menschen haben mich auf dem Weg der Promotion begleitet und mich bei der Entstehung dieser Arbeit unterstützt. All diesen Personen gilt mein besonderer und größter Dank!

Zu Beginn möchte ich Herrn Prof. Joachim Spatz meinen außerordentlichen Dank aussprechen. Es war mir eine besondere Ehre, als Mitglied seiner Forschungsgruppe am Max-Planck-Institut für medizinische Forschung tätig sein zu dürfen. Die Mitarbeit an einer Vielzahl spannender und abwechslungsreicher Projekte war für mich eine unschätzbare bereichernde und wertvolle Erfahrung.

Mein besonderer Dank gebührt ebenfalls meinem Betreuer, Herrn Dr. Ilia Platzman, für seine kontinuierliche Unterstützung, jede wertvolle Idee, Anregung und all die konstruktiven Ratschläge. Er stand mir stets mit großem Engagement zur Seite und gab mir immerzu neue Motivation und Inspiration.

Im ersten Abschnitt meiner Promotion hatte ich ebenfalls das Glück, Teil des „PolyAntiBak“-Projektes zu sein. Im Rahmen dieses Projektes danke ich Herrn Prof. Ralf Kemkemer, Herrn Prof. Rumen Krastev und Frau Dr. Tonya Andreeva von der Hochschule Reutlingen, Herrn Prof. Martin Möller und Herrn Dr. Jan Tenbusch vom DWI in Aachen sowie Herrn Dr. Rainer Bargon und Herrn Dr. Christof Merckle als Vertreter der Aesculap AG für die zahlreichen interessanten Ideen, Anregungen, Diskussionen und die spannende Zusammenarbeit.

Vielen Dank auch an meine Masterstudentin Ariadna Benimeli Borràs für die Unterstützung im Labor im Rahmen des Mikrokapsel-Projektes. Ein großer Dank außerdem an Ann-Kathrin Gelmroth und Anastassiya Schramm für die Unterstützung und Hilfe innerhalb der Projekte sowie die wertvollen und ideenreichen Diskussionen.

Ein großes Dankeschön für die tolle und hilfsbereite Arbeitsatmosphäre, die wertvolle Unterstützung im und außerhalb des Labors, die vielen lustigen, geselligen, aber auch ideenreichen Mittags- und Kaffeepausen. Ein Dank für die spaßigen und ausgelassenen Stammtische geht an alle „Spatzen“, im Besonderen aber an meine tollen Kolleginnen und Kollegen Elke Völkle, Darya Freimann, Pascal Jeschenko, Jonathan Bodenschatz, Manuel Baumann und Jan Tenbusch. Ich kann mit großer Freude sagen, dass ihr in dieser Zeit nicht

nur meine KollegInnen wart, sondern dass ich euch nun auch zu meinen Freunden zählen darf.

Für die wertvollen Diskussionen, die unterstützenden Ratschläge, eure Geduld, sowie die Korrektur meiner Arbeit danke ich besonders Pascal, Jan, Elke, Manuel, Theresa und Nathalie.

Abschließend gilt mein größter Dank meinen Freunden und im Besonderen meiner Familie. Sie haben mich nicht nur während der Promotion, sondern auch während des Studiums und außerhalb des Berufslebens kontinuierlich unterstützt, bestärkt und motiviert. Aus dieser Gruppe von für mich ganz besonderer Menschen, fällt es mir sehr schwer einzelne Personen herauszuheben und dennoch:

Ein besonderer Dank geht an meine Mädels und viele weitere tolle und herzliche Menschen vom SV Leonberg/Eltingen Handball. Gekommen, um zu bleiben!

Besonders du, liebe Jenny, hast mich mit einer Freundschaft auf der Überholspur aus dem Alltag rausgeholt. All die unvergesslichen Erlebnisse haben mir nicht nur immerzu gute Laune, neue Motivation und neuen Fokus gegeben, sondern werden auf ewig ganz besondere Erinnerungen fürs Leben bleiben. Urlaub für die Seele - auf noch viele weitere unvergessliche Abenteuer!

Liebe Theresa, danke für eine ganz besondere Freundschaft, die uns nun schon so lange durch alle Höhen und Tiefen und mit unzähligen besonderen Erlebnissen und Momenten auf unseren Wegen begleitet. Danke für die unermüdliche Unterstützung, deinen Glauben in mich, die Motivation und die immerzu positive Bestärkung in allen Lebenslagen.

Lieber Philipp, als kleines Mädchen hätte ich mir keinen besseren großen Bruder vorstellen können. Nun bin ich kein kleines Mädchen mehr und dennoch hat sich das bis heute nicht geändert. Ich bin mir sicher, dass wir stets ein gutes Team sein werden.

Liebe Mama, lieber Papa, ihr habt von Anfang an immer an mich geglaubt, seid mir in allen Lebenslagen mit eurer vollen Unterstützung, eurem positiven Zuspruch und euren wertvollen Ratschlägen zur Seite gestanden. Ihr habt mir Vertrauen, Zuversicht und Motivation gegeben, wenn ich nicht mehr an mich geglaubt oder gezweifelt habe und habt mir stets vollen Rückhalt und endlose Liebe geschenkt. Dafür gebührt euch meine größte und tiefste Dankbarkeit! Ohne euch wäre ich heute nicht dort, wo ich nun bin!

Danke – für alles!

Abstract

Despite the advancements in sterilization and aseptic techniques, bacterial infections associated with medical implants and devices have not been eradicated. Consequently, the utilization of antibiotic-based treatment has become the preferred approach due to its efficiency, rapidity, and versatility. Nevertheless, the overuse or misuse of antibiotics in the healthcare-related sector is a primary factor contributing to the emergence of antibiotic-resistant bacteria. The existence of such antimicrobial resistance has been demonstrated to result in a significant increase in surgical interventions, an elevated risk for medical complications and even an increased mortality rate. This situation has led to an urgent need to explore and develop alternative, efficient, antibiotic-free therapeutic options. A promising alternative approach involves the coating of medical devices and implants with antibacterial agents to combat bacterial infections. Despite the progress made in recent years, antibacterial coatings have not reached a complete protection against severe inflammation. This can be attributed, at least in part, to the "open-space" design of the current coatings, which expose surrounding cells and tissues to the released contents of the dying and dead bacteria.

This thesis focuses on the design and development of two modular antibacterial systems, utilizing a "confined space" in which the bacteria are entrapped/engulfed, and subsequently eliminated, thereby protecting the surrounding tissue from bacterial fragments and the released bacterial toxins. The first approach involves the high-throughput formation of mechanically robust, highly porous polymer-based microcapsules. A careful selection of the polymers, solvents, pore-forming agents and the manufacturing process conditions was essential for the creation of stable biodegradable microcapsules with a porous polymer shell and an inner hollow cavity. The developed porous microcapsules demonstrated effective trapping properties for motile bacteria. Moreover, the functionalization of the capsule's shells with gold nanorods (AuNRs) facilitated the integration of a near-infrared (NIR) light-triggered bacteria-killing module into the porous microcapsules. It is important to note that the efficient killing of bacteria that are either entrapped within the microcapsules or in close proximity has been achieved. Due to the advanced mechanical stability and antibacterial properties, the developed polymer-based porous microcapsules have the potential to be implemented as an antibiotic-free coating on orthopedic implants.

The second approach focused on engineering bioinspired phagocytotic-like antibacterial systems. In this regard, giant unilamellar vesicles (GUVs) have been selected as compartments for the uptake of bacteria in a target-specific manner. To this end, the GUV membrane has been functionalized with a bacteriophage-derived tail protein. Tail protein-mediated adhesion enabled efficient engulfment of targeted bacteria by the GUVs. Moreover, in order to equip the synthetic phagocytotic system with the NIR light-triggered bacteria-killing mechanism, the vesicle membranes were functionalized with AuNRs. With these properties, the developed bioinspired phagocytotic antibacterial system has the potential to be implemented as an antibacterial washing solution.

Deutsche Zusammenfassung

Trotz signifikant verbesserter und über die Jahre weiterentwickelter Sterilisationstechniken und aseptischer Verfahren konnten bakterielle Infektionen im Zusammenhang mit medizinischen Implantaten und Geräten bis heute nicht vollständig eliminiert werden. Antibiotika stellen in diesem Kontext einen effizienten, schnellen und vielseitig einsetzbaren Behandlungsansatz dar, welcher jedoch zu einer übermäßigen und in vielen Fällen auch inadäquaten Verwendung führt. Insbesondere im Gesundheitswesen trägt der fehlerhafte und übermäßige Einsatz als einer der Hauptfaktoren zur Entstehung antibiotikaresistenter Bakterien bei. Nachweislich führen antimikrobiellen Resistenzen zu einer signifikanten Zunahme an chirurgischen Eingriffen, einem erhöhten Risiko medizinischer Komplikationen und sogar zu einer erhöhten Sterblichkeit. Dies unterstreicht die Dringlichkeit der Entwicklung und Erforschung alternativer, effizienter und insbesondere antibiotikafreier Therapieansätze. Ein vielversprechender, alternativer Ansatz besteht in der Beschichtung medizinischer Geräte und Implantate mit antibakteriellen Wirkstoffen und Materialien. Obwohl in den vergangenen Jahren signifikante Fortschritte im Bereich der antibakteriellen Oberflächenbeschichtungen erzielt wurden, existiert nach wie vor kein Therapieansatz, welcher einen vollständigen Schutz vor schweren, bakteriellen Entzündungen gewährleisten kann. In diesem Kontext erweist sich das „offene“ Design der gegenwärtig maßgeblich eingesetzten antibakteriellen Beschichtungen als ein wesentlicher Nachteil. Infolge dieses Designs werden die umliegenden Zellen und das umliegende Gewebe den freiwerdenden Toxinen und Bestandteilen der Bakterien schutzlos ausgesetzt.

Der Fokus dieser Arbeit liegt daher auf der Entwicklung zweier modularer, antibakterieller Systeme unter der Verwendung eines „begrenzten Raums“. Ziel dieser räumlichen Trennung ist es, Bakterien hierin eingeschlossen abzutöten und dadurch das umliegende Gewebe vor freiwerdenden bakteriellen Toxinen und Fragmenten zu schützen. Der erste in diesem Zusammenhang verfolgte Ansatz umfasst die Entwicklung mechanisch stabiler, polymerbasierter Mikro kapseln mit hoher Porosität. Für die Erzeugung resistenter, biologisch abbaubarer Mikro kapseln mit einer porösen Polymerhülle und einem inneren Hohlraum ist eine präzise Auswahl der verwendeten Polymere, des Lösungsmittels, der Porogene (Porenbildner) und der Prozessbedingungen von entscheidender Bedeutung. Im Rahmen der durchgeführten Experimente zeigte sich, dass die entwickelten porösen Mikro kapseln eine hohe Effektivität in der Aufnahme und beim Einschluss von beweglichen (motilen) Bakterien aufwiesen. Des Weiteren wurde durch die Implementierung von Goldnanostäbchen (AuNRs) auf der Mikro kapselhüllen das aktive Abtöten der Bakterien ermöglicht. AuNRs sind hierbei in der

Lage durch die Verwendung von nahinfraroter (NIR) Strahlung, lokal Hitze zu erzeugen, welche zur Eliminierung der Bakterien verwendet wird. In diesem Kontext zeigt sich eine besonders effiziente Abtötung von eingeschlossenen oder in unmittelbarer Nähe der Kapseln befindlichen Bakterien. Aufgrund der signifikanten mechanischen Belastbarkeit sowie der antibakteriellen Eigenschaften der entwickelten polymerbasierten, porösen Mikrokapseln könnte eine Anwendung als Oberflächenbeschichtung in orthopädischen Implantaten in Betracht gezogen werden.

Im zweiten Forschungsansatz fokussiert sich diese Arbeit auf die Entwicklung eines bioinspirierten, phagozytoseähnlichen antibakteriellen Systems. Für diesen angestrebten Zweck wurden große, synthetische, unilamellare Vesikel (GUVs) als Kompartimente für die gezielte Aufnahme von Bakterien ausgewählt. Die Funktionalisierung der Lipiddoppelschicht mit einem aus Bakteriophagen stammenden Schwanzprotein ermöglicht hierbei eine gezielte Bindung und Aufnahme von Bakterien durch die synthetischen Vesikel. Zusätzlich dazu wurde die Membran der Vesikel mit AuNRs modifiziert. Dies ermöglicht eine durch NIR-Licht-induzierte Abtötung von Bakterien durch Hitze. Die dargelegten Eigenschaften des entwickelten bioinspirierten Phagozytose-Systems ermöglichen unter anderem den Einsatz als antibakterielle Waschlösung.

Acronyms

3D	-	three-dimensional
AA	-	ascorbic acid
AMR	-	antimicrobial resistance
AMP	-	antimicrobial peptides
AR	-	aspect ratio
AuNR	-	gold nanorods
Cryo	-	cryogenic
Chol	-	cholesterol
CIEDI	-	cardiovascular implantable electronic device infection
CLSM	-	confocal laser scanning microscope
CMC	-	critical micelle concentration
CTAB	-	cetyltrimethylammonium bromide
DCM	-	dichloromethane
DNA	-	deoxyribonucleic acid
DOPC	-	1,2-dioleoyl- <i>sn</i> -glycero-3-phosphocholine
DOPG	-	1,2-dioleoyl- <i>sn</i> -glycero-3-phospho-(1'-rac-glycerol) (sodium salt)
EMA	-	european medicines quality agency
EO	-	ethylene oxide
EPS	-	extracellular polymeric substance
FDA	-	US food and drug administration
GA	-	glycolic acid
GFP	-	green fluorescent protein
GUV	-	giant unilamellar vesicle
His	-	histidine
HLB	-	hydrophilic–lipophilic balance
HFE	-	hydrofluoroether
IAI	-	implant-associated infection
LA	-	lactic acid
LB	-	lysogeny broth
LED	-	light-emitting diode
LPS	-	lipopolysaccharides

LSPR	-	longitudinal surface plasmon resonance
LTF	-	long tail fiber
LUV	-	large unilamellar vesicle
μ C	-	Microcapsule
MUA	-	11-mercaptoundecanoic acid
NIR	-	near-infrared
NSI	-	neurosurgical infection
NTA	-	nitrilotriacetic acid
OD	-	optical density
PAH	-	poly(allylamine hydrochloride)
PBS	-	phosphate-buffered saline
PEG	-	polyethylene glycol
PEO	-	poly(ethylene oxide)
PFOB	-	perfluorooctyl bromide
PGA	-	polyglycolic acid
PI	-	propidium iodide
PJI	-	prosthetic joint infection
PLA	-	poly-lactic acid
PLGA	-	poly(lactide-co-glycolide) acid
PMMA	-	polymethyl methacrylate
PO	-	propylene oxide
PPO	-	poly(propylene oxide)
PSS	-	polystyrene sulfonate
PTT	-	photothermal therapy
PVA	-	poly(vinyl alcohol)
PVP	-	polyvinylpyrrolidone
QAC	-	quaternary ammonium compound
RNA	-	ribonucleic acid
ROS	-	reactive oxygen species
SAM	-	self-assembled monolayer
SE	-	second electron
SEM	-	scanning electron microscopy
SPR	-	surface plasmon resonance

STF	-	short tail fibers
SUV	-	small unilamellar vesicle
TSPR	-	transversal surface plasmon resonance
UV	-	ultraviolet
USI	-	ureteral stent infection
Vis	-	visible
WHO	-	world health organization

Introduction

Chapter 1

1 Introduction

1.1 Bacteria - Background

Bacteria are ubiquitous single-celled organisms found within our bodies and in a variety of environments. Bacteria are prokaryotic organisms that lack a nucleus and other internal structures (e.g., mitochondria, Golgi bodies, endoplasmic reticulum) and carry a single, circular DNA genome.^{1, 2} This relatively simple structure allows for rapid and high adaptability, a large number of spontaneous mutations, as well as quick reproduction rates via asexual division. Bacteria come in a variety of shapes (e.g., spherical, rod-shaped, and spiral) and sizes ranging from about 0.5 μm to 3 μm or even larger.^{1, 3} Most bacteria are harmless to humans and highly important for all kinds of natural phenomena and biological cycles (e.g., decomposition processes, nitrogen fixation in soil, digestive processes, etc.).^{1, 4} It is crucial to mention that pathogenic bacteria can lead to significant infections and diseases. One effective and frequently used approach to combating bacteria and bacterial infections is the use of antibiotics. However, the overuse and misuse of antibiotics has led to a significant increase in antibiotic resistance, necessitating the development of effective alternatives to combat bacterial infections.

1.1.1 Bacterial Structure

In order to develop effective antibacterial agents and approaches, it is essential to gain a comprehensive understanding of the bacterial structure, particularly the bacterial cell wall and its mode of action. Similarly to eukaryotic cells, the cytoplasmic cell membrane has a lipid bilayer structure with actin-like proteins on the inside of the membrane, which gives the bacterium its shape. With regard to the cell wall, bacteria are grouped into gram-positive and gram-negative categories.^{2, 3}

1.1.1.1 Gram-Positive Bacteria

Gram-positive bacteria possess a multilayer cell wall comprising a thick peptidoglycan layer (150 - 500 Å) (Figure 1-1, left).^{1,5} The presence of a thick peptidoglycan layer results in the bacteria being stained purple by gram staining (gram-positive). The lysis of bacteria is frequently initiated by the degradation of peptidoglycan, which is triggered by the action of lysozymes that cleave the glycan backbone.¹ In addition to the peptidoglycan layer, other components, such as teichoic and lipoteichoic acids, can be present in the cell wall of gram-positive bacteria. The water-soluble teichoic acid molecules play an important role in the virulence of the bacterium, providing an anionic structure and being linked to peptidoglycan. Lipoteichoic acids are attached to the cytoplasmic membrane and exhibit a fatty acid, playing a crucial role in the adhesion of the bacterium to host cells.^{1,5}

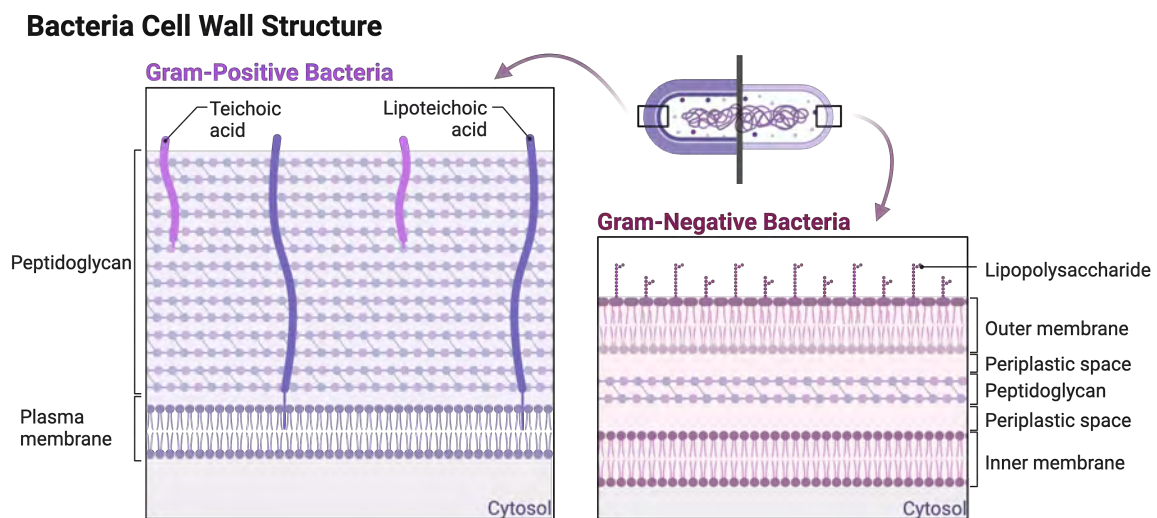


Figure 1-1: Simplified, schematic illustrations of gram-positive and gram-negative bacterial cell walls. The gram-positive cell wall is composed of a thick peptidoglycan layer and teichoic and lipoteichoic acids that are integrated into the wall structure. The gram-negative cell wall presents a thin layer of peptidoglycan situated between the outer (including lipopolysaccharides) and inner membrane. Created with BioRender.com.

1.1.1.2 Gram-Negative Bacteria

Bacteria classified as gram-negative exhibit a thin peptidoglycan layer sandwiched between an outer and an inner membrane (Figure 1-1, right). The gram staining procedure results in a characteristic pink coloration, which differs from the purple color observed in gram-positive bacteria. This characteristic coloration allows for the classification of these

bacteria as gram-negative. Only 5 to 10% in weight of the gram-negative bacteria cell wall is composed of peptidoglycan. Most of the cell wall consists of the outer membrane, a defining feature of gram-negative bacteria, and contains lipopolysaccharides on the outer leaflet. The region between the outer and plasma membranes (which contains the peptidoglycan layer) is referred to as the periplasmic space. The inner (plasma) membrane consists of a phospholipid bilayer, which is also present in gram-positive bacteria.^{1, 5}

1.1.2 Bacterial Mobility

1.1.2.1 Motile versus Non-Motile Bacteria

The ability of bacteria to move is a significant factor influencing their capacity to adapt and survive in diverse environments. Bacterial mobility is classified into five categories of movement, including swimming, swarming, sliding, gliding, and twitching. Swimming and swarming are primarily facilitated by a rotating hair-like structure, called a flagellum, which enables the bacteria to move. In contrast, twitching is enabled by the extension, attachment, and retraction of a type IV pili and gliding by a movement machinery that uses adhesion to move forward. This capacity enables these bacterial types to actively seek out and approach favorable environments (chemotaxis). The last type of movement, sliding, is, unlike the other four mobility types, a passive way of movement. Sliding uses the collective cell community and the forces generated via cell growth to propel cells outward and forward while undergoing growth.⁶ Bacteria that are capable of generating their own active movement through the methods previously described are referred to as motile bacteria (e.g., *Escherichia coli*⁷, *Pseudomonas aeruginosa*⁸, *Enterobacter spp.*⁹). In contrast, bacteria lacking the structures necessary for active movement but instead rely on passive transportation, such as liquid flow or host organism movement, are classified as non-motile bacteria (e.g., *Staphylococcus*⁸, *Enterococcus faecalis*¹⁰, *Klebsiella pneumoniae*¹¹, and *Acinetobacter baumannii*¹²).

1.1.3 Bacterial Biofilm-Formation

Bacteria not only swim or move freely, they also adhere to surfaces and form biofilms, which are defined as highly resistant, irreversible layers of adherent bacteria. These biofilms are integrated within an extracellular polymeric substance (EPS).¹³ The formation of such a biofilm is a complex and multi-step process (Figure 1-2). In the initial phase, the

bacteria attach to the surface in a reversible and loosely bound manner. The second step entails the rearrangement of bacteria on the surface, resulting in their irreversible attachment. Starting from this point, many bacterial biofilms show increased resistance against a large number of physical factors and antibacterial agents applied to avoid biofilm formation. The third step (maturation) is characterized by the secretion of EPS and the proliferation of bacteria on the surface, forming a 3D structure. The EPS is a crucial element in preserving the 3D biofilm from external stressors, including the immune system response, antibiotics, antimicrobials, and oxidative stress. In the final stage of biofilm formation, the layer starts to disperse and rupture, releasing bacteria from the film and enabling infection of other parts of the host. Given the considerable resistance of completely formed biofilms, strategies to combat biofilm formation primarily concentrate on disrupting the process at its initial stages.^{13, 14}

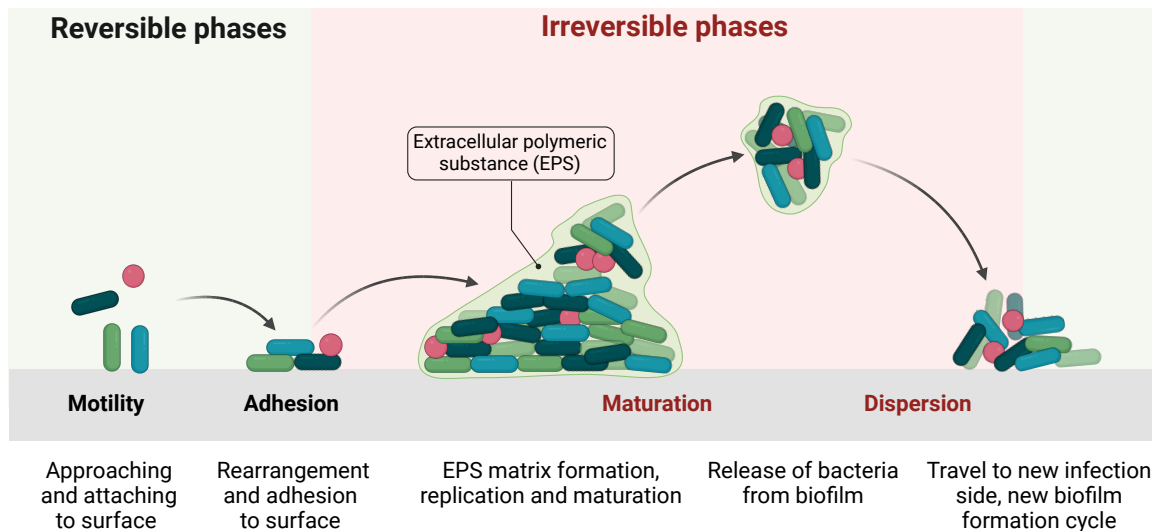


Figure 1-2: Multi-step process of bacterial biofilm formation. Step one includes the reversible adhesion of bacteria on the surface, followed by a rearrangement of the bacteria and the irreversible attachment. In the third step, extracellular polymeric substance (EPS) is excreted, protecting and forming a resistant 3D-structure. In the final step, the 3D-structure is dispersed and bacteria are released to infect other parts in the host system. Created with BioRender.com.

1.2 Antibiotics, Antibiotic-Resistances and Antibiotic-Alternatives

Antibiotics represent the most prominent therapeutic agents in the treatment of bacterial infections. Nevertheless, the extensive and inappropriate use of antibiotics has led to the

emergence of antibiotic-resistant bacteria. The World Health Organization (WHO) has identified antimicrobial resistances (AMRs) and their dissemination as one of the major public health threats globally. Antibiotic resistance is not only associated with a significant economic burden, but is also responsible for a considerable number of deaths with an even more severe projection of 10 million deaths by 2050.¹⁵⁻¹⁷ In 2022, 4.95 million deaths were estimated to be associated with bacterial AMRs.¹⁸ *Escherichia coli* and *Staphylococcus aureus* were among the leading pathogens developing resistances and leading to death in 2019.¹⁶ The burden of AMRs is affecting countries all over the planet regardless of region or income level.¹⁶

Following the discovery of penicillin in 1929 by Alexander Fleming, the first cases of antibiotic resistance began to emerge. The emergence of antibiotic resistance has increased exponentially due to the widespread misuse of antibiotics and the delayed discovery and development of new types of antibiotics.¹⁵ The primary mechanism of action of antibiotics is the inhibition of peptidoglycan, nucleic acid, and protein synthesis. However, by modifying their uptake behavior, drug degradation mechanisms, and target sites, bacteria evade the effects of antibiotics and pass this evolutionary advantage on to the next generation, thus developing resistance to antibiotics.¹⁹ It is therefore imperative that alternative antibiotic treatments are developed to combat bacterial infections through alternative approaches. The acronym ESKAPE refers to a group of six highly infectious and antibiotic-resistant pathogens (i.e., *Enterococcus faecium*, *Staphylococcus aureus*, *Klebsiella pneumoniae*, *Acinetobacter baumannii*, *Pseudomonas aeruginosa*, and *Enterobacter species*). In many cases, these pathogens are resistant to multiple drugs, which further complicates treatment and increases the risk of complications, particularly in the context of nosocomial (healthcare-associated) infections.¹⁵ It is therefore of the utmost importance to develop alternative methods of combating bacterial infections and to prevent the emergence of new resistances.

1.2.1 Antimicrobial Peptides (AMPs)

Antimicrobial peptides (AMPs) are short, positively charged amino acid sequences constituting an innate immune system component found in a diverse range of organisms, including animals and plants.¹⁵ AMPs have the ability to disrupt the cell membrane of both gram-positive (targeting lipoteichoic acid) and gram-negative (targeting polysaccharides)

bacteria, by their charge-mediated interactions. This mechanism of action renders it nearly impossible for pathogens to develop resistance and makes the AMPs effective against a broad range of pathogens (e.g., bacteria, fungi, and viruses).^{15, 20} However, despite these promising properties, AMPs are often complex to isolate, which makes them less accessible. Moreover, they often display local and systemic toxicity, as well as low stability.²¹

1.2.2 Bacteriophages and Phage Therapy

Bacteriophages are small viruses ranging in size from 20 to 200 nm. They are capable of infecting bacterial cells and utilizing these host cells for replication.²² Following the injection of the genetic material, the phage genome is replicated by the bacterial replication machinery. Upon completion of the replication process, the bacterial cell is lysed, resulting in the secretion of 50 to 200 newly synthesized phages.²³ The phages consist of a protein capsid as the head, which includes endolysins and the genetic material (either DNA or RNA, single or double stranded) and a tail (Figure 1-3a).²⁴ It is important to note that phages are not able to move independently and rely on Brownian motion for movement.²⁵ Bacteriophages exhibit a high degree of specificity in recognizing and binding to receptors on the surface of the host cell via tail proteins (see subsequent chapter for more details). Following the recognition and binding of the bacteriophage to the bacterial cell, the phage injects its genetic material into the cell, which is either integrated into the bacterial genome for further replication (lysogenic cycle) or it is replicated using the replication machinery of the bacterial cell, which then results in the direct lysis of the host cell (lytic cycle).^{15, 23}

The so-called phage therapy employs phages as an alternative to antibiotics, specifically targeting antibiotic-resistant bacteria.²² In the context of therapeutic use, only the lytic phages are considered relevant.²³ Phages exhibit high target specificity, targeting individual bacterial species or even individual variants of a species, due to their ability to bind to specific receptors on the host cells. The high degree of specificity presents both advantages and disadvantages when employing these phages as antibacterial agent. On the one hand, only target cells are killed without harming other bacteria species that are essential for a vital function of the body. On the other hand, it also requires precise and laborious identification of the target pathogens and the isolation of phages that are active against these target bacteria.

An alternative approach utilizes solely the endolysins derived from the bacteriophage. This method facilitates a more rapid bactericidal action, obviating the necessity for phage replication and secretion. Endolysins are peptidoglycan hydrolases encoded by the phages, capable of enzymatically degrading the structural components (i.e., the peptidoglycan) of the cell membrane of bacteria.²⁶ Moreover, endolysins are incapable of replication, thereby circumventing the potential for unintended consequences associated with horizontal gene transfer. In addition, the utilization of endolysins as a stand-alone agent eliminates the necessity for a host cell, facilitates a rapid killing response and reduces the probability of antibiotic resistance development. The high specificity of endolysins could simplify the regulatory approval process for widespread as well as commercial use in medical applications.^{15, 26, 27}

1.2.2.1 Bacteriophages and Their Specific Adhesion

Bacteriophages have developed a specific recognition-binding mechanism to achieve highly host-specific interactions. In the context of this thesis, this recognition-binding process is of particular interest and will be illustrated in more detail in the following section using the T4 phage, the most widely studied lytic phage.

The target host cells of the tailed T4 phage are *Escherichia* and *Shigella*. The bacterial components recognized by the T4 phage are either *E. coli* B-type lipopolysaccharides (LPS) or the ompC protein. A T4 phage possesses long (LTF) and short tail fibers (STF), which are both involved in the process of phage adsorption (Figure 1-3a). T4 bacteriophages exhibit six LTFs, of which at least three bind reversibly to the receptor of the host cell in the initial step. The high degree of specificity is achieved through the involvement of an adhesion protein located in the tip of each LTF. This protein is referred to as receptor-recognizing protein gp37, derived from the gene 37.^{28, 29} It consists of 1026 amino acids (per monomer), binds with its C-terminal region to the *E. coli* host and forms the LTFs with three other proteins (pg34, pg35, gp36) (Figure 1-3b).²⁸ The subsequent phase involves irreversible attachment of the STF to the inner core lipopolysaccharides of the host cell.^{28, 29} The long tail fiber proteins are not only useful for the bacteriophages themselves, but their isolated form can also be implemented in receptor-binding studies, structural studies with high resolution, and for specific detection and binding of bacteria.²⁸

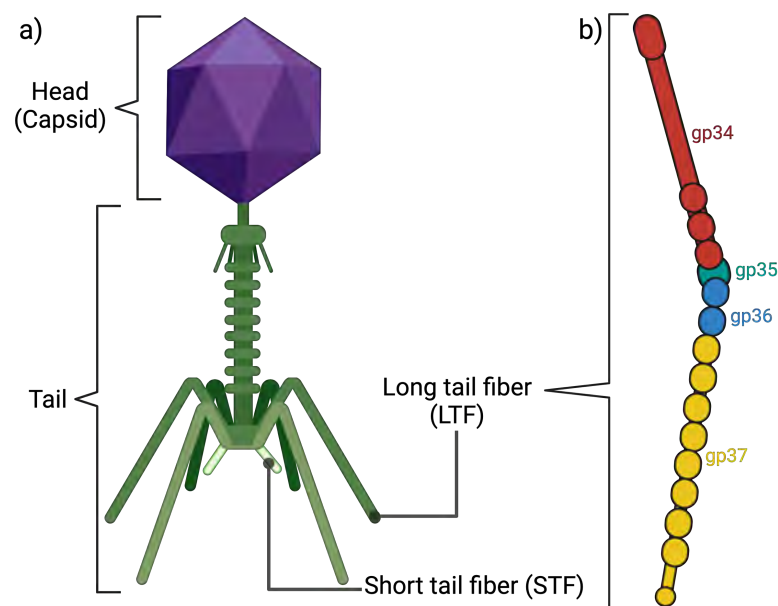


Figure 1-3: a) Schematic structure of T4 bacteriophage with head and tail. The tail includes long (LTF) and short tail fibers (STF). b) Structure of the LTF, consisting of the gp34, gp35, gp36, and gp37 proteins. Adhesion is mediated by gp37, binding by its C-terminal region to the *E. coli* host. Part b) adapted from Ref. ³⁰. Created with BioRender.com.

1.3 Nosocomial and Implant-Associated Infections

Nosocomial infections, or infections acquired in a healthcare setting, are considered secondary infections and are a leading cause of mortality and morbidity worldwide.^{31, 32} Despite the existence of strict protocols and guidelines for disinfecting surgical areas before and during surgery, there are still numerous potential sources of infection that can be delivered with medical devices or implants.³² The presence of microorganisms arranged in a biofilm on surfaces has been observed to result in elevated antibiotic resistance and the production of virulence-associated factors. Both of these aspects contribute to the complexity of treatment for medical device-related infections.^{13, 14} It is of particular importance to mention implant-associated infections (IAIs) in this context, as they are connected to high morbidity and healthcare costs.³³⁻³⁵ Examples of IAIs include prosthetic joint infections (PJIs), ureteral stent infections (USIs), cardiovascular implantable electronic device infections (CIEDIs), or neurosurgical infections (NSIs). Medical devices include both those that cross the anatomic barrier, such as venous catheters or dental implants, and completely integrated devices, such as hip and knee implants or cardiac implants.³⁴ The implantation of such devices is typically intended to substitute or support

various functions within the patient's body, with the objective of improving the patient's overall condition.³⁴

The occurrence of a PJI was estimated in 2023 to be around 3 - 5% with an even larger recurrence rate of around 15% following an infection treatment.³⁵ Staphylococci were reported as the most common bacteria provoking PJI.³⁴ Implants can be constructed from a variety of materials, including metals (e.g., stainless steel, titanium, silver, gold), ceramics, or polymeric structures.³⁶ In the context of biofilm formation, the surface properties of the implanted material, including surface energy, roughness, wettability, and elasticity, have been demonstrated to play a pivotal role in the process of (bacterial) adhesion.^{37, 38} Consequently, researchers concentrate on the development of specific biomaterials and surface coatings with the objective of modifying the implant surface properties in order to prevent biofilm formation.

1.4 Biomaterials

A report from the National Institutes of Health indicates that approximately 65% of microbial infections and 80% of chronic infections are attributable to the formation of a biofilm, which can occur not only on implanted medical devices but also on tissue.¹⁴ Hence, there is an urgent need to combat bacterial infections in general, with a particular focus on the prevention of bacterial biofilm formation on medical devices. Biomaterials are materials constructed to interact with biological systems mainly for medical purposes. Examples of these materials include polymers, ceramics, metals, and composites, which are utilized in a multitude of applications spanning therapeutic, diagnostic, and research-related fields.³⁹⁻⁴¹

1.4.1 Antibacterial Coatings

Antibacterial coatings can be defined as a subgroup of biomaterials, which are developed with the intention of impeding bacterial growth on surfaces such as medical devices, implants, or other healthcare-associated applications. Literature proposes a subdivision of antibacterial coatings into three major groups: (a) anti-adhesion/protein-repellent, (b) contact-killing and (c) antibacterial agent release coatings (Figure 1-4).^{32, 42} Anti-adhesion/protein-repellent coatings, such as the use of polyethylene glycol (PEG), are

designed to prevent biofilm formation in the initial stages. Contact-killing strategies are based on the disruption of the bacterial cell membrane by antibacterial molecules anchored to the surface (e.g., AMPs). Agent release coatings comprise materials that release antibacterial agents in a gradual, controlled manner. The temporary antibacterial effect is provided in a highly localized manner over time and can be delivered in a high concentration of antibacterial agent without inducing systemic toxicity.^{32, 43}

The majority of techniques classified within the subcategories of contact-killing and antibacterial agent release coatings are designed to eliminate pathogens and facilitate bacterial lysis in an "open space" manner. This approach results in the release of bacterial toxins into the surrounding environment leading to the recruitment of immunological cells and tissue inflammation. An alternative approach to combine bacterial killing and tissue protection is the creation of a "closed space" killing system, which prevents the contact of the bacteria and their released toxins with the surrounding tissue during the initial stages of medical device implantation. Such a system can entrap the pathogens and destroy them within a confined space, thereby shielding the surrounding cells from the bacteria as well as the released bacterial toxins. In this regard, hydrogels emerge as a highly promising material due to their capability to track bacteria.⁴⁴⁻⁴⁶

1.4.1.1 Anti-Adhesion/Protein-Repellent Coatings

Anti-adhesion/protein-repellent coatings (Figure 1-4) are passive coating materials designed to deploy their antibacterial properties in the early stage of biofilm formation, thereby preventing bacteria from attaching. The low surface energy of such surfaces results in poor wettability, high contact angles, and hence reduces the number of adsorbed bacteria, preventing biofilm formation.⁴⁷ One example for creating non-adhesive surfaces is through the coating of surfaces with polymers, either through physical adsorption or chemical attachment. In the case of physical adsorption, no covalent bonds are formed between the surface and the polymer (e.g., spin-, roller-, spray-, or layer-by-layer coating). The coatings are achieved by binding the polymers via van der Waals forces, hydrogen bonds, or electrostatic interactions. Despite the progress made in recent years, these coatings suffer from relatively poor stability.

In case of chemical attachment, the polymer coatings are covalently bound to the surface (e.g., self-assembled monolayers (SAMs), graft polymerization), thereby offering a high

coating stability.⁴⁸ A number of different polymers have been identified as potential candidates for use in anti-fouling polymer coatings: Hydrophilic polymers (e.g., PEG) form a protective hydration layer of water on the surface, which hinders protein adsorption both physically and energetically. Another group of polymers is zwitterionic polymers, which possess both positive and negative charges. Like the hydrophilic polymers, they form a robust hydration layer that has been demonstrated to be even more robust and efficacious than that of hydrophilic polymer alternatives.^{43, 48}

In addition to the mentioned hydrophilic surfaces, superhydrophobic surfaces are also utilized as anti-fouling surfaces. The efficacy of these surfaces is attributed to the phenomenon known as the "lotus effect," which is characterized by a high contact angle exceeding 150°. This property enables the surfaces to exhibit a self-cleaning mechanism due to their water repellency. The application of water to the surface results in the removal of contaminants, dirt, and pathogens. Moreover, the adhesion forces are reduced, which impedes bacterial adhesion. These superhydrophobic structures also result in a thin layer of air between the surface and the water droplets, promoting the simplified removal of adhering bacteria.^{43, 48}

1.4.1.2 Contact-Killing Coatings

Instead of chemical alteration of the surface itself, there is also the possibility to induce mechanical stress on the bacteria by e.g., modifying the topography of the surface (Figure 1-4). The application of mechanical stress forces the bacteria to adapt their contact area, thereby altering the area of interaction between the bacteria and the surface. Such an increased demand of energy prompts the bacterial cells to seek an alternative location for settlement, thereby reducing bacterial adhesion. Moreover, specifically designed surface topographies (e.g., nanopillars, nanowires, nanotubes) can not only prevent bacterial adhesion, but also physically rupture the cell membrane by causing stress, leading to cell death.⁴⁹ In this instance, the cell membrane does not offer enough elasticity to cope with the applied tensile forces skewering the cell membrane.⁵⁰

In addition to the physical-based contact-killing coating, there is also the possibility of biomolecule-based contact-killing of bacteria by immobilizing biocides or antibacterial substances on the surface.^{43, 49} Antibacterial polymers including quaternary ammonium compounds (QACs), as well as antimicrobial enzymes or peptides, represent two distinct

categories of synthetic and natural compounds, respectively.⁴³ QACs are the most prevalent contact-killing agents, offering a central nitrogen atom with four alkyl groups covalently attached to it.⁴² The functional principle of QACs (e.g., alkyl pyridiniums) is based on the electrostatic interaction and attraction between the negatively charged bilayer of bacteria and the positively charged QAC molecules. These interactions result in the disruption of the bacterial cell membrane and leakage of cellular contents.^{43, 50} The advantage of this approach is that the immobilized biocides are attached to the substrate, thereby unleashing their antibacterial effect locally without leaching into the surrounding environment.⁴² Application fields are dental material modifications⁵¹ or personal care products (e.g., disinfectant, soaps, disinfecting wipes etc.)⁵². Despite these advantages, QAC-based surfaces were seen to have the potential to induce inflammatory, irritating, and immune responses, which represents a significant drawback.^{50, 53, 54}

Other antibacterial contact-killing compounds include antibacterial metals and metal particles (e.g., Ag^+ , Mg^{2+} , Zn^{2+}).⁵⁵ Oxidative stress and reactive oxygen species (ROS) induced by the metals, as well as the release of free metal ions from metal surfaces have been identified as potential mechanisms responsible for the inactivation of bacteria.⁵⁰

1.4.1.3 Agent-Release Coatings

Agent-release coatings (Figure 1-4) are based on different kinds of carriers loaded with a variety of antibacterial drugs/biocides released over time, allowing for high concentration to be applied locally.⁴⁹ Potential carriers include hydrogels, ceramics, and other polymer-based systems. However, the release kinetics of these carriers is suboptimal, resulting in the rapid release of a high dose of biocide without a sustained effect. This limitation considerably constrains the prospective applications of these materials. A variety of studies have been conducted with different kinds of antibiotics loaded and applied in a variety of carrier systems, including biodegradable (PLGA-)nanofibers⁵⁶ or -particles⁵⁷, as well as alginate, chitosan or collagen.⁴⁹ In addition to antibiotics, such systems can also be used to load and release other materials, such as silver and copper nanoparticles.⁵⁸ Here, the antibacterial action is primarily based on the release of ions (i.e., silver ions) creating ROS, which block certain protein expression processes in bacteria.^{31, 49}

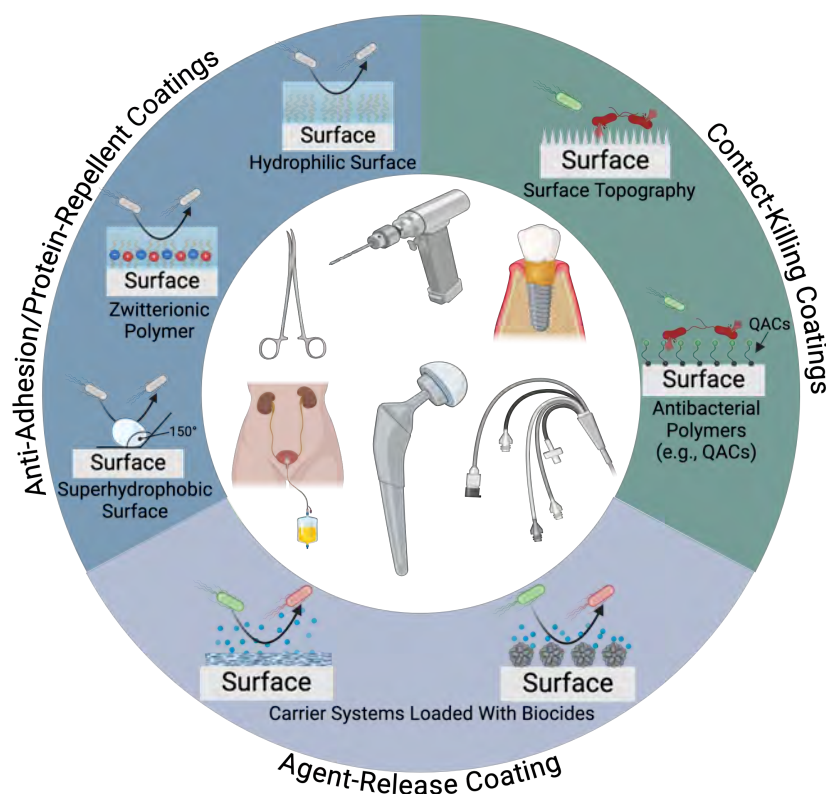


Figure 1-4: Three major groups of antibacterial surface coatings. a) Anti-adhesion/protein-repellent coatings (e.g., hydrophilic, zwitterionic and superhydrophobic (polymer) coatings). b) Contact-killing surfaces (e.g., micro- and nanostructured surfaces (surface topography) and antibacterial polymers such as quaternary ammonium compounds (QACs). c) Agent-release coatings (e.g., alginate, chitosan layers or PLGA particles as carrier systems loaded with antibiotics or antibacterial drugs). Created with BioRender.com.

The major advantage of releasing therapeutic agents over time into the blood of patients, particularly in the form of nano- or microparticles, is that the drug is stable and protected against physiological degradation within the particles. This protection increases the therapeutic efficacy and minimizes drug toxicity and side effects.⁵⁹ However, the difficulty in controlling the release kinetics persists as a challenge in the development of reliable systems.⁴² The majority of previously illustrated and described antibacterial approaches result in the destruction of bacteria in an open space, leading to the fragmentation of bacteria and the subsequent release of toxins into the surrounding tissue. The development of antibacterial systems that kill within a "confined space" could prevent this issue. Such systems could shield and protect the surrounding tissue from bacteria and their toxins.

Accordingly, this thesis is devoted to the development of modular systems capable of trapping and killing bacteria in a “confined space”.

1.5 Poly(Lactide-Co-Glycolide) Acid (PLGA)

Especially in the context of biomedical applications, there has been considerable interest in poly(lactide-co-glycolic) acid (PLGA). It is well-established and has already been extensively utilized in a multitude of medical and pharmaceutical applications, including drug delivery⁶⁰⁻⁶², tissue engineering^{63, 64} or bone regeneration⁶⁵. Its exceptional biocompatibility, biodegradability, and favorable plasticity properties have contributed to its widespread implementation, which has also resulted in official approvals by the US Food and Drug Administration (FDA) and the European Medicines Quality Agency (EMA).^{60, 63, 66, 67} The amorphous co-polymer PLGA (Figure 1-5) is synthesized by copolymerization of the two monomers lactic acid (LA) and glycolic acid (GA).⁶³ Polylactic acid (PLA) is commonly used in the *D,L*-PLA form, which is an amorphous polymer. In contrast, polyglycolic acid (PGA) is a crystalline polymer that lacks the methyl side group present in PLA.⁶⁰

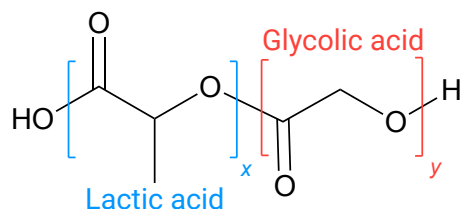


Figure 1-5: Chemical structure of poly(lactic-co-glycolic) acid (PLGA). The average number of repeating units of lactic acid (LA, blue) and glycolic acid (GA, red) are presented as x and y, respectively.

The ratio of the two monomers can be modified during the synthesis process, resulting in significant alterations to the copolymers' physicochemical properties (Figure 1-6a).⁶³ LA-rich copolymers exhibit enhanced hydrophobicity in comparison to GA-rich copolymers, due to the increased tendency of GA to absorb water.⁶⁰ Furthermore, this enhanced affinity towards water affects the degradation time, resulting in accelerated degradation properties due to the faster penetration of water into the polymer matrix of GA-rich PLGA polymers. This is because GA-rich copolymers are hydrolytically more unstable than those with a higher LA content.^{60, 68} In comparison to the other compositions, the 50:50 LA:GA

compositions exhibit an accelerated degradation rate, demonstrating the most rapid degradation of all the compositions.⁶⁹ The ratio of monomers in the polymer is not only a factor in determining the hydrophobicity/hydrophilicity and, consequently, the degradation properties of the polymer; it is also a determinant of the mechanical strength. A higher ratio of crystalline PGA results in an increased amorphous structure of PLGA, which in turn results in a more flexible polymer with reduced mechanical robustness.⁶⁹ Furthermore, the mechanical resistance is also linked to the glass transition temperature (T_g), which represents the point at which the polymer transitions from a hard, glassy state to a softer state. This temperature was shown to be between 45 °C and 55 °C for various PLGA polymer compositions (Figure 1-6b).^{63, 68, 69}

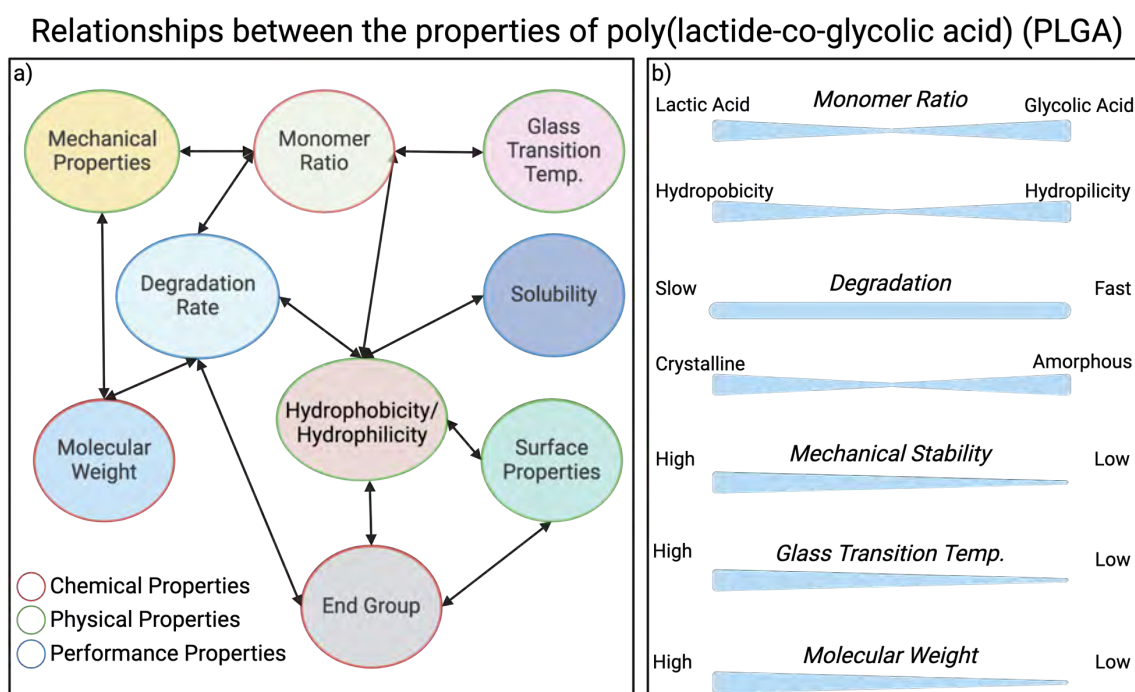


Figure 1-6: a) Relationships between different selected properties of PLGA and their impact on the final polymer properties. b) Actual relationships between selected PLGA properties. Created with BioRender.com.

PLGA can provide a variety of end groups, which can also impact the characteristics of the resulting polymer. The most prevalent end groups are hydroxyl (-OH), carboxyl (-COOH), ester, and amine (-NH₂). In general, acid end groups have the effect of increasing hydrophilicity and, consequently, the degradation rate, while decreasing crystallinity, which in turn is connected to mechanical stability. In contrast, ester end groups tend to have the opposite effect, by increasing hydrophobicity and slowing down the degradation rate.⁷⁰

1.6 Poloxamer (Pluronic®)

Poloxamers (trademarked name “Pluronic®”) are A-B-A triblock copolymers offering an amphiphilic and water-soluble class of copolymers with good biocompatibility, high water extractability, low tissue adhesion and hence broad usage in biomedical applications.⁷¹⁻⁷³ Poloxamers consist of a central hydrophilic block of poly(ethylene oxide) (PEO) flanked by two hydrophobic poly(propylene oxide) (PPO) parts, leading to a PEO-PPO-PEO structure (Figure 1-7). The presence of hydrophilic as well as hydrophobic blocks provides the polymers with an amphiphilic nature allowing them to self-assemble into micelles in aqueous solutions.⁷¹ By tuning the molar mass ratio of the blocks, the chemical and physical properties can be adjusted, modifying the potential applications and *in vivo* interactions. Similarly to PLGA and PEG, Pluronic® is employed as a drug delivery system or surfactant, to form hydrogels, or as an extractable proagen.^{71, 73, 74} BASF (Badische Anilin- und Sodafabrik) introduced a specific nomenclature system for Pluronic® with the initial letters F, L, and P representing its state as either flakes, liquid, and paste, respectively. The first or first and second numbers following the letter relate to the molar mass of the PPO blocks (multiplied by 300) and the last number indicates the weight fraction of the PEO block in percentage (multiplied by 10).^{71, 73} This nomenclature is only a rough estimation to categorize the different types of Pluronics®, the average unit numbers of F-127 and F-68 which are both used in this thesis are ≈ 200 units of PEO, ≈ 65 units of PPO and ≈ 154 units of PEO, ≈ 29 units of PPO, respectively.⁷¹

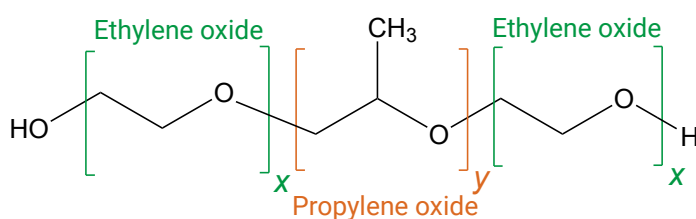


Figure 1-7: Chemical structure of poloxamers (Pluronics®) with the central, hydrophobic propylene oxide (PO) block in the middle flanked by the two, hydrophilic ethylene oxide (EO) blocks on both sides. The average numbers of repeating EO and PO blocks are presented by x and y, respectively.

1.7 Polyethylene Glycol (PEG)

Polyethylene glycol (PEG) is a frequently utilized and highly versatile FDA-approved polymer, particularly in the context of pharmaceutical applications.⁷⁵⁻⁷⁶ PEG is a neutral polyether (Figure 1-8) with hydrophilic properties, making it soluble in water but also in a multitude of other organic solvents, including dichloromethane and toluene. Moreover, it is non-toxic for most molecular weights⁷⁷ (M) and does not harm cells in most cases, yet it still interacts with cell membranes.^{75, 78} The polymer is available in a range of molecular weights, exhibiting a liquid, viscous state at M values below 1000 g/mol. As the M of PEG increases, the polymer obtains a solid, waxy state. The production process involves polymerization of ethylene oxide and water, resulting in a variety of degrees of polymerization and the possibility for further functionalizing the polymer by different functional groups (e.g., PEG-amine, PEG-aldehyde, PEG-thiol).⁷⁶ Due to its high water solubility, PEG is frequently employed as a porogen in the context of polymer materials and particles⁷⁹⁻⁸¹. This renders PEG a promising polymer/porogen candidate for this thesis.

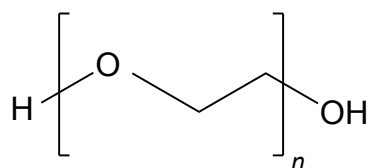


Figure 1-8: Chemical structure of polyethylene glycol (PEG). The average number of repeating units is presented by n .

1.8 Polymer Particle Production

1.8.1 Particle Preparation Techniques

Nanoparticles, in particular those with a porous structure based on polymers, are a widely utilized class of drug carrier systems. They are employed in the delivery of therapeutic agents to infected sites and in tissue engineering applications.⁸² The range of available preparation techniques is dependent on the desired application and requirements. They can be categorized in two main groups of bulk production techniques and microfluidic approaches. Microfluidic-based technology is especially useful to produce polymer-based particles with narrow size distributions in a highly controlled and finely tuned manner.⁸³ In

case of microfluidic approaches, the dispersed phase (i.e., polymer-solvent mixture) is cut by the flow (e.g., flow focusing, cross-flow, co-flow) of the continuous phase into droplets. Therefore, the flow rates determine the droplet size, enabling the formation of highly monodisperse particle distributions.^{84, 85} While microfluidic approaches facilitate precise and homogeneous particle production, this thesis primarily focuses on bulk production techniques, as they offer a more rapid and straightforward production process.

Bulk production techniques are sub-grouped into bottom-up or top-down techniques (Figure 1-9). Each of them offers a distinct set of advantages and disadvantages outlined in the following section. The most famous top-down methods are the emulsion solvent evaporation, emulsion diffusion and salting-out techniques. For the bottom-up techniques, which utilize a monomer as a starting point, the emulsion polymerization, interfacial polymerization and precipitation polymerization methods are used.^{86, 87} Since the bottom-up techniques need more complex chemical processes to form the desired particles out of atomic or molecular precursors, the desired particles are accompanied by contaminations (e.g., unreacted monomers, initiators, surfactants). Therefore, to obtain particles of the highest quality, it is necessary to implement a series of rigorous purification processes which are time consuming, costly and complex.⁸⁷ In general, bottom-up methods provide more precise control over particle size and properties; however, they are more complex due to the necessity of additional purification and solvent removal steps. Top-down methods are typically more straightforward, facilitating large-scale production. However, they tend to result in broader size distributions and a greater range of particle shapes.⁸⁷⁻⁸⁹

The selection of particle preparation technique is dependent upon the specific application and the desired characteristics of the final particles. In the case of polymer-based particles that are used as drug delivery systems, it is of particular importance to consider the hydrophilic/hydrophobic properties of the drug to be delivered. In order to encapsulate the drug efficiently while producing the particles, it is necessary to select an appropriate production technique. Some of the most widely used approaches are those that are based on emulsions, which are simple and allow for large-scale production. Examples of these approaches include emulsion evaporation and emulsion diffusion.⁸⁷ Emulsion techniques employ the use of polymers that have been dissolved in water-immiscible, volatile organic solvents emulsified in an aqueous-based solution. The emulsification process itself can be conducted by a variety of techniques, including the use of mechanical shear forces, ultrasonic homogenization, or high-pressure homogenization. Once an emulsion has been

formed, the volatile solvent is removed either by diffusion or evaporation, resulting in the solidification of the polymer particles.^{90, 91}

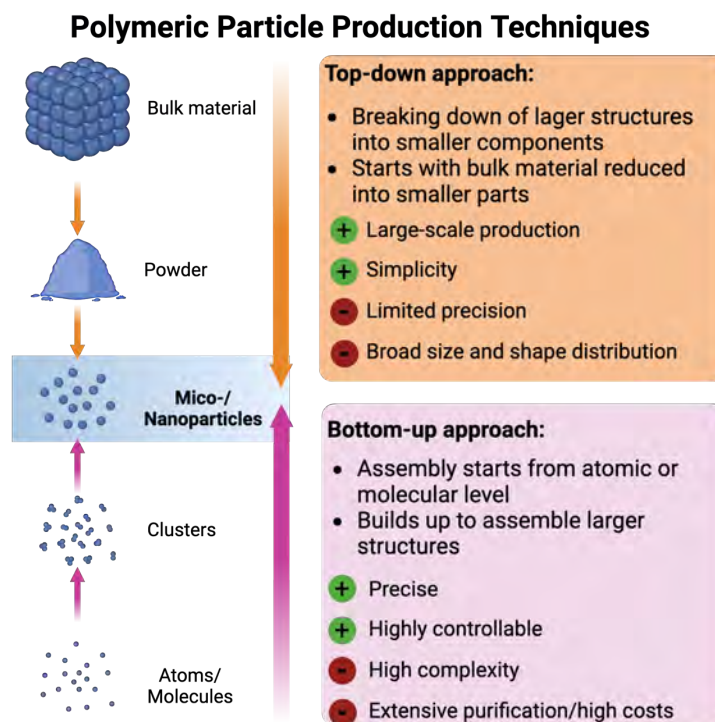


Figure 1-9: Basic principles of top-down and bottom-up approaches for the polymer-based particles production. Created with BioRender.com.

Hollow polymer particles have attracted significant attention due to their potential applications in diverse fields (e.g., drug delivery, coatings, cosmetics, catalysts, or photonic crystals).⁹² Various techniques have been developed and described to form such hollow polymer-based particles, including template-assisted methods⁹³, self-assembly⁹⁴⁻⁹⁶, or spray-drying⁹⁷. Another well-known and widely used method for the production of microspheres, especially in the field of drug delivery, is the double emulsion method. This method is particularly useful for encapsulating and delivering hydrophilic as well as hydrophobic drugs.⁹⁸ Additionally, it is an effective approach for forming hollow polymer-based microcapsules, not for the purpose of encapsulating drugs, but to create a confined space within the particles to trap bacteria.

1.8.2 Pore-Forming Agents – Porogens

Porogens are pore-forming agents that are utilized to introduce porosity within a micro- or nanoparticle system. The existing literature classifies pore-forming agents into two major

categories based on their physical characteristics: soft and hard porogens.⁸² These two groups include several sub-groups. In the case of hard templates, a distinction can be made between two sub-divisions: (a) conventional hard-templating and (b) sacrificial-templating.⁹² In both cases, the template material is simply incorporated into the material and occupies some space.^{99, 100} Once the particle formation process is complete, the hard template is removed, resulting in the formation of a porous structure. A disadvantage of the hard template approach is the potential collapse of the particle structure after template removal.⁸² Examples of conventional hard-templates are silica and carbon particles.⁹² In the case of sacrificial-templating, the template material is typically more straightforward to remove and often includes solvent-dissolvable porogen (e.g., polymer latex particles, polystyrene beads).⁹²

In addition to hard templates, soft templates are also utilized. These templates exhibit inter- and intramolecular interactions with the polymeric particle core material and self-assemble into various structures during the formation process, occupying space and leaving behind cavities upon template removal. Template removal is mainly accomplished through solvent extraction.^{82, 92} Typically, a porogen is introduced during polymer-based particle formation and production, requiring its inert composition to facilitate uniform distribution within the organic phase.⁸² Polymers with low molecular weight (e.g., polyethylene glycol) or gas-producing particles (e.g., ammonium bicarbonate) have also been reported in the literature as pore-forming agents.⁸²

1.9 Thermodynamic Spreading Coefficient

To predict the morphology of a particle in a system comprising two phases (polymer/solvent and oil) within a third continuous phase (aqueous phase), three spreading coefficients (S) are defined with the interfacial tensions (γ_{ij} , γ_{ik} , γ_{jk}) acting between the three phases i, j and k . Generally, the thermodynamic spreading coefficient represents the ability of a liquid to spontaneously spread on a solid or another liquid surface and is defined by the following equation:

$$S = \gamma_{jk} - (\gamma_{ij} + \gamma_{ik}) \quad (1-1)$$

In case of a positive spreading coefficient ($S_i > 0$), the liquid will spontaneously spread over the surface. Conversely, no spreading occurs when the spreading coefficient is negative

($S < 0$). In order to transfer the system to a polymer/oil system in a continuous aqueous phase, the spreading coefficients S_p , S_o and S_w are assigned to the polymer, oil and aqueous phase, respectively. In such a system, the thermodynamic spreading coefficient plays a critical factor determining the final morphology of the system. Four distinct situations are possible, resulting in either a core-shell particle (Figure 1-10a), wherein the oil phase is enclosed by the polymer phase, an “acorn” particle (Figure 1-10b), two separated droplets (Figure 1-10c), or an inverse core-shell morphology (Figure 1-10d).¹⁰¹

Nevertheless, these assumed morphologies are only theoretical approximations; real systems are typically much more complex, exhibiting a variety of additional morphologies (e.g., multi-core morphology, non-centered core morphology, “raspberry” morphology etc.) due to the influence of additional factors (e.g., viscosity, temperature, evaporation, and stirring rate etc.).¹⁰¹

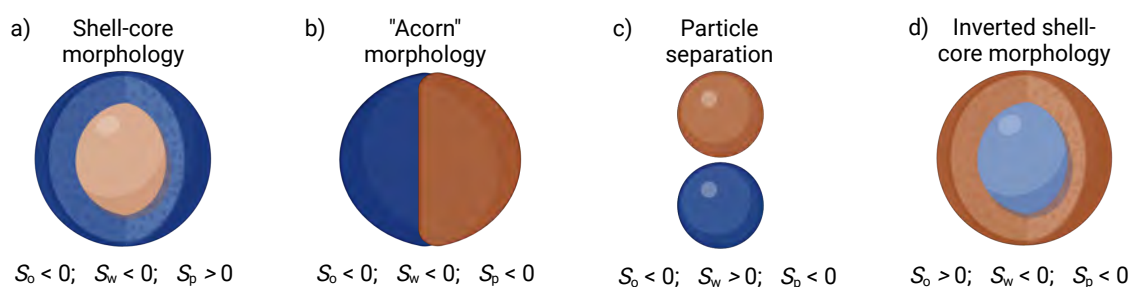


Figure 1-10: Correlation between thermodynamic spreading coefficients (S) and particle morphology of a polymer (p, blue)-oil (o, brown) system in a continuous aqueous (w) phase. Created with BioRender.com.

1.10 Synthetic Lipid Vesicles – Liposomes

Liposomes are spherical, artificially created vesicles composed of an aqueous core which is enclosed by one or multiple lipid bilayer(s). In most cases, liposomes are composed of phospholipids consisting of a hydrophobic tail group and a hydrophilic head. These amphiphilic characteristics favor the formation of lipid bilayers in aqueous solutions. In the bilayer structure, the hydrophobic tails face towards each other, while the hydrophilic heads face towards the outside aqueous phase (Figure 1-11).¹⁰² Hydrophobic and van der Waals interactions are the main driving force for the lipid bilayer formation. Additionally, the hydrophilic head groups interact with the water molecules (hydrogen bonds and polar interactions) further stabilizing the lipid bilayer.¹⁰²

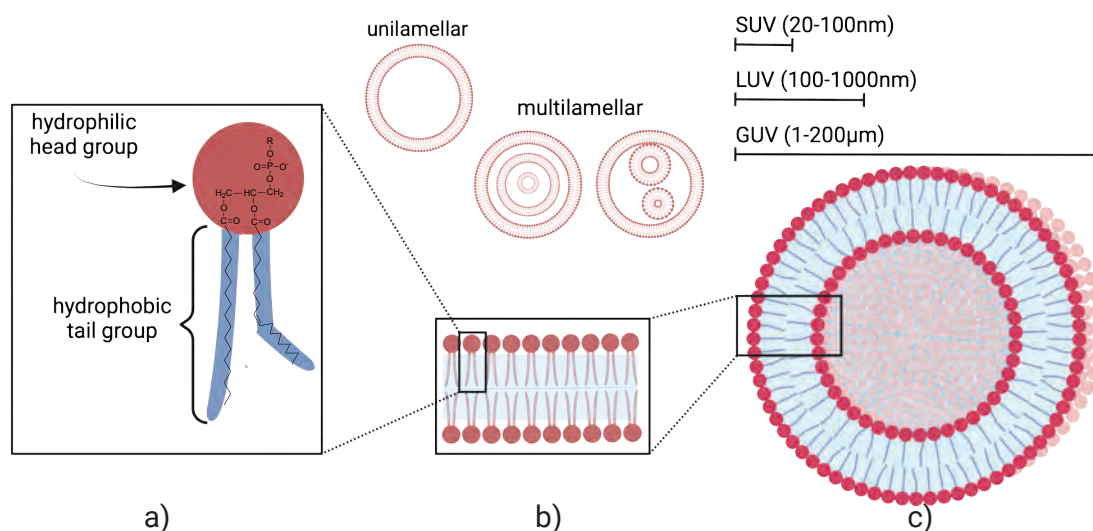


Figure 1-11: Schematic illustration of structure of liposomes. a) Phospholipid with hydrophilic head group (including phosphate and glycerol) and hydrophobic tails with a saturated and unsaturated fatty acid. b) Phospholipids arrange in a bilayer. c) Liposome formed out of phospholipid bilayer. Liposomes can either be unilamellar or multilamellar and are as well classified according to their size as small-(SUV), large-(LUV), and giant unilamellar vesicles (GUV). Created with BioRender.com.

This process is driven by the desire of the system to reduce its free energy and is considered one of the most powerful tools in bottom-up assembly.¹⁰³ Liposomes are categorized by either size into small (20 - 100 nm), large (100 - 1000 nm), or giant (1 - 200 μm) vesicles¹⁰⁴ and/or their number of bilayers (unilamellar, oligolamellar, or multilamellar).¹⁰³ The bilayer itself offers a thickness of 3 - 5 nm.¹⁰⁴ Liposomes are not only capable of carrying hydrophobic as well as hydrophilic agents as drug delivery systems, but are also frequently used in synthetic biology as mimetics to the cellular systems.^{103, 105} They are also implemented as a simplified model system to study biological cell membranes in terms of membrane dynamics, permeability, or protein and molecule interactions.^{102, 104}

1.10.1 Synthetic Vesicles – Formation Techniques

Synthetic vesicles are artificially constructed structures that are designed to mimic the structural and functional characteristics of natural cell membranes. Synthetic vesicles are utilized in a multitude of medical and scientific applications, including investigations into the mechanisms of cellular uptake, cell division, and drug delivery. The formation of synthetic vesicles can be achieved through a variety of techniques, depending on the desired

properties and the intended application. The most significant of these are (a) thin-film hydration: A phospholipid film is dried on a substrate by evaporating the organic solvent in which the lipids were dissolved (e.g., chloroform, ethanol). Subsequently, the stacked layers of lipids are gently hydrated, resulting in the formation of liposomes in an aqueous solution (Figure 1-12a). This formation method is particularly advantageous for charged lipids. (b) Electro-formation: The lipids, dissolved in an organic solvent, are distributed as a thin film on a conductive surface (e.g., an indium tin oxide-coated glass substrate). The lipid film is hydrated in the presence of an alternating electric field applied across the lipid film. The electric field induces swelling and facilitates the detachment of the formed liposomes (Figure 1-12b). This technique is especially useful for the formation of giant unilamellar vesicles. (c) Phase/emulsion transfer method: This method entails the formation of an emulsion, whereby the organic phase is mixed with an aqueous phase, resulting in the generation of water-in-oil droplets encapsulated by a lipid monolayer. The emulsion is then transferred through an oil-water interface, facilitating the addition of another lipid layer on top of the emulsion droplets, thereby creating a lipid bilayer (Figure 1-12c). The phase/emulsion transfer method is particularly advantageous for the formation of cargo-loaded liposomes. (d) A method that allows for precise control over vesicle size and composition is the formation via microfluidics (Figure 1-12d). The process begins with the creation of a water-in-oil droplet surrounded by a lipid monolayer using a microfluidic device. Subsequently, these droplets flow through an oil-water interface, forming vesicles with a lipid bilayer.^{106, 107} In addition to the fundamental microfluidic technique, Weiss et al., have developed a methodology employing microfluidics and pico-injection to generate droplet-stabilized giant unilamellar vesicles (dsGUVs). These dsGUVs exhibit a high degree of mechanical and chemical stability and can be loaded with diverse biomolecules in a sequential manner. This facilitates the development of prototypes for complex synthetic cells.¹⁰⁸

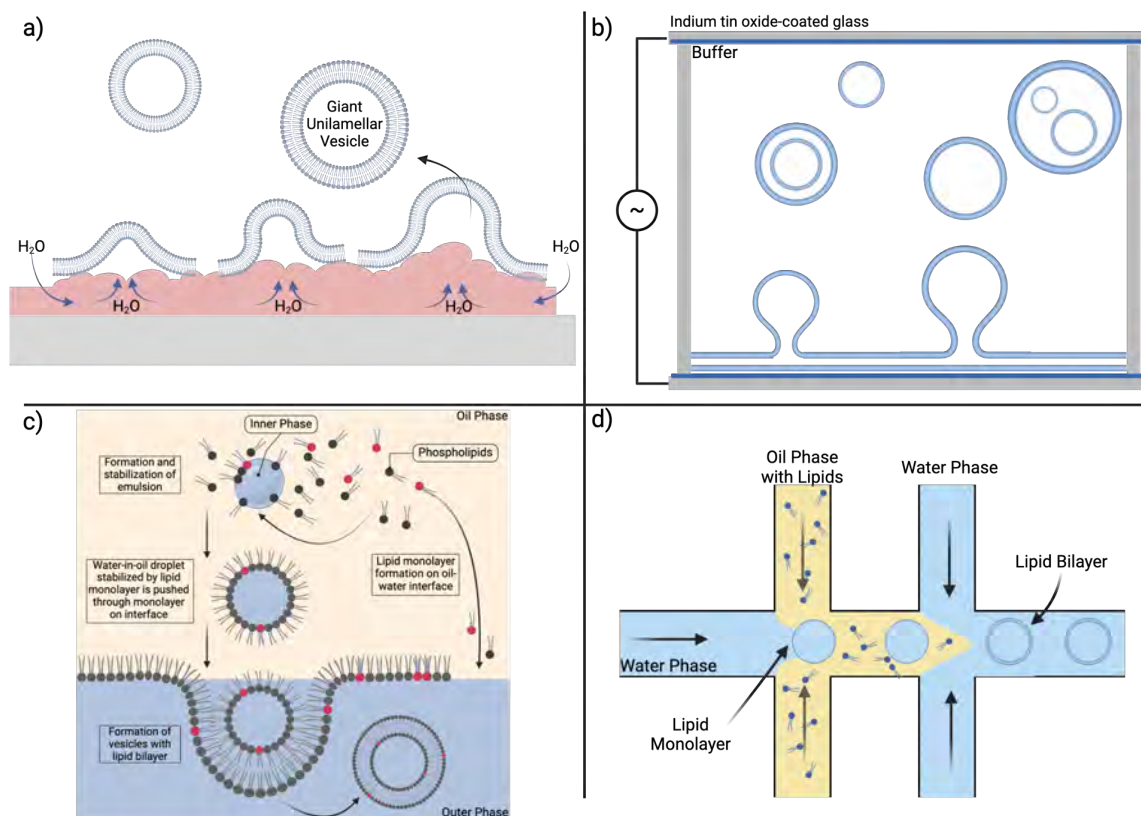


Figure 1-12: Schematic illustrations of synthetic vesicles formation techniques. a) Thin-film hydration technique, b) electro-formation technique, c) phase transfer/emulsion transfer method and d) microfluidics. Created with BioRender.com.

1.10.2 Particle Endocytosis by Liposomes

Apart from drug delivery and biological membrane mimicking, liposomes are used to study the process of endocytosis to achieve closer insights into the process of receptor-mediated endocytosis and phagocytosis. In this context, a significant number of studies were conducted on the engulfment process of spherical particles to achieve a more profound understanding of the process itself.¹⁰⁹⁻¹¹³ However, bacteria and viruses are mostly anisotropic in shape, making the endocytosis process even more complex.¹¹⁴ Nevertheless, the development of a dynamic and active system consisting of synthetic vesicles specifically targeting single types of bacteria would be a great tool to battle bacterial infections.

Endocytosis is a complex process affected by many different aspects (e.g., particle size, shape and surface chemistry, lipid composition of liposome, liposome size, environmental

conditions, etc.).^{112, 114, 115} The following paragraph will briefly explain the basic process of particle engulfment by synthetic vesicles.

The complex process of synthetic liposomes engulfing particles involves several important steps and aspects (Figure 1-13):¹¹⁵⁻¹¹⁷

- a) *Membrane curvature and bending energy*: the bilayer of the liposome needs to bend to a certain degree to engulf the particle. This process involves a membrane curvature change. This change is also connected to the bending energy ($\Delta G^{bending}$) necessary to overcome and dependent on the elasticity properties of the membrane.
- b) *Adhesion energy*: the adhesion energy ($\Delta G^{adhesion}$) generated by the interactions between the particle and the lipid membrane needs to overcome the bending energy of the membrane as well as the energy created due to the areal expansion caused by the extra volume of the particle internalized. This implies that particle volume is a highly critical factor in the process of engulfment. As the adhesion energy increases, so does the percentage of wrapped particles. Nevertheless, exceeding a certain adhesion energy will rupture the membrane of the vesicle.
- c) *Thermodynamic stability*: the system with engulfed particle must be thermodynamically stable with a minimized free energy state.
- d) *Fission energy*: in the last step of engulfment, the particle is completely encapsulated by the liposome making membrane scission necessary. For this process a certain energy barrier ($\Delta G^{fission}$) needs to be overcome associated with breaking and reforming the lipid membrane.¹¹⁶

In summary, to achieve full engulfment of a particle by a synthetic vesicle, the following simplified theoretical equation needs to be fulfilled:¹¹⁷

$$|\sum \Delta G^{adhesion}| > \Delta G^{bending} + \Delta G^{expansion} + \Delta G^{fission} \quad (1-2)$$

Furthermore, Azadbakht et al.¹¹⁴ investigated the engulfment process of a dumbbell-shaped particle by a GUV and made several noteworthy observations. First, the wrapping time was found to increase with an elevated initial membrane tension, thereby establishing membrane tension as a pivotal factor influencing the duration of engulfment. Second, contrary to expectations, the initial orientation of the dumbbell was identified as a minor contributor to the final wrapping state. Third, an increase in adhesion energy was observed to accelerate the engulfment process.

Another crucial element to consider is the synthetic vesicle size, which is in turn linked to the membrane tension. Lin et al. observed a reduction in membrane tension as vesicle size increased. This phenomenon is on the one hand connected to the interfacial tension acting between the water and the hydrophobic tails of the lipid bilayer. With increasing vesicle size, the area density of the hydrophilic lipid head groups increases, forming a denser bilayer and thereby reducing the contact between the hydrophobic tails and the water phase. On the other hand, as the vesicle radius increases, the membrane curvature decreases, which also reduces the membrane tension.¹¹⁸

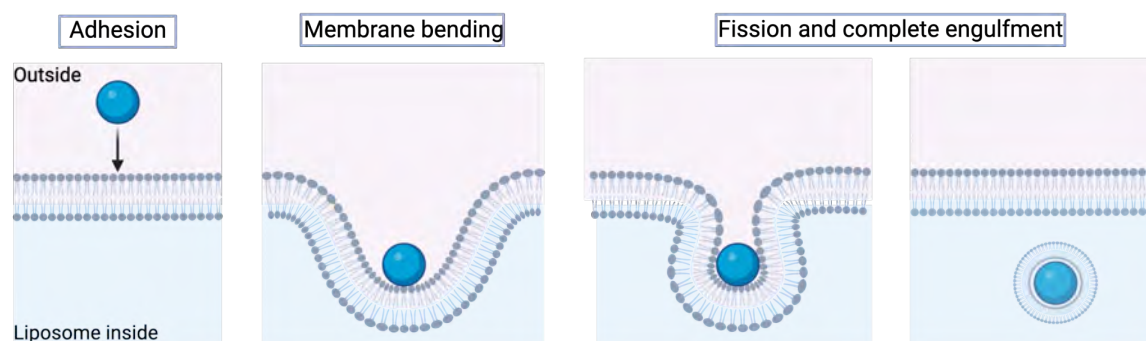


Figure 1-13: Schematic illustration of engulfment process of a rigid, spherical particle by a flexible, synthetic lipid vesicle membrane. In the first step, the particle adheres to the lipid membrane. In the second step, the membrane is bending. The last steps include fission of the membrane and complete particle engulfment. Created with BioRender.com.

1.11 Plasmonic Nanoparticles – Gold Nanorods (AuNRs)

1.11.1 Properties

Plasmonic nanoparticles, particularly gold nanorods (AuNRs), have gained increasing interest within the field of nanotechnology due to their distinctive optical properties, which led to the emergence of a diverse range of potential applications. The motion of electrons and the available space for their movement within the material exert a significant influence on the material's physical and chemical properties. Due to the significant space constraints, this phenomenon is particularly pronounced in nanoscale materials. Moreover, the high surface-to-volume ratio leads to an accentuated effect of surface properties. This aspect renders nano-sized materials considerably different from their bulk material, gathering many new optical, catalytic and electrical properties.^{119, 120}

Plasmonic nanoparticles are frequently composed of noble metals, such as silver or gold due to the presence of free conduction electrons at the surface of the particles. If the nanoparticles are exposed to an external, oscillating electromagnetic field of light with a frequency that matches the inherent frequency of the free surface electrons, a collective coherent oscillation of the conduction band electrons is induced (Figure 1-14a). This oscillation results in the separation of the ionic core and free electrons, thereby creating a dipole oscillation. This occurs due to the oscillating motion of electrons on the surface, driven by Coulomb forces.^{120, 121} This collective resonant oscillation of the electrons is referred to as surface plasmon resonance (SPR) and highly depends on the particle's shape, size and aspect ratio as well as the surrounding medium. The strong absorption of light caused by the SPR also gives rise to the characteristic UV-vis spectrum and color of plasmonic nanoparticles.

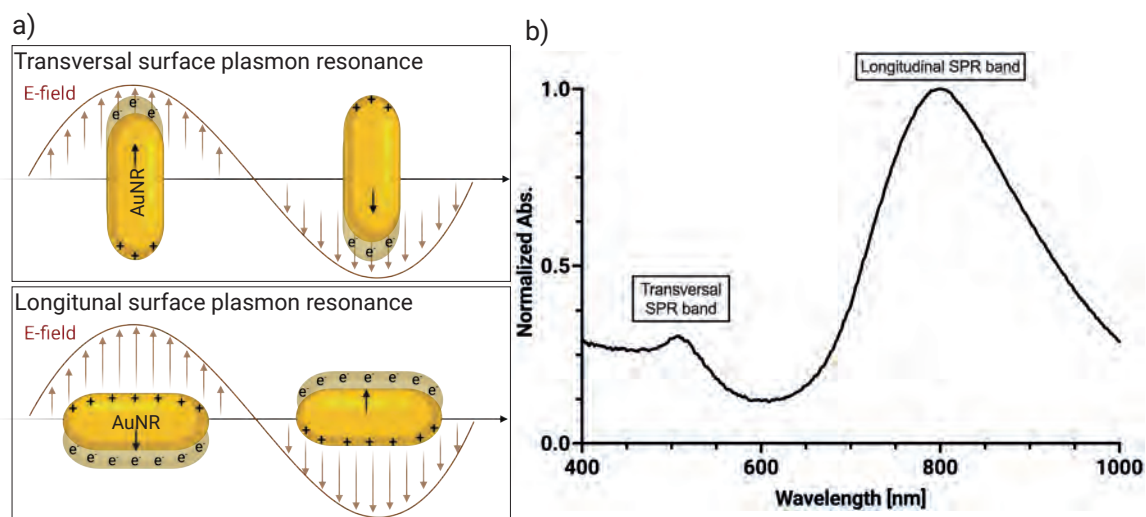


Figure 1-14: a) Schematic illustration of the interaction of the electric field (E-field) with gold nanorods (AuNRs) inducing collective oscillation of the free conduction band electrons (e^-) resulting in the characteristic transversal and longitudinal surface plasmon resonance (TSPR and LSPR). b) Characteristic, exemplary absorbance spectrum of AuNRs with the two SPRs. Parts were created with BioRender.com, adapted from Ref.¹²¹.

AuNRs are in this context specifically interesting due to their readily and extensively tunable SPR wavelength. Their structural anisotropy causes the presence of two SPR modes, in contrast to the single band observed in spherical particles. The transversal SPR oscillates along the short axis and can be observed within the visible region of the spectrum. The second, stronger longitudinal SPR mode is attributed to the oscillation along the long

axis and shifted to higher wavelengths in the spectrum (Figure 1-14b). The location of the absorbance maximum of the longitudinal SPR (LSPR) band can be tuned and shifted from the visible to the near-infrared (NIR) region, by manipulating the aspect ratio (AR , length/width) of the particles. In contrast, the transversal SPR (TSPR) band stays unchanged in case of size alterations. Moreover, AuNRs are known for their efficient conversion of light into thermal energy, a process known as photothermal conversion. If AuNRs are exposed to light at their resonant frequency, the light energy is converted into heat via photophysical processes, which is primarily based on electron-photon and photon-photon interactions.¹²⁰⁻¹²²

1.11.2 Biomedical Applications Applying AuNRs

The distinctive characteristics of AuNRs make them suitable for a multitude of applications, including optoelectronics, catalysis, imaging, and medical procedures. Focusing on the latter, AuNRs are utilized in the context of drug delivery, biosensing, biomedical imaging or photothermal and cancer therapy.¹²⁰ Therefore, it is especially important to account for biocompatibility and toxicity of the AuNRs. AuNRs are normally produced and stabilized by the use of cetyltrimethylammonium bromide (CTAB), a molecule that is considered harmful to cells due to its highly-positive charge.¹²³⁻¹²⁵ A number of studies have demonstrated that unbound CTAB can induce cytotoxic effects on human cells. However, the application of excessive cleaning, centrifugation, and the removal of excess unbound CTAB has been shown to result in higher cell viability rates and a non-toxic profile for AuNRs.^{120, 126} After excessive purification, even CTAB-stabilized AuNRs are expected to be safe for the application in clinical and *in vivo* studies. To entirely circumvent the toxicity of CTAB, alternative studies have replaced or coated the stabilizing CTAB molecule with biocompatible molecules (e.g., polyethylene glycol (PEG), polystyrene sulfonate (PSS) or 11-mercaptoundecanoic acid (MUA)).^{123, 127, 128} This bioconjugation process further eliminates any potential sources of toxicity, making the AuNRs an optimal tool for a multitude of applications within the medical sector.

To date, photothermal therapy (PTT) has been primarily used in the context of cancer treatment, offering the potential to eradicate cancer cells through heat generation while minimizing damage to surrounding tissue. PTT is effective for tumors that are challenging to treat with conventional methods due to their location, as AuNRs are capable of ablating

the tumor cells. The minimally invasive procedure of PTT with AuNRs makes it an effective and promising approach in the field of oncology.

PTT using AuNRs can also be implemented against bacterial cells. Given that the protective matrix of bacterial cells includes nucleic acid and proteins, localized heat can induce protein denaturation, accompanied by damage and inactivation of the protective cell layer allowing for simplified drug penetration and killing.¹²² Consequently, AuNRs can also be employed as antibacterial agents to generate localized heat sufficient to kill pathogens. This approach could be a promising treatment option for bacterial infections, particularly in cases where the pathogens are resistant to conventional antibiotics. The combination of AuNRs' diverse properties, including PTT and drug delivery capabilities, with the gold surface modifications through the incorporation of antibacterial peptides, has led to the development of highly effective antibacterial materials, which have been extensively investigated by numerous research groups.^{122, 129-133} Qiao et al.¹³¹ for example designed AuNRs with a charge-switchable coating induced by pH changes. These polymethacrylate with pendant carboxyl betaine groups decorated AuNRs offered a negative surface charge at physiological conditions, allowing for long blood circulation. The surface charge switched to positive charge values at lower pHs as present in bacterial infection sites. This positive surface charge allowed for enhanced nanoparticle binding to the negatively charged bacterial cell wall and hence improved killing properties. Ramasamy et al.,¹³⁴ combined the photothermal heating properties of AuNRs with the magnetic properties of SiO₂/Fe₂O₃ nanoparticles, both integrated into polystyrene Janus particles. This combination allowed for particle tracking combined with antibacterial effects via photothermal heat generation. The presented examples illustrate the diverse applications of AuNRs, particularly as a potential alternative to antibiotics and a strategy to circumvent antibiotic resistance.

Motivation

Chapter 2

2 Motivation

The misuse and overuse of antimicrobials to treat, prevent, and control bacterial infections in humans are main contributing factors to the emergence of antibiotic resistance (AMR).^{15, 17} Bacteria can adapt and develop resistance to the administered antibiotics, thereby reducing their effectiveness. AMR leads to an increase in mortality rates and elevated medical costs due to more complex and prolonged treatments.^{15, 17} Due to the emergence of AMR, a range of antibiotic alternatives has been explored by researchers, including but not limited to bacteriophages including phage therapy^{15, 23, 135}, antimicrobial peptides^{15, 135}, or micro- and nanoparticles^{15, 58, 59, 135}. These antibacterial approaches are operating effectively in an "open-space" manner. This approach results in the release of bacterial fragments and toxins into the surrounding space, inducing serious inflammation processes. To overcome these challenges, this thesis aims to design and develop an antibiotic-free, antibacterial approach that consists of modular polymer-based capsules or giant unilamellar vesicles that can engulf/entrap bacteria for lysis in a "confined-space".

The following chemical and physical criteria of the polymer-based capsules have been identified in this thesis as essential for their successful antibacterial implementation:

- 1) *Utilization of biocompatible and biodegradable polymers* and the development of a high-throughput bulk approach for the assembly of stable microcapsules. These properties are also essential for a potential application as a stable, antibacterial coating for orthopedic implants, such as knee or hip implants.
- 2) To ensure efficient penetration and trapping of bacteria in polymer-based microcapsules, a high degree of *trans-shell porosity* as well as the presence of a *hollow cavity* (Figure 2-1a and b) have to be achieved.
- 3) Due to the passive nature of polymer-based microcapsules in capturing bacteria, the intrinsic mobility of the bacteria will be essential for their penetration. In order to achieve an efficient elimination of bacteria entrapped within the microcapsules' hollow cavity (motile bacteria) and in close proximity to the capsules (non-motile bacteria), a

light-triggered killing module has to be integrated. Towards this end, the microcapsules will be functionalized with gold nanorods (Figure 2-1c).

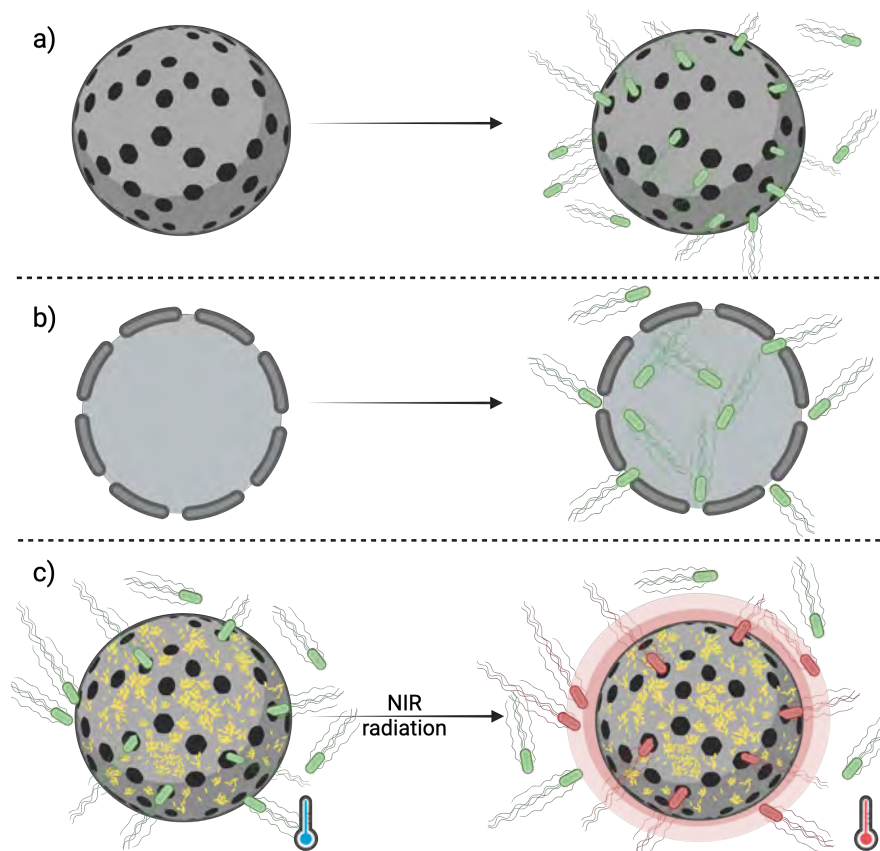


Figure 2-1: Schematic representation of the main physical and chemical properties of the designed antibacterial, polymer-based, porous microcapsules. (a) and (b) represent a high degree of trans-shell porosity and a hollow cavity as essential criteria for efficient bacteria uptake, respectively. (c) Integration of gold nanorods for a light-triggered bacteria killing module. Created with BioRender.com.

The second system will be designed to possess the unique ability to act as artificial phagocytes, in other words, to actively engulf motile or non-motile bacteria prior to disrupting them. The following chemical and physical criteria of the lipid-based vesicles have been identified in this thesis as essential for their successful antibacterial implementation:

- 1) Giant unilamellar vesicles (GUVs) with optimized lipid composition serving as synthetic phagocytes.
- 2) To achieve the specific interaction and adhesion of the targeted bacteria, bacteriophage-derived adhesion proteins will be linked to the vesicle's membrane. Strong and specific adhesion is required to facilitate the engulfment of bacteria by the vesicles (Figure 2-2).

- 3) To equip the designed vesicles with an active killing mechanism, gold nanorods will be immobilized on the lipid membrane. Similarly to polymer-based microcapsules, light-triggered illumination will be implemented to trigger thermal bacterial killing (Figure 2-2).

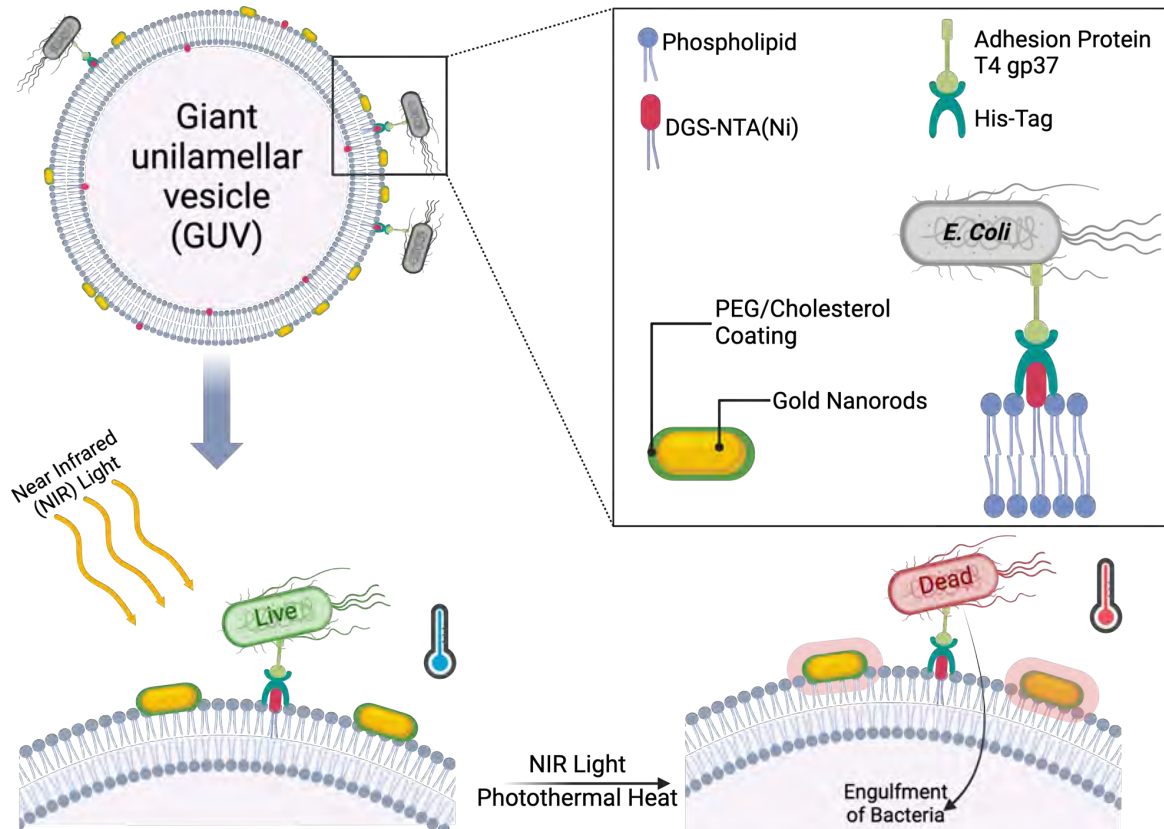


Figure 2-2: Schematic illustration of the GUV-based phagocytotic system. GUVs are functionalized with a bacteriophage tail protein to induce the interaction and adhesion of bacteria on the lipid membrane. Moreover, gold nanorods will be implemented to allow NIR light-triggered bacteria killing module. Created with BioRender.com.

Material & Methods

Chapter 3

3 Materials & Methods

3.1 Modular Porous Polymer-Based Microcapsules for Trapping and Near-Infrared Light-Triggered Killing of Bacteria

The following chapters present a comprehensive description and explanation of the materials and methods employed in the context of modular porous polymer-based microcapsules (μ Cs). A detailed list of all chemicals employed is provided in Chapter 3.1.1. The following Chapter provides a general overview of the production procedure for the polymer-based μ Cs, followed by a detailed elaboration on the post-production treatment and the production and functionalization of the gold nanorods (AuNRs). Subsequently, the characterization and analysis methods employed are described.

3.1.1 Materials

Unless otherwise indicated, all chemicals were utilized as received without further modification or purification.

3.1.1.1 Polymer-Based Microcapsules

Table 3-1: Chemicals used for polymer-based μ C production and functionalization.

Name	Specification	Manufacturer
Poly(lactic- <i>co</i> -glycolic acid) copolymer	PLGA, Resomer® RG 505, $M = 54\text{-}69\text{ kDa}$, LA:GA 50:50	Sigma-Aldrich, Germany
Pluronic®	F-127 and F-68	Sigma-Aldrich, Germany

Polyethylene glycol	PEG ₄₀₀₀ , $M \approx 4$ kDa	Sigma-Aldrich, Germany
Dichloromethane	DCM, Rotipuran®, $\geq 99.5\%$	Carl Roth GmbH & Co. KG, Germany
HFE-7500, fluorinated oil	FC oil, Novec 7500, $> 99\%$	IoLiTec-Ionic Liquids Technologies GmbH, Germany
Polyvinylpyrrolidone	PVP, 55 kDa	Sigma-Aldrich, Germany
Sodium hydroxide pellets	NaOH, 99.99% metals basis, semiconductor grade	Sigma-Aldrich, Germany

3.1.1.2 Calcium Carbonate Particles

Table 3-2: Chemicals used for calcium carbonate (CaCO_3) particle production and layer-by-layer coating.

Name	Specification	Manufacturer
Sodium carbonate	Na_2CO_3 , Powder, $\geq 99.5\%$	Sigma-Aldrich, Germany
Calcium chloride	CaCl_2 , Anhydrous, granular, $\geq 93.0\%$	Sigma-Aldrich, Germany
Poly(allylamine hydrochloride)	$M \approx 50$ kDa	Sigma-Aldrich, Germany
Poly(sodium 4- styrenesulfonate)	Powder, $M \approx 70$ kDa	Sigma-Aldrich, Germany

3.1.1.3 Gold Nanorods (AuNRs)

Table 3-3: Chemicals used for AuNR production and functionalization.

Name	Specification	Manufacturer
Hydrogen tetrachloroaurate(III)trihydrate	$\text{HAuCl}_4 \cdot 3\text{H}_2\text{O}$, $\geq 99.9\%$	Sigma-Aldrich, Germany

Hexadecyltrimethylammonium bromide	CTAB, $\geq 99.9\%$	Sigma-Aldrich, Germany
Silver nitrate	AgNO_3 , $\geq 99.9\%$	Sigma-Aldrich, Germany
Sodium borohydride	NaBH_4 , 99%	Sigma-Aldrich, Germany
Hydrochloric acid	HCl, ACS reagent, 37%	Sigma-Aldrich, Germany
<i>L</i> -ascorbic acid	AA, $\geq 99\%$	Sigma-Aldrich, Germany
PLGA-SH	$M(\text{PLGA}) = 5 \text{ kDa}$, LA:GA 50:50, R-PL8281	RuixiBiotechCo.Ltd, China
Ethanol	$\geq 98\%$, technical, denatured	Carl Roth GmbH & Co. KG, Germany

3.1.1.4 Bacteria Culturing

Table 3-4: Chemicals used for bacteria culturing.

Name	Specification	Manufacturer
Lysogeny broth medium	LB-medium, Lennox	Sigma-Aldrich, Germany
Kanamycin sulfate	BioChemica	AppliChem GmbH, Germany
Phosphate-buffered saline	PBS, Gibco	Life Technologies Limited, UK
<i>D</i> -(+)-glucose	$\text{C}_6\text{H}_{12}\text{O}_6$	Sigma-Aldrich, Germany
Ammonium sulfate	$(\text{NH}_4)_2\text{SO}_4$	Sigma-Aldrich, Germany

3.1.2 Methods

3.1.2.1 (Cryogenic-)Scanning Electron Microscopy (cryo-SEM)

For the characterization of the μ Cs as well as the AuNRs, (cryo-)SEM was utilized. Solidified, freeze-dried μ Cs were analyzed by field emission (cryo-)scanning electron microscopy (cryo-FE-SEM, Zeiss Ultra 55 field emission electron microscope, Carl Zeiss AG, Germany) at room temperature or under low temperature conditions (-150 °C). For all experiments, the working distance was set to 5 - 7 mm. The in-lens detector as well as the in-lens second electron detector (SE2) were used at acceleration voltages of 5 - 10 kV. For all samples investigated at room temperature, small amounts of sample ($\approx 10 \mu\text{L}$) were pipetted on a silicon wafer and left for solvent evaporation in a fume hood. After complete solvent evaporation, all samples except pure AuNRs were coated with a thin layer of carbon (8 - 20 nm, Leica EM ACE 200, Leica Microsystems GmbH, Germany) to avoid charging while sample investigation. To evaluate characteristics as the μ C shell thickness and the inside structure, freeze-fracturing of the μ Cs was necessary, which was executed at cryogenic conditions. To execute these low temperature experiments, μ C powder was redispersed in MilliQ-water and a 3 μL droplet placed in a sample holder with small pits. By dipping the sample holder with the sample into the liquid nitrogen-filled loading station, the samples were shock-frozen and prepared for transfer via a loading and transfer system (Leica EM VCT100 Vacuum cryogenic (cryo) transfer system, Leica Microsystems GmbH, Germany). The sample holder was transferred into the sample preparation system (Leica EM BAF060, Leica Microsystems GmbH, Germany) for freeze-fracturing, freeze-drying, and platinum coating (5 nm). All these steps were executed under high vacuum conditions and at -150 °C. Sublimation was executed for at least 45 min at an increased temperature of -90 °C. The prepared sample was then transferred after coating to the cryo-SEM for observation.

3.1.2.2 Confocal Laser Scanning Microscope (CLSM) Imaging

To further investigate the morphological μ C characteristics (i.e., hollow core structure, shell thickness, μ C size) as well as the μ C trapping, retaining and killing performance, fluorescent CLSM was used. For this purpose, a LSM980 and LSM900 with Airyscan2 (Carl Zeiss AG, Germany) with 5x/0.16, 10x/0.45, and 20x/0.8 air objectives and 40x/1.3,

and 63x/1.4 oil objectives (Carl Zeiss AG, Germany) were used. Fluorescently labeled samples were excited using 405 nm, 488 nm, 561 nm and 640 nm diode lasers. The settings were adjusted to achieve optimal image quality and no oversaturation. For samples comparing treatments effects (i.e., near infrared (NIR)-radiation), imaging settings were kept the same for identical samples before and after treatment. If not noted differently the samples were analyzed using a small imaging chamber, where the sample was sandwiched between two glass slides spaced by using four stripes of double-sided tape. The edges were sealed with two-component glue to avoid evaporation. All measurements were executed at room temperature unless otherwise stated. The recorded images were analyzed and adjusted in contrast and brightness using the Fiji software (ImageJ, NIH).

3.1.2.3 *UV-Vis Spectroscopy*

UV-Vis spectroscopy was used to determine the absorbance spectrum of the AuNRs as well as to check the growth state of bacteria. All measurements were executed by an Infinite M200 (Tecan Trading AG, Switzerland). AuNR absorbance spectra were determined for the range of 400 - 1000 nm with a resolution of 2 nm. Bacterial growth state was measured at a wavelength of 600 nm.

3.1.2.4 *Zeta Potential Measurements*

Zeta potential measurements were performed using a Malvern Panalytical ZetaSizer Nano ZS with Zeta cell cuvettes (DTS1070, Malvern Panalytical) at 25 °C. The equilibrium time was set to minimum 60 sec. Samples of lyophilized capsules were re-suspended in MilliQ-water. AuNR samples were diluted in deionized water. The dispersant viscosity and refractive index (RI) of water were set to 0.8904 Pc and 1.333, respectively. The RI of the PLGA μ Cs was set to 1.47 and for the AuNRs to 0.181. All samples were measure in triplicates.

3.1.2.5 *Polymer-Based Microcapsules Production Procedure*

Over the course of this thesis, the process of μ C formation varied in terms of the used formation methods as well as in composition and materials used. Variations are noted and discussed directly at the respective section Results & Discussions. The optimized polymer-based μ Cs were produced via a one-pot emulsification formation process which can be divided into three main steps. First, both, the aqueous and the oil phase were prepared.

Following amounts were used for all μ C compositions if not indicated differently. PLGA (100 mg) was dissolved together with the porogen (50 mg, PEG or Pluronic®) and HFE-7500 oil (100 μ L) in DCM (4 mL) to form the oil phase. For AuNR-decorated μ Cs, PLGA-functionalized AuNRs dispersed in DCM were added to the oil phase in this step. For the aqueous phase, PVP (0.5%) was dissolved in MilliQ water. The second step includes the formation of an oil-in-water (o/w) emulsion. For this purpose, oil and water phase were mixed (1:5 volume ratio) and emulsified via high-shear homogenization (T10 basic ULTRA-TURRAX, IKA, Germany) for 20 sec at 8300 rpm (if not indicated differently). In the third step, the produced emulsion was immediately after homogenization poured into a large volume of MilliQ water (1 L, if not indicated differently), covered with aluminum foil and mixed via magnetic stirring (\approx 200 rpm, if not indicated differently) overnight for at least 12 h. The solidified μ Cs were collected by centrifugation (1520 rcf for 1 min, EBA 20 centrifuge, Hettich, Germany), washed with deionized water, frozen in liquid nitrogen and lyophilized overnight (Alpha 2-4 LSCplus, Martin Christ Gefriertrocknungsanlagen GmbH, Germany). Dry μ C powder was stored at -20°C until further use.

3.1.2.6 Calcium Carbonate Particle Production and Layer-by-Layer Coating

Calcium carbonate particles as hard templates for pore formation were produced by emulsifying 20 mL of an aqueous sodium carbonate (Na_2CO_3 , 0.33 M) solution with 20 mL of an aqueous calcium chloride (CaCl_2 , 0.33 M) solution for 30 sec. The emulsification speed was adjusted according to the desired particles size. Mixture was centrifuged (1520 rcf for 1 min, EBA 20 centrifuge, Hettich, Germany) and supernatant was discharged. The production process was followed by a layer-by-layer coating according to Luo et al.¹³⁶. Particles were immersed alternately in poly(allylamine hydrochloride) (PAH, 1 mg/mL in 0.5 M NaCl) and poly(sodium 4-styrenesulfonate) (PSS, 1 mg/mL in 0.5 M NaCl) with NaCl (0.5 M) washing steps between each coating cycle. Seven layers were coated with PAH as the first and PSS as the last layer. Subsequently, particles were additionally immersed in a coating solution consisting of PLGA (25 mg/mL) in acetone to achieve an outermost layer consisting of PLGA. Particles were washed afterwards twice with MilliQ water and dried overnight in the oven at 60°C .

3.1.2.7 Microcapsule Post-Production Etching Procedure

To improve the μC porosity, μCs underwent after lyophilization an additional post-production treatment step. Dry μC powder was re-dispersed in 0.3 M NaOH for different time periods under constant mixing. The sample was instantly centrifuged for 1 min at 1520 rcf (EBA 20 centrifuge, Hettich, Germany), the supernatant removed, and the sample washed at least three times with distilled water. After the final washing step, the etched μCs were again frozen in liquid nitrogen and freeze-dried to remove all excess water. The μC powder was stored at -20°C until further use.

3.1.2.8 Bacteria Capturing Performance of Microcapsules

All bacteria experiments were executed with two different types of bacteria: BL21(DE3) competent *Escherichia coli* (*E. coli*) with a pET His6-GFP TEV LIC plasmid (conveying the ability to express GFP) and kanamycin resistance as well as *Staphylococcus sciuri* (*S. sciuri*) (ATCC 29062). *E. coli* was cultured in LB medium containing $50\ \mu\text{g}/\text{mL}$ kanamycin, *S. sciuri* in LB medium without additional kanamycin. Both were cultured overnight at 37°C under shaking (210 rpm). Fresh medium was inoculated from the overnight culture and incubated again at 37°C , 210 rpm until the optical density (OD, measured at 600 nm) reached $\text{OD}_{600} \approx 0.6$. Bacteria were centrifuged at 10,000 rcf for 10 min to remove the growth medium, which was replaced by minimal medium (97% 1x PBS, 1% w/v glucose, 1% w/v $(\text{NH}_4)_2\text{SO}_4$, 1% LB medium) and additional $50\ \mu\text{g}/\text{mL}$ kanamycin only in the *E. coli* culture. Bacteria in minimum medium were mixed with the different samples of polymer-based μCs ($\approx 5.6 \times 10^6$ capsules/mL) and incubated at room temperature under slow shaking for 1 h. Microcapsules were centrifuged (10,000 rcf for 10 min) to remove the excess of bacteria from the surrounding medium and fresh minimum medium was added. To visualize the bacteria and to also distinguish the live/dead state of the bacteria, a two-color fluorescent assay (LIVE/DEAD BacLight Bacterial, Viability Kit, Thermo Fisher Scientific, USA) was added to the suspension ($\approx 1\ \mu\text{L}$ per 1 mL bacteria culture). Samples were incubated for 15 min in the dark and afterwards directly transferred to the confocal laser scanning microscope for characterization/investigation.

3.1.2.9 Gold Nanorod Synthesis

AuNRs were synthesized according to the seed-mediated growth method.¹³⁷ The used amounts were upscaled and adjusted to achieve a higher yield and AuNRs with an

absorbance maximum of around 808 nm, corresponding to an aspect ratio of 4. All solutions were prepared and kept in a water bath set to 26 °C. In the first step, the seed solution was prepared in a 30 mL flask. Under gentle stirring, CTAB (19.5 mL, 0.1 M), HAuCl₄ (0.5 mL, 0.01 M) and freshly prepared, ice-cold NaBH₄ (1.2 mL, 0.01 M) were mixed for 2 min and kept undisturbed for 2 h. In the second step, the growth solution was prepared by adding HAuCl₄ (10 mL, 0.01 M), AgNO₃ (1.6 mL, 0.01 M), and HCl (4 mL, 1 M) to an aqueous CTAB solution (180 mL, 0.1 M). After thoroughly mixing the yellowish solution, AA (1.6 mL, 0.1 M) was added until the solution turned completely colorless. In the final step, the seed solution (20 mL) was added after 2 h to the readily prepared growth solution, mixed for 30 sec and kept overnight at 26 °C undisturbed. The whole process is summarized in Figure 3-1. A reddening of the solution indicates successful rod growth. To remove the excess of CTAB, the solution was centrifuged at 14,000 rpm ($\approx 24,038$ rcf, Optima L-80 XP Ultracentrifuge, rotor: SW 32 Ti, Beckman Coulter GmbH, German) for 25 min at 26 °C. The supernatant was removed and AuNRs were washed with MilliQ-water. This step was repeated at least three times. AuNR stock solutions were stored in glass vials in the dark at 4 °C until further use.

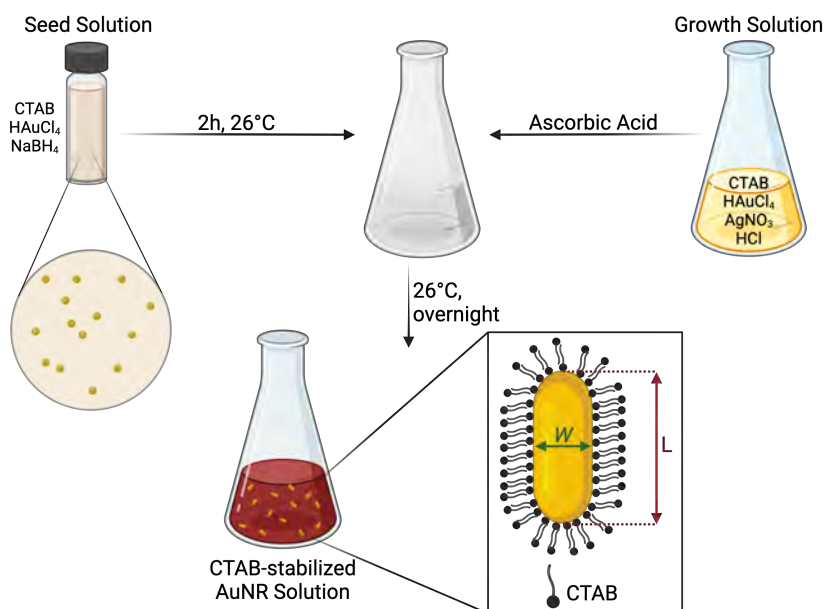


Figure 3-1: Schematic illustration of seed-mediated AuNR production method. Seed and growth solution are produced separately and mixed afterwards to form CTAB-stabilized AuNRs with specific length (L) and width (W). Created with BioRender.com.

3.1.2.10 Gold Nanorod Concentration Calculations

To calculate the concentration of AuNRs based on absorbance, the dimensions of the rods are critically important. Extracted from SEM micrographs taken from the CTAB-stabilized rods, the dimensions are assumed to be ≈ 40 nm in length (L) and ≈ 10 nm in width (W). The shape is approximated to be cylindrical, which leads to a AuNR volume calculated by eqn. (3-1). With the calculated volume and the density of gold ($\rho_{\text{Au}} = 1.932 \times 10^4 \text{ kg/m}^3$) the mass of a single AuNR is calculated by eqn. (3-2) and determined to be $m_{\text{AuNR}} = 6.070 \times 10^{-20} \text{ kg}$, which relates to $n = 3.081 \times 10^{-19} \text{ mol}$ per single AuNR. By using the absorbance measured at 400 nm (A_{400}) together with the molar extinction coefficient of a gold atom at 400 nm ($\varepsilon_{400} = 2.02 \times 10^3 \text{ M}^{-1} \cdot \text{cm}^{-1}$)¹³⁸, the concentration of Au (c_{Au}) was determined via eqn. (3-3). The final AuNR particle number (N_{AuNR}) in the measured solution can then be calculated with eqn. (3-4), where $V_{\text{Dispersion}}$ represents the used volume of the measured sample.

$$V_{\text{AuNR}} = \pi L \left(\frac{W}{2} \right)^2 \quad (3-1)$$

$$m_{\text{AuNR}} = V_{\text{AuNR}} * \rho_{\text{Au}} \quad (3-2)$$

$$c_{\text{Au}} = \frac{A_{400}}{\varepsilon_{400} * d} \quad (3-3)$$

$$N_{\text{AuNR}} = \frac{c_{\text{Au}} * V_{\text{Dispersion}}}{n} \quad (3-4)$$

3.1.2.11 Gold Nanorod PLGA-Functionalization

AuNRs with an absorbance peak around 808 nm were utilized for further functionalization by means of PLGA-SH to decreased toxicity provoked by CTAB and to improve the integration efficiency of AuNRs into the μCs . First, CTAB-stabilized AuNRs ($c \approx 1.9 \text{ mg/mL}$) were incubated for around 1 h in a freshly prepared 50 mM NaBH_4 solution (dispersed either in H_2O or ethanol, Figure 3-2a), following the protocol published by J. He et al.¹²⁵ Afterwards, the solution was centrifuged for 25 min at 26°C and 14,000 rpm ($\approx 24,038 \text{ rcf}$), the supernatant removed, and finally PLGA-SH (5 kDa, RuixiBiotechCo.Ltd, China) dissolved in DCM (1.25 mM, 2000 μL) added (Figure 3-2b). Ethanol (90%, 2000 μL) was added and the solution was kept in the cold room overnight to avoid DCM evaporation. The next day, agglomerated rods were visible at the bottom of the vial. The supernatant was removed and the AuNRs were re-dispersed in DCM

(3000 μL) mixed with PLGA-SH (50 μL , 25 mM). The solution was incubated for at least 15 min and centrifuged for 25 min at 20 $^{\circ}\text{C}$ and 14,000 rpm (24,038 rcf). The supernatant was removed and DCM was added at the desired concentration (Figure 3-2c). PLGA-functionalized AuNRs were stored until further use in glass vials in the dark at 4 $^{\circ}\text{C}$. The whole process of AuNR functionalization is summarized in Figure 3-2.

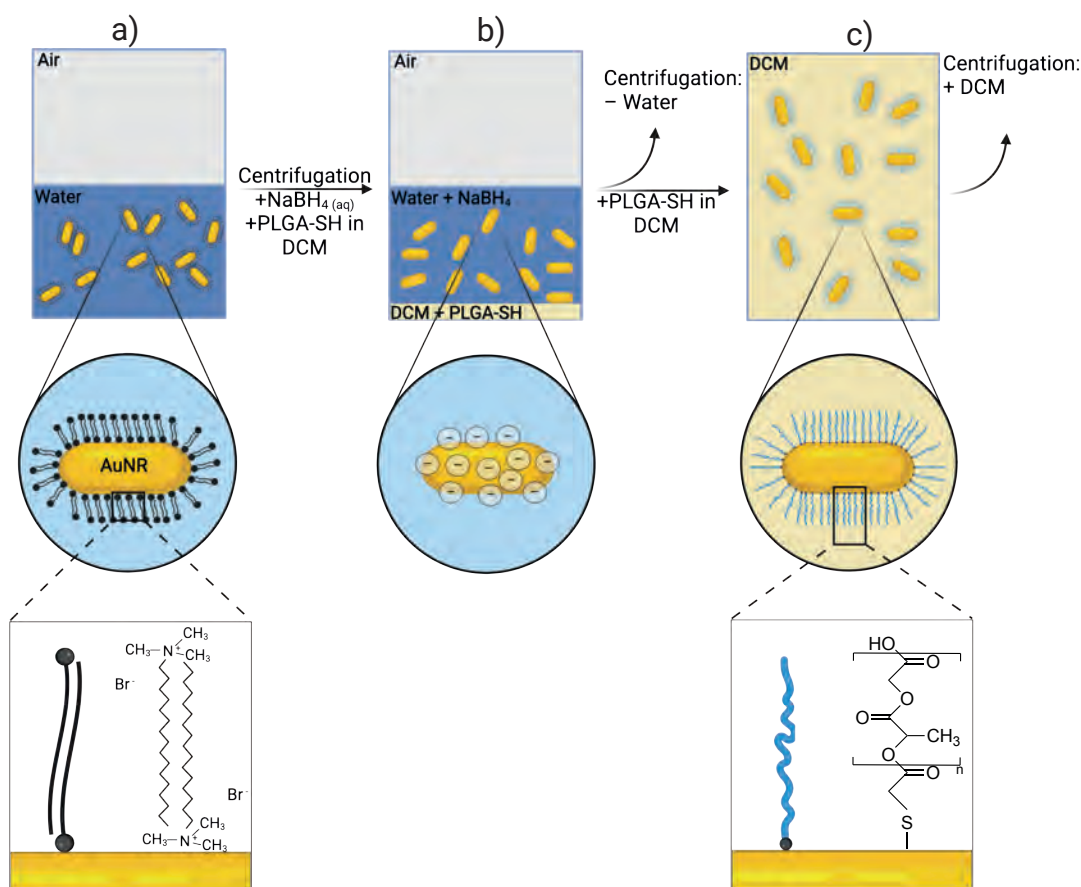


Figure 3-2: Schematic illustration of AuNR-functionalization process with PLGA-SH. a) Removal of CTAB from gold surface by use of NaBH_4 in aqueous solution. b) Bare gold surface in aqueous solution is going to be stabilized by PLGA-SH added in DCM. c) PLGA-SH binding via a strong thiol-gold bond to the AuNR surface stabilizing the gold particles in DCM solution. Created with BioRender.com.

3.1.2.12 Cell Viability Tests with Microcapsules

To assess cell viability in the presence of microcapsules human fibroblast were used. 4000 cells per well were seeded in a 96-well plate and incubated in a humidified 5% CO_2 incubator at 37 $^{\circ}\text{C}$. The μCs were twice sterilized inside the fume hood before and after the

addition of culture medium by the use of UV-C light. After 24 h different types of μ Cs were added to the cells in various concentrations and incubated (37°C, humidified, 5% CO₂ atmosphere) for 24 h. A luminescent cell viability assay (CellTiter-Glo® 2.0 Assay, Promega Corporation, USA) was used to examine cell viability. The reagent was used as described by the manufacturer. The luminescent signal was recorded by a plate reader (Infinite M200, Tecan Trading AG, Switzerland) at an integration time of 0.5-1 sec per well. At least three replicates per sample were measured. To confirm that the cells grew as expected and that the assay worked correctly, a standard curve was performed in parallel.

3.1.2.13 Bacteria Viability Tests with Microcapsules

Bacterial viability was examined employing a two-color fluorescence assay (LIVE/DEAD BacLight Bacterial, Viability Kit, Thermo Fisher Scientific, USA) and fluorescent CLSM (Carl Zeiss AG, Germany). Bacteria were cultured as described in the section Bacteria Capturing Performance of Microcapsules. The freshly grown bacteria were then mixed in minimum medium with the respective μ C type at a concentration of 1 mg/mL and incubated for 24 h at room temperature while shaking (500 rpm). The negative control included the addition of minimum medium without μ Cs. For the positive control the bacteria were incubated in a 50/50 composition of minimum medium and 70% ethanol solution. After 24 h, the bacteria were briefly centrifuged to remove the μ Cs, a two-color fluorescent assay solution (LIVE/DEAD BacLight Bacterial, Viability Kit, Thermo Fisher Scientific, USA) was added to the suspension (\approx 1 μ L per 1 mL bacteria culture) to analyze the live/dead state of the bacteria. All samples were imaged and analyzed by the use of a CLSM.

3.1.2.14 Live/Dead Bacteria Quantification

To quantify the number of live versus dead bacteria (*E. coli* and *S. sciuri*) the fluorescent CLSM images at different conditions were analyzed using the Fiji software (ImageJ, NIH). Images were split into separate channels. Each channel was adjusted to 8-bit format. Afterwards the 'Find Maxima' function was used to detect fluorescently labeled single bacteria cells. The green channel detected the total number of bacteria cells in the image. Red signal was representing dead bacteria cells. Hence, note that the percentage of live cells was calculated by the number of total cells (green signal) minus the number of dead cells (red signal) divided by the total number of bacteria cells multiplied by 100.

3.1.2.15 Near Infrared (NIR)-Laser (808 nm) Setup

The laser setup included an 808 nm laser (Fabry-Perot benchtop laser source, ThorLabs, USA) connected to a single mode patch cable with an additional collimator (TC18FC-780, ThorLabs, USA) connected to an achromatic zoom beam expander (ZBE3B, ThorLabs, USA). The arrangement of the setup was aiming to create a relatively big spot of illumination while maintaining a certain power density. To meet these requirements, a beam expander was placed inversely within the laser beam path to further decrease the diameter of the beam after collimation. The beam was then coupled via two kinematic mirrors into an inverted microscope (Axiovert 200M, Carl Zeiss AG, Germany). A dichroic mirror implemented in the microscope was directing the beam through an 10x objective (Plan-Apochromat 10x/0.45 M27) on the sample. Directing the laser beam through the objective on the sample led to an enlargement of the final beam diameter irradiating the sample (Figure 3-3). The size of the laser beam was calculated via the ISO11146 method given a beam diameter of $\approx 562 \mu\text{m}$. The laser power was measured by a laser power meter (PM100A, ThorLabs, USA) connected to a power sensor (S142C, ThorLabs, USA).

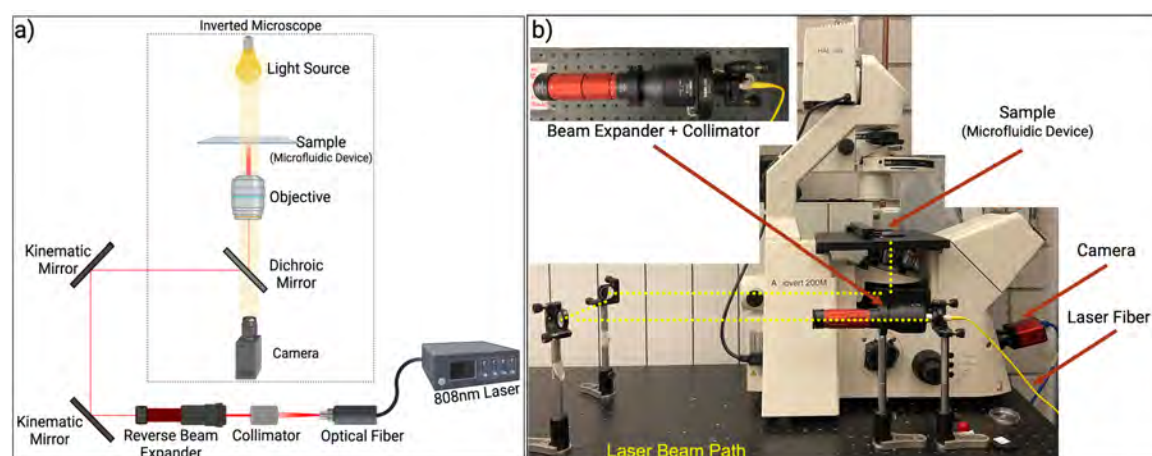


Figure 3-3: a) Schematic illustration of NIR-laser-microscope setup. b) Picture of NIR-laser-microscope setup with zoom-in of reverse beam expander and collimator. Parts were created with BioRender.com.

3.1.2.16 NIR-Laser Treatment of Single Bacteria Loaded Microcapsules

In the first step, the bacteria were prepared as described before in the Section 3.1.2.8. To assess the effect of the NIR-laser treatment on the bacteria before versus after treatment, a microfluidic device was designed (Figure 3-4), which made it possible to trap, illuminate,

image and compare an entrapped set of μ Cs. Towards this end, the microfluidic device was flushed with the microcapsule-bacteria solution and microfluidic traps with a sufficient number of trapped bacteria-loaded μ Cs were chosen for imaging and NIR-laser treatment. CLSM was used to analyze the live/dead state of the bacteria before NIR-laser treatment. Afterwards, the microfluidic device was transferred to the NIR-laser system and irradiated while simultaneous observation with the inverted microscope implemented in the laser setup. Irradiation was applied for three different time periods. Live/dead state analysis via fluorescent CLSM analysis was repeated with the same settings after radiation treatment.

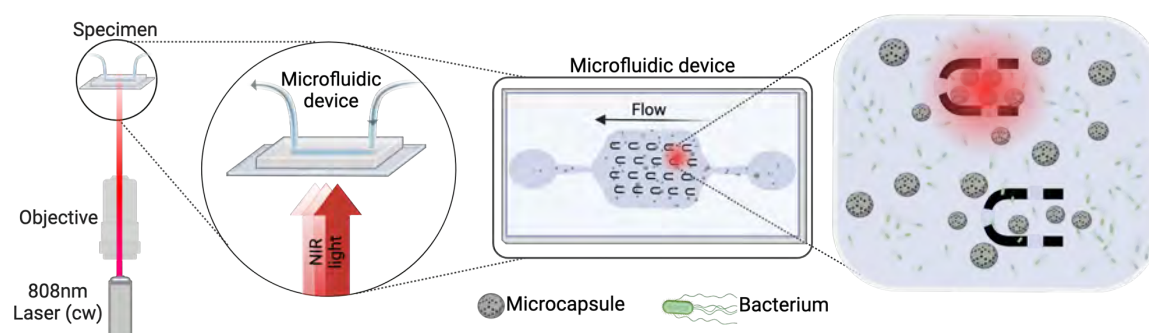


Figure 3-4: Schematic illustration of microfluidic device used for μ C trapping and single μ C NIR light illumination via the 808 nm laser setup described in Figure 3-3. Created with BioRender.com.

3.1.2.17 NIR Light-Emitting Diode (LED)-Setup

Apart from the 808 nm laser setup described in Section 3.1.2.15 used for single particle illumination, a second NIR light setup was built and used to illuminate bacteria in a bulk solution. The setup presented in the following was developed and implemented by Prof. Dr. Stefan Schramm and consisted of a 100 W LED module with a wavelength of 770 nm. The LED-system was actively cooled by a 12 V, 80 mm fan mounted to the LED. On the front part of the LED, a 60° reflector and a planar-convex polymethyl methacrylate (PMMA) lens was mounted. This system was then connected to a collimator with a 3D-printed sample holder. The whole system was connected to a power supply (HANMATEK HM310T). With this setup, it was able to illuminate bacteria in a bulk solution. For this purpose, the bacteria solution was placed in the sample holder in front of the collimator and front lens.

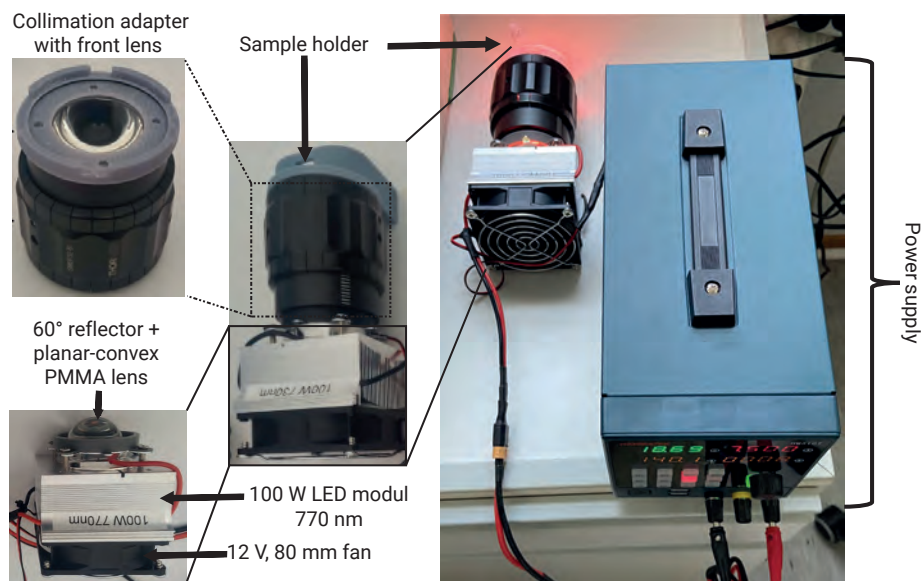


Figure 3-5: LED-setup with detailed component description using a 770 nm, 100 W LED. System was developed by Prof. Dr. Stefan Schramm and images were provided and developed by Anastassiya Schramm.

3.1.2.18 Agar-Plate Bacteria Viability Tests with Microcapsules

E. coli was cultured in fresh LB medium at 37 °C under shaking (210 rpm) until the optical density (OD, measured at 600 nm) reached $OD_{600} \approx 0.6$. Bacteria were centrifuged at 10,000 rcf for 10 min to remove the growth medium, which was replaced by Dulbecco's Balanced Salt Solution (DPBS, 1X, Gibco, Life Technologies Limited, UK). Bacteria (500 μ L, 2×10^8 bacteria/mL) in DPBS were mixed with 500 μ L of different samples of polymer-based μ Cs dispersed and sterilized in DPBS at two different concentrations (1 mg/mL and 0.5 mg/mL) and incubated at room temperature for 1 h. The different samples were illuminated in an Eppendorf tube for five minutes with the NIR light LED setup presented in Section 3.1.2.17 (770 nm, 3.53 W/cm²). After NIR-treatment, the different samples were plated on LB-agar plates (1.5% agar) at different concentrations (1×10^8 , 1×10^7 , 1×10^6 bacteria/mL) and incubated at room temperature for 24 h.

3.2 Adhesion-Mediated Engulfment and Killing of Bacteria by Synthetic Vesicles

In the following chapters, a comprehensive description and explanation of the materials and methods employed in the context of synthetic vesicles are described and explained. Chapter 3.2.1 lists all chemicals employed during these experiments. Chapter 3.2.2 gives a general overview about the GUV formation processes, followed by the isolation and purification of the adhesion protein, the production and functionalization of the applied AuNRs and culturing of used bacteria. Subsequently, all the methods utilized for characterization and analysis are described.

3.2.1 Materials

Unless other stated, all chemicals were used as received without further modification or purification.

3.2.1.1 Giant Unilamellar Vesicles (GUVs) Formation

Table 3-5: Chemicals used for the production of GUVs via gel-assisted GUV formation¹³⁹.

Name	Specification	Manufacturer
1,2-dioleoyl- <i>sn</i> -glycero-3-phosphocholine	DOPC	Avanti Polar Lipids, USA
1,2-dioleoyl- <i>sn</i> -glycero-3-phospho-(1'- <i>rac</i> -glycerol) (sodium salt)	DOPG	Avanti Polar Lipids, USA
1,2-distearoyl- <i>sn</i> -glycero-3-phosphoethanolamine-N-[methoxy(polyethylene glycol)-2000] (ammonium salt)	18:0 PEG2000PE	Avanti Polar Lipids, USA
1,2-dioleoyl- <i>sn</i> -glycero-3-[(N-(5-amino-1-carboxypentyl)iminodiacetic acid)succinyl] (nickel salt)	18:1 DGS-NTA(Ni)	Avanti Polar Lipids, USA

1,2-dioleoyl- <i>sn</i> -glycero-3-phosphoethanolamine-N-(lissamine rhodamine B sulfonyl) (ammonium salt)	18:1 LissRhod PE	Avanti Polar Lipids, USA
1,2-Dioleoyl- <i>sn</i> -glycero-3-phosphoethanolamin labeled with Atto 647N	Atto 647N DOPE	Sigma-Aldrich, Germany
Chloroform	EMSURE®	Sigma-Aldrich, Germany
Polyvinyl alcohol	PVA, $M \approx 145$ kDa	Sigma-Aldrich, Germany
<i>D</i> (+)-Sucrose	$\geq 99,5\%$, p.a.	Carl Roth GmbH & Co. KG, Germany
Imidazole	PUFFERAN® $\geq 99\%$, p.a., ultra quality	Carl Roth GmbH & Co. KG, Germany
<i>N</i> -Decane	For synthesis	Sigma-Aldrich, Germany
Silicone oil		Sigma-Aldrich, Germany
OptiPrep™ Density Gradient Medium		Sigma-Aldrich, Germany
Hydrochloric acid	HCl, ACS reagent, 37%	Sigma-Aldrich, Germany
Phosphate-buffered saline	PBS, Gibco	Life Technologies Limited, UK

3.2.1.2 Gold Nanorods (AuNR)

Table 3-6: Chemicals used for AuNR production.

Name	Specification	Manufacturer
Hydrogen tetrachloroaurate(III)trihydrate	$\text{HAuCl}_4 \cdot 3\text{H}_2\text{O}$, $\geq 99.9\%$	Sigma-Aldrich, Germany

Hexadecyltrimethylammonium bromide	CTAB, $\geq 99.9\%$	Sigma-Aldrich, Germany
Silver nitrate	AgNO ₃ , $\geq 99.9\%$	Sigma-Aldrich, Germany
Sodium borohydride	NaBH ₄ , 99%	Sigma-Aldrich, Germany
Hydrochloric acid	HCl, ACS reagent, 37%	Sigma-Aldrich, Germany
<i>L</i> -ascorbic acid	AA, $\geq 99\%$	Sigma-Aldrich, Germany
PLGA-SH	$M(\text{PLGA}) = 5 \text{ kDa}$, LA:GA 50:50, R-PL8281	RuixiBiotechCo.Ltd, China
Ethanol	$\geq 98\%$, technical, denatured	Carl Roth GmbH & Co. KG, Germany

3.2.1.3 Gold Nanorod Functionalization

Table 3-7: Chemicals used for AuNR functionalization.

Name	Specification	Manufacturer
Poly(ethylene glycol) methyl ether thiol	mPEG-SH, $M \approx 2 \text{ kDa}$	Sigma-Aldrich, Germany
Cholesterol-poly(ethylene glycol)-thiol	Chol-PEG-SH, $M \approx 2 \text{ kDa}$, $\geq 95\%$	Biopharma PEG, USA
Tris-(hydroxymethyl)-amino methane	TRIS PUFFERAN®, $\geq 99.9\%$, p.a.	Carl Roth GmbH & Co. KG, Germany
Sodium dodecyl sulfate	SDS, $\geq 99\%$	Carl Roth GmbH & Co. KG, Germany
Hydrochloric acid	HCl, fuming 37% in water	VWR International GmbH, Germany

3.2.1.4 Bacteria Culturing

Table 3-8: Chemicals used for bacteria culturing.

Name	Specification	Manufacturer
Lysogeny broth medium	LB-medium, Lennox	Sigma-Aldrich, Germany
Kanamycin sulfate	BioChemica	AppliChem GmbH, Germany
Phosphate-buffered saline	PBS, Gibco	Life Technologies Limited, UK
<i>D</i> -(+)-glucose	C ₆ H ₁₂ O ₆	Sigma-Aldrich, Germany
Ammonium sulfate	(NH ₄) ₂ SO ₄	Sigma-Aldrich, Germany

3.2.2 Methods

3.2.2.1 Formation Techniques of Giant Unilamellar Vesicles

GUVs were either formed by the so-called emulsion-transfer method or according to the previously reported and adjusted gel-assisted GUV formation protocol by Weinberger et al.¹³⁹. Both production methods are explained briefly in the following.

Emulsion-Transfer GUV Formation Process

In the first step, all lipids were prepared and mixed in brown glass vials in the desired concentration (mostly 643 μ M in 1 mL buffer volume) and with the desired composition. After mixing, the vials with the lipids were placed under vacuum to remove the chloroform. Afterwards, the solution for the outer phase was prepared in a separate 2 mL Eppendorf tube by mixing imidazole (50 μ L, 50 mM at pH 7.64), sucrose (128 μ L, 1 M) and MilliQ water (322 μ L). After complete removal of the chloroform from the lipids, the lipids were dispersed in *N*-decane (60 μ L) and kept under nitrogen atmosphere until further use. In the next step, silicon oil (940 μ L) was added to the lipid-*N*-decane mixture and vortexed for at least 10 sec. Parts of the oil-lipid phase (400 μ L) were now carefully added on top of the previously prepared outer phase. The two-phase mixture was incubated for 45-90 min to

form a monolayer of lipids and the remaining oil-lipid mixture was kept under nitrogen atmosphere. In the meantime, the inner phase was prepared by mixing OptiPrep™ (3.3 μL) and PBS (6.6 μL , 1X) in separate, small tubes. After incubation, the inner phase was transferred by a Pasteur pipette to remaining oil-lipid phase by pipetting it several times up and down. This solution was then completely and carefully transferred to the previously prepared lipid-outer phase system. To form a complete bilayer, the tubes were subsequently centrifuged at around 400 rcf for 3 min and the remaining oil phase was removed from the top, leaving behind readily formed synthetic vesicles in the bottom of the tube. Vesicles were used for all further experiments on the same or the following day and were stored at 4 °C.

Gel-Assisted GUV Formation Process

The gel-assisted GUV formation process is based on the work of Weinberger et al.¹³⁹. Here, all lipides were dissolved in chloroform at the desired concentration and stored at -20 °C in brown glass vials before use. PVA (50 mg/mL) was dissolved with sucrose (100 mM) in deionized water. PVA-coated glass slides (24x60 mm) were then produced by spreading a drop of the mixture (40 μL) with the pipette tip on the substrate. Two coated glass slides per sample were produced. Coated substrates were dried for 1 h at 37 °C in the oven. Meanwhile, lipids were mixed in the desired lipid composition and at a final concentration of 12000 μM up to a final volume of 50 μl . To create a thin lipid film, $\approx 5 \mu\text{L}$ of mixed lipids were spread with a Hamilton syringe on top of the PVA coating. The substrates were placed in the oven at 37 °C for another 30 min. After drying of the lipid film, a Teflon spacer was sandwiched between two of the coated substrates and fixed with two claps on either side. The formed chamber (Figure 3-6a) was then filled with a sucrose solution ($\approx 1 \text{ mL}$, 280 mM) a syringe via a small hole on one side of the Teflon spacer. Filled chambers were left at room temperature for 1 - 2 h. After GUV formation, clamps were removed and the top glass slide was carefully moved aside to transfer the obtained GUVs (Figure 3-6b) from the chamber into an Eppendorf tube. GUVs were stored at 4 °C for maximum one week until further use.

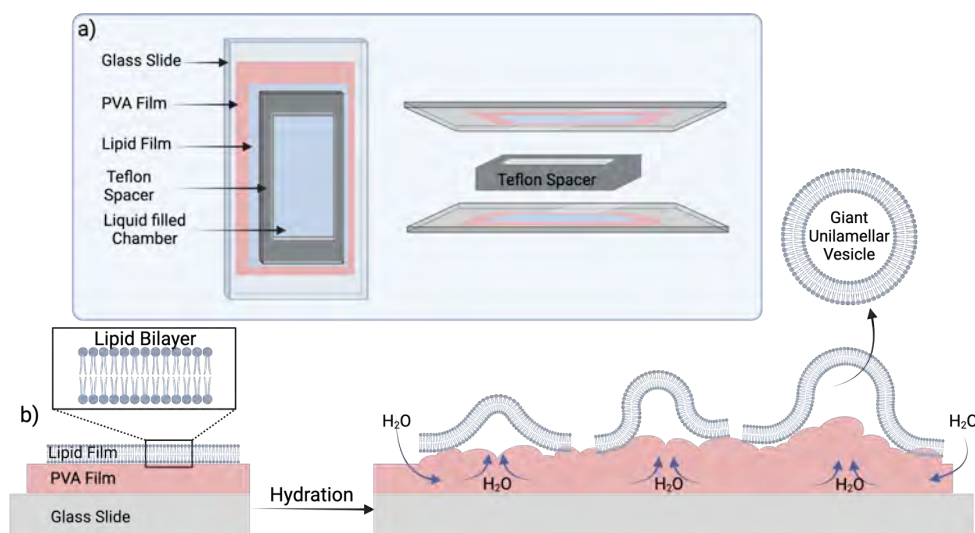


Figure 3-6: Schematic illustration of GUV formation via gel-assisted hydration method. a) Chamber used for GUV formation consisting of two glass slides coated with a PVA and a lipid film. Teflon spacer is sandwiched and filled with liquid. b) GUV formation mechanism. Created with BioRender.com.

3.2.2.2 Adhesion Protein (*gp37*) Isolation and Purification

This protocol as well as the complete process of protein isolation and purification was provided and conducted by Ann-Kathrin Gelmroth (Max-Planck-Institute for Medical Research). The entire process of protein purification was conducted in accordance with the methodology described by Bartual et al.²⁸. Additionally, the provision of the constructs for purification by this working group was greatly appreciated. Briefly, the plasmids pCDF-Duet::T4_gp38::T4_gp37 and pET21a::T4_gp57 were transformed into competent *E. coli* BL21(DE3) cells and induced with 0.1 mM isopropyl 1-thio- β -D-galactopyranoside (IPTG) at OD₆₀₀=0.8 overnight at 20 °C and 140 rpm. The cultures were harvested at 4,000rcf for 30 min at 4 °C and the pellets were resuspended in 30 mL lysis buffer supplemented with protease inhibitor (Roche, Basel, Switzerland). The solubilized protein fraction was obtained by tip sonication at 70% power, 5 cycles x 10% and 20 min. The soluble fraction was supplemented with 50 mM imidazole and remaining debris was separated from the supernatant by centrifugation at 20,000rcf for 30 min at 10 °C. The soluble fraction was loaded onto a HisTrap HP column (Cytiva, Marlborough, MA, USA), washed twice with 5 mL each and eluted in 2 mL fractions, except the first one which was collected as a 1 mL fraction. All fractions, except the first one, were pooled, concentrated

and desalted using PD-10 columns (Cytiva, Marlborough, MA, USA). Recombinant proteins were long-term stored at -80°C , thawed and desalted for experiments if necessary.

3.2.2.3 Bacteria Adhesion and Engulfment Studies

To study the specific adhesion and subsequent process of engulfment of bacteria via different types of GUVs (with and without anchor lipids), they (1 mL) were incubated with the purified gp37 protein (250 nM) for 1 h, at RT. Subsequently, the mixture was centrifuged for 3 min at 400 rcf, after which the supernatant was discarded and buffer solution was added to restore the original volume of 1 mL. This additional centrifugation step was incorporated to remove any excess free gp37 protein present in the solution. Thereafter, the readily grown and prepared bacteria in the appropriate buffer solution were added to the GUV-gp37 mixture and incubated for a minimum of 30 min, after which they were examined via CLSM.

3.2.2.4 Gold Nanorod Synthesis

AuNRs were synthesized according to the seed-mediated growth method.¹³⁷ The used amounts were upscaled and adjusted to achieve a higher yield and AuNRs with an absorbance maximum of around 808 nm, corresponding to an aspect ratio of 4. All solutions were prepared and kept in a water bath set to 26°C . In the first step, the seed solution was prepared in a 30 mL flask. Under gentle stirring, CTAB (19.5 mL, 0.1 M), HAuCl₄ (0.5 mL, 0.01 M) and freshly prepared, ice-cold NaBH₄ (1.2 mL, 0.01 M) were mixed for 2 min and kept undisturbed for 2 h. In the second step, the growth solution was prepared by adding HAuCl₄ (10 mL, 0.01 M), AgNO₃ (1.6 mL, 0.01 M), and HCl (4 mL, 1 M) to an aqueous CTAB solution (180 mL, 0.1 M). After thoroughly mixing the yellowish solution, AA (1.6 mL, 0.1 M) was added until the solution turned completely colorless. In the final step, the seed solution (20 mL) was added after 2 h to the readily prepared growth solution, mixed for 30 sec and kept overnight at 26°C undisturbed (Figure 3-1). A reddening of the solution indicates successful rod growth. To remove the excess of CTAB, the solution was centrifuged at 14,000 rpm ($\approx 24,038$ rcf, Optima L-80 XP Ultracentrifuge, rotor: SW 32 Ti, Beckman Coulter GmbH, German) for 25 min at 26°C . The supernatant was removed and AuNRs were washed with MilliQ-water. This step was repeated at least three times. AuNR stock solutions were stored in glass vials in the dark at 4°C until further use.

3.2.2.5 Gold Nanorod Functionalization

After synthesis, AuNRs are stabilized by CTAB which is considered toxic at a certain concentration.¹²⁴ For this reason, CTAB is replaced by PEG-thiol molecules proven to show good biocompatibility.¹²³ AuNRs were coated according to the adjusted protocol of Zhang et al.¹²⁸. In brief, CTAB-stabilized AuNRs were centrifuged (1 mL, $c \approx 2$ mg/mL, $\approx 24,038$ rcf, Optima L-80 XP Ultracentrifuge, rotor: SW 32 Ti, Beckman Coulter GmbH, German, 25 min at 26 °C), supernatant was removed and mPEG-SH (95 μ L, 8 mM), Chol-PEG-SH (5 μ L, 8 mM) and Tris-buffer (800 μ L, 50 mM, pH3 adjusted by HCl) were added. The solution was kept mixing for 30 min at ≈ 200 rpm on a shaker. Incubation was followed by centrifugation ($\approx 24,038$ rcf, 25 min, 26 °C), supernatant was removed and AuNRs were dispersed in water or appropriate GUV buffer (sucrose, 280 mM). To re-dissolve agglomerates, re-dispersed samples were placed in the ultrasound bath for 15 min. Samples were stored at 4 °C until further use. The whole process is schematically illustrated in Figure 3-7.

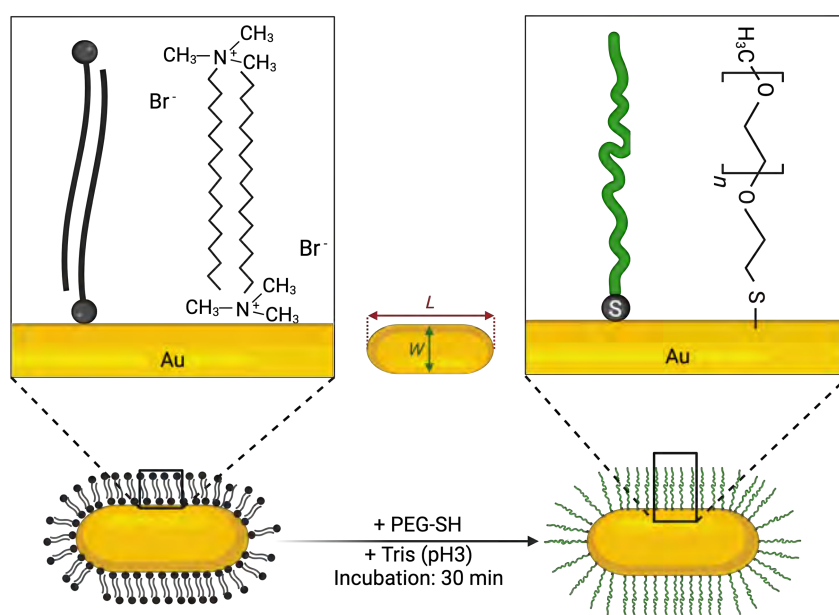


Figure 3-7: PEG-coating procedure of AuNRs. Addition of PEG-thiol together with Tris-buffer to CTAB-stabilized AuNRs (left) results in replacement of CTAB on the gold surface by PEG-thiols (right). Created with BioRender.com.

Results & Discussions

Chapter 4

4 Results & Discussions

4.1 Modular Porous Polymer-Based Microcapsule System for Trapping and Light-Triggered Killing of Bacteria

Polymer-based microcapsules (μC) employed in the context of antibacterial applications must exhibit specific characteristics to ensure optimal efficiency in trapping, retaining, and killing different types of bacteria. In this context, it is crucial to consider a number of parameters, particularly surface, size, and shape (the “3S” parameters), in order to develop an optimized system for the desired application. The following paragraphs describe the step-by-step design of an optimized polymer μC , offering insights into the μC production and formation process, as well as the impact of composition alterations. Consequently, the initial paragraph will delineate the fundamental production processes and methodologies, elucidating their advantages and disadvantages with respect to the development of an efficacious and optimized μC .

The second paragraph will concentrate on the experimental preparation and composition of the μC . This section will present the role(s) that each component plays during μC formation, as well as the final outcome that is produced by the component in isolation and/or in conjunction with other components. Furthermore, the section will provide insight into the general mechanisms of μC formation and additional post-production modifications that enhance the microcapsules' trapping and retaining performance.

Following the identification of the most suitable composition, which features a μC with optimized trapping and retaining properties, the third paragraph will address the issue of bacterial killing using photothermal heating properties of implemented gold nanorods. Therefore, the process of AuNR functionalization, which results in the effective incorporation of AuNRs into the μC s, is outlined. Additionally, the bacterial killing efficacy of the AuNR-functionalized μC is compared to that of the non-functionalized ones.

4.1.1 Demanded Design of Polymer-Based Microcapsules

PLGA particles are well-established in the medical field and are frequently utilized in a variety of applications. Mostly solid or porous micro- and nano-PLGA particles are utilized as drug delivery systems, capable of carrying specific drugs¹⁴⁰ (e.g., antibiotics^{141, 142}, anti-cancer agents^{143, 144} or pulmonary drugs^{145, 146}) to a designated target. The required properties of the particles are determined by the intended field of application, with the objective of optimizing the targeted performance. In the context of polymer particles utilized as antibacterial traps to retain bacteria in a confined space, kill them, and protect surrounding tissue, ideal particles would need to offer certain parameters (Figure 4-1):

- *Hollow cavity*

In order to achieve the primary objective of capturing and retaining bacteria within a confined space, it is essential that the polymer particles provide a hollow cavity of sufficient volume to accommodate a specified number of bacteria.

- *Size*

The objective is to achieve a particle size in the low micrometer range. If we assume a μC shell thickness of approximately 2 - 4 μm , the diameter of the entire capsule should be at least 15 - 20 μm (with a volume \approx 700 - 3000 μm^3). These dimensions facilitate the potential uptake of several bacteria (with average bacterial cell volumes of primary models ranging from 0.4 - 3 μm^3)¹⁴⁷. Secondly, the surface-to-volume ratio is a crucial aspect of μCs . The surface-to-volume ratio of smaller μCs is higher, which means that there is more available surface for potential bacteria to contact and penetrate. Furthermore, an increase in available surface area would be advantageous for potential surface modifications as well. Accordingly, the previously mentioned μC diameter of 15 - 20 μm is considered an appropriate compromise.

- *Porosity*

Bacteria can only penetrate the hollow interior of the μC through pores that connect the surrounding environment with the microcapsule's interior (Figure 4-1). The pores must have a specific size range to permit bacterial penetration (e.g., *E. coli*: length \approx 1 - 3 μm , diameter \approx 0.25 - 1 μm)¹⁴⁸ while simultaneously reducing the likelihood of bacterial escape from the hollow cavity. Hence, a pore diameter of

0.5 - 4.5 μm was considered suitable for the intended application. Moreover, the number of pores is critical to increasing the probability of bacterial penetration. An increase in the number of pores enhances the likelihood of bacteria encountering a pore. However, the degree of porosity also presents a trade-off with mechanical stability. An elevated degree of porosity would result in a reduction in the quantity of material available for particle stabilization, thereby diminishing the mechanical stability.

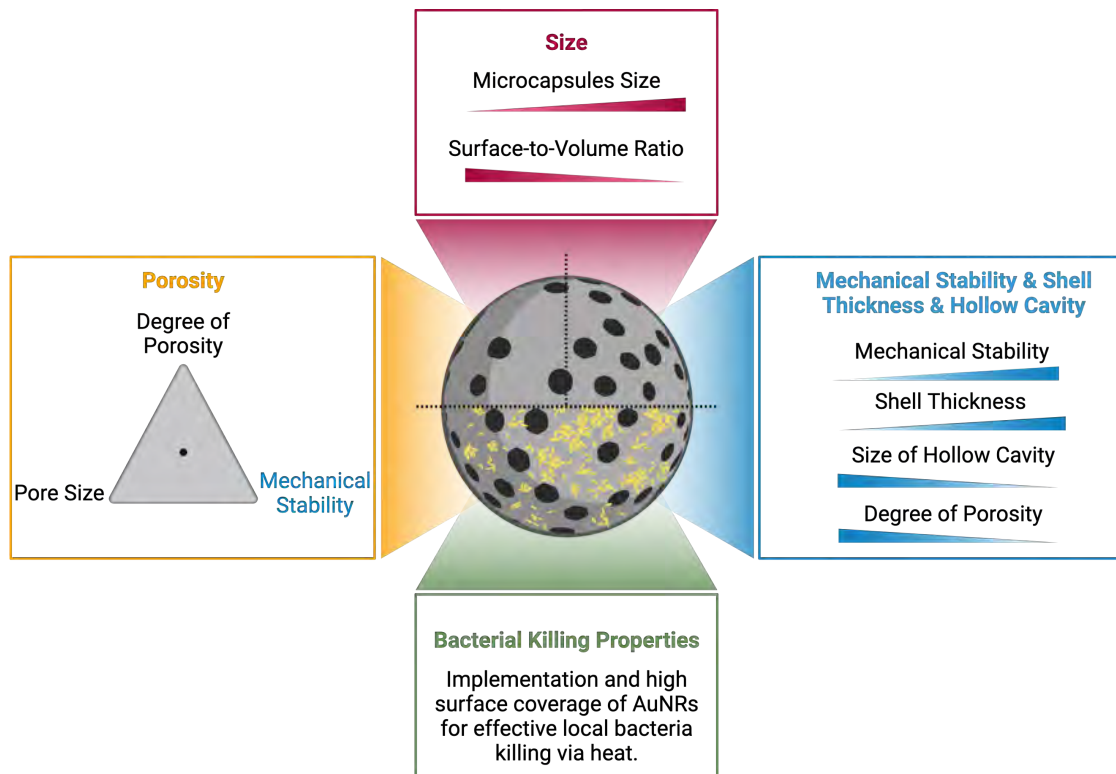


Figure 4-1: Desired μC properties (i.e., size, mechanical stability, shell thickness, hollow cavity, porosity, and bacteria-killing properties) for optimized bacteria capturing, retaining and killing. Created with BioRender.com.

- *Mechanical stability & shell thickness*

Moreover, the system must provide a sufficient degree of mechanical stability. This is a requirement for potential applications involving μCs as a surface coating, as these must be capable of withstanding certain mechanical forces (e.g., hammering during the integration of orthopedic implants into the patients' body). This aspect is also correlated with the thickness of the μC shell. A reduction in the thickness of the shell would result in a decrease in stability, as less material is available for the capsule shell (Figure 4-1).

- *Killing properties*

To achieve the desired antibacterial properties of the μ Cs, it is necessary to implement a killing mechanism into the system (Figure 4-1). In this thesis, gold nanorods (AuNRs) were incorporated into the μ C shell and surface, with the objective of eliminating bacteria through the generation of photothermal, localized heat.

4.1.2 Polymer-Based Microcapsules Production and Formation Procedure

The primary objective of this thesis was to develop a reliable technique for producing the fundamental framework of PLGA-based particles that possess three principal characteristics: 1) A size in the micrometer range, which is sufficiently large to trap bacteria. 2) A hollow cavity formed within the particle, creating a space that encloses the bacteria, and 3) a porous shell structure to enable active bacteria penetration from the outside into the confined space. Moreover, the objective was to develop a process that could be easily and rapidly implemented, resulting in high yields within a relatively short time frame.

A variety of techniques can be employed to produce polymer-based particles (for further details, see Chapter 1.8). In consideration of the desired and previously discussed μ C properties, the emulsion solvent evaporation technique as a bulk approach was selected as the most appropriate production method as it offers a high-throughput, fast and reliable way to produce the desired type of μ Cs. A second option would be the use of a microfluidic device, thereby affording precise control over particle size and morphology. Nevertheless, this method is relatively complex in device production and particle formation as well as time-consuming, resulting in a significant reduction in the quantities produced. Consequently, this thesis focused on the bulk emulsion solvent evaporation technique. Accordingly, we developed a one-pot, bulk emulsification formation process that fulfills the desired and previously specified requirements.

The following chapter will first describe the general, technical process of μ C production, followed by a detailed examination of the actual formation process, the used technical details (i.e., emulsification speed) and the effects each added chemical/additive had during

the μC formation (i.e., different core-forming oils, variation of polymer quantities, different pore-forming methods, addition of additives).

4.1.2.1 Polymer Particle Formation – The Emulsion Evaporation Process

The developed μC production process can be divided into a three-step procedure (Figure 4-2). The initial step of the process entailed the preparation of the oil and water phases (Figure 4-2, step 1). The oil phase comprised all polymers utilized to fabricate the intended μC type, dissolved in an organic, volatile solvent. Here, PLGA was used as the main μC forming polymer due to its biocompatibility, biodegradability, and FDA- and EMA-approved status.^{63, 66, 69, 70, 149} Dichloromethane (DCM) was used as solvent due to its low boiling point/high volatility and low solubility in water.^{150, 151}

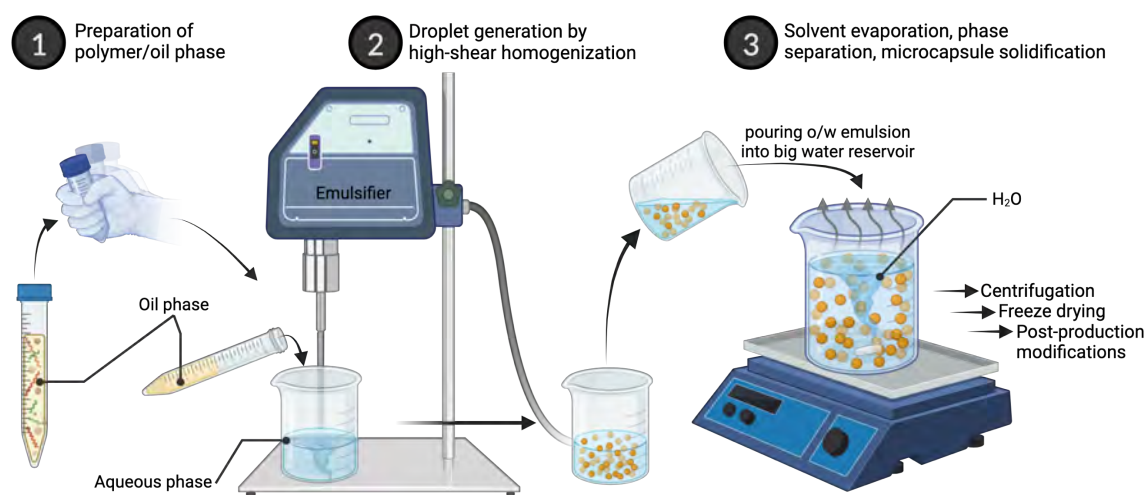


Figure 4-2: Illustration of the three major steps of the one-pot bulk emulsification process of μC formation: 1) Production of oil phase and addition of aqueous phase. 2) High-shear homogenization to generate the oil-in-water emulsion. 3) Addition of o/w emulsion into a large volume of water achieving complete solvent removal, phase separation, and polymer solidification. Created with BioRender.com.

In order to achieve the desired, specific features of the polymer particles (e.g., a porous shell structure, hollow cavity), additional polymers and additives were incorporated into the oil phase. The water phase contained a surfactant, which served to stabilize the formed oil-in-water (o/w) emulsion. The o/w emulsion itself was formed by applying mechanical shear forces produced by an emulsifier (Figure 4-2, step 2). The produced o/w emulsion was rapidly poured into a large volume of water (Figure 4-2, step 3) triggering PLGA precipitation. Since degradation of PLGA is triggered by hydrolysis of the ester bonds in

the polymer backbone when exposed to water^{66, 152}, freeze-drying enabled long-time storage of the particles without significant degradation of the PLGA due to removal of water residues. Subsequently, the μC powder was utilized for post-production modifications.

4.1.2.2 Solid Particle Formation

The initial step involved the production of solid PLGA particles, with the objective of confirming the efficacy of the emulsion solvent evaporation process. PLGA with a LA:GA ratio of 50:50 (Resomer® 505) was employed as the polymer of choice, dissolved in DCM. Initially, a single oil-in-water emulsion was generated in a low volume of a surfactant (PVP)-containing aqueous solution through emulsification (Figure 4-3a, step 1). To ensure efficient droplet generation, the prepared oil and water phases were mixed at a water-to-oil volume ratio of 5:1. At lower ratios, the formation of an efficient o/w emulsion was not observed, likely due to insufficient water-surfactant volume to stabilize the produced emulsion. Higher ratios were also found to stabilize the produced emulsion, although this resulted in a reduction in production efficiency. Accordingly, the optimized water-to-oil ratio was determined and established at a ratio of 5:1. The as-produced o/w emulsion was then immediately poured into a large volume of water, which triggered the dissolution of the solvent into the surplus water and the subsequent evaporation over time via continuous stirring (Figure 4-3a, step 2). This process resulted in the precipitation of the polymer, leading to the formation of solid PLGA particles (Figure 4-3a, step 3). Subsequent SEM analysis of the collected and freeze-dried PLGA particles revealed homogeneous particles with a spherical shape and an average size range of $11.8 \pm 3.5 \mu\text{m}$ ($N=200$). Moreover, the particles exhibited a smooth, non-porous surface structure (Figure 4-3a and c). The DCM/PLGA phase was fluorescently labeled, thus enabling the analysis of the internal structure of the particles by fluorescent microscopy. Additional CLSM analysis corroborated the presence of a solid core structure in the particles, as illustrated in Figure 4-3b and d.

Furthermore, the impact of an increased solvent portion and a reduction in polymer concentration within the oil phase was investigated. similar spherical, solid, non-porous particles with a smooth surface were observed (Figure 7-1). The reduction in particle size was found to be $\approx 15\%$ ($10.0 \pm 2.5 \mu\text{m}$, $N=200$), which can be attributed to the lower

concentration of polymer in the oil phase, resulting in a decreased viscosity and, consequently, a simplified breakdown of the oil phase into smaller droplets during emulsification.

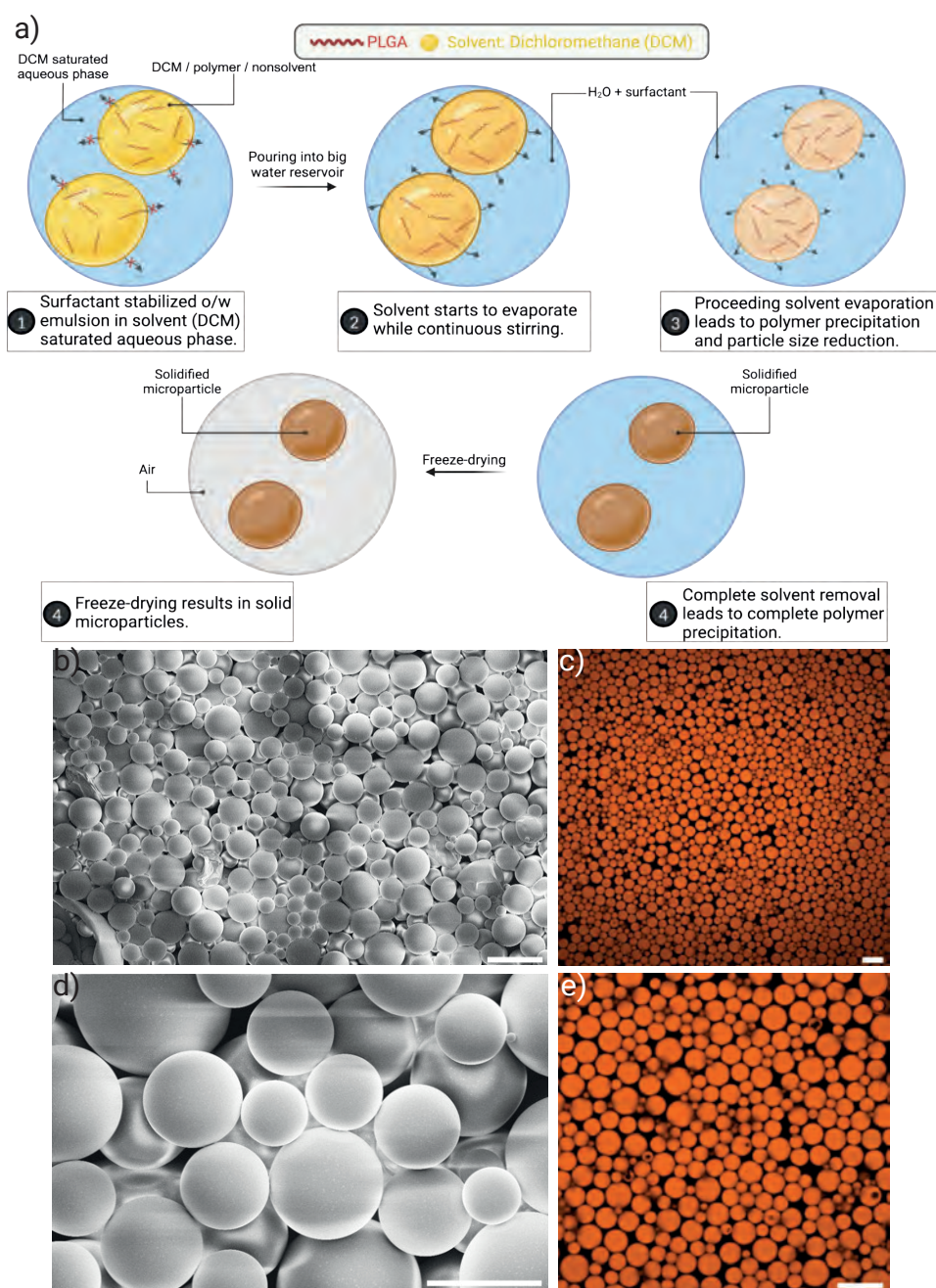


Figure 4-3: a) Step-by-step illustration of the single-emulsion solvent evaporation formation process to form single-phase polymer particles. SEM (b and d) and CLSM (c and e) micrographs of the continuous polymer particles with solid core produced by one-pot emulsion solvent evaporation methods ($C_{PLGA} = 25$ g/L). DCM/PLGA phase was fluorescently labeled with Nile red (orange). Scale bars: b) and c): 20 μ m, d) and e): 10 μ m. a) created with BioRender.com.

4.1.2.3 Hollow Core Generation

In the process of creating μ Cs with the aforementioned properties, the next step was the formation of a hollow cavity. Therefore, the double emulsion and solvent evaporation techniques were combined to create PLGA particles with a hollow core, similar to those produced by the double emulsion technique alone. In contrast to the classical double emulsion technique where two emulsification steps are required to form hollow capsules, the technique applied here with the used composition required only a single emulsification step leading to a single o/w emulsion as starting point (Figure 4-4, step 1). Due to the presence of fluorinated oil in the oil phase, a double emulsion was subsequently generated, accompanied by phase separation due to the progressive evaporation of the solvent over time (Figure 4-4, step 2 and 3). Prior to emulsification and solvent evaporation, solvent, nonsolvent and polymer should be adjusted in concentration and volume to form one homogeneous oil phase. A variety of nonvolatile nonsolvents are suitable for the formation of hollow PLGA particles. Two potential nonsolvents were tested here to identify the most appropriate for the formation of the desired hollow μ Cs (i.e., perfluorooctyl bromide (PFOB) and HFE-7500).

Table 4-1: Selected properties of HFE-7500 and perfluorooctyl bromide (PFOB).¹⁵³⁻¹⁵⁵

Properties	HFE-7500	PFOB
Density [g/cm ³], [@ 25 °C]	1.61	1.93
Kinematic viscosity [cSt]	0.77 [@ 25 °C]	1.0 [@ 25 °C]
Solubility in water [ppm]	0.0213 [@ 23 °C]	0.0025
Molar mass [g/mol]	414	499

The three components of the oil phase (i.e., DCM, PLGA, HFE-7500 or PFOB) were combined and emulsified in an aqueous phase (Figure 4-4, step 1). Subsequently, solvent diffused into the aqueous phase and evaporated (Figure 4-4, step 2). This process of solvent evaporation led to a gradual depletion of the volatile solvent (DCM) from the system, resulting in phase separation between the polymer and the nonsolvent. To achieve the desired core-shell μ C morphology, it was necessary to obtain a fully encapsulated core-forming nonsolvent by the polymer phase in the middle of the particle.

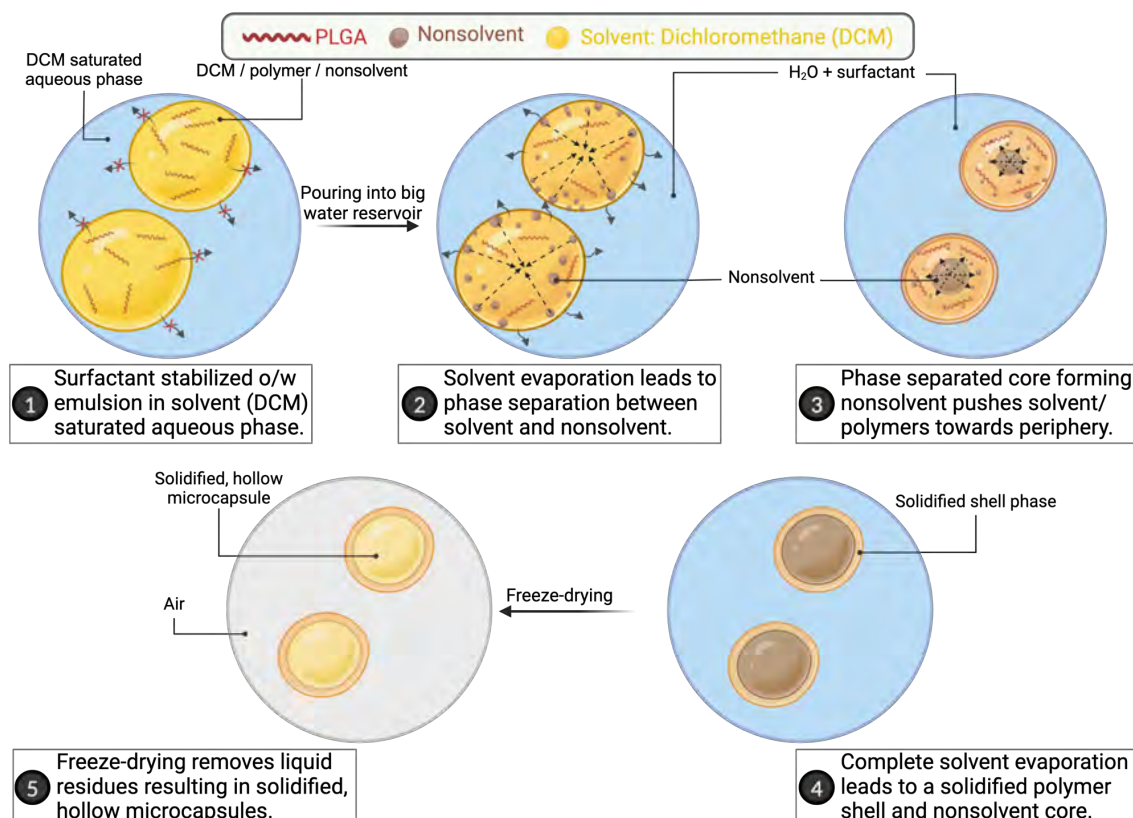


Figure 4-4: Step-by-step illustration of the single-emulsion solvent evaporation formation process to form hollow polymer particles. 1) Oil-in-water emulsion was formed and stabilized by PVP, 2) solvent was evaporated leading to phase separation. 3) Phase separated nonsolvent (i.e., HFE-7500 or PFOB) was forming the core. 4) Complete solvent evaporation led to polymer precipitation and core-shell morphology. 5) Final μ Cs were observed after freeze-drying. Created with BioRender.com.

The crucial parameter to be taken into account here was the interfacial tension (see Chapter 1.9). The selection of a highly hydrophobic nonsolvent as a core-forming material results in the formation of an energetically favorable core-shell morphology due to the significantly higher interfacial tension between HFE-7500 or PFOB (γ_{ow}) and the aqueous phase compared to PLGA and the aqueous phase (γ_{pw}).¹⁰¹ As a result, the nonsolvent forms the core, surrounded and shielded from the surrounding aqueous phase by the less but still hydrophobic polymer (PLGA). Both chemicals tested as nonsolvents (HFE-7500 and PFOB) were found to be highly hydrophobic and practically insoluble in water (Table 4-1), due to their perfluorinated structure. Ester bonds in the PLGA main chain allow for some hydrogen bonding between water and polymer to occur, leading to a reduced interfacial tension compared to perfluorinated substances. Therefore, the subsequent evaporation of DCM and phase separation resulted in the formation of a core comprising the hydrophobic

nonsolvent, which was positioned towards the center of the structure, while the polymer (PLGA) was pushed towards the periphery, forming a shell-like structure (Figure 4-4, step 3 and 4, Figure 4-5, b and d).

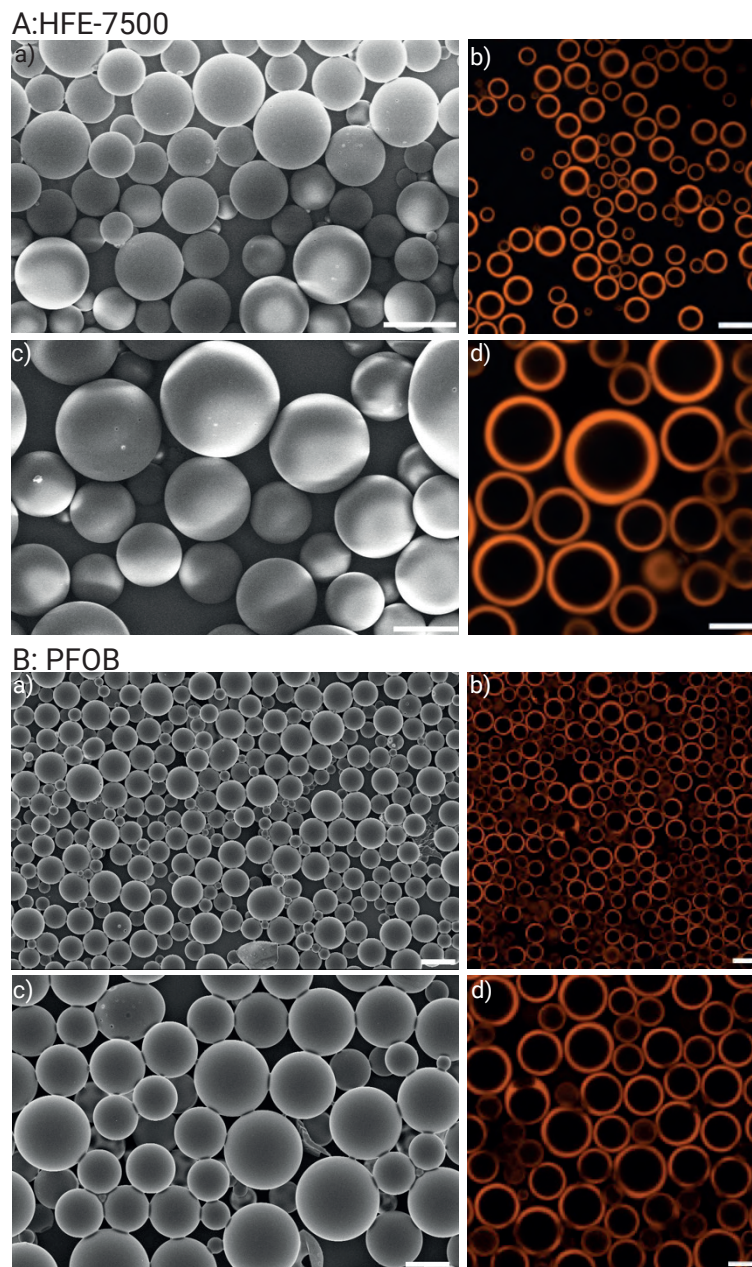


Figure 4-5: Comparison of μ Cs produced by using HFE-7500 (A) and PFOB (B) as core forming chemicals. (A) SEM (a and c) and fluorescence CLSM images (b and d) of μ Cs produced by using HFE-7500 as core-forming nonsolvent. (B) SEM (a and c) and fluorescent, CLSM images (b and d) of μ Cs produced by using PFOB as core-forming nonsolvent. Nile red was used as fluorescent dye to label the polymer phase (orange). Scale bars: a) and b): 20 μ m, c) and d): 10 μ m.

The formation process was accompanied by a reduction in particle size due to the removal of DCM, resulting in a final average capsule size of $13.9 \pm 3.8 \mu\text{m}$ for the μCs produced with HFE-7500 and $12.4 \pm 3.9 \mu\text{m}$ ($N=200$) for PFOB. Following the freeze-drying process, SEM analysis confirmed the homogeneous spherical particle shape with smooth, non-porous surface structure (Figure 4-5, a and c). Core-shell morphology of both batches was confirmed by CLSM (Figure 4-5, b and d) validating that both core-forming chemicals were appropriate candidates to form the desired core-shell morphology. The increased average particle size of the hollow compared to the solid core PLGA particles might be attributed to the fact that hollow particles require less polymer per particle than particles with solid core. Therefore, there was a greater quantity of material remaining for the formation of larger particles. Moreover, the incorporation of the core-forming oil may potentially elevate the viscosity of the oil phase, thereby rendering it more challenging to disperse the oil phase into smaller droplets.

4.1.2.4 Microcapsules Size Variation

The final μC size was determined by a combination of factors, including the composition of the oil and water phase during the formation of μC via the o/w emulsion evaporation process, and the process of emulsification. The o/w droplet size, and consequently the size of the final μCs , can be adjusted and tuned via the speed of emulsification and hence the mechanical forces applied to break down the oil phase into an o/w emulsion.¹⁵⁶ After identifying a suitable composition of the oil and aqueous phase, further optimizations concerning μC size were investigated to produce the most efficient μC type for bacteria trapping and retaining.

On the one hand, a reduction in particle size, which would result in an increase in the number of smaller particles, would lead to an enhancement in the surface-to-volume ratio of the system. This would result in a greater available surface area for potential pore formation, which, in turn, would increase the probability of bacterial penetration through these increased number of pores. Furthermore, the availability of a larger surface area for potential surface functionalization is another consequence of smaller particles. It is crucial to note that the hollow cavity of the particles must possess a specific volume to enable effective bacteria retention, while the pores must be sufficiently large to permit bacterial penetration. Achieving an appropriate equilibrium between these factors is therefore important in order to carefully adjust the μC dimensions to an appropriate size.

As previously outlined, the o/w emulsion was formed through the application of mechanical shear forces (i.e., emulsification). These forces enabled the fragmentation of the oil phase into smaller oil droplets, which was subsequently stabilized within the aqueous phase through the action of a surfactant. Four distinct emulsification speeds were evaluated. For simplification, a systematic nomenclature was introduced for the various sample types. The numeral in the middle indicates the PLGA concentration, while the letter and number at the end indicate the level of emulsification. All specifications and the measured μC sizes are displayed in Table 4-2. The overall dimensions of the freeze-dried μC s exhibited a range of sizes, varying from $17.4 \pm 3.9 \mu\text{m}$ at the lowest emulsification velocity ($\mu\text{C-25-L1}$) to a size of $2.7 \pm 0.7 \mu\text{m}$ at the maximum speed of emulsification ($\mu\text{C-25-L6}$).

Table 4-2: Specifications of μC s produced at different emulsification speeds.

Sample name	Emulsification level	Speed of emulsification [rpm]	PLGA concentration [g/L]	μC size [μm]
$\mu\text{C-25-L1}$	Level 1 (L1)	8,300	25	17.4 ± 3.9
$\mu\text{C-25-L2}$	Level 2 (L2)	9,100	25	16.9 ± 3.6
$\mu\text{C-25-L4}$	Level 4 (L4)	14,500	25	9.2 ± 2.7
$\mu\text{C-25-L6}$	Level 6 (L6)	28,500	25	2.7 ± 0.7
$\mu\text{C-37.5-L6}$	Level 6 (L6)	28,500	37.5	3.5 ± 1.3

These measured overall sizes of the μC s provide confirmation that the oil phase was effectively broken down into smaller and smaller droplets with increasing emulsification speed. Analysis of the SEM and CLSM micrographs (Figure 4-6a-c) demonstrated that complete capsule formation occurred up to an emulsification speed of 14,500rpm ($\mu\text{C-25-L4}$). This situation changes when the speed of emulsification is further increased to a maximum of 28,500rpm ($\mu\text{C-25-L6}$). Here, SEM and CLSM analysis showed incomplete capsule formation for the majority of particles, resulting in a considerable number of bowl-shaped, half-formed particles (Figure 4-6d). At these increased emulsification speeds, the oil droplets were dispersed into small droplets, thereby resulting in a high surface-to-volume ratio. It is postulated that under these conditions, the quantity of polymer available is insufficient to form a complete shell in all droplets. Therefore, an

adjustment of the PLGA concentration would be necessary to guarantee the complete formation of the capsules.

To substantiate this hypothesis, the identical sample formation conditions were employed while utilizing an elevated concentration of PLGA in the oil phase. SEM analysis of the sample confirmed an improvement in particle formation, with a decreased number of bowl-shaped particles compared to the sample with a lower concentration of PLGA (Figure 4-6e). A size increase of around 23% to a particle diameter of $3.5 \pm 1.3 \mu\text{m}$ for the sample with a larger PLGA concentration ($\mu\text{C-37.5-L6}$), compared to the one with a lower PLGA concentration but at the same emulsification rate ($\mu\text{C-25-L6}$) can be attributed to the increased viscosity of the organic phase resulting from the elevated number of PLGA molecules per volume (Figure 4-7a, $\mu\text{C-25-L6}$ versus $\mu\text{C-37.5-L6}$).

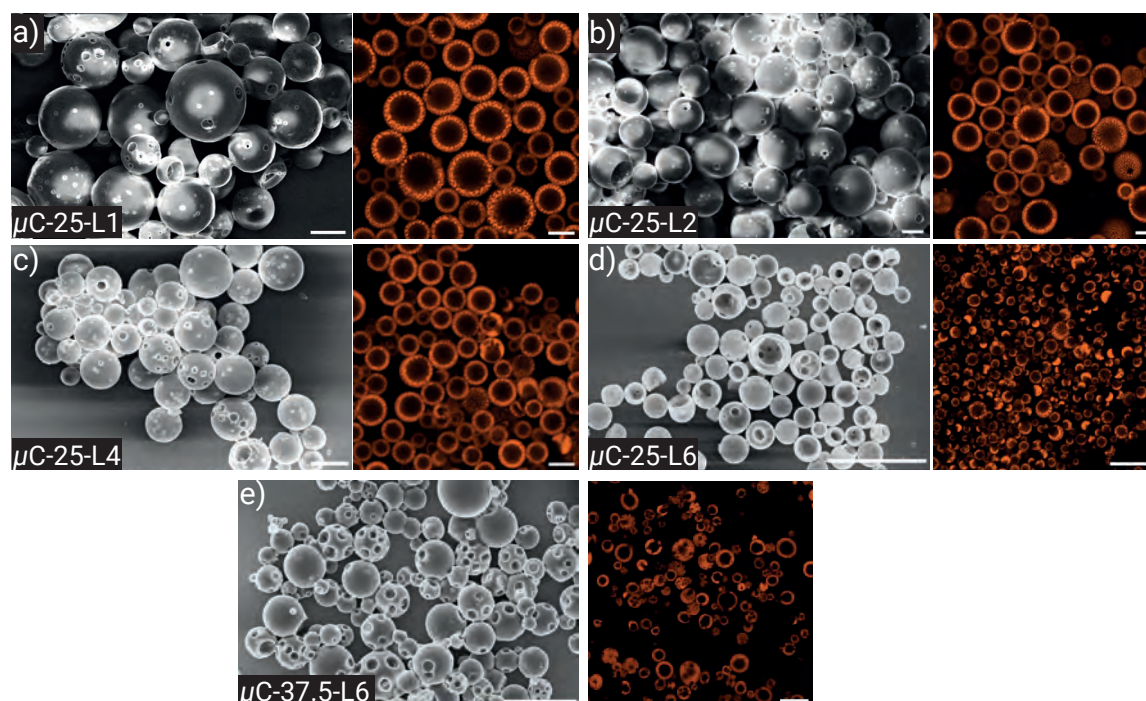


Figure 4-6: a)-d): Representative SEM and CLSM images of μCs produced at varying emulsification speeds at constant PLGA concentration (25 g/L). e) Polymer particles produced at highest speed of emulsification (28,500 rpm) but with an increased concentration of PLGA (37.5 g/L). Scale bars: 10 μm .

In addition to the overall μC size, the diameter of the hollow cavity was determined by analyzing the CLSM images. Capsules produced at the two lowest emulsification speeds ($\mu\text{C-25-L1}$ and $\mu\text{C-25-L2}$) showed nearly identical cavity diameter, with values of $9.0 \pm 2.3 \mu\text{m}$ and $9.6 \pm 3.1 \mu\text{m}$, respectively (Figure 4-7b). Relating the slightly increased cavity size of the sample formed at 9,100 rpm ($\mu\text{C-25-L2}$) to the overall μCs size of the

same sample, the data indicated that the polymer shell was found to be thinner than that of μ Cs produced at the lowest speed (μ C-25-L1). This observation can be attributed to the fact that the slight decrease in overall particle size due to higher speeds for μ C-25-L2 resulted in an increased particle number and, hence, an increased surface-to-volume ratio. Therefore, the availability of PLGA for capsule formation is reduced, resulting in thinner shells and, subsequently, an enlarged cavity size for μ C-25-L2 in comparison to μ C-25-L1. It should be noted that the cavity size was not determined for samples with emulsification speeds exceeding 14,500 rpm, due to the prevalence of bowl-shaped particles and incomplete capsule formation. With all these observations, it was concluded that an emulsification speed up to 14,500 rpm produced μ Cs suitable for the targeted application of bacteria trapping and retaining. Nevertheless, particles produced at a speed of 14,500 rpm (μ C-25-L4) exhibited a relatively small inner, hollow volume, which shifted the focus for all further capsule formation and production experiments towards samples produced at slower speeds. The diameter of the μ Cs and the diameter of the hollow cavities (Figure 4-7b) exhibited only minor discrepancies at the two lowest speeds (μ C-25-L1 and μ C-25-L2). Therefore, the slowest emulsification speed (μ C-25-L1) was selected for all subsequent experiments, providing an optimal balance between particle size, hollow cavity diameter, and resulting shell thickness.

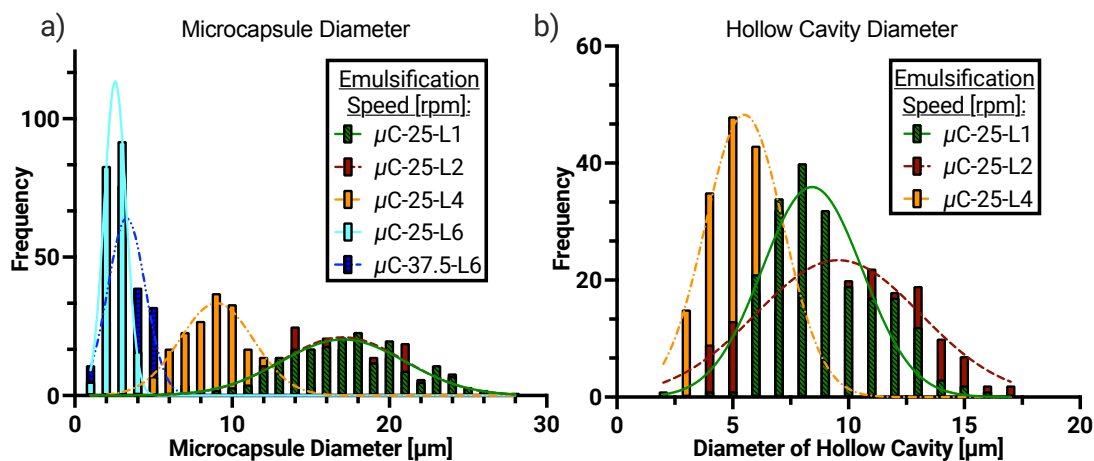


Figure 4-7: μ C diameter (a) and diameter of the hollow cavity (b) displayed as frequency histograms with fitted Gaussian distribution at different emulsification speeds. For the highest emulsification speed of 28,500 rpm two different PLGA concentrations were tested (μ C-25-L6 and μ C-37.5-L6). The size of the hollow cavity for samples produced with emulsification speeds higher than 14,500 rpm was not measured due to the high number of bowl-shaped particles. $N=200$ for each condition.

4.1.2.5 Importance of DCM-to-Water Volume Ratio

Another essential factor in the process of μ C formation is the ratio of DCM-to-water, which plays a key role in ensuring the proper and complete formation of the μ Cs. The efficacy and completeness of solvent removal are influenced by the volume of the aqueous phase, which is a significant factor that must be taken into consideration. At 20 °C, the solubility of DCM in water is approximately 17 g/L.¹⁵⁷ Therefore, taking into account that at optimized conditions, 4 mL of DCM ($\rho = 1.33 \text{ g/cm}^3$) were utilized in the μ C bulk formation process, a water volume of at least 313 mL was theoretically required for complete and fast solvent removal via diffusion and evaporation (i.e., DCM-to-water volume ratio $\approx 1:80$). To further examine the influence of the solvent-to-water ratio, the composition and volume of the oil phase were maintained while the volume of water the emulsion was added to was varied (Figure 4-2, step 3). Testing of different DCM-to-water volume ratios revealed capsule formation for three of the four tested solvent-to-water ratios (Figure 4-8). Below the critical value, μ C formation was possible resulting in core-shell morphologies for the samples with a solvent-to-water ratio of 1:500, 1:250 and 1:125 (Figure 4-8a-c). However, the decreased water volume affected capsule formation already at levels above the theoretical threshold. The particles produced at a ratio of 1:125 still exhibited complete hollow cavity formation; however, the shape of the particles was observed to be affected, resulting in less spherical and more irregular particles. Further reduction of the water amount below that critical ratio prevented complete capsule formation (Figure 4-8d). The emulsion droplets exhibited a tendency to fuse prior to the completion of polymer solidification. This phenomenon can be attributed to the decelerated solvent diffusion and evaporation, which resulted in delayed polymer precipitation. This led to the formation of larger, irregularly shaped, and incomplete particles, and even prevented the formation of any capsules. Optimal spherical capsule morphology was achieved at a DCM-to-water volume ratio of 1:250 (i.e., 4 mL of DCM poured into 1000 mL of water, Figure 4-8b). The discrepancy between the theoretically and experimentally determined DCM-to-water volume ratio can be attributed to factors such as local concentration fluctuations which were more efficiently balanced at higher aqueous phase volumes. Additionally, the kinetics of DCM removal may be altered when the surrounding aqueous phase starts to become saturated. With these insights, it is important to not only carefully tune the oil and aqueous phase composition as well as the speed of emulsification,

but it is also necessary to account for the volume of water used during μC production to achieve the desired polymer capsule dimensions and morphologies.

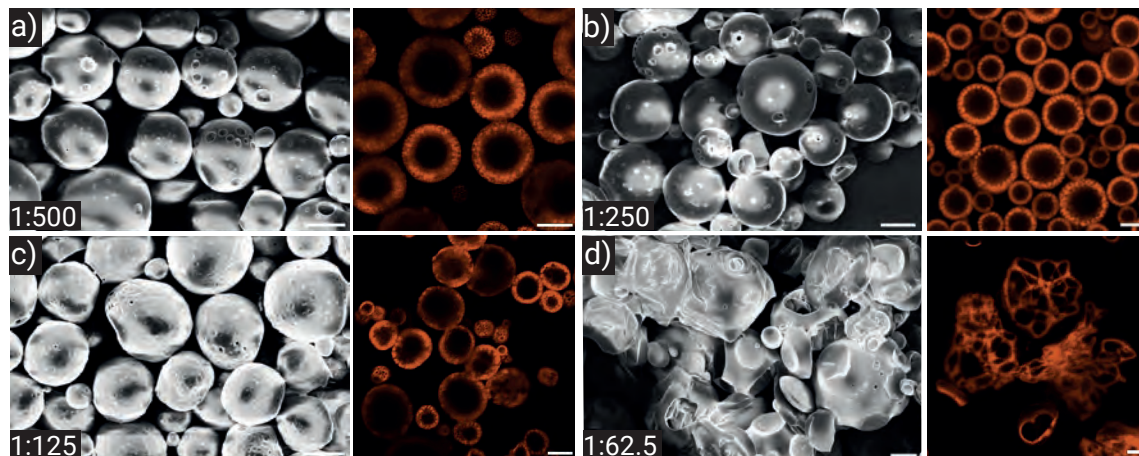


Figure 4-8: SEM and CLSM images of μC s produced at different DCM-to-water ratios. Oil phase composition was kept constant for all samples. Chosen solvent-to-water ratios were a) 1:500, b) 1:250, c) 1:125, d) 1:62.5. Scale bar: 10 μm .

4.1.2.6 Effect of Polyvinylpyrrolidone (PVP)

The key parameter which needs to be considered in the context of analyzing the effect of PVP within the system was the surface tension. In the majority of cases, a dispersing agent is introduced into a system with the objective of influencing the interfacial tensions between the phases present in the system (theoretical background see Chapter 1.9). PVP is employed in numerous applications as a surfactant-like agent.^{158, 159} During the emulsification process, the addition of PVP to the continuous aqueous phase resulted in the accumulation of PVP molecules at the interface between the water and organic phases. This significantly lowered the interfacial tension between these two phases (γ_{pw}), which in turn resulted in a higher value of the respective spreading coefficient (S_p).¹⁰¹ When this aspect is considered in conjunction with the experimental observations made by Eriksson et al.¹⁰¹ for a system with similar conditions, the following situation emerges: the higher value of S_p together with negative spreading coefficients for the oil-phase (HFE-7500, S_o) and the aqueous phase (S_w), would lead to a tendency of the system to form a core-shell morphology since this would be the theoretically calculated energetically most favorable state (Figure 1-10a). This theoretical assumption is supported by the experimental results, which demonstrate that the addition of PVP, as a dispersant, results in the formation of

uniformly shaped capsules with a core-shell morphology (Figure 4-9a). In contrast, in the absence of PVP in the aqueous phase during μC production, γ_{pw} is left unchanged, which in turn produced a more negative S_{p} theoretically leading to the formation of “acorn”-shaped particles as the most energetically favorable state. This situation was experimentally demonstrated in Figure 4-9b, showing a large portion of “acorn”- or bowl-shaped particles. These findings suggest that the use of a dispersant in the aforementioned system is of significant importance to ensure the complete and well-preserved formation of μCs .

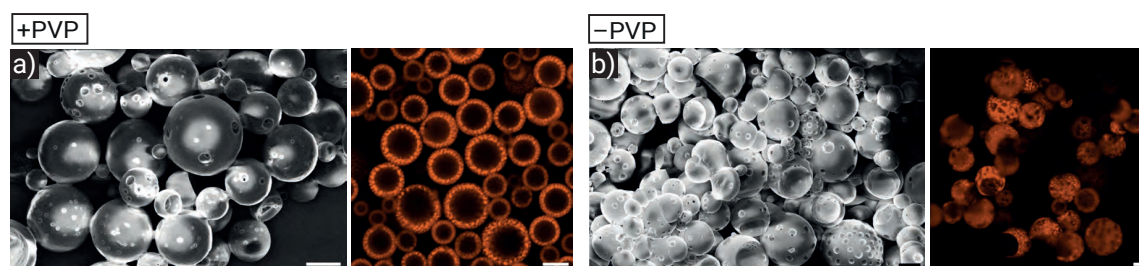


Figure 4-9: Effect of PVP on the μC formation process specifically on the capsule morphology. a) Microcapsules produced with the used of PVP (0.5% (w/v)) in the continuous aqueous phase and b) without PVP. Scale bars: 10 μm .

4.1.2.7 Pore Generation via Porogens

Once a confined space had been created within the polymer particles, the next step was to generate pores within the PLGA shell, in order to enable active penetration of bacteria from the outside into the cavity. In general, substances that create pores within polymer matrices and serve as pore-forming agents are referred to as porogens. Here, a variety of porogens and strategies were tested to identify the most efficient method for forming trans-shell pores of an appropriate size range for the desired application.

4.1.2.7.1 Pluronic®: F-127 vs. F-68

The initial polymer candidates identified as potentially suitable porogens were two distinct types of Pluronic® (F-127 and F-68). This choice was made due to the fact that Pluronic® are widely documented in the literature as polymers capable of inducing porous structures in a multitude of materials.^{74, 160, 161} Some of the most important properties of the chosen F-68 and F-127 are listed in Table 4-3.

Table 4-3: Chemical properties of the two types of Pluronic®, F-68 and F-127.⁷¹

Properties	F-68	F-127
EO units (average number)	153	200
PO units (average number)	29	65
Molar mass [Da]	≈ 8400	≈ 12600
CMC in water [mol/L]	4.8×10^{-4}	2.8×10^{-6}
HLB	29	22

EO: ethylene oxide, PO: propylene oxide, CMC: Critical micelle concentration, HLB: hydrophilic-lipophilic balance

Generally, the mechanism of pore formation by Pluronics® can be attributed to the amphiphilic character of the molecules. Immediately following the formation of an o/w emulsion, Pluronic® molecules exhibit a tendency to migrate towards the organic/aqueous interface, a phenomenon that can be attributed to their surface-active properties minimizing the systems energy. As the solvent proceeds to evaporate, Pluronic molecules may exhibit an aggregation tendency as a consequence of their amphiphilic nature. Subsequently, the porogen agglomerates become entrapped within the PLGA matrix as a result of polymer precipitation. The high water-extractability properties of Pluronics® facilitate the dissolution of trapped polymer during subsequent washing steps, thereby creating a porous structure.

The objective of this study was to evaluate the performance of F-127 and F-68 as porogens for the formation of a desired pore structure that would facilitate bacterial penetration and trapping. To this end, both materials were tested at different concentrations and PLGA/Pluronics® ratios. HFE-7500 was chosen as the core-forming chemical for all samples. Generally, all μ C samples including Pluronic® in the oil phase at the tested concentrations exhibited a visible difference in surface structure and shape compared to pure PLGA μ Cs. Firstly, both Pluronic® variants were tested at a PLGA-to-Pluronic® ratio of 2:1 and respective concentrations of 25 g/L and 12.5 g/L. The surface structure underwent a notable transformation, evolving from a smooth and non-porous surface for the pure PLGA capsules to a rougher and bumpier surface with the presence of small pores for both F-127 and F-68 (SEM images in Figure 4-10). Nevertheless, the degree of porosity was observed to be low in both cases. Only a limited amount/number of shell-permeating pores were identified, which would impede bacterial penetration. Moreover, a considerable

proportion of the particles within both samples did not exhibit the previously observed spherical structure, but rather a partially formed, bowl-like structure with a single large opening, analogous to a hemisphere (Figure 4-10). This observation might be also connected to the hollow core formation, which was also detected to be affected by the addition of Pluronic®. Especially F-127 at a concentration of 12.5 g/L and a PLGA/F-127 ratio of 2:1 exhibited a significant number of particles with either half formed cavity or a complete absence of hollow spaces within the particles. This observation could be attributed to the amphiphilicity of Pluronic®, which has the potential to disrupt the system to such an extent that the formation of a complete core-shell morphology becomes unfeasible. It is possible that the HLB value of the two porogens may be a significant factor in this context (Table 4-3). The HLB value of F-127 is lower than that of F-68 (22 vs. 29), making it a more suitable option for stabilizing hydrophobic substances in aqueous solution. Given these characteristics, it is plausible that F-127 may function as a surfactant at the DCM/HFE-7500/water interface, thereby reducing the surface energy and consequently the system's overall energy.

Eriksson et al.¹⁰¹ found that the complete formation of a core-shell morphology of a PLGA/non-solvent system in a continuous aqueous phase occurs relatively late in the process of evaporation. Furthermore, during DCM evaporation, the system was observed to transition from an intermediate state, where the particles are "acorn"-shaped, to a core-shell structure in the final stage of the formation process.¹⁰¹ This late transition in morphology could provide a potential explanation for the observed bowl-shaped particles. This hypothesis is supported by the observation that for some systems, the transition to the desired core-shell structure is too slow, resulting in polymer precipitation occurring before rearrangement was possible. This hypothesis is also supported by the observation that increasing the viscosity of the system by adding Pluronic® while maintaining the solvent concentration constant (i.e., increasing the overall polymer concentration in the oil phase) further complicates phase rearrangement, thereby increasing the likelihood of "acorn"-shaped particles, which ultimately result in bowl-shaped particles after freeze-drying. Moreover, the ability of Pluronic® to form micelles is further increasing the viscosity of the polymer phase¹⁶², compared to other porogens, promoting "acorn"-shaped particle formation.

For both samples displayed in Figure 4-10, a PLGA/Pluronic ratio of 2:1 was used (total polymer concentration: 37.5 g/L) while keeping the solvent volume at the same constant volume as for all samples presented in the chapters before. By increasing the total polymer

concentration, the viscosity of the DCM phase also increased. This could be one contributing factor to the larger particle size of the PLGA/Pluronic/HFE-7500 particles compared to the pure PLGA particles. As viscosity increases, it becomes more challenging to break down oil droplets into smaller units, resulting in larger final particle sizes of $13.3 \pm 4.7 \mu\text{m}$ ($N=200$) and $16.3 \pm 4.9 \mu\text{m}$ ($N=200$) for particles with F-127 and F-68 as porogen, respectively.

The so far tested and presented compositions provided evidence that both types of Pluronic® were capable of significantly altering the surface, shape, and porosity properties of the polymer particles. However, none of the previously tested compositions led to μCs with the desired properties, particularly in regard to porosity and overall structural integrity. Consequently, a series of supplementary Pluronic® concentrations and PLGA/Pluronic® ratios were subjected to testing and analysis. To reduce the number of bowl-shaped particles and simultaneously maintain a certain degree of porosity, the Pluronic® concentration was reduced to 6.25 g/L at a constant PLGA concentration (Figure 7-2B and Figure 7-3B). The overall integrity was observed to be improved with a reduced number of bowl-shaped particles and properly formed hollow cavities. In contrast, the porosity remained relatively unchanged, with a low number of trans-shell pores.

To account for the influence of both the porogen and the overall polymer concentration on the viscosity of the oil phase, the Pluronic® concentration was maintained at 6.25 g/L while the PLGA concentration was reduced to 12.5 g/L. By lowering the total polymer concentration, the viscosity of the oil phase was reduced, which improved the μC integrity and cavity formation. In the case of F-127, the porosity remained insufficient for the intended application. In contrast, a significant increase in porosity was observed for the sample in which F-68 was used as porogen at a concentration of 6.25 g/L (Figure 7-3C).

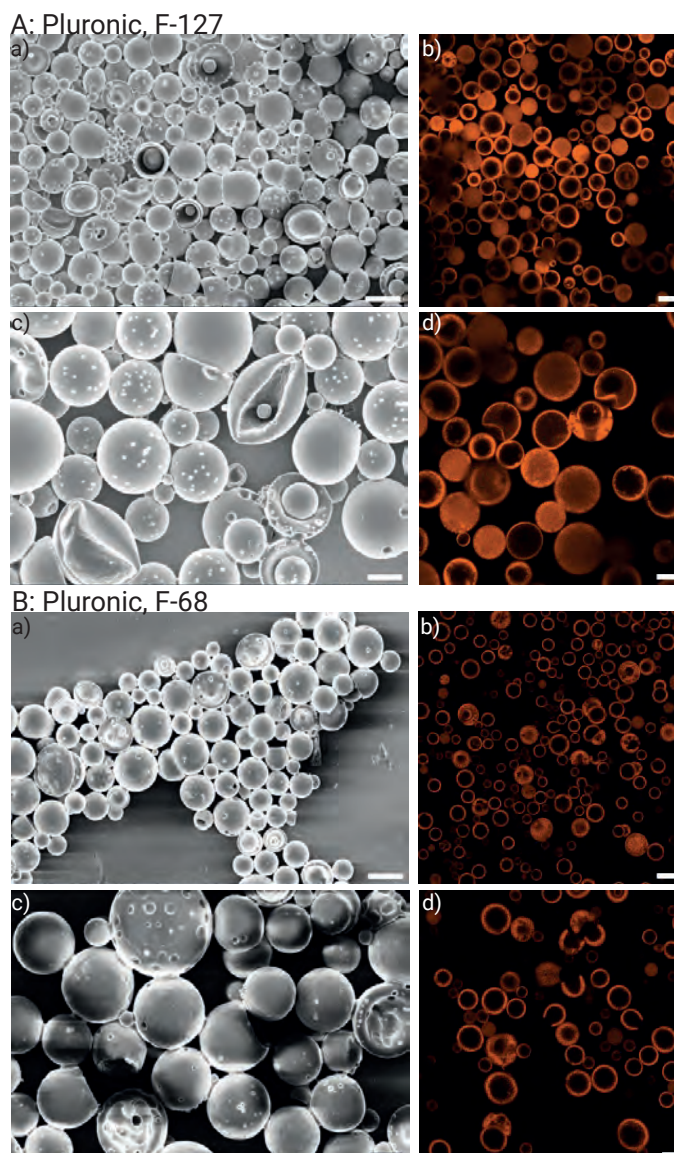


Figure 4-10: Comparison of μ Cs produced with two different types of Pluronic® as pore-forming agents. PLGA and Pluronic® concentration was 25 g/L and 12.5 g/L, respectively. (A) SEM (a and c) and fluorescent, CLSM micrographs (b and d) of μ Cs produced by using F-127 as pore-forming agent. (B) SEM (a and c) and fluorescent, CLSM images (b and d) of μ Cs produced by using F-68 as pore-forming chemical. Nile red was used as fluorescent dye to label the polymer/DMC phase (orange). HFE-7500 was used as core-forming agent for both samples. Scale bars: a) and b): 20 μ m, c) and d): 10 μ m.

4.1.2.7.2 Polyethylene Glycol (PEG)

In addition to Pluronic®, another organic additive was evaluated as a potential porogen, specifically PEG. Literature already reported pore-introducing effects of various PEGs with differing molecular weights.^{79, 80, 163, 164} To identify a suitable type of PEG for the presented system, six different molecular weights (M : 600, 1,500, 2,000, 4,000, 6,000, 10,000 g/mol)

and at least two different concentrations (i.e., 1.56 mmol/L, 3.13 mmol/L, additionally 6.25 mmol/L for M of 2,000, 4,000 and 6,000 g/mol) were tested. Subsequently, the samples were imaged and analyzed by SEM and CLSM in terms of their pore-forming performance. Representative SEM and CLSM micrographs of all molecular weights and concentrations are presented in the Appendix (Figure 7-4 to Figure 7-9). Generally, all samples which included PEG within the DCM/PLGA/HFE-7500 oil phase exhibited discernible differences in their surface structure relative to pure PLGA μ Cs produced without the use of a porogen. The concentration of PLGA and HFE-7500 was maintained constant across all tested samples.

The lowest molecular weight tested, PEG₆₀₀, demonstrated the highest percentage of intact μ Cs, with no detected bowl-shaped particles, and a fully formed shell-core structure (Figure 7-4). The same high integrity was obtained for samples using PEG with a molecular weight of 1.5kDa. Moreover, the presence of small pores was observed for both PEG₆₀₀ and PEG₁₅₀₀ at the tested concentrations of 1.56 mmol/L and 3.13 mmol/L. However, the pore size was observed to be notably small for both PEG types, which was considered inadequate for effective bacterial penetration. The pore diameter of the sample prepared with PEG₆₀₀ was analyzed to be in a range of $0.48 \pm 0.16 \mu\text{m}$ for PEG₆₀₀ and $0.45 \pm 0.18 \mu\text{m}$ for PEG₁₅₀₀ (Table 4-4). Given these relatively small average pore diameters, PEG₆₀₀ and PEG₁₅₀₀ were excluded from the choice as potential porogen, since bacteria like *E. coli* with an average diameter of $\approx 0.25 - 1 \mu\text{m}$ ¹⁴⁸ would not be able to effectively penetrate through the pores into the cavity.

Table 4-4: Diameter of pores formed in μ C shell by using PEG as porogen at different molecular weights.

Sample	Molecular weight of PEG [g/mol]	Concentration of PEG [mmol/L]	Average pore diameter [μ m] ($N = 100$)
PEG ₆₀₀	600	3.13	0.48 \pm 0.16
PEG ₁₅₀₀	1,500	3.13	0.45 \pm 0.18
PEG ₂₀₀₀	2,000	3.13	0.79 \pm 0.33
PEG ₄₀₀₀	4,000	3.13	2.04 \pm 0.65
PEG ₆₀₀₀	6,000	3.13	0.77 \pm 0.55
PEG ₁₀₀₀₀	10,000	3.13	0.93 \pm 0.43

In light of the aforementioned observations, namely the high integrity and complete, homogeneous shell-core structure, it can be posited that the addition of PEG did not exert a significant influence on the solvent-diffusion/evaporation process. It was postulated that PEG molecules with such a small molecular weight would be leached out from the PLGA/DCM system into the aqueous phase before complete PLGA solidification, having no significant impact on the μ C appearance. This hypothesis is corroborated by the observation that μ Cs including low molecular weight PEGs exhibit a comparable morphology to those produced without the use of a porogen (PLGA/DCM/non-solvent system, Figure 4-5). Moreover, the hypothesis that the majority of PEG was leached from the oil phase into the aqueous phase prior to the completion of PLGA solidification was further substantiated by the observation that altering the PEG concentration did not significantly impact the porosity or pore diameter (Figure 7-5 a/b vs. c/d). Only a small portion of PEG agglomerates seem to be trapped and retained within the PLGA shell of the μ C visible as small dark spots in the fluorescent CLSM micrographs, indicating free spaces left behind by these PEG agglomerates after PLGA solidification (Figure 7-4 and Figure 7-5). These free spaces are then also partially visible in the SEM images as small pores.

The rapid leaching into the aqueous phase and subsequent ineffective pore formation of PEGs with low M can be mainly attributed to the small molecule size of these PEGs (e.g., PEG₆₀₀, PEG₁₅₀₀). In general, it is anticipated that PEG will undergo phase separation

during the solvent diffusion and evaporation process, given the hydrophilic properties of PEG compared to the hydrophobic nature of the PLGA phase (Figure 4-11).

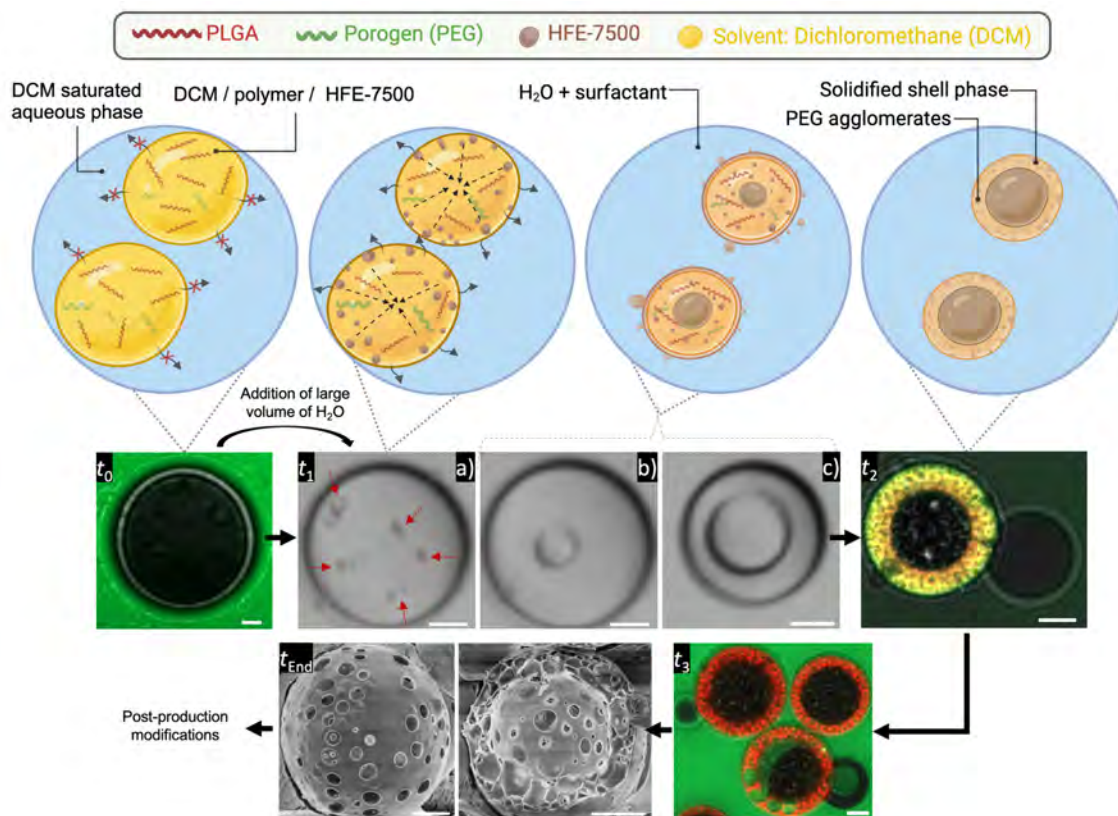


Figure 4-11: Schematic illustrations and representative CLSM images of the mechanism to form hollow, porous μ Cs. PEG₄₀₀₀, HFE-7500 and PLGA were dissolved in DCM and used in the oil phase as porogen and core-forming agent, respectively. An o/w emulsion is created in an aqueous surfactant solution (green) (t_0 , scale bar: 5 μ m). After adding the o/w emulsion droplets to a large water volume (transition t_0 to t_1), organic solvent depletion at the DCM-water interface occurred, leading to phase separation and droplet size reduction. The process is accompanied by o/DCM/w droplet formation at the DCM/water interface (t_{1a} , red arrows). These droplets travel towards the center of the emulsion droplet (t_{1b}), fuse and form the hollow core of the capsules (t_{1c}) (t_{1a-c} : scale bar: 10 μ m). Further solvent diffusion leads to phase separation, polymer precipitation and solidification (t_2 and t_3 , scale bar: 5 μ m). The final freeze-dried μ Cs (t_{End} , scale bar: 5 μ m) were utilized for post-production modifications. Parts were created with BioRender.com.

In consequence, phase separation would result in the formation of regions within the PLGA phase that are enriched in PEG. Subsequently, if the PLGA-PEG blend is exposed to an

aqueous solution, the leaching of PEG will occur over time, dependent on the size of the molecule and the rate of diffusion. In the event that the process of DCM evaporation and PLGA solidification is completed in a shorter timeframe than the leaching of PEG from the system, the latter will be trapped within the PLGA phase. Furthermore, the non-solvent utilized for core formation will act to push the PEG agglomerates towards the periphery of the PLGA shell (Figure 4-11 t_1 and t_2). Once the μ Cs have undergone complete solidification and re-immersion in an aqueous solution, PEG will begin to leach out, leaving behind free spaces or pores within the PLGA phase (Figure 4-11 t_{End}). In light of the aforementioned considerations, the primary aspects that must be taken into account in the presented system are the molecular weight, the chain length, the amphiphilicity, and the PEG concentration.

Following the theory that the molecular weight and hence the molecule size of PEG is critically important, the M was further increased to 2 kDa. As with the previously tested molecular weight, the formation of homogeneous capsules with high integrity and thin shell walls was observed. The pore size at a concentration of 3.13 mmol/L was analyzed with a size of $0.79 \pm 0.33 \mu\text{m}$ (Table 4-4 and Figure 4-12) indicating a slight increase in size compared to the previously used M . Nevertheless, as for the tested M s before, the observed average pore diameter was assumed to be too small for successful bacteria penetration, excluding PEG₂₀₀₀, as PEG₆₀₀ and PEG₁₅₀₀, as potential porogen.

The slight increase in pore size increasing M from 1.5 kDa to 2 kDa supports the assumption that longer PEG chains with higher M might be more suitable as pore-forming agent due to the reduced diffusion speed. Hence, M was even further increased to 4 kDa, 6 kDa and 10 kDa. A notable change in porosity, along with a change in shell thickness and integrity, was observed with PEG₄₀₀₀. SEM images revealed a notable enlargement in pore diameter, particularly at concentrations of 1.56 mmol/L and 3.13 mmol/L and also a fraction of bowl-shaped particles presumably induced by the slightly increased viscosity due to increased molecular weight of PEG (Figure 7-7). At high PEG₄₀₀₀ concentrations (6.25 mmol/L), cavity formation was suppressed leading to solid particles and low μ C integrity due to the high overall polymer concentration in the sample (Figure 7-7 e and f). When comparing the medium PEG₄₀₀₀ concentration of 3.13 mmol/L (Figure 4-13 and Figure 7-7c and d) to the so far tested samples, it showed the highest degree of porosity so far with a pore diameter suitable for bacteria penetration of $2.04 \pm 0.65 \mu\text{m}$ (Table 4-4 and Figure 4-12). With the increased M , the diffusion of the PEG molecules was reduced, allowing DCM

diffusion/evaporation accompanied with PLGA solidification to take place before PEG could leach out from the oil phase. Hence, during the diffusion/evaporation and solidification process, PEG still tends to diffuse towards the aqueous phase, but at a decreased diffusion speed. Along this way, it tends to form hydrophilic PEG agglomerates to minimize the overall surface energy in the hydrophobic PLGA/DCM phase. Moreover, the CLSM images show that the larger molecule chain length also affects the overall formation process leading to a less homogeneous shell wall and cavity. Nevertheless, the drastically improved porosity, as well as the still comparatively high integrity of the μ Cs made PEG₄₀₀₀ a suitable porogen (Figure 4-13).

To explore whether further increasing the M would lead to even larger pores, two additional types of PEGs with 6 kDa and 10 kDa were tested (Figure 7-8 and Figure 7-9). Surprisingly, the trend of increasing pore diameter with larger PEG chain length did not continue. Instead, the measured pore diameter dropped to an average diameter of $0.77 \pm 0.55 \mu\text{m}$ for PEG₆₀₀₀ and $0.93 \pm 0.43 \mu\text{m}$ for PEG₁₀₀₀₀ (Table 4-4 and Figure 4-12). A detailed examination of the CLSM micrographs of these two PEG types revealed that, particularly at elevated PEG concentrations, the μ C formation process was significantly affected, resulting in the complete inhibition of cavity formation. For PEG₆₀₀₀ at the lowest concentration, capsule formation was still possible and resulted in particles with similar morphologies as μ Cs prepared with PEG₄₀₀₀ as porogen (Figure 7-8a and b). Nevertheless, increasing the concentration led to a high portion of solid and incompletely formed particles with small pore diameters (Figure 7-8c-f). Particles produced with PEG₁₀₀₀₀ showed deformed, incomplete and solid particle formation at a concentration of 1.56 mmol/L (Figure 7-9a and b). Further increasing the PEG amount led to cavity formation but with thick shell walls and drastically altered surface structure (Figure 7-9c and d).

It is also noteworthy that by comparing the same molar masses but increasing the M s and hence the chain lengths of the used PEGs, the gravimetric polymer concentration also increases. Consequently, the percentage of PEG in the oil phase increases substantially for PEGs with higher M . This continuously rising portion of porogen in the oil phase appears to influence the process of μ C formation and pore formation, thereby altering the equilibrium of the system to a degree that μ C formation becomes infeasible.

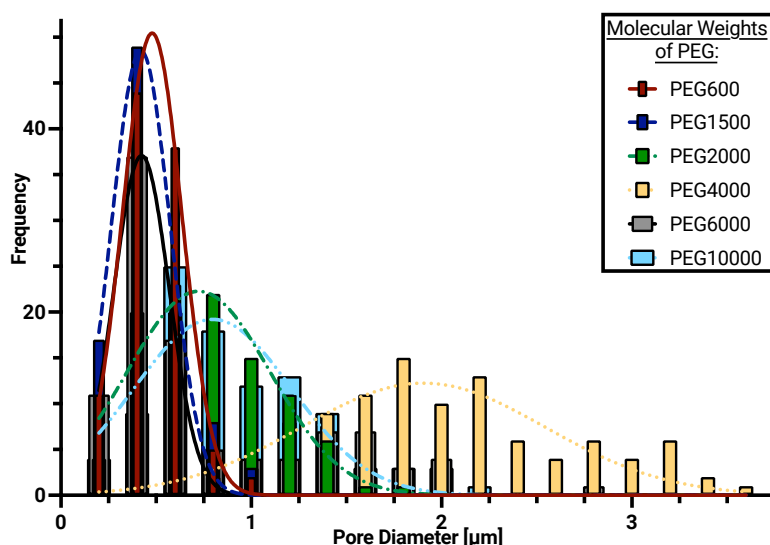


Figure 4-12: The frequency histogram illustrates the diameter of the pores created by the use of PEG as a porogen with varying molecular weights (M). A Gaussian distribution was fitted to the histograms. Six different M were tested (600 Da, 1.5 kDa, 2 kDa, 4 kDa, 6 kDa, 10 kDa) at a concentration of 3.13 mmol/L. $N = 100$ for each condition.

After analyzing the μ C integrity and pore-forming performance of the six chosen types of PEGs via SEM and CLSM, PEG₄₀₀₀ at a concentration of 3.13 mmol/L was identified as the most suitable porogen for the desired applications. Hence, all future experiments executed in the course of this work were done with μ Cs containing PEG₄₀₀₀ as porogen. Nevertheless, note that the pore diameter was extracted from SEM micrographs, showing only pores visible from the outside of the μ C, lacking proof that these pores are completely formed trans-shell pores. Therefore, further investigations using cryo-SEM and bacteria uptake efficiency tests were necessary to ensure that the pores were trans-shell and practical for bacteria penetration.

To further investigate the porosity created by PEG₄₀₀₀, additional analysis by cryo-SEM of μ Cs with PEG₄₀₀₀ was executed. Cryo-SEM is a technique where samples are shock frozen and fractured at -150°C . Microparticles were fractured and cracked open under high vacuum conditions with the help of a sharp knife. This provides an opportunity to view the μ Cs cavity, offering deeper insight into the shell structure and inside porosity of the μ Cs (Figure 4-13c and d). Cryo-SEM analysis revealed a porous structure for the capsule out- and inside supporting the choice of PEG₄₀₀₀ as a suited porogen. Nevertheless, some hollow spaces inside the polymer shell, connecting the outside with the capsule interior, seem to be separated by thin PLGA walls, assumed to prevent complete and effective bacteria

penetration. To further investigate this assumption, actual bacteria penetration tests were conducted to provide insight into the trapping efficiency of the produced μ Cs.

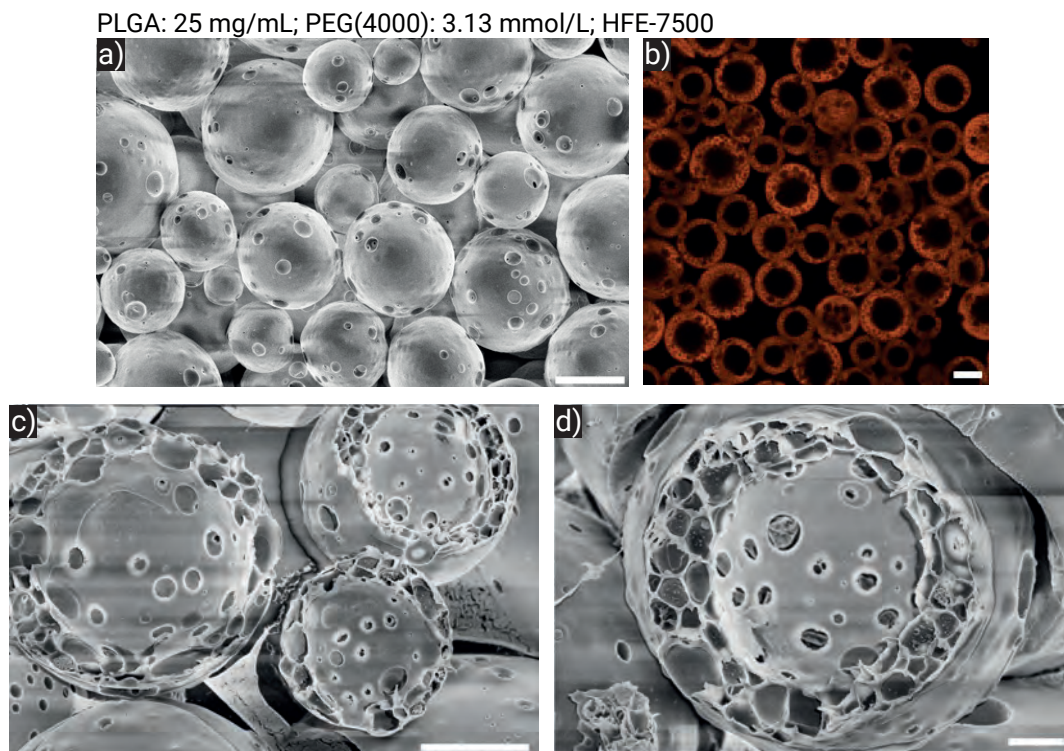


Figure 4-13: Representative (cryo-)SEM (a and c-d) and CLSM (b) images of μ Cs produced with PEG₄₀₀₀ as porogen. Nile red (orange) was used to fluorescently label the PLGA phase (b). Microcapsules were freeze-fractured by cryo-SEM (c and d) to analyze the inside porosity as well as the polymer shell structure. Scale bars: a) and b): 10 μ m, c): 5 μ m, d): 2 μ m.

4.1.2.8 Pore Generation via Solid Templates

4.1.2.8.1 Calcium Carbonate (CaCO_3) particles

The polymeric porogens described in the previous sections were successfully used as pore-forming agents, aggregating during the μ C formation process and leaching out afterwards, creating a porous structure. Another method also considered as template method, was the use of solid template particles (e.g., CaCO_3 particles), integrated in the shell, acting as spacers and removed or dissolved afterwards. The implementation of this method in combination with the previously described polymeric porogens has the potential to yield enhanced porosity. Generally, the template particles should consist of a biodegradable

material with pre-selected properties according to the characteristics the final pores should offer. Here, CaCO_3 particles were chosen as template particles, which were added to the initial oil phase as solid, spherical particles with the desired pore dimensions. Furthermore, the template material should not dissolve in the solvent (i.e., DCM) or break while applying emulsification shear forces. Ideally, the template particles arrange randomly but centered within the polymer shell, connecting the interior with the outside environment. For template removal, an appropriate washing solvent is used, dissolving the template particles but not the polymer particles. In case of CaCO_3 , hydrochloric acid (HCl) can be used to dissolve the integrated particles. Since PEG was already identified as a promising porogen, the template particles were only used in addition to PEG to investigate further improved porosity properties of the μCs .

The objective was to achieve a particle size of approximately 1 - 4 μm in diameter to achieve pores with a suitable diameter for bacteria penetration. Moreover, to achieve a better integration into the PLGA shell, the template particles were first coated by a layer-by-layer coating using poly(styrene sulfonate) (PSS) and poly(allylamine hydrochloride) (PAH), followed by one layer of PLGA. The layer-by-layer coating was based on the electrostatic interaction of the two polymers, since PAH and PSS are positively and negatively charged, respectively. Since bare CaCO_3 particles offer a negative charge in the utilized NaCl-containing coating solution,¹⁶⁵ positively charged PAH was applied to bind as first coating layer. Electrostatic interactions were also used for the outermost layer, since PAH interacted here with the negatively charged PLGA.¹⁶⁶ Template particles were then added before emulsification to the oil phase during the μC formation. After complete formation, polymer solidification and μC collection, the particles were immersed in a HCl solution to trigger dissolution of CaCO_3 .

Analysis of the produced CaCO_3 particles revealed an average particle size of $3.25 \pm 0.4 \mu\text{m}$. This size was considered adequate for the application of the particles in the subsequent experiments (Figure 4-14a). (Cryo-)SEM analysis provided evidence that the particles were successfully integrated into the PLGA μCs (Figure 4-14c, white arrows) creating large hollow spaces. Nevertheless, the presence of large agglomerates of single template particles on the μC surface was observed, resulting in a rough surface texture (Figure 4-14b, white arrows) significantly affecting the capsule's shape. Despite the template particles exhibiting a size range comparable to that of the μC shell, no significant enhancement in porosity was observed due to the non-central positioning of the particles

within the shell. Hence, the effect of the CaCO_3 was observed to be rather detrimental, achieving no improved porosity and negatively affecting the surface structure due to the large number of agglomerates. Moreover, spherical particles were not the optimized shape for the intended purpose. For this reason, the template method using CaCO_3 particles as spacer was not pursued further.

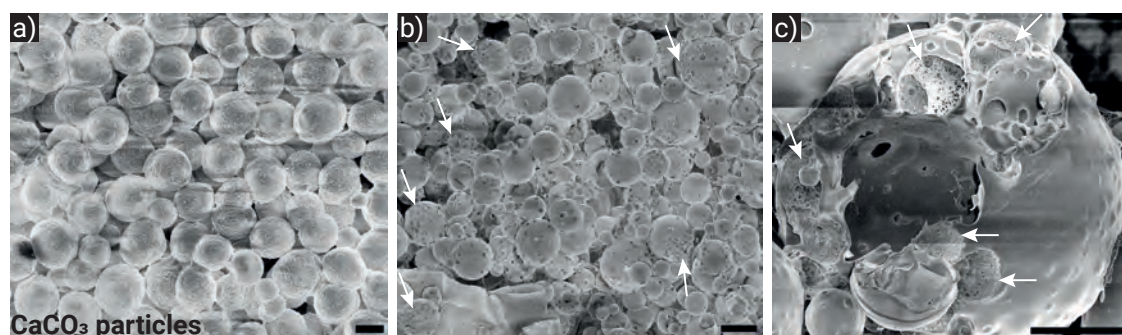


Figure 4-14: SEM micrographs of μCs produced with CaCO_3 particles as pore template. a) CaCO_3 particles after production and before integration in PLGA μCs . Scale bar: $2\ \mu\text{m}$. b) PLGA μCs with CaCO_3 particles as porogen after HCl treatment. White arrows indicate agglomerates of template particles on the μC surfaces dissolved by HCl. Scale bar: $5\ \mu\text{m}$. c) Zoom-in of freeze-fractured μC . White arrows indicate free spaces left behind by the CaCO_3 particles. Scale bar: $20\ \mu\text{m}$.

4.1.2.9 Bacteria-Microcapsule Penetration Tests and Post-Production Etching Process

PEG₄₀₀₀ was identified as the porogen of choice producing a porosity with the most suitable pore size and quantity of pores among the tested approaches. To further analyze the trans-shell nature of the pores formed by PEG₄₀₀₀ and the uptake efficiency of the μCs , bacteria (i.e., *E coli*) were added to the produced, freeze-dried, porous μCs . Note that *E coli* was chosen as bacterium due to its own and active swimming motion, which enabled active penetration of the bacterium into the μC cavity if the particles offer large enough trans-shell pores. By fluorescently labeling the μC shell with Nile red (Figure 4-15, orange) as well as the bacteria by SYTO 9 (green), it was possible to detect trapped bacteria cells within the hollow cavity of the μCs (white arrows in Figure 4-15). Nevertheless, the occurrence of bacterial entrapment and retention was detected on a limited basis, suggesting that the pores generated by PEG used as porogen were predominantly no trans-shell pores. This validates the previously stated apprehension that the shell offers a high

degree of porosity but the free spaces created by agglomerates of PEG were still separated by thin polymer walls, preventing bacteria from complete penetration into the inner hollow cavity.

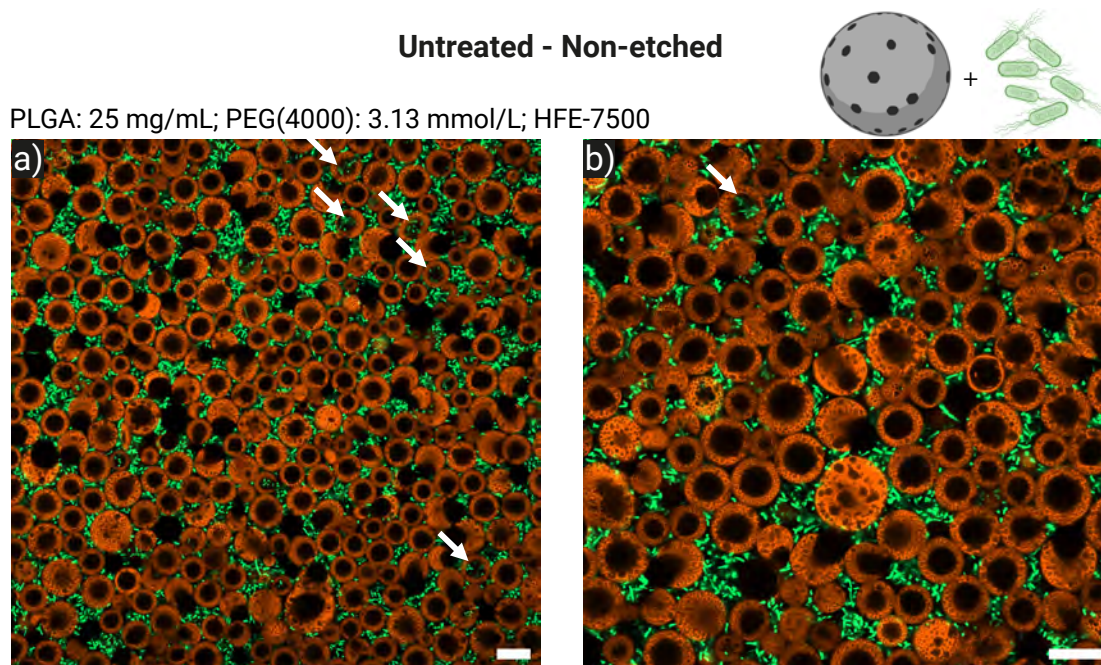


Figure 4-15: Low (a) and higher (b) magnification CLSM images of porous μ Cs (orange) added to a bacteria (*E. coli*, green) suspension to analyze bacteria penetration into the μ C cavity. μ Cs were directly used after production and freeze-drying; no additional treatment was executed. White arrows indicate bacteria trapped within μ C cavities. Scale bars: 20 μ m. Parts were created with BioRender.com.

To improve the efficiency of bacteria penetration, an additional post-production etching treatment step of the μ Cs was imperative. To improve the bacteria-capturing properties, PLGA was partially hydrolyzed using a NaOH solution to achieve trans-shell pores suitable for effective bacteria penetration. This process triggered PLGA hydrolysis, breaking down the ester linkages of the co-polymer into its monomeric components, glycolic acid and lactic acid.⁶⁹ Such a polymer degradation process was reported in the literature to enlarge the pores and increase porosity.¹⁶⁷ The hydroxide ion (OH^-) attacks the electrophilic carbonyl carbon as a nucleophile, facilitating the cleavage of the ester bond and forming a carboxylic acid and a primary alcohol (Figure 4-16).¹⁶⁸

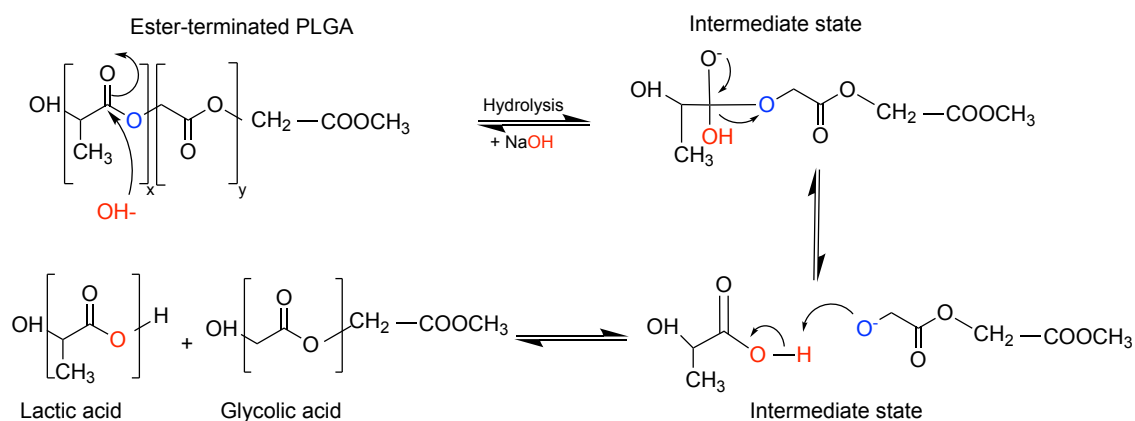


Figure 4-16: Degradation process and breakdown of the ester bond of PLGA via nucleophilic attack of NaOH. The OH^- ion acts as a nucleophilic attacking the electrophilic carbonyl carbon forming an unstable intermediate state. The intermediate state rearranges resulting in a carboxylic acid and a primary alcohol due to the ester bond breakage.

This breakdown of the ester bonds, which occurred in a basic environment, led to the accelerated degradation of the thin PLGA walls that separated the hollow cavity from the external environment. For this purpose, it is important to identify an appropriate balance between the degree of etching to ensure trans-shell pores while maintaining the microcapsules' integrity and preserving a certain degree of mechanical stability. Hence, the freeze-dried μCs were immersed in a 1.25% (w/v) NaOH solution for either 2 or 4 min and analyzed by SEM (Figure 7-10). An NaOH-treatment time of 2 min already showed a significant difference compared to the untreated μCs (Figure 4-17 and Figure 7-10a/b versus c/d) in terms of porosity. Capsules treated for 2 min offered a visibly increased degree of porosity with an enlargement of the pre-formed pores and the formation of new, additional pores. Additionally, the pre-existing pores, initially covered by a thin layer of PLGA on the outer particle surface, were exposed following degradation and removal of this top layer. The supposition that the applied etching treatment resulted in the degradation of the thin polymer walls between the pre-formed pores, as well as the formation of new pores, was validated through the implementation of the identical etching procedure on μCs produced without porogen (Figure 7-11). The process resulted here in a marked increase in surface roughness and porosity of the originally smooth, non-porous capsule surface (Figure 7-11c and d). In order to examine the potential for further enhancement of these properties, an extended etching time period of 4 min was subjected to testing (Figure 7-10e and f). Due to the rapid degradation of PLGA under these conditions, the extended

treatment duration resulted in an 'over-etching' state. The μ Cs had already undergone such extensive degradation that some of them had lost their spherical shape. Consequently, an etching duration of 4 min at a 1.25% (w/v) NaOH concentration was regarded as excessive for obtaining the desired characteristics. Moreover, such extensive degradation would have a substantial negative impact on the mechanical stability of the particles due to the substantial degree of degraded polymer.

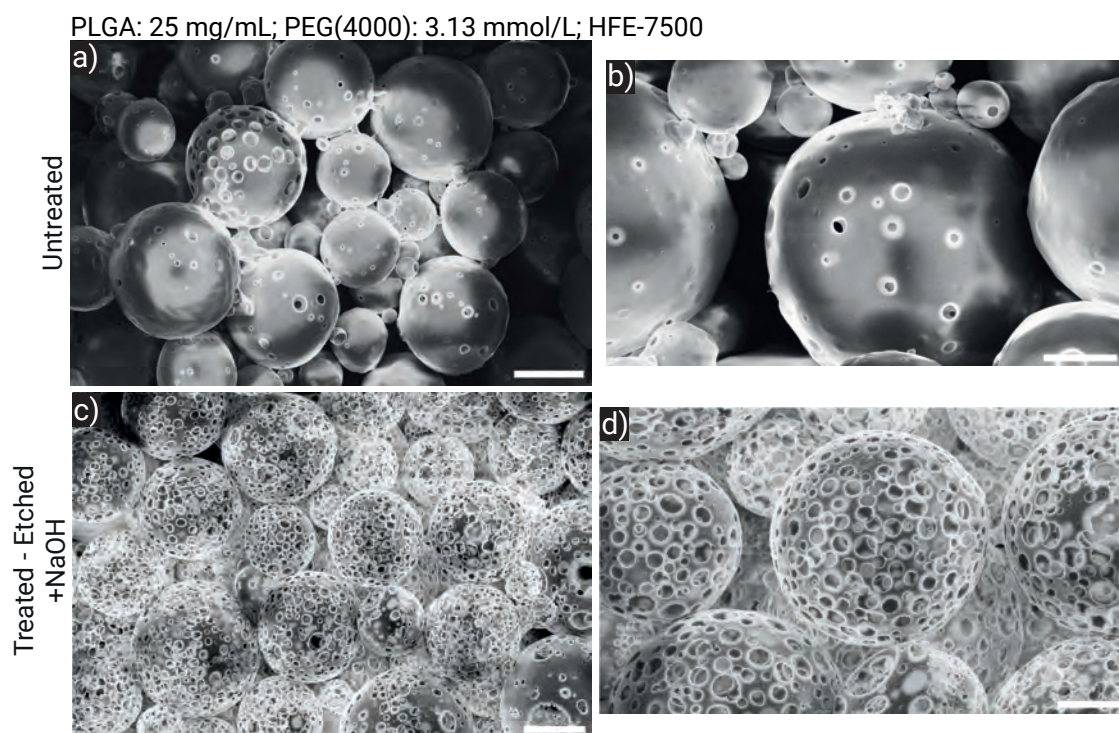


Figure 4-17: SEM micrographs showing the comparison between untreated (a and b) versus NaOH-treated (c and d) μ Cs produced with PEG₄₀₀₀ as porogen. Treated μ Cs were etched for 2 min in an aqueous (1.25%, w/v) NaOH solution resulting in PLGA degradation. Scale bars: a) and c): 10 μ m, b) and d): 5 μ m.

To further investigate the particle properties after etching and to prove the porosity increase after post-production etching treatment, zeta (ζ -) potential measurements as well as the number of pores per apparent area were evaluated. Untreated μ Cs revealed a negative charge of -40.8 ± 6.2 mV which was even further decreased down to a value of -74.9 ± 11.6 mV for the NaOH-treated sample (2 min), as PLGA degradation leads to the exposure of carboxylic acid and hydroxyl groups on the particles' surface contributing to a more negative surface charge (Table 4-5). The porosity analysis was conducted by determining the number of pores per unit area of 951.2 μm^2 , which corresponded to the area

of an average μC with a diameter of $17.4 \pm 3.9 \mu\text{m}$, as determined for the μC s under study. The analysis yielded an average number of 20 pores per average μC . In comparison, the NaOH-treated μC s exhibited an average of 209 pores per average μC , indicating a more than ten-fold increase in pore number. To ensure effective bacteria penetration and to minimize the chances for bacterial escape from the μC inside, a pore diameter threshold was implemented for the analysis and set to $0.5 - 4.5 \mu\text{m}$ ($d_{E. coli} \approx 0.25-1 \mu\text{m}^{148}$). Applying this threshold to the analysis, the pore size was measured to be in the range for $1.5 \pm 1.0 \mu\text{m}$ for the untreated μC s. Due to the creation of new pores the average pore size for NaOH-treated μC s was analyzed to be smaller ($0.9 \pm 0.5 \mu\text{m}$), but still in a range for bacteria to be able to penetrate through. These improved porosity properties for the NaOH-treated particles facilitated an improved probability for bacteria, especially motile bacteria, to meet a pore and actively enter the hollow cavity inside the particles.

Table 4-5: Comparison of physico-chemical properties of μC s before versus after NaOH-treatment (2 min, 1.25% (w/v)).^a

Properties	Untreated	NaOH-treated
Zeta potential [mV]	-40.8 ± 6.2	-74.9 ± 11.6
Average number of pores per area of $951.2 \mu\text{m}^2$	20	209
Average pore diameter [μm]	1.5 ± 1.0	0.9 ± 0.5

^aThe surface area of $951.2 \mu\text{m}^2$ corresponds to the surface area of μC s with diameter of $17.4 \mu\text{m}$ which was calculated as the average diameter for capsules produced at these conditions. The pore diameter threshold was set to $0.5 - 4.5 \mu\text{m}$ for the statistical analysis.

In the next step, experiments incubating the μC s with bacteria were aiming to provide evidence for increased penetration and retention of the bacteria cells inside the hollow cavity. The ability of the bacteria to penetrate the μC s was analyzed via CLSM. An additional washing step was added after incubation to remove the bacteria surrounding the particles. This allowed for improved visualization and simplified differentiation, so that only trapped and retained bacteria were visible in the fluorescent channel. Figure 4-18 shows an improved trapping efficiency of bacteria of the NaOH-treated particles compared to the untreated μC s (Figure 4-15). The result indicated that the NaOH-treated μC s exhibited not only an increased porosity but also a greater proportion of trans-shell pores,

thereby confirming the efficacy of the etching procedure as a reliable method for enhancing porosity.

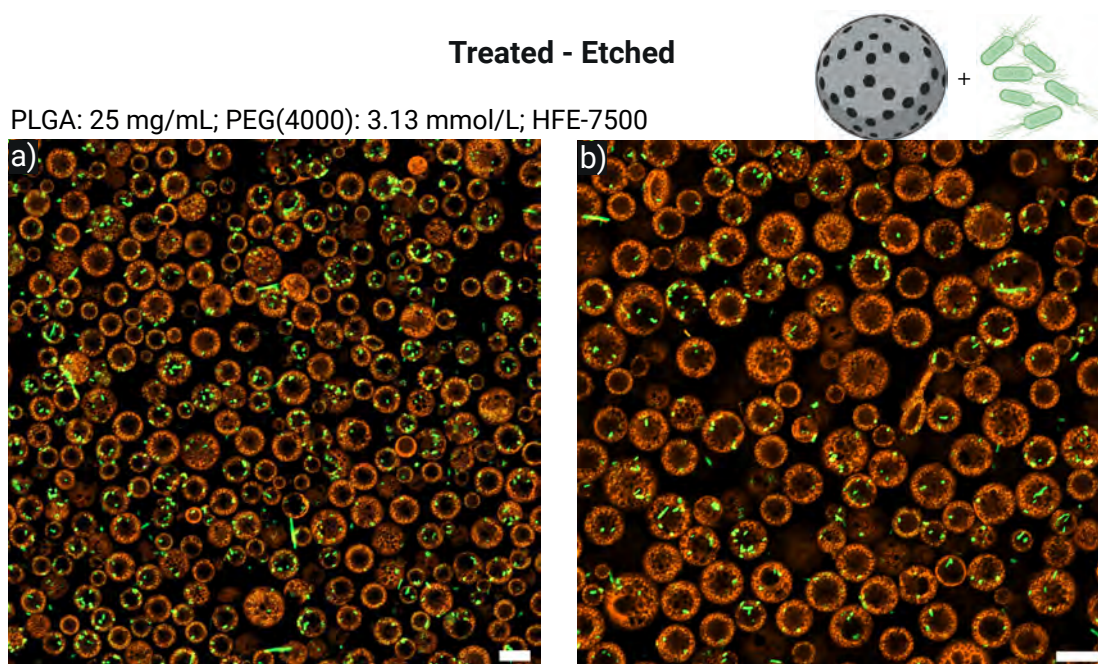


Figure 4-18: Low (a) and high (b) magnification CLSM micrographs of etched μ Cs (orange), treated for 2 min with an aqueous NaOH solution (1.25% (w/v)) and immersed in a bacteria (*E. coli*, green) suspension to account for bacteria penetration and retention. Scale bars: 20 μ m. Parts were created with BioRender.com.

To further investigate the penetration and retention behavior of the NaOH-treated particles, μ Cs were tested and analyzed at different concentrations of bacteria. For this purpose, a constant concentration of post-production etched μ Cs was co-cultured with *E. coli* at varying concentrations. Such an experimental design also allowed for accounting for bacterial escape over time from the μ C cavity. Especially at high bacteria concentrations, large numbers of bacteria cells were accumulated and trapped, which made distinguishing single cells increasingly difficult. Thus, capsules with a large number of trapped bacteria were assumed to include 25 cells/capsule on average. The results indicate a clear correlation between the efficiency and the number of bacteria cells in the surrounding medium, with a marked increase in efficiency with increasing cell number (Figure 4-19a). This observation emphasizes the statistical probability of motile bacteria encountering a μ C pore and subsequently entering the hollow cavity. Furthermore, the observation of a high concentration and accumulation of bacteria within the cavity of μ Cs serves as evidence

supporting the hypothesis that the number of bacteria entering the μ Cs exceeds the number escaping (Figure 4-19b).

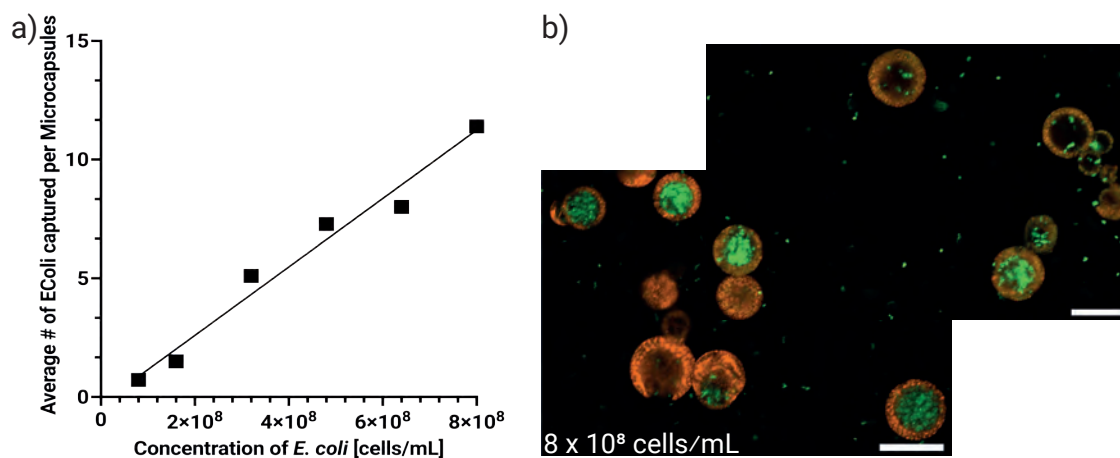


Figure 4-19: Uptake and trapping efficiency of post-production etched μ Cs at varying *E. coli* concentrations. a) Average number of *E. coli* captured by μ Cs ($N = 50$ capsules per concentration). b) Representative CLSM micrographs of post-production etched μ Cs (orange) with trapped bacteria (green) at a bacteria concentration of 8×10^8 cells/mL. Single cell counting was not possible for capsules with large number of accumulated and trapped bacteria inside the hollow cavity, thus an average number of 25 bacteria/capsule was assumed for these cases. Scale bars: 20 μ m.

4.1.2.10 Microcapsule Uptake Efficiency: Motile vs. Non-Motile Bacteria

As shown previously, the degree of porosity plays a critical role to achieve efficient bacteria trapping and retention. Nevertheless, bacterial penetration through the pores into the hollow cavity is mainly driven by the bacteria's own mobility. Hence, achieving penetration for non-motile bacteria without actively attracting them is challenging. To investigate the behavior of non-motile bacteria in the presence of porous, post-production treated PLGA μ Cs, capturing experiments were conducted with *Staphylococcus sciuri* (*S. sciuri*) and compared to the behavior of motile *E. coli* (Figure 4-20). As already presented and discussed in the previous chapter, *E. coli* cells were able to actively enter the μ C cavities with a high efficiency by their own swimming motions (Figure 4-20a). While *E. coli* demonstrated a higher tendency to enter the cavity, it was only in a limited number of cases that non-motile bacteria cells (*S. sciuri*) entered the hollow cavity, a phenomenon that can be attributed to the absence of swimming motions in these cells. Interestingly, *S. sciuri* cells

were observed to stick and accumulate around the μ Cs (Figure 4-20b). This increased accumulation of bacteria cells around the μ Cs was attributed to a combination of facts. Firstly, the NaOH etching treatment increased the surface roughness, thereby enlarging the surface area available for potential adhesion. Secondly, PLGA particles are known to exhibit an overall hydrophobic character^{74, 169}, a property that is also possessed by gram-positive bacteria such as *S. sciuri*. The main factor here contributing to a hydrophobic character of the bacteria is their thick peptidoglycan layer within the bacterial cell wall including teichoic acid.¹⁷⁰⁻¹⁷² Consequently, *S. sciuri* was presumed to exhibit a general propensity for adhesion to hydrophobic surfaces, which would naturally incline it toward greater adhesion to PLGA particles. Another aspect which was necessary to consider was electrostatic forces acting in the system. Bacteria are known to offer a net-negative surface charge.¹⁷³ A negative ζ -potential was also reported for the μ Cs leading to repulsive electrostatic forces acting between the particles and bacteria. However, the observed active accumulation around the μ Cs suggested that the repellent electrostatic forces were surpassed by the attractively acting hydrophobicity and the increased surface roughness. Moreover, gram-positive bacteria offer a decreased negative surface charge compared to gram-negative bacteria,¹⁷³ making adhesion and accumulation easier for gram-positive pathogens.

Given the fact that non-motile bacteria lack the capacity to penetrate the confined space of the μ Cs, it was necessary to further upgrade the designed particles to create an effective system capable of addressing bacterial contaminations for both types of bacteria (non-motile and motile). To achieve a system capable of killing both trapped motile and accumulated non-motile bacteria, further μ C modifications were necessary. To this end, the particles' surface was decorated with PLGA-functionalized gold nanorods (AuNRs), capable of generating heat by means of NIR light in a highly localized manner.

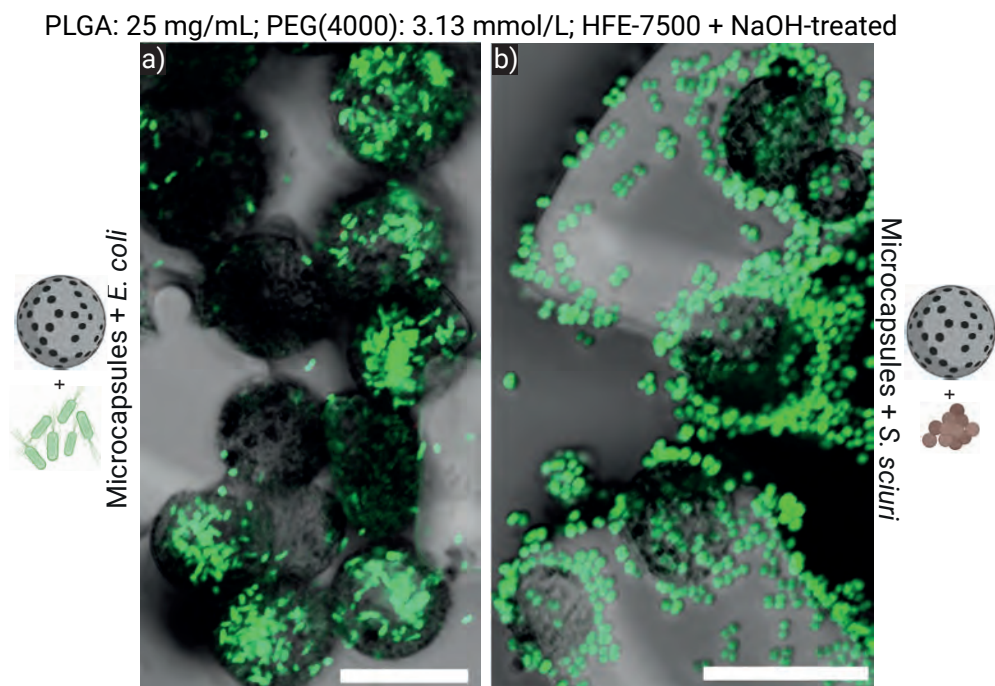


Figure 4-20: CLSM micrographs comparing bacterial penetration behavior of between motile *E. coli* (a) and non-motile *S. sciuri* (b) into post-production NaOH-treated μ Cs. Bacteria cells were stained with STYO 9 (green). Scale bars: 20 μ m. Parts were created with BioRender.com.

4.1.3 Gold Nanorods (AuNRs)

In order to introduce an antibacterial effect and effectively kill different types of bacteria in a localized manner, the polymer μ Cs were functionalized by AuNRs. These particles have the unique properties of strongly absorbing light resonating with the oscillation of their surface plasmons. This oscillation in turn is rapidly converted via a photothermal process into heat used here to kill bacteria. The following chapters will first describe the synthesis and functionalization of the AuNRs necessary to achieve a high covering rate of the AuNRs on the μ C surface and to suppress toxic effects.

4.1.3.1 AuNR Synthesis

Particles were synthesized with and stabilized by cetyltrimethylammonium bromide (CTAB) (Figure 4-21a, left) based on the protocol of Mbalaha et al.¹³⁷ with slight modifications to achieve the desired particle properties. The AuNRs were designed to

exhibit an aspect ratio (AR) of 4, corresponding to a rod size of approximately 40 nm in length (L) and 10 nm in width (W). By adjusting the amount of silver nitrate employed during the AuNR synthesis, the AR and with that the absorbance maximum was tuned to the targeted wavelength of approximately 808 nm. NIR light has already found extensive use in various medical applications due to its favorable properties, which include its ability to penetrate deep into tissue with minimal damage to the tissue.^{174, 175} Thus, this wavelength was considered suitable for the desired application. After AuNR synthesis, the absorbance spectrum of the CTAB stabilized rods (Figure 4-21b, red, solid line), as well as the length and width of the particles were extracted by UV-vis spectroscopy and SEM (Figure 4-21c and d). A characteristic absorbance spectrum was observed, exhibiting two surface plasmon resonance bands (SPR). The minor peak at approximately 508 nm corresponds to the transverse surface plasmon band (TSPB) induced by the surface electrons oscillating along the short axis of the rod-shaped particles. The second major peak presenting the absorbance maximum was detected at exactly 808 nm and was induced by the plasmons oscillating along the long axis of the rods in the longitudinal surface plasmon band (LSPB). With this characteristic two peak spectrum, a successful AuNR production with the desired properties was proven. The rod shape was further confirmed by SEM showing properly formed rods (Figure 4-21c, left) and desired dimensions (Figure 4-21d, left). Nevertheless, the presence of the highly toxic CTAB stabilizing the AuNRs¹⁷⁶ made an additional functionalization step unavoidable.

4.1.3.2 AuNR Functionalization by PLGA-SH

An AuNR-functionalization protocol was established based on the CTAB removal protocol of He et al.¹²⁵. Further adjustments of the protocol were necessary since the hydrophilic CTAB was needed to be replaced by hydrophobic PLGA-SH which made a phase transfer from aqueous to organic phase necessary. In the first step, NaBH_4 was added to the freshly synthesized AuNRs removing the CTAB molecules from the gold surface. According to He et al.¹²⁵ the removal was facilitated by the hydride ion of NaBH_4 replacing the CTAB molecules from the gold surface due to its strong affinity. Subsequently, the H_2 gas was formed in water due to hydride ions dissociating from the gold surface leaving a bare gold surface free for binding other molecules. At this point, hydrophobic PLGA-SH dissolved in DCM was added serving as new capping agent to avoid re-binding of CTAB or agglomeration of the rods. Due to the fact that thiolated molecules form a strong covalent

bond between the sulfur atom of the thiol group and gold surfaces¹⁷⁷, the AuNRs were assumed to be rapidly stabilized by the PLGA-SH (Figure 4-21a, right). This process was also accompanied by the transfer of the AuNRs from aqueous to organic phase due to the hydrophobic properties of PLGA-SH. With the present PLGA-functionalization, it was no longer possible to re-disperse the AuNRs in an aqueous solution (Figure 7-12).

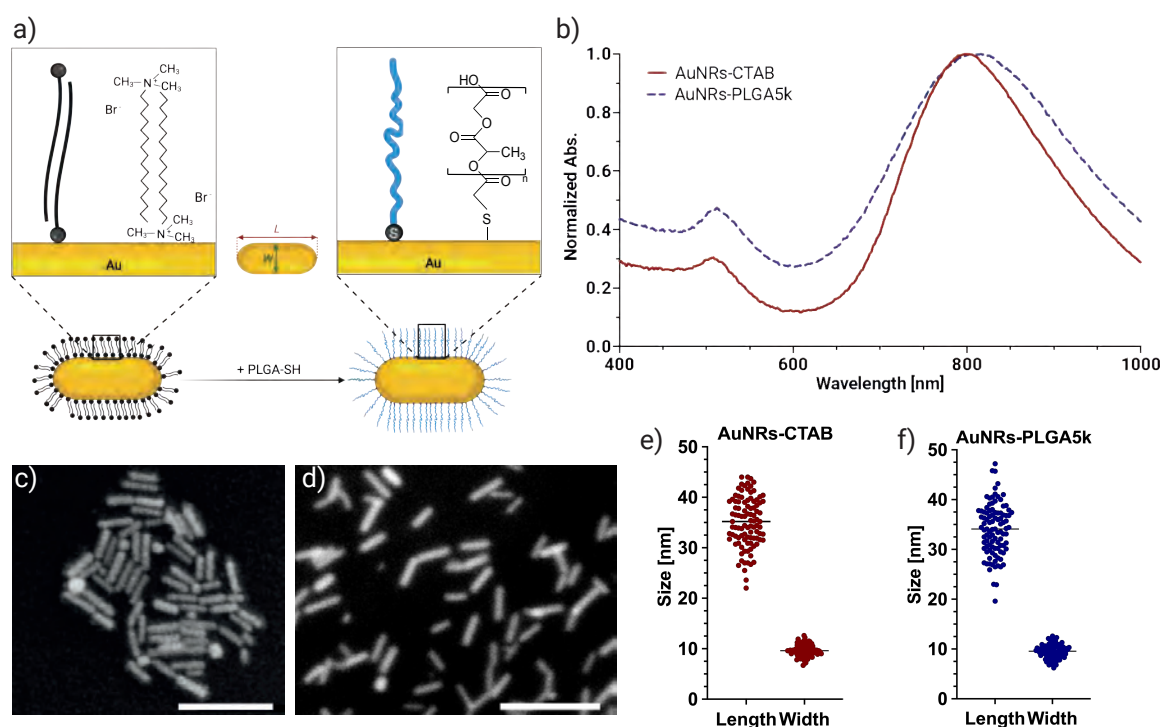


Figure 4-21: Comparison of AuNRs coated with CTAB versus PLGA. a) Schematic illustration of CTAB (black) and PLGA (blue) molecules bound to the gold surface. b) Absorbance spectrum of CTAB (red, solid line) and PLGA coated (blue, dashed line). c) SEM images of AuNRs right after synthesis stabilized by CTAB (left) and after PLGA coating (right). Scale bars: 50 nm. d) Size distribution of CTAB (left, red) and PLGA (blue, right) stabilized AuNRs ($N = 100$). Parts were created with BioRender.com.

This finding provided evidence for the successful removal of CTAB and the effective PLGA functionalization process. Moreover, the UV-vis spectrum showed the same two characteristic SPR bands. For the TSPB of the PLGA-coated AuNRs no peak shift was detected, which is consistent with previous observations that the TSPB was found to be insensitive to size and refractive index changes.¹²¹ In contrast, the absorbance maximum corresponding to the LSPB, shifted slightly to higher wavelengths (826 nm), which can be attributed to refractive index (RI) changes caused by the different capping agents. PLGA

(1.46-1.47)¹⁷⁸ as well as DCM (1.42)¹⁷⁹ offer a higher *RI* compared to CTAB (≈ 1.435)^{125, 180} and water (1.33)¹⁸¹, which might be one explanation causing an absorbance shift. Furthermore, the SPR band is known to be sensitive to changes in the dielectric constant of the medium surrounding the rods.¹²⁰ Hence, the change of surrounding medium from water to DCM might be another explanation for the slight shift of the LSPB. SEM micrographs supported the observation of properly formed AuNRs (Figure 4-21c, right) without significant size changes due to the coating procedure (Figure 4-21d, right). A comprehensive evaluation of the collected data yielded substantial evidence that the PLGA-functionalization process of the rods was successful.

4.1.4 Functionalization of Microcapsules by PLGA-Coated AuNRs

The successfully PLGA-functionalized AuNRs were utilized in the μ C formation to obtain AuNR-decorated porous polymer μ Cs for the use of trapping, retaining and killing bacteria. For this purpose, the PLGA-functionalized AuNRs were added to the oil phase during μ C production. Both, non-functionalized and AuNR-functionalized μ C were exposed to the NaOH treatment. SEM analyses were executed to confirm proper capsule formation, high surface coverage of AuNRs on the polymer surface and the integrity of the AuNRs. These experiments revealed a high surface coverage and equally distributed AuNRs on the surface of the microcapsules (Figure 4-22b-d). Moreover, cryo-SEM analysis confirmed the presence of PLGA-coated AuNRs on the inner shell of the μ Cs, allowing for local heat generation not only on the μ C surface but also within the cavity. Furthermore, the AuNRs on the surface did not appear to be affected by the post-production etching procedure applied to the microcapsules after production. ζ -potential measurements of the non-etched, AuNR-decorated capsules revealed a decreased value of -46.1 ± 3.8 mV compared to the non-functionalized capsules, proving that the major properties of the particles were not drastically altered by the implementation of the AuNRs.

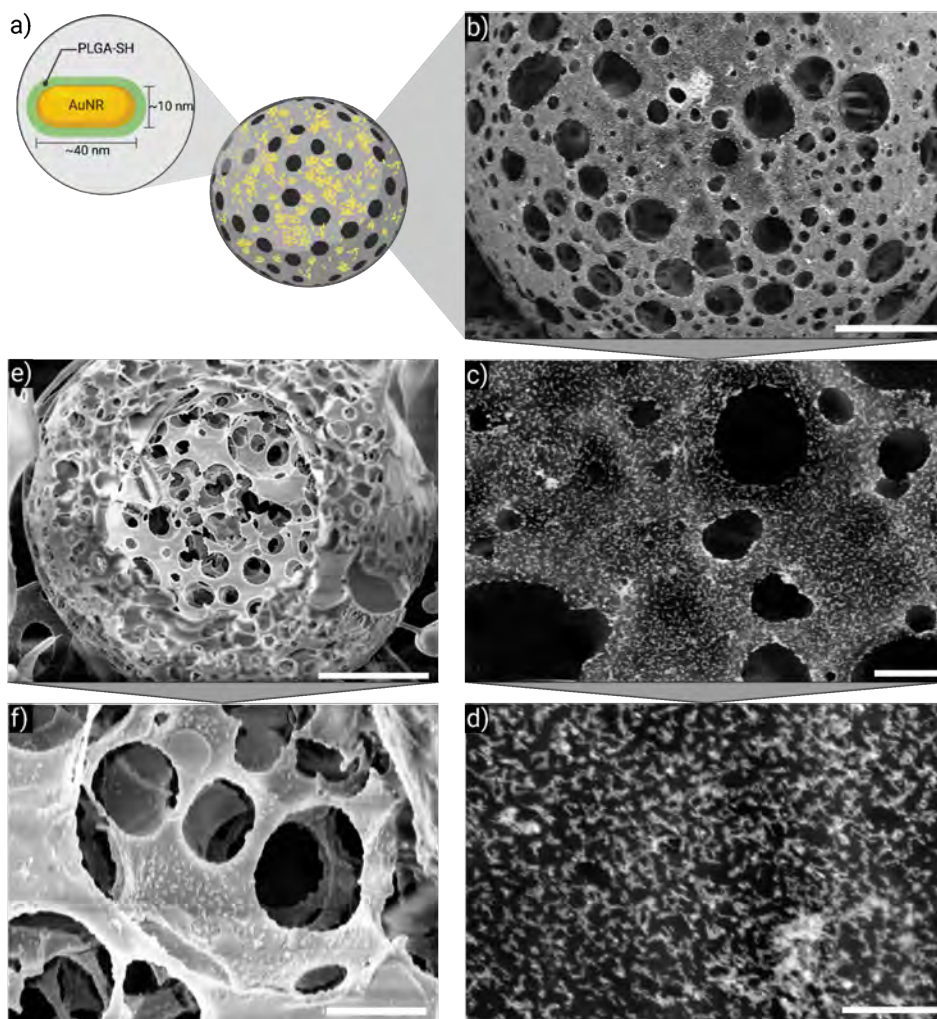


Figure 4-22: Porous, polymer-based μ Cs functionalized with AuNRs. a) Schematic illustration of a μ C functionalized with PLGA-coated AuNRs on the surface. b)-d): Increasing magnification SEM images of AuNRs on the surface of a post-production etched PLGA- μ C. e)-f): Cryo-SEM images of freeze-fractured μ C and the present AuNRs on the inside of a microcapsule's hollow cavity. Scale bars: b) and e): 5 μ m, c) and f): 1 μ m, d): 500 nm. Images e) and f) taken and provided by Ariadna Benimeli Borràs. Parts were created with BioRender.com.

4.1.5 Cell Viability Tests with Microcapsules

In order to apply the developed system in the context of medical applications, it was necessary to analyze the biocompatibility properties of the optimized μ Cs. Non-functionalized (Figure 4-23, green, solid line) as well as AuNR-decorated (Figure 4-21, blue, dotted line) μ Cs after NaOH-treatment were tested at two different concentrations

(0.01 g/L and 0.5 g/L). The selection of fibroblast cells as the model was based on two key factors: their capacity for rapid proliferation and their established reliability as a model system. Following a 24h incubation period with distinct types of μ Cs, fibroblast cells exhibited nearly 100% viability across all conditions tested, as well as no significant variations compared to the positive control, which represented untreated, cultured cells. A slight decrease in viability was detectable for AuNR-decorated particles at the lowest tested concentration. Nevertheless, the mean cell viability was still found to be 92%. These findings indicated a high degree of biocompatibility for both capsule types and confirmed the absence of cytotoxic effects induced by the incorporation of AuNRs into the system. Furthermore, the findings confirmed the successful removal of CTAB from the AuNR surface through the established coating procedure, thereby ensuring the absence of detectable toxicity.

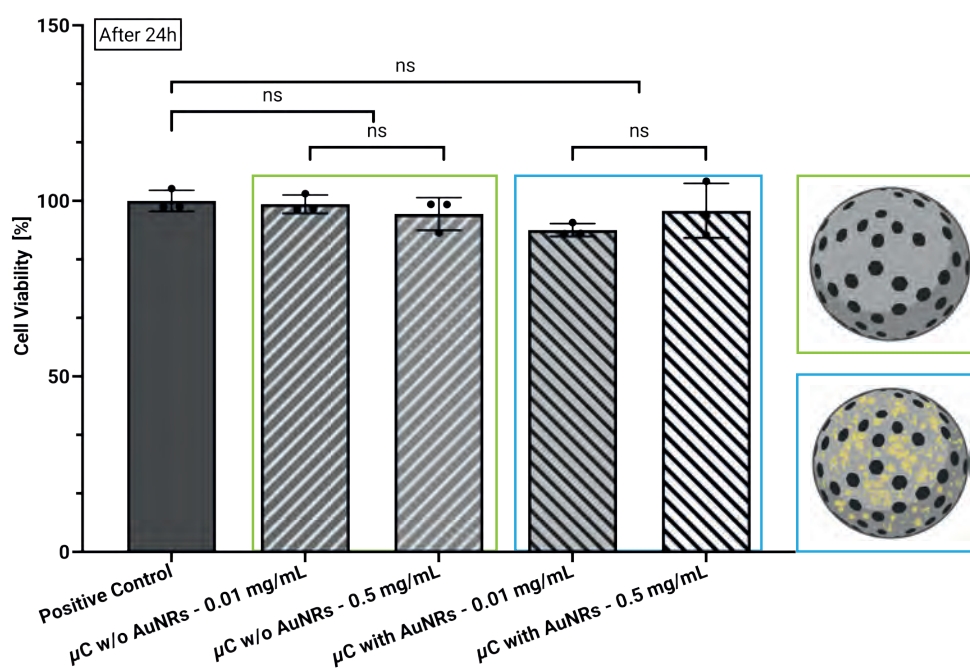


Figure 4-23: Luminescence viability tests using fibroblast cells with non-functionalized (green, solid line) and AuNR-functionalized (blue, dotted line) μ Cs at two different concentrations (0.01 g/L and 0.5 g/L) after 24h. Positive control represents untreated fibroblast cells. ns: $p > 0.05$. Parts were created with BioRender.com.

4.1.6 Bacteria Viability Tests with Microcapsules

Prior to the testing of the actual killing properties of the μ Cs induced by the implemented AuNRs on the polymer surface, the viability of bacteria was tested in the presence of

AuNR-functionalized μ Cs. This analysis was conducted to ensure that the potential killing properties of the AuNR-functionalized particles were not induced by the mere presence of AuNRs in the system, but rather by NIR light-triggered heat generation. A live/dead staining assay was utilized for this purpose, in which all bacteria cells were dyed in green (*E. coli*: Figure 4-24, top row, *S. sciuri*: Figure 4-24, bottom row) and only dead bacteria exhibited a green as well as a red signal detected in the fluorescent channel of the CLSM. A comparison of the bacteria cultures incubated with AuNR-functionalized, etched μ Cs after 24 h (Figure 4-24a and b) with bacteria cultured without additives (Figure 4-24c-d) revealed no detectable increase in the amount of dead bacteria. This finding suggests that the mere presence of AuNR-functionalized μ Cs did not elicit increased toxicity against either of the two bacterial types.

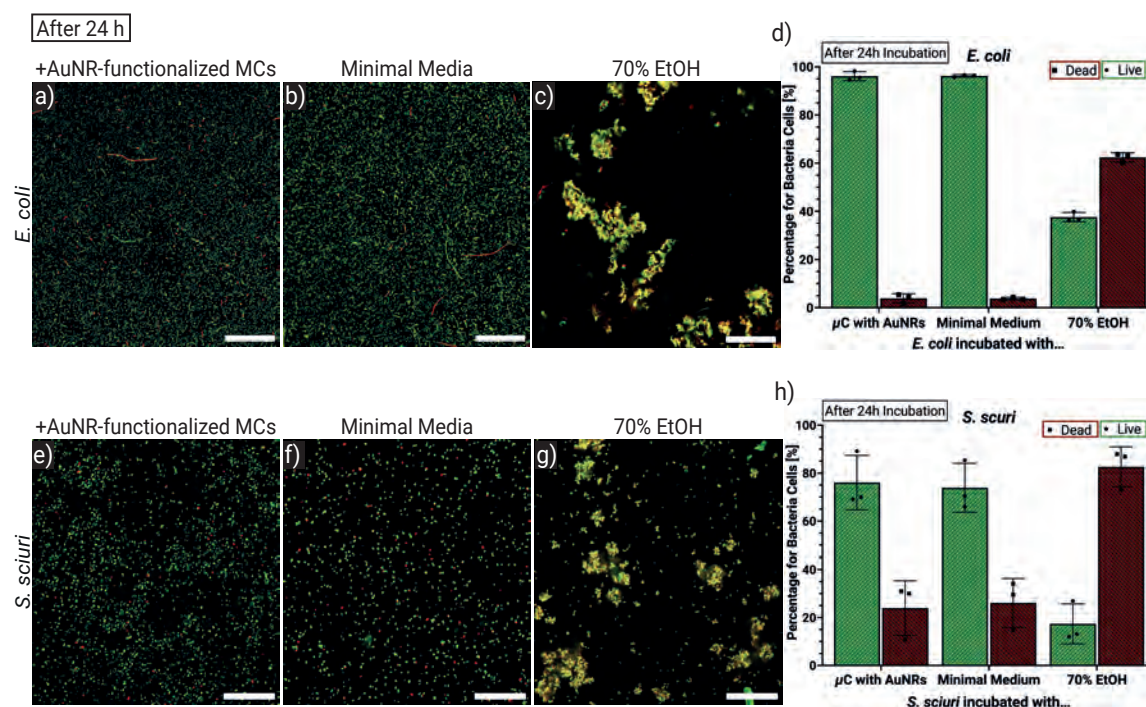


Figure 4-24: CLSM micrographs of live (green) and dead (red) *E. coli* and *S. sciuri* cells in the presence of AuNR-functionalized, post-production treated μ Cs (a and e). Bacteria were cultured in minimal medium (b and f) as a negative control and in 70% (v/v) Ethanol (EtOH) as positive control (c and g). Quantification plots representing the percentage of live versus dead bacteria cells at the different conditions (d and h). Scale bars: 50 μ m.

4.1.7 Killing Performance of Single AuNR-Functionalized Microcapsules

The most important experiment to provide a proof of principle of the developed system was to test for NIR light triggered bacteria killing via the AuNR generated heat. A customized laser setup was incorporated into the experimental workflow (Figure 4-25) to ensure the achievement of optimized, experiment-specific conditions. Firstly, the different bacteria types (*E. coli* and *S. sciuri*) were incubated (Figure 4-25, step 1) with the different μ C types (Figure 4-25, step 2). Non-functionalized, NaOH-treated μ Cs were utilized as control. In the third step, a customized microfluidic device was flushed with the μ C-bacteria mixture to immobilize the μ Cs in the channel and allow for single particle illumination and visualization (Figure 4-25, step 3). The trapped particles were irradiated by the 808 nm NIR-laser setup at a predetermined power rate and time period (Figure 4-25, step 4).

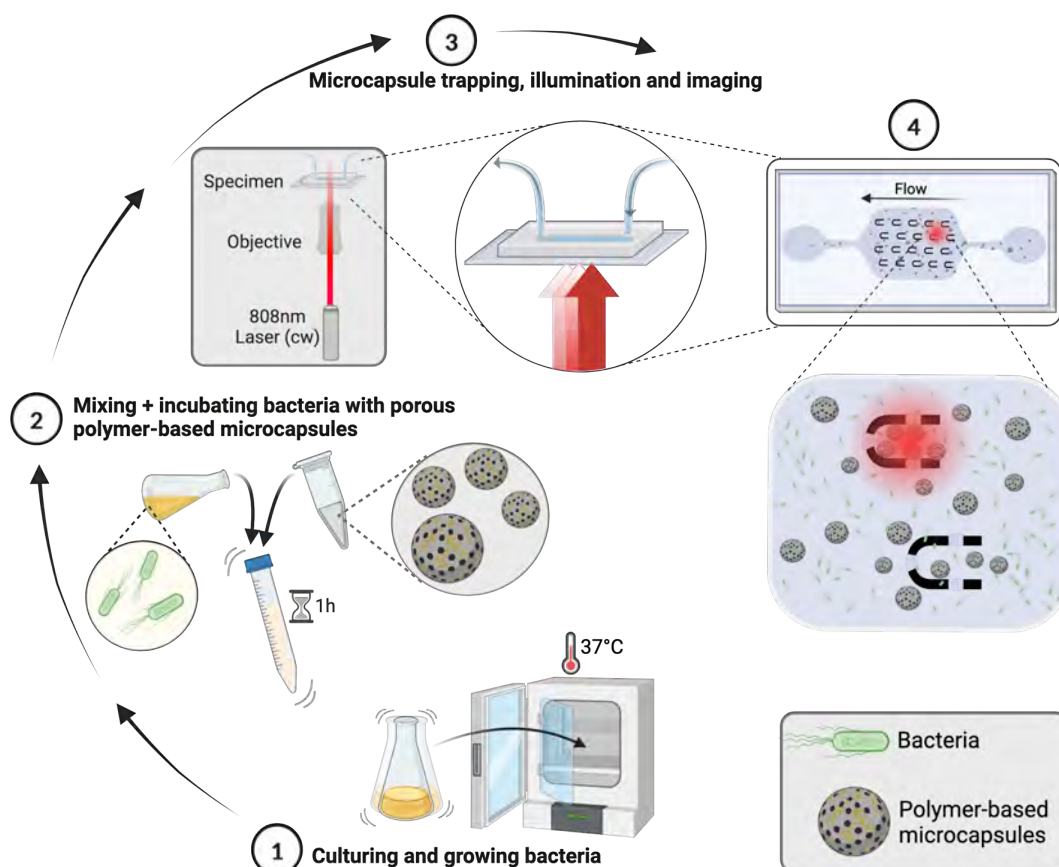


Figure 4-25: Schematic illustration of experimental workflow of μ C-bacteria-laser experiment. 1) and 2) Bacteria were cultured and incubated with μ Cs for 1 h. 3) The sample was irradiated through the objective with an 808 nm laser. 4) A customized microfluidic device was utilized to immobilize, irradiate and analyze the μ Cs and the live/dead state of the bacteria before and after NIR-treatment. Created with BioRender.com.

The live/dead state of the bacteria was visualized through the implementation of a live/dead staining assay, which employed the green SYTO 9 and the red propidium iodide (PI) as fluorescent dyes. SYTO 9 can penetrate the cell membrane to bind to nucleic acid of both live and dead cells. In contrast, PI is only able to bind to nucleic acid in case of a ruptured cell membrane, thus only staining dead cells.¹⁸²

To validate the system's capacity to eliminate bacteria, a maximum illumination duration of 10 min at high laser power (6.5 W/cm^2) was chosen. Both bacteria types (*E. coli*: Figure 4-26a, *S. sciuri*: Figure 4-26b) were tested with AuNR-functionalized and post-production etched μCs . Comparing the CLSM images, before versus after NIR-laser treatment, a clear bacterial killing effect was observed for both bacteria. Prior to the application of NIR light (Figure 4-26a and b, left panels) negligible fluorescent signal in the red channel, corresponding to the PI signal, was observed for both types of bacteria, suggesting high bacterial viability. However, a notable shift in this dynamic was observed following the application of NIR light for a duration of 10 min. The presence of a significant PI signal indicated a substantial quantity of dead bacteria (Figure 4-26a and b, right panels).

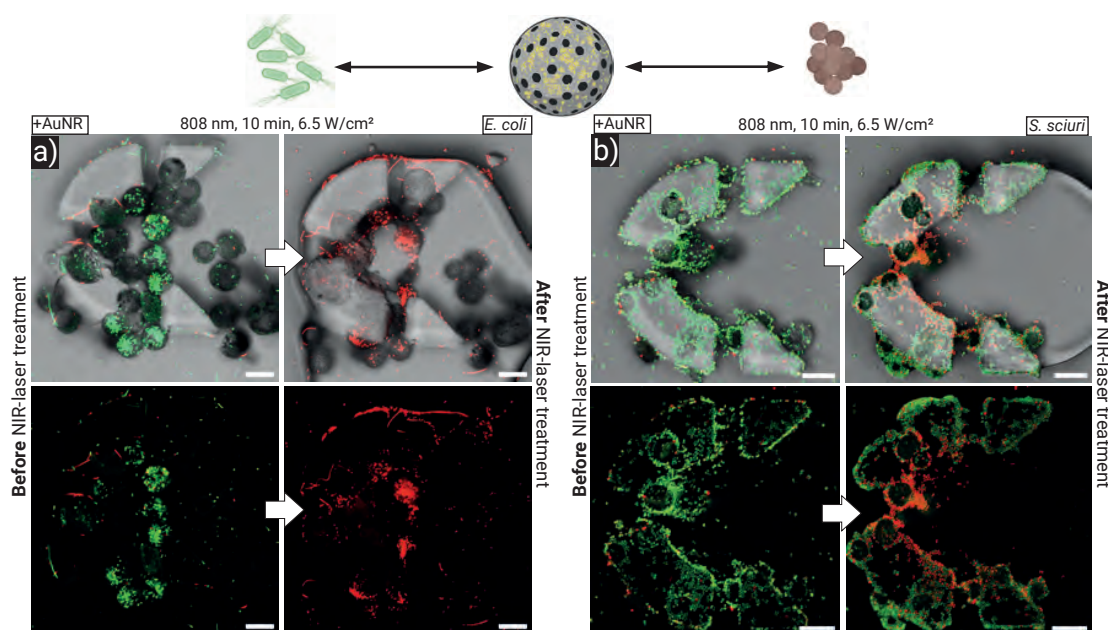


Figure 4-26: NIR light triggered bacteria killing induced by AuNR-functionalized μCs . CLSM micrographs of *E. coli*- (a) and *S. sciuri*- (b) loaded AuNR-functionalized μCs before (left panels) and after (right panels) NIR-laser treatment. Samples were radiated at 808 nm for 10 min at 6.5 W/cm^2 . Scale bars: $20 \mu\text{m}$. Parts created with BioRender.com.

It was observed that bacteria in close proximity to the μ Cs were killed, while bacteria cells distant from the AuNRs implemented on the μ Cs remained viable and appeared to be undamaged by the heat generation. This observation provides evidence that the heat was produced in a highly localized manner. Another observation made during the course of the experiments was the partial deformation of some μ Cs subsequent to the application of NIR light. This finding indicates that a high temperature was generated, which exceeded the glass transition temperature of the μ C polymers. In the case of *E. coli*, as a motile bacterium, the majority of the cells were trapped and successfully killed inside the hollow cavity. However, a similar efficient and successful killing process was observed for the non-motile *S. sciuri* cells that accumulated around the μ Cs. These findings provide evidence that the system was capable of eliminating diverse bacterial strains, which were inside or in close proximity to the μ Cs. In the subsequent stage of the experiment, it was essential to verify that the system's antibacterial efficacy was exclusively attributable to the AuNR-induced heat generation and that NIR radiation did not exert harmful effects on bacteria in general. For this purpose, the previously described experiment was executed with non-functionalized μ Cs. By focusing on the PI signal in the red fluorescent CLSM channel, no signal increase was detected before versus after laser application, indicating a non-harmful effect of the NIR-laser treatment itself (Figure 4-27). This finding serves to further substantiate the conclusion that the previously observed effect of cell death can be exclusively attributed to the presence of AuNRs on the μ C surface.

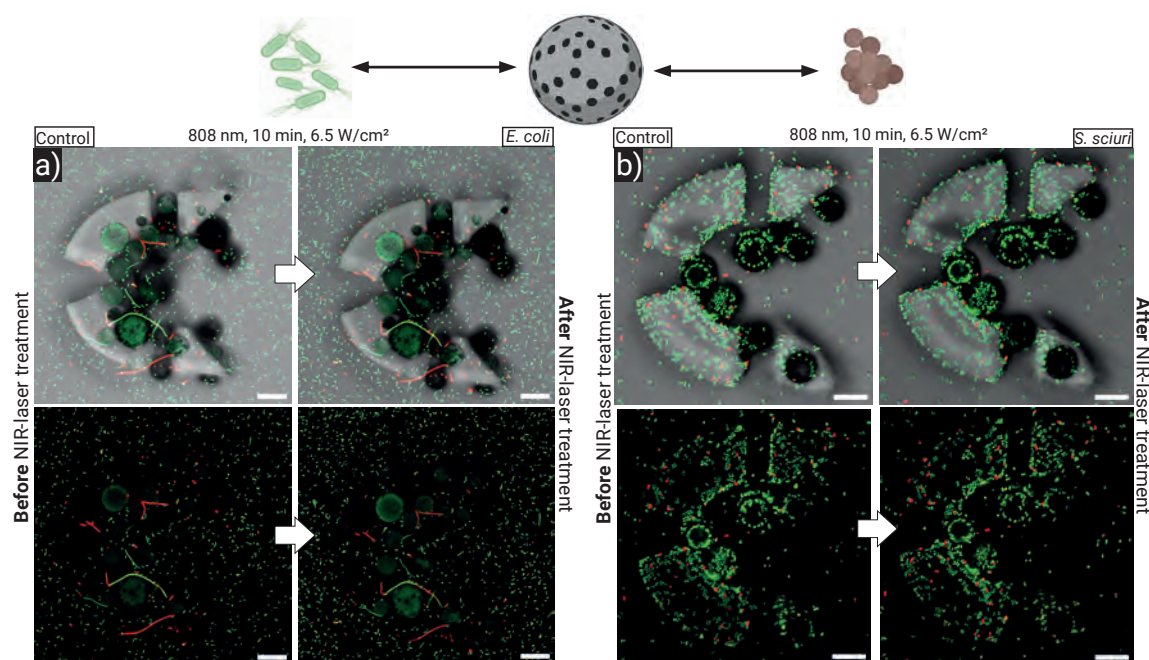


Figure 4-27: CLSM micrographs of *E. coli*- (a) and *S. sciuri*- (b) loaded, non-functionalized μ Cs before (left panels) and after (right panels) NIR-laser treatment. Samples were radiated at 808 nm for 10 min at 6.5 W/cm². Scale bars: 20 μ m. Parts were created with BioRender.com.

The requirements for the application of medical devices permit the utilization of NIR light only up to a certain power level, depending on the specific area of application. Therefore, in order to have the capacity to utilize the developed system in the context of medical applications, it was necessary to make further adjustments to the illumination properties applied in terms of time and power. Consequently, the duration of laser application was reduced from 10 min to 2 min and 1 min (Figure 4-28). The applied power per area was kept constant and *E. coli* was used here as representative model organism. A strong PI signal was observed indicating a high killing efficiency and substantial cell death after an illumination time of 2 min (Figure 4-28a). A further reduction in the NIR-laser treatment time to 1 min resulted in bacterial killing as well, although the efficacy was diminished. (Figure 4-28b). Combining these observations indicates that the system was capable of killing different types of bacteria in an efficient and highly localized manner by applying NIR light. It was also observed that the killing effects were obtained for an illumination time down to 1 min, although these effects were less pronounced and less efficient than those obtained for longer illumination times. Furthermore, it would be advantageous to

assess additional power ranges over a minimal timeframe. Such adjusted application settings would render the system more suitable for potential applications in the medical sector.

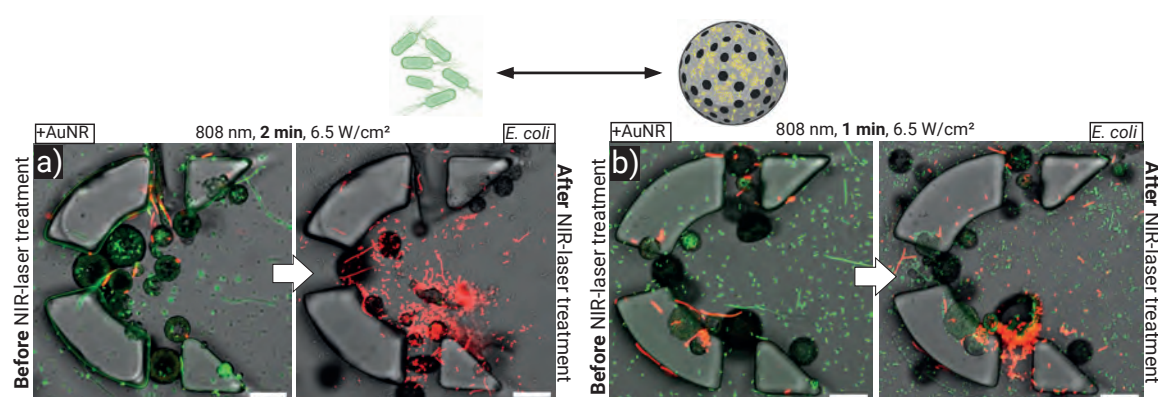


Figure 4-28: NIR light triggered bacteria killing induced by AuNR-functionalized μ Cs. CLSM micrographs of *E. coli*-loaded, AuNR-functionalized μ Cs before (left panels) and after (right panels) NIR light exposure. NIR-laser treatment (808 nm) was executed for 2 min (a) and 1 min (b) at 6.5 W/cm². Scale bars: 20 μ m. Experiments were executed by Ariadna Benimeli Borràs. Parts were created with BioRender.com.

4.1.8 Killing Performance of AuNR-Functionalized Microcapsules in Bulk Solutions

To not only account for single events of bacteria killing, the anti-bacterial properties of AuNR-functionalized μ Cs were additionally tested in bulk conditions. For this purpose, AuNR- and non-functionalized μ Cs (1 g/L and 0.5 g/L) were mixed with bacteria (10^6 , 10^7 , 10^8 bacteria/mL) and were irradiated in bulk with NIR light for 5 min. A customized LED-setup (770 nm) was utilized to achieve a larger area of illumination compared to the laser-setup. This setup ensured illumination of the full volume of the sample. After NIR light treatment, the sample was plated on agar plates to account for surviving bacteria, facilitating bacterial growth. In the event of complete elimination of bacteria, it was not possible for the bacteria to regrow on the culture medium. Consequently, no colonies would be visible on the agar plates for these samples. A pure *E. coli* suspension was irradiated under the same conditions to account for harmful effects potentially triggered by the light treatment. Moreover, an untreated bacteria culture was plated as well, providing evidence for healthy growing bacteria.

The absence of bacterial growth on LB-agar plates for AuNR-functionalized μC illuminated with NIR light (Figure 4-29) confirmed the substantial antibacterial effect of the system even in bulk. No growth was detected at both μC concentrations and all applied bacteria concentrations for the sample including AuNRs on the polymer surface (Figure 4-29a). In contrast, bacterial growth was detected for the samples including non-functionalized polymer μC s (Figure 4-29b) as well as for all control samples (Figure 4-29c). The results obtained demonstrate the high efficacy of AuNR-functionalized μC s in eliminating bacteria in a bulk solution through the application of NIR light. Moreover, the NIR light treatment was proven to be harmless to the bacteria themselves. Furthermore, to make sure the bacterial growth on the LB-agar growth medium was not affected by the presence of the μC s, an additional control experiment was executed with both capsule types mixed and cultured with *E. coli* not applying NIR light (Figure 4-29d). Bacterial growth was observed to be unaffected by the presence of either μC type, supporting the aspect that the μC s were assumed to be biocompatible.

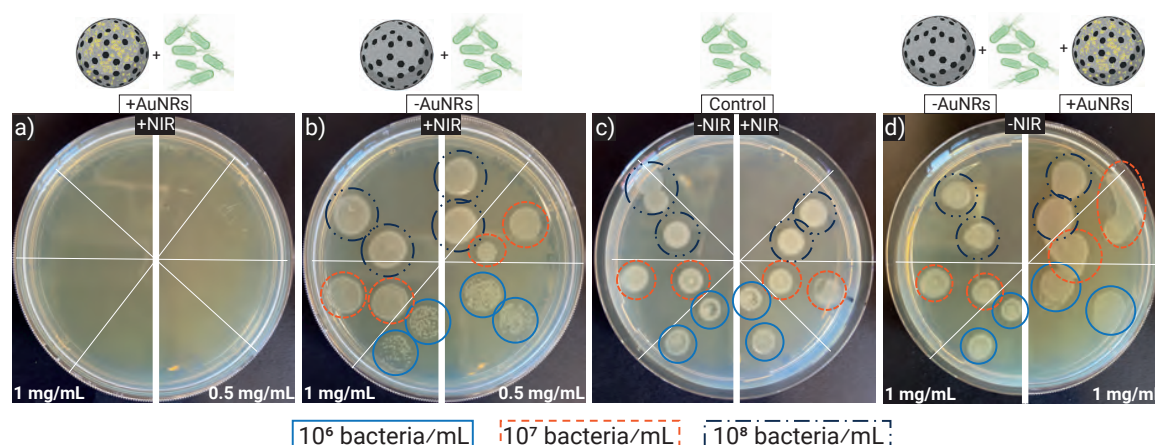


Figure 4-29: Agar-plate experiments with AuNR- and non-functionalized, etched μC s with and without NIR light irradiation in an *E. coli* suspension. Two μC concentrations were used (1 g/L and 0.5 g/L). Samples with NIR light treatment were irradiated for 5 min (770 nm, 3.53 W/cm²) in the bulk solution. a) AuNR-functionalized μC s, b) non-functionalized μC s, both with NIR light treatment, c) control sample of pure *E. coli* suspension with and without NIR light treatment and d) AuNR- and non-functionalized μC s in *E. coli* suspension without NIR light illumination. Parts were created with BioRender.com.

4.1.9 Effect of NIR-Laser-Treatment on Skin Model Tissue

NIR-radiation has been shown to penetrate biological tissue more deeply than light with a wavelength in the visible region. These properties are attributed to the NIR light minimally absorbed by abundant components in biological tissue, such as hemoglobin, melanin and water.^{183, 184} Nevertheless, to confirm the harmless properties of the NIR light system used here, a skin tissue model was exposed to the used laser settings at maximum power and for the longest time period used. Microscopic analysis of skin tissue samples obtained prior to, during, and following NIR light treatment revealed no observable alterations in tissue structure (Figure 4-30a-c), providing initial evidence that the system utilized in this thesis at the specified settings does not cause harm to skin tissue. This renders the AuNR-functionalized μ C system a promising tool for medical applications within the human body. However, further validation is required to ascertain the safety of the system and its settings on skin tissue. This validation should include live/dead analysis of skin tissue cells in and around the illuminated area. This could entail a cryostat sectioning of the skin model followed by staining to facilitate detailed analysis.

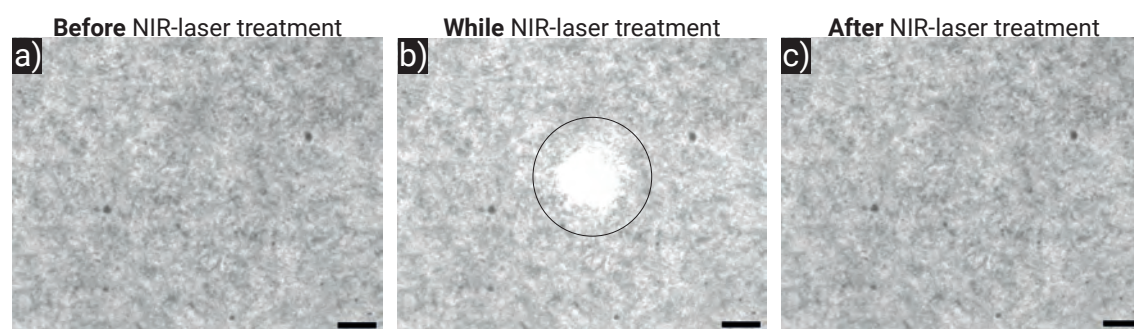


Figure 4-30: Effect of NIR-laser on skin model. Tissue model was irradiated for 10 min at maximum power (6.5 W/cm^2) by the customized 808 nm laser-setup. Effects on skin model were analyzed before (a), while (b) and after (c) irradiation by microscope. Black circle indicates area of illumination. Scale bars: $100 \mu\text{m}$.

4.2 Adhesion Mediated Engulfment and Killing of Bacteria by Synthetic Vesicles

Endocytosis is a fundamental cellular process that not only allows cells to internalize molecules such as nutrients and hormones but is also exploited by many pathogens, including viruses and bacteria, as part of the endocytic pathway.¹¹⁴ Especially the latter is of critical importance, as a deeper understanding of this mechanism is essential and leads to the development of novel infection-preventing strategies and the design of novel antimicrobial treatments. A multitude of studies employing a range of synthetic cells have been conducted to investigate the engulfment of bacterial cells. In a particular study, Dai et al.¹⁸⁵ utilized cationic gemini amphiphiles that possessed a positive membrane charge, thereby enabling electrostatic interactions with the negatively charged bacterial cell. This electrostatic adhesion was proposed to be the primary driving force for the successful engulfment of bacteria by this amphiphilic-modified GUVs. However, it has been demonstrated that the presence of positively charged (nano-)particles can induce systemic toxicity and immune system activation, thereby rendering these particles suboptimal for medical applications. In addition, Kostina et al.¹¹⁷ achieved *E. coli* engulfment by means of ultraweak interactions between the utilized cell-like dendrimersomes and the bacterial cell. Although active engulfment was achieved, such a system offers no specificity, which renders it inappropriate for targeted bacteria engulfment. Bacteriophages, in particular, are of significant interest in the context of endocytosis and engulfment due to their ability to specifically target and destroy bacterial pathogens.¹⁸⁶

By leveraging this target specificity provided by bacteriophage-derived adhesion proteins, the following chapters focus on developing a dynamic system composed of synthetic vesicles, specifically giant unilamellar vesicles (GUVs), capable of actively engulfing bacteria via target-specific adhesion-mediated interaction. To achieve not only specific adhesion and engulfment, but also the destruction of targeted bacteria, a switchable killing system, namely gold nanorods (AuNRs), was incorporated into the vesicles' membrane. This system enables target-specific bacterial killing through AuNR-generated heat, triggered by near-infrared (NIR) light illumination.

In the first part, the formation of GUVs using two different techniques is outlined to identify the most suitable lipid composition and formation method. The following paragraphs will

then describe the target-specific binding of bacteria to the GUVs, mediated by the receptor-recognizing binding protein gp37. Finally, PEG-coated AuNRs were introduced to the mixture to enable bacterial killing through AuNR-induced heat.

4.2.1 Requirements, Formation and Composition of Giant Unilamellar Vesicles

To achieve a system of synthetic vesicles capable of specifically binding to and actively engulfing bacteria, the vesicles must meet certain requirements:

- a) *Vesicle composition and size*: It is essential that the vesicle membrane exhibits a certain flexibility and size to be able to deform and wrap around the bacteria.¹¹² Nevertheless, a certain degree of stability is required, as well as a lipid composition that is biologically plausible, avoiding effects like toxicity or an enhanced tendency to elicit an immune response.
- b) *Adhesion protein anchor points*: Anchor points (i.e., DGS-NTA(Ni)) integrated into the synthetic vesicle lipid membrane capable of linking to adhesion proteins (i.e., gp37) and facilitating binding and strong adhesion between the vesicle and the bacteria (i.e., *E. coli*).
- c) *Membrane tension and fluidity*: Higher membrane fluidity allows for easier deformation, wrapping and fission. A high membrane tension offers an increased membrane barrier in the process of particle engulfment, but also ensures particle stability.¹¹⁵ Hence, it is crucial to achieve a certain balance between these two parameters. Both of these components can not only be varied by the lipid composition, but also by external parameters such as temperature or osmotic pressure.

Two different formation methods for the GUV production were applied. First, the method of emulsion-transfer was used due to its easy handling, fast production, and comparatively high yield. In the latter stage of the project, the formation was changed to a gel-assisted formation process, yielding GUVs with less contamination of perfluorinated oil and/or other components used in the formation process.¹⁸⁷

Different lipid compositions were tested to achieve stable GUVs with anchor points to bind the adhesion protein gp37.²⁸ The final GUVs were composed of two different types of lipids: 1,2-dioleoyl-*sn*-glycero-3-phosphocholine (DOPC) and 1,2-dioleoyl-*sn*-glycero-3-

phospho-(1'-rac-glycerol) (DOPG). The difference between these two phospholipids lies in the head group bound to the negatively charged phosphate group, where DOPC offers a choline group with a positive charge and DOPG a neutral glycerol group (Figure 4-31). Due to these structures, DOPC offers a dipole with net-neutral charge compared to DOPG with a net-negative charge.

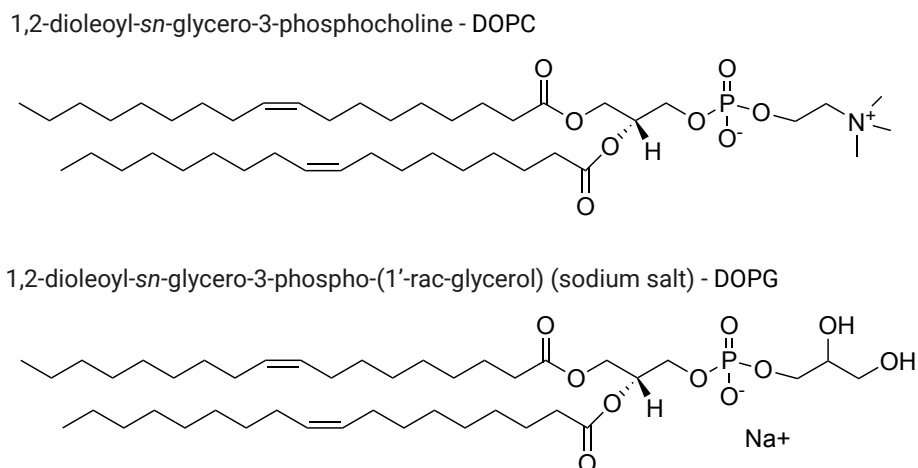


Figure 4-31: Molecular structure of 1,2-dioleoyl-*sn*-glycero-3-phosphocholine (DOPC) and 1,2-dioleoyl-*sn*-glycero-3-phospho-(1'-rac-glycerol) (sodium salt) (DOPG).

Both lipids are considered natural lipids. Phosphatidylcholine (PC) lipids are major components of cell membranes in animals, plants and microorganisms and are generally considered the most abundant phospholipids in cell membranes of mammals.^{188, 189} DOPG is a type of phosphatidylglycerol which is found in the inner mitochondrial membrane.¹⁸⁹ Due to these properties, DOPC and DOPG were selected as the lipids of choice, with DOPC as the main component (percentage ratio \approx 80:20). Furthermore, to avoid nonspecific adhesion to the vesicle membrane, a small portion of a PEGylated lipid was added (18:0 PEG2000 PE). To allow for specific adhesion of bacteria to the GUV through the adhesion protein gp37, a linker protein (DGS-NTA(Ni)) was integrated into the lipid membrane. For this purpose, the isolated gp37 protein was modified with a poly-histidine (His-tag), which was linked to the protein. The His-tag normally includes around six histidine residues in one tag (His₆-tag). Such His-tag systems show strong affinity to transition metal ions, such as Ni²⁺ or Co³⁺. Together with the chelating agent nitrilotriacetic acid (NTA), a strong interaction via coordinated bonds can be formed. With these modifications, the His-tagged gp37 protein was shown to bind specifically to this anchor lipid allowing for a specific surface modification.¹⁹⁰ For visualization, some of the GUVs

were labeled by fluorescent lipids (i.e., Atto647N DOPE, Atto488 DOPE Liss Rod PE). The final composition of the GUVs is listed in the following table.

Table 4-6: Lipid composition of GUVs. In case of the control sample, no anchor lipids (DGS-NTA(Ni)) were included.

Lipid	Sample [%]	Control sample [%]
DOPC	75.5	78.5
DOPG	18	19
PEG2000 PE	2	2
Fluorescent lipid	0.5	(0.5)
DGS-NTA(Ni)	4	-

The GUV composition was initially examined utilizing the emulsion-transfer formation technique. In order to create a control sample, no anchor lipids (DGS-NTA(Ni)) were incorporated into the synthetic vesicle membrane. Stable GUVs with an average diameter of $6.9 \pm 2.7 \mu\text{m}$ ($N = 150$) were observed by CLSM (Figure 4-32).

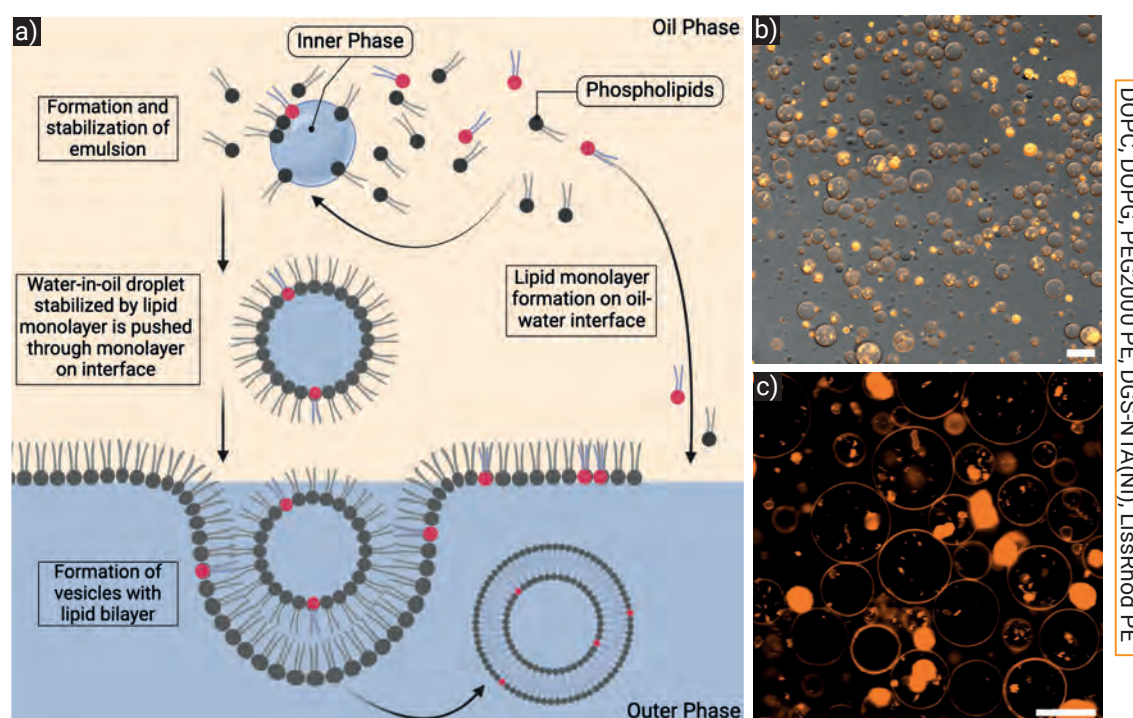


Figure 4-32: a) Schematic illustration of emulsion-transfer method. b) and c) CLSM micrographs of fluorescently labeled GUVs formed via the emulsion-transfer method. Scale bars: b): $20 \mu\text{m}$, c): $10 \mu\text{m}$. a) created with BioRender.com.

Despite undergoing multiple centrifugation and cleaning cycles, the formed GUVs were still accompanied by a significant number of contaminations. The necessity and utilization of an oil phase in the emulsion-transfer GUV formation process may have been one potential source for these contaminations. Nevertheless, due to the rapid formation process and the high yield achieved by this method, further experiments were conducted by using the emulsion-transfer method.

Once stable GUVs had been formed with the selected lipid composition, it was necessary to demonstrate successful and sufficient integration of anchor lipids within the lipid membrane. Towards this end, non-fluorescently labeled vesicles including DGS-NTA(Ni) lipids were formed and mixed with histidine-tagged GFP (His-GFP). In the event of successful integration of anchor lipids into the lipid membrane, the nickel ions of the DGS-NTA(Ni) would form a specific coordination complex with the histidine residues appearing as green fluorescent ring on the outside of the GUVs (Figure 4-33a). The presence of such a fluorescent ring was demonstrated by CLSM, providing evidence that the anchor lipids were successfully integrated into the vesicle membrane in adequate quantities (Figure 4-33b).

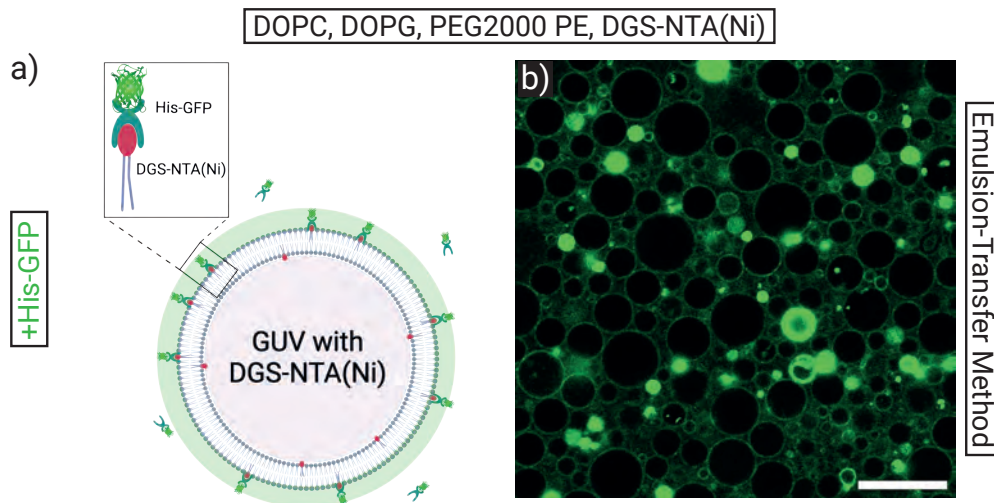


Figure 4-33: His-GFP tagged GUVs: a) Schematic illustration of His-GFP tag binding to DGS-NTA(Ni) anchor lipids integrated in the membrane of the GUVs. b) CLSM micrograph of GUVs fluorescently labeled by His-GFP coordinating to the anchor lipids in the lipid bilayer appearing as green ring in the fluorescent channel. Scale bar: 20 μm . Parts were created with BioRender.com.

4.2.2 Adhesion Protein (gp37) Mediated Binding of Bacteria

Emulsion-Transfer Formation Method

The purified and histidine-tagged adhesion protein (His-gp37) was applied in combination with *E. coli* to facilitate specific binding of the vesicles to the bacteria. Firstly, the His-gp37 protein was introduced to achieving coordinated binding between the histidine residues and the anchor lipids. Secondly, the bacteria were added. It was anticipated that the gp37 protein would be able to bind with its C-terminal end to the bacterial cell, thereby facilitating a strong adhesive interaction between the bacterium and the vesicle membrane. The experimental setup yielded the anticipated outcome, although it also resulted in some unexpected findings. The combination of His-gp37 protein and bacteria did not form the single bonds that were expected; instead, it formed multiple bonds between multiple GUVs and bacteria, resulting in the formation of large agglomerates (Figure 4-34). The observation was made despite the fact that the GUV-gp37 protein mixture was subjected to centrifugation steps prior to the addition of bacteria to eliminate the excess of unbound protein from the solution. Based on this observation, it was assumed that the bacteria were forming a bridge between single GUVs, thereby connecting multiple vesicle-gp37 complexes with one another resulting in large agglomerates. Additionally, the agglomerates hindered the ability to account for and visualize single engulfment processes of bacteria into the vesicles. Instead of being engulfed, the bacteria appeared to merely adhere to the lipid membrane (Figure 4-34c).

To investigate whether the agglomerations were initiated by the "bridging" effect of the bacteria connecting GUVs to form large agglomerates, only the His-gp37 protein was introduced to the bare GUVs (with anchor protein). Contrary to the hypothesis that the addition of bacteria would result in agglomeration, GUVs were observed to already agglomerate following the addition of the gp37 protein (Figure 7-13). This led to the assumption that it was not the bacteria, but rather the His-gp37 proteins bound to the lipid membrane, that were bridging the GUVs and resulting in agglomerations.

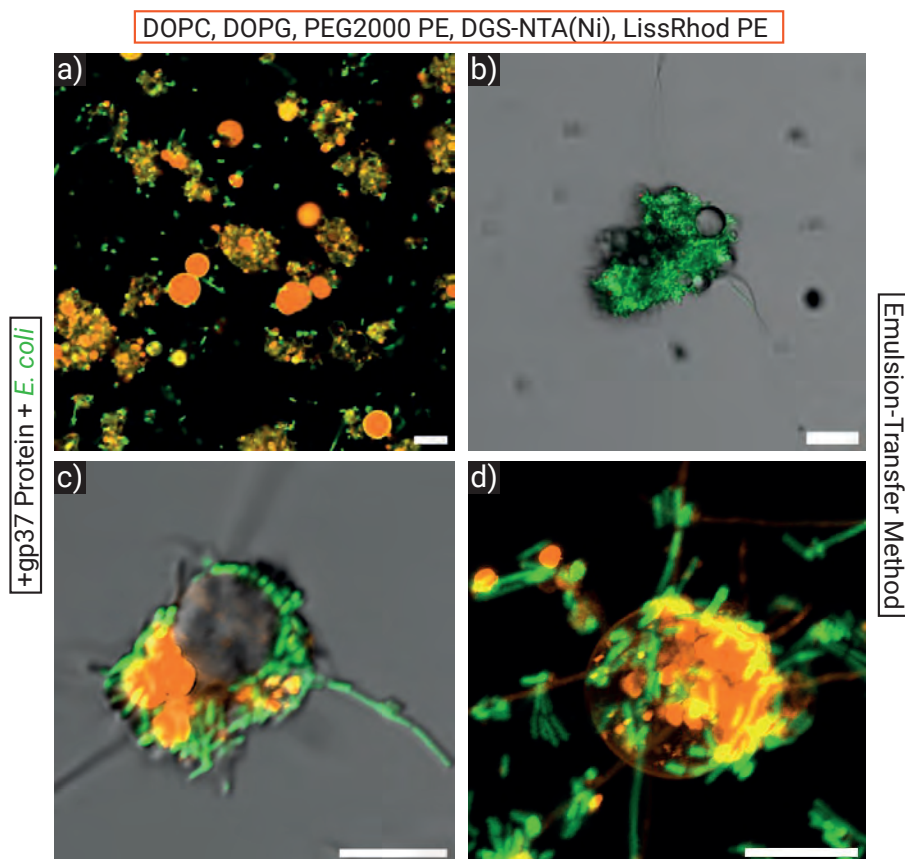


Figure 4-34: CLSM images gp37-decorated GUVs after addition of bacteria. a-c) His-gp37 (250 nM) added to GUVs (orange), interacting with the subsequently added *E. coli* forming large agglomerates. d) 3D-projection of bacteria adhering to gp37-protein decorated GUV. Scale bars: a-b: 20 μm , c-d: 10 μm .

To further confirm that the His-gp37 protein was binding specifically and exclusively to GUVs containing anchor lipids (DGS-NTA(Ni)) in the lipid bilayer, GUVs with and without DGS-NTA(Ni) lipids were mixed, His-gp37 was added, and subsequently bacteria were added. The formation of aggregates was observed once more, but only in the case of GUVs that included anchor lipids (Figure 4-35a, orange). Additionally, after the introduction of *E. coli*, the bacteria were observed to be predominantly located and agglomerated around the GUV-gp37 complexes (Figure 4-35b). In the absence of anchor lipids within the membrane of GUVs, bacterial adhesion was not observed. This finding underscores the system's target-specificity, which is only achieved through the integration of anchor lipids in combination with the adhesion protein.

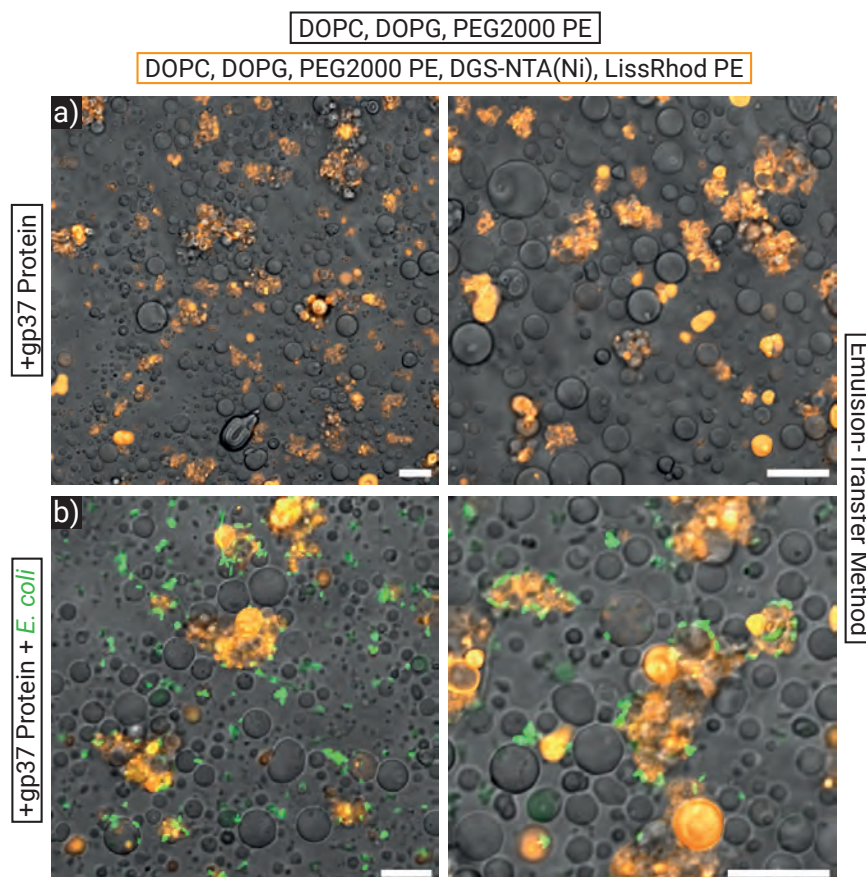


Figure 4-35: CLSM micrographs of a mixture of two different types of GUVs. Mixture of GUVs without anchor lipids (fluorescently unlabeled) and GUVs with DGS-NTA(Ni) as anchor lipids (orange). a) GUV mixture after addition of His-gp37 protein, resulting in agglomerates of anchor lipids including GUVs. b) Additional to the His-gp37 protein, *E. coli* bacteria were added, predominantly binding to fluorescently labeled GUV-gp37 complexes. Scale bars: 20 μm .

Gel-Assisted Hydration Formation Method

The previously presented experiments provided evidence that the system of His-gp37 protein-decorated GUVs was capable of binding bacteria, specifically *E. coli*. However, contamination elicited by the emulsion-transfer technique and the resulting larger agglomerations impeded a precise and detailed analysis of single GUVs interacting with bacteria. Therefore, an oil-free GUV formation technique (i.e., gel-assisted hydration method) was tested to ensure a contamination-free GUV sample. Furthermore, the emulsion-transfer produced GUVs offered a relatively small average diameter ($d = 6.9 \pm 2.7 \mu\text{m}$) compared to the size of *E. coli* (length $\approx 1 - 3 \mu\text{m}$, diameter $\approx 0.25 - 1 \mu\text{m}$). It can be reasonably assumed that larger GUVs would increase the

probability of particle engulfment, given that the membrane tension is drastically reduced for larger synthetic vesicles, as explained in Chapter 1.10.2. An increase in vesicle size would also result in a reduction in membrane curvature, thereby creating a larger available contact area with a greater number of contact points. This in turn was anticipated to enhance the adhesion energy between the bacterium and the vesicle. Accordingly, the gel-assisted hydration method was selected not only for the production of cleaner, oil-free GUVs, but also for the formation of vesicles within a size range that extends beyond the previously observed diameters.

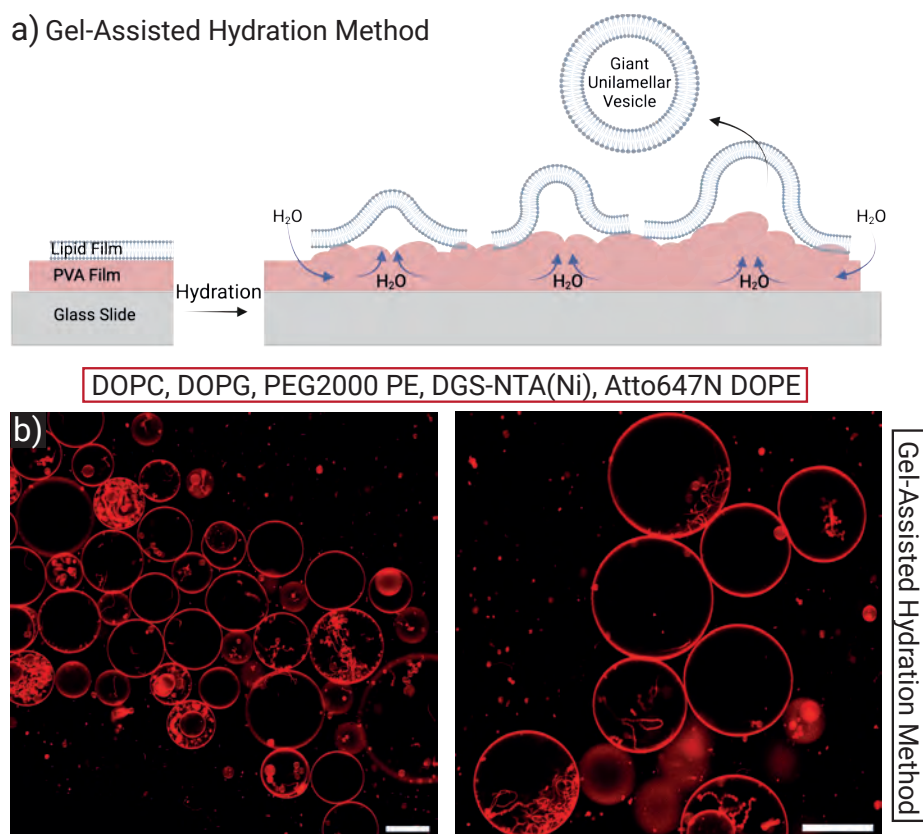


Figure 4-36: GUVs formed by the gel-assisted hydration method. a) Schematic illustration of the formation technique. b) CLSM images of fluorescently labeled GUVs formed by the gel-assisted hydration method. Scale bars: 50 μm . Parts were created with BioRender.com.

Figure 4-36 illustrates GUVs produced via the gel-assisted hydration method, exhibiting a markedly reduced prevalence of contamination in comparison to the previously employed emulsion-transfer technique. Additionally, the average diameter of these GUVs was considerably larger with an average diameter of $d = 59.89 \pm 24.66 \mu\text{m}$ ($N = 150$). To identify whether the reduction of contamination and the enlarged GUV size had an impact on the binding and engulfment of bacteria, as well as restricted the formation of

agglomerates, the newly formed GUVs were subjected to the same experimental procedure as before. The number of agglomerates was found to be decreased. However, the initially anticipated "bridging" effect was observed in the sample as well, with multiple GUVs connected via bacteria (Figure 4-37a). Hence, it was again not feasible to directly observe a discrete engulfment event. However, several bacterial cells appeared to be partially integrated into the vesicles' lipid membrane (Figure 4-37b and c, white arrows), suggesting an ongoing process of engulfment. Other studies, which conducted detailed analyses of the engulfment process for a range of particle types, observed comparable behaviors and wrapping appearances.^{114, 185}

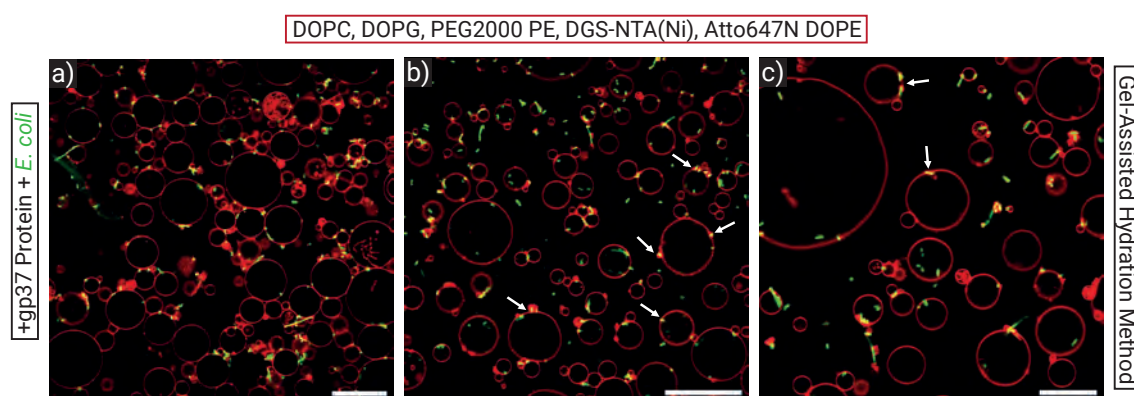


Figure 4-37: Fluorescently labeled GUVs (red) formed by the gel-assisted hydration method, subsequently mixed with the His-gp37 adhesion protein binding to the anchor lipids in the lipid bilayer and *E. coli* (green). White arrows indicate bacteria cells which seem to be integrated in the lipid bilayer of the GUVs. Scale bars: a-b): 50 μm , c): 20 μm .

Additionally, CLSM revealed bacteria cells within the GUVs, which could indicate a successful engulfment event. Figure 4-38 depicts gp37-decorated GUVs at varying stages of engulfment. By analyzing the fluorescence intensity signal across the membrane of the vesicle, it was observed that for a bare membrane (lacking adhering bacteria), only a red signal in the fluorescence intensity signal plot was apparent representing the signal induced by the fluorescent lipids present in the bilayer (Figure 4-38a₁ and b₁, red peak at $\approx 22.5 \mu\text{m}$). In the event of an adhering or wrapped bacteria cell on/by the lipid membrane, the intensity plot exhibited two signals: one representing the red channel (GUV membrane) and one representing the green channel (bacteria cell). It is noteworthy that in the case of a membrane wrapped bacteria cell, these two signals were located at the same position (Figure 4-38a₁ and b₁, peak at $\approx 2.5 \mu\text{m}$). This observation supported the hypothesis that the bacteria cell observed in Figure 4-38a₁ was indeed surrounded by the lipid membrane of

the vesicle, thereby providing evidence for an ongoing engulfment process. If the bacterial cell would only adhere to the membrane from the outside, the green signal would exhibit a slight shift in position, occurring before the intensity peak exhibited by the membranes' fluorescent lipids.¹⁸⁵ In the event of a fully internalized bacterium within the GUV, the fluorescence intensity plot should display a green signal from the bacterium between two red membrane signals. It is important to note that the green signal of the bacterium should be accompanied by a diminished membrane signal at the same peak location. This finding indicates that the membrane is wrapped around the bacterium after a successful engulfment process.¹⁸⁵ These observations were made in Figure 4-38a₂, indicating that the bacteria visible inside the vesicles were successfully wrapped and internalized by the GUV. Furthermore, it is also important to note that this was not an anecdotal observation as displayed in several publications before, but a regular observation that could be reproduced. To further substantiate this observation, it would be important to capture the process of engulfment in greater detail, enabling a step-by-step, real-time observation of the engulfment process.

The utilization of an identical experimental procedure with GUVs that lacked anchor lipids for interaction with the adhesion gp37 protein resulted in the absence of agglomeration or bacterial binding to the vesicles (Figure 7-14). This suggests that the combination of anchor lipid, His-gp37 adhesion protein, and bacteria enabled specific bacterial binding and even more important bacteria engulfment. Since engulfment is only achieved for large enough adhesion energies (Equation (1-2)) needs to be satisfied), it can be concluded that the adhesion energy, mediated by the gp37 protein, exceeded the bending, expansion, and fission energy of the system. Furthermore, no bacterial cells were observed within GUVs without anchor lipids, providing evidence that firstly, bacterial engulfment occurred only in the context of GUVs with anchor lipids and secondly, that bacterial binding and internalization was facilitated by the combination of anchor lipids and gp-37 adhesion protein.

The switch from the emulsion-transfer to the gel-assisted hydration method to form GUVs enabled a reduction in contamination levels affecting the binding and adhesion processes. Furthermore, the formation of larger GUVs was observed to have a beneficial impact on the general system and specifically on the interactions between gp37-protein decorated GUVs and bacteria. A comparison of the two techniques also showed that agglomerates were predominantly created with smaller GUVs, which were less prevalent in samples

produced by gel-assisted hydration formation. Nevertheless, further research is required to allow for a deeper understanding, particularly on a single-GUV observation approach.

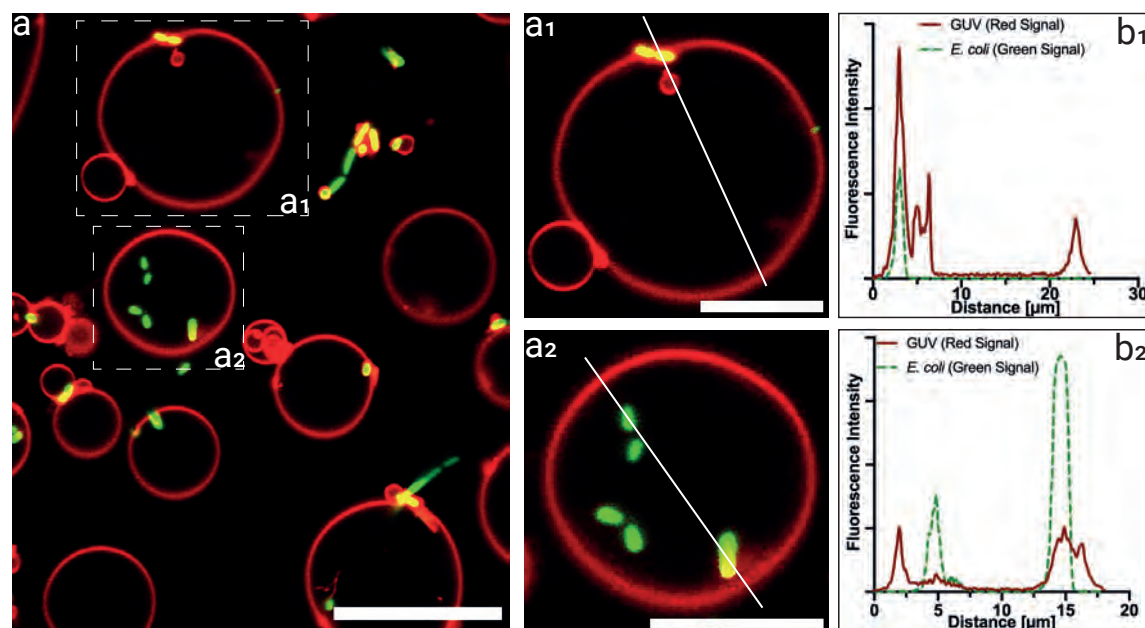


Figure 4-38: a) CLSM image capturing gp37-decorated GUVs (red) mixed with bacteria (*E. coli*, green). (a₁-a₂): Zoom-ins of GUVs at different stages of engulfment. (b₁-b₂): Fluorescence intensity profiles (GUV membrane: red signal, bacteria cell: green signal) along the indicated white lines in the respective image (a₁-a₂). Scale bars: a): 20 μm, (a₁-a₂): 10 μm.

4.2.3 AuNR-Decorated Synthetic Vesicles as Active Bacteria Killing System

The observed engulfment of bacteria demonstrated the system's ability to provide a confined space that actively protected the surrounding area from pathogens. However, to additionally impede bacterial growth and effectively combat bacterial contamination, it was necessary to further advance the system with an active bacterial killing mechanism. AuNRs were chosen for this purpose due to their unique photothermal characteristics. After producing AuNR, removing the bound CTAB from the gold surface to prevent toxic effects. A variety of thiols, most commonly PEG-thiols (PEG-SH), find application due to their demonstrated biocompatible properties and the strong affinity exhibited by the sulfur atom toward the gold surface.^{123, 191} Furthermore, PEG coatings do not affect the crucial photothermal properties of the gold particles and provide the particles with extended *in vivo* circulation times.¹⁹² For these reasons, mPEG-SH (methoxy-PEG-thiol) was selected as the

primary coating agent for the AuNRs. Furthermore, it was combined with a minor quantity of cholesterol-PEG-thiol (Chol-PEG-SH) to facilitate the binding of AuNR to the lipid bilayer of the synthetic vesicles. The Chol-PEG-SH molecule, capable of integrating its hydrophobic cholesterol part into the lipid bilayer's hydrophobic core, was used as a linker, binding to the gold surface on one side and integrating into the vesicle's membrane on the other.¹⁹³

CTAB-stabilized AuNRs exhibited a longitudinal SPR peak at 796 nm, along with a positive ζ -potential of 51.7 ± 2.5 mV. Replacing CTAB with PEG-SH notably resulted in reduced ζ -potential (9.1 ± 0.4 mV) due to the replacement of the positively charged CTAB-molecules by thiols on the gold surface. PEG is a neutral polymer (Figure 4-39a), facilitating surface charge reduction towards charge neutralization.¹²³ Moreover, after PEG-functionalization, a slight shift in the LSPR peak (Figure 4-39b) towards lower wavelengths (780 nm) was observed, indicating an alteration in surface chemistry and refractive index.

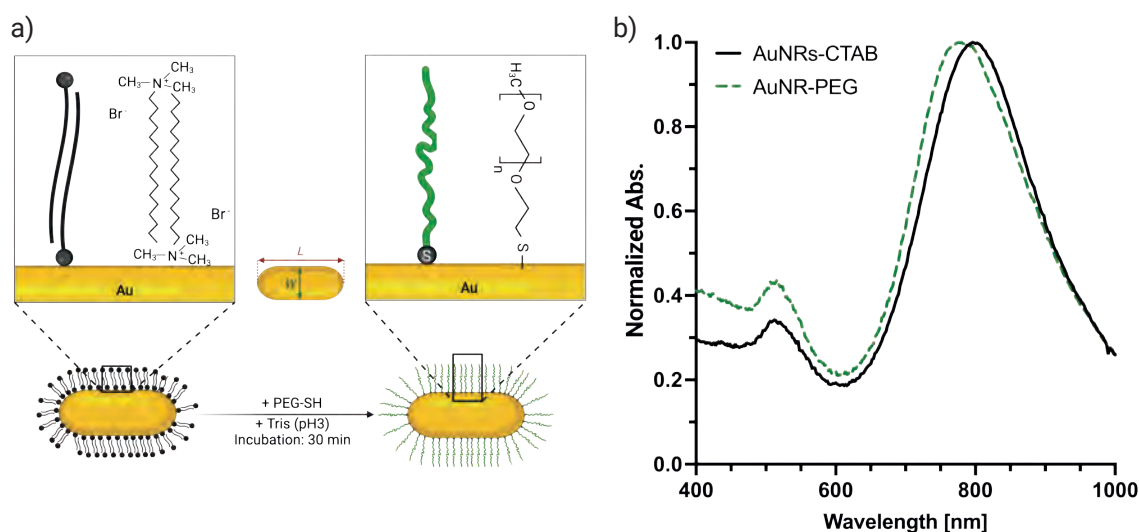


Figure 4-39: Functionalization of AuNRs with PEG. a) Surface chemistry and functionalization process of CTAB- and PEG-stabilized AuNRs. b) Normalized absorbance spectrum of CTAB- (black curve) and PEG-stabilized (green curve) AuNRs. Parts were created with BioRender.com.

The absorbance spectrum shown in Figure 4-39b demonstrated that the unique properties of the AuNRs were retained after PEG-coating. After successful functionalization, the PEG-coated AuNR were combined with the GUVs to create AuNR-decorated GUVs. The

linkage was facilitated by the intercalation of the cholesterol segment of Chol-PEG-SH molecules, which were bound to the AuNR surface, into the lipid membrane. Subsequently, the AuNR-decorated GUVs were incubated with the gp37 protein, which resulted in the formation of AuNR- and gp37-decorated GUVs. The objective was to create a system that would bind, engulf, and subsequently kill bacteria via NIR light-induced heat. To ascertain that neither the stability of the GUVs nor the binding and adhesion properties of the gp37 protein was compromised by the introduction of AuNRs, the system was subjected to an analysis prior to NIR light treatment. In addition, it was necessary to assess the viability of the bacteria that had been incubated with the gp37- and AuNR-decorated GUVs to ensure that the system itself did not possess toxic properties. To this end, a live/dead staining procedure was employed, utilizing propidium iodide (PI) and SYTO 9. PI was selected as the fluorescent dye, capable of intercalating into the nucleic acid of damaged bacterial cells, thereby imparting a red fluorescent signal. SYTO 9 was utilized for the general identification of bacterial cells, as it is capable of penetrating both live and dead bacterial cells, resulting in a green fluorescent signal.¹⁹⁴ The GUV membrane was labeled in magenta by Atto647N-DOPE (Figure 4-40). CLSM images indicated that the addition of AuNRs to the GUV-gp37 protein system did not affect the stability of the GUVs. The GUVs were still present in sufficient quantities and exhibited sizes comparable to the samples without AuNRs presented before (Figure 4-40b). Furthermore, bacterial adhesion was facilitated, as indicated by the observation of *E. coli* cells adhering to the GUV surfaces and partial engulfment/wrapping of the bacteria by the membrane (Figure 4-40b₁). It is important to note that some of the bacterial cells displayed not only a green but also a red signal resulting from the penetration of PI into the cell, indicating cell death. This observation may be taken as an indication of an incomplete AuNR coating procedure and the presence of residual CTAB, causing toxic effects. Therefore, it is imperative to first conduct further investigations into the AuNR coating procedure and the general biocompatibility of the overall system in the future to guarantee complete biocompatibility and the absence of any toxic effects. Subsequent to confirming the biocompatibility of the AuNR- and gp37-decorated GUVs, the system can be utilized in the future in NIR light experiments to further investigate the antibacterial properties attributed to the photothermal properties of the AuNRs.

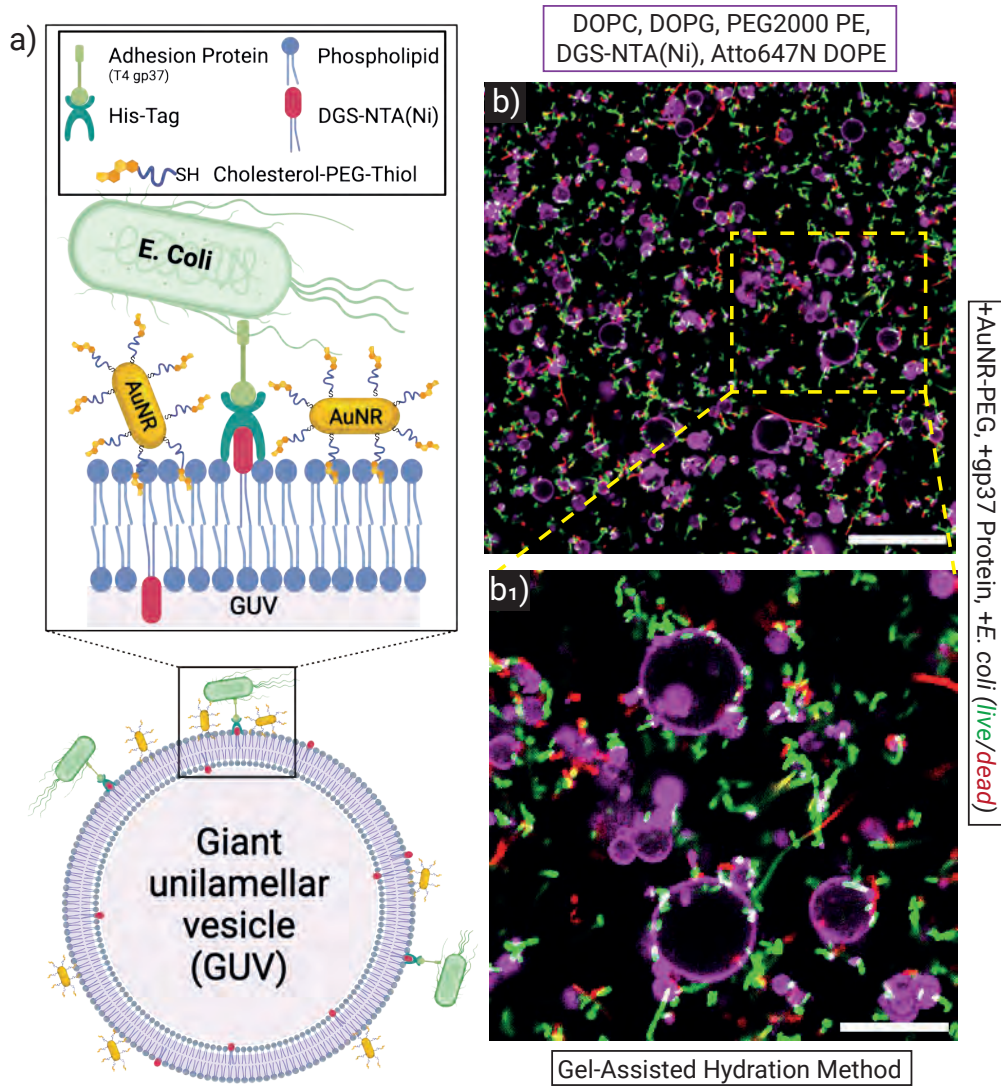


Figure 4-40: a) Schematic illustration of AuNR- and gp37-decorated GUVs with bound *E. coli* on the surface. b) Overview and b1) zoom-in CLSM images of AuNR- and gp37-decorated GUVs (magenta) incubated with *E. coli* (green/red). Scale bars: b): 50 μm , b1): 20 μm . Parts were created with BioRender.com.

Summary & Conclusions

Chapter 5

5 Summary & Conclusions

Overuse and misuse of antibiotics are among the primary contributing factors leading to the development of antibiotic-resistant bacteria. Antimicrobial resistance (AMR) has been observed to result in a considerable increase in mortality rates and significant economic costs. This situation has led to an urgent need for the development of antibiotic-free therapeutic options. The majority of existing antibacterial approaches operate in an “open-space” manner, leading to inflammation due to the release of bacterial toxins and fragments into the surrounding space. This present thesis has thus focused on the development of two synthetic antibacterial systems capable of entrapping/engulfing, retaining, and killing bacteria within a “confined space” with minimal impact on the surrounding tissue.

The primary focus of this thesis was on the design of porous, polymer-based stable microcapsules (μ Cs), which are intended for use as antibacterial coatings for medical devices and implants. To this end, a high-throughput method has been designed to generate porous μ Cs that are capable of capturing and retaining bacteria in the hollow cavity. It was observed that the process of bacteria capturing was primarily driven by the bacteria's own mobility, which rendered the system particularly effective for motile bacteria (Figure 5-1, left).

The primary motivation behind the development of a second antibacterial synthetic system was the mimicking of a natural phagocytotic system. Therefore, GUV-based compartments were engineered as a dynamic system, actively capturing bacteria via engulfment. To enhance the interactions and adhesion between the GUVs and bacteria the GUV membrane was functionalized with the bacteriophage tail protein gp37 (Figure 5-1, right).

In addition to the ability of the systems to capture and retain bacteria, both systems were equipped with a bacteria killing module. To this end, the systems were successfully modulated with specially coated AuNRs for NIR-light-triggered heat generation.

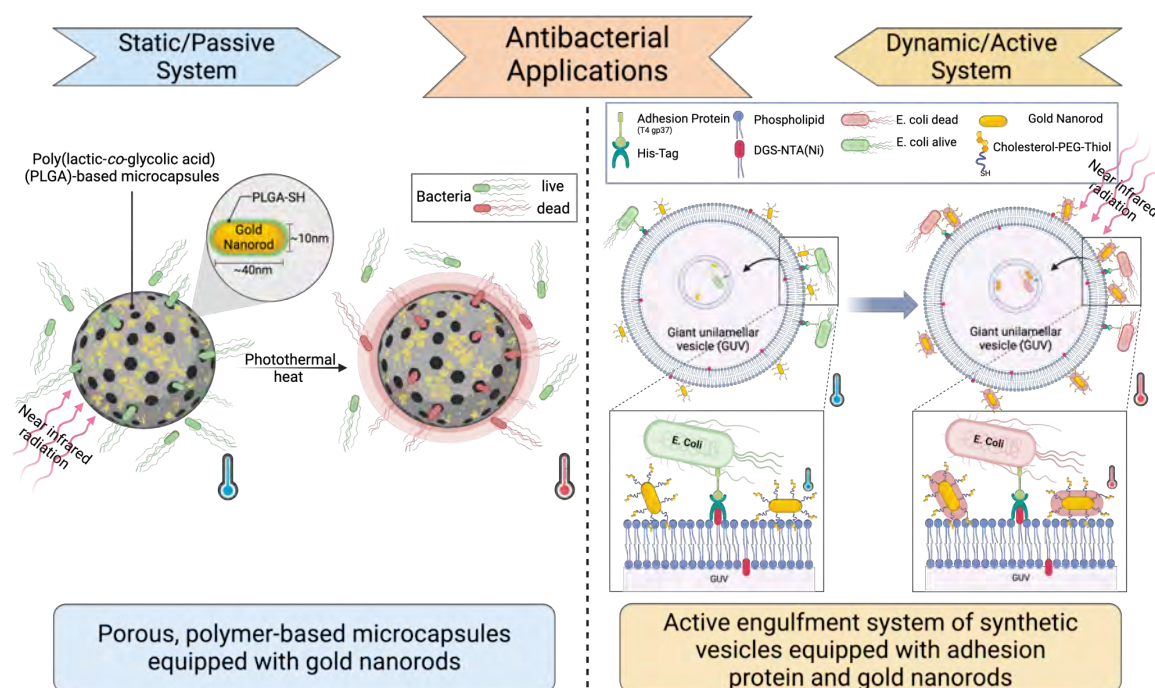


Figure 5-1: Schematic representation of the two antibacterial synthetic systems as have been designed in this thesis. Left: Modular, porous, polymer-based μ Cs capturing and retaining different types of bacteria within the hollow cavity. Right: Adhesion protein functionalized GUVs, actively binding *E. coli* to facilitate adhesion-mediated engulfment. The implementation of AuNRs in both systems enabled the use of NIR light-triggered and local heat generation, which was utilized to achieve bacterial elimination. Created with BioRender.com.

5.1 Modular Porous Polymer-Based Microcapsule System for Trapping and Light-Triggered Killing of Bacteria

In the scope of this thesis, a robust, high-throughput bulk formation technique was developed to produce mechanically and chemically stable porous, polymer-based μ Cs. Through a systematic approach involving the careful selection of polymer, porogen, solvent and water ratios, μ Cs within a suitable size range and with a high degree of porosity were successfully designed. In order to enhance the porosity characteristics of the μ Cs system, a straightforward and rapid post-production etching procedure was introduced. This method led to a substantial enhancement in the bacteria penetration and trapping capabilities of the μ Cs.

The developed and optimized μ Cs type was utilized in a series of bacterial capture experiments with the objective to analyze the general capturing efficiency as well as to compare the number of captured bacteria for motile versus non-motile bacteria. As a result, a high capturing efficiency was detected for motile bacteria, especially at high bacteria concentrations. In contrast, non-motile bacteria were predominantly observed to adhere to the outer surface of the μ Cs. This finding indicates that the capturing process was predominantly driven by the intrinsic mobility of the bacteria rendering the system particularly interesting for applications as implant coatings.

To include an active killing module of the trapped bacteria, AuNRs were integrated into the shell of the developed μ Cs. For this purpose, AuNRs with the desired optical properties were produced and subsequently functionalized by a polymeric coating. This functionalization process efficiently substitutes the cytotoxic CTAB molecules by a PLGA-thiol coating on the AuNRs surface, rendering the AuNRs biocompatible and suitable for the integration into the μ Cs.

Subsequent experiments have demonstrated the efficacy of the AuNRs-functionalized μ Cs system for NIR-triggered bacteria killing. It is important to mention that the efficient killing of motile and non-motile bacteria within the capsules and in close proximity to them was achieved with a 2 min illumination time and a power density of 6.5 W/cm². In order to assess the biocompatibility of the used laser setup and the applied power density, the system was applied to a human skin model. Microscopic examination revealed no visible skin damage in this experiment.

5.2 Adhesion Mediated Engulfment and Killing of Bacteria by Synthetic Vesicles

The second antibacterial system developed in the course of this thesis featured an active engulfment approach designed to mimic a phagocytotic system consisting of synthetic vesicles. To this end, emulsion transfer and gel-assisted hydration methods were implemented and evaluated for their efficacy in producing stable GUV-based compartments with the desired properties. An improved sample quality with fewer contaminants and a suitable GUV size was identified for the gel-assisted hydration method. The utilization of bacteria-specific adhesion proteins towards targeted pathogens resulted

in the formation of strong adhesion, which subsequently triggered engulfment. For this purpose, a bacteriophage-derived gp37 adhesion protein was modified by a His-tag, enabling the linkage of the protein to the GUVs including DGS-NTA(Ni) functional lipids. This modification facilitated a strong adhesive interaction between *E. coli* cells and the lipid membrane, which is essential for successful engulfment. However, bacterial adhesion to the GUVs was accompanied by the occurrence of large agglomerates. In this case, it was hypothesized that bacteria cells in combination with the adhesion protein led to a "bridging" effect, connecting several GUVs and bacteria to the observed large agglomerates. This situation rendered it unfeasible to analyze individual engulfment events within the executed experiments. This condition was improved by utilizing the gel-assisted hydration method instead of the emulsion transfer method. Consequently, the gel-assisted hydration technique became the primary method of choice. The application of this optimized system permitted the observation of bacteria cells that were partially or completely enclosed/engulfed by the synthetic vesicles.

In the next step, similarly to the μ C system, the GUV-based antibacterial system was equipped with AuNRs to implement an active killing mechanism. To this end, the CTAB molecules on the gold surface of the AuNRs were substituted by mixture of PEG-thiol/cholesterol-PEG-thiol molecules to render the system biocompatible and to allow for integration into the lipid bilayer. A notable benefit of this AuNR-facilitated method of killing is its external and noninvasive trigger. This ensures that the killing process is initiated after engulfment, thereby preventing the release of bacterial toxins into the surrounding tissue. The synthetic system presented here has been demonstrated to have the capacity to actively and target-specifically engulf and kill pathogens in a confined space. Consequently, this system emerges as a promising antibiotic alternative, with applications in various medical domains, including potential use as a washing solution.

Outlook

Chapter 6

6 Outlook

This section presents a range of prospective future perspectives and experiments that have the potential to further enhance and modulate the presented antibacterial systems.

6.1 Modular Porous Polymer-Based Microcapsule System for Trapping and Light-Triggered Killing of Bacteria

The developed μC has the potential to function as an antibacterial coating, thereby impeding the formation of bacterial biofilms. Through further modulation of the system by the integration of magnetic particles (e.g., iron oxide particles) into the μC shell, the capsules could be actively guided and tracked. The presence of these properties would render the system suitable not only for use as an implant coating, but also as a flushing solution. Integration of antibacterial particles (e.g. quaternary ammonium compounds (QACs)) or bacterial attractants within the hollow cavity could further enhance the system's functionality by facilitating enhanced uptake and killing ability. QAC, on the one hand, would allow for bacterial killing via electrostatic interaction resulting in the disruption of the bacterial cell membrane.¹⁹⁵ Chemoattractants, for example, nutrients such as sugar¹⁹⁶ or amino acids¹⁹⁷, on the other hand, could serve to generate a chemical gradient, thereby actively drawing bacteria towards the inside of the μC .¹⁹⁸⁻²⁰⁰

In order to expand the range of applications, further studies with a variety of capsule materials should be conducted. These studies would explore, enhance, and adjust properties such as biodegradability or mechanical stability, with the aim of aligning them with the intended application. In this regard, the addition of a thin layer of TiO_2 to the μC s would significantly modify the mechanical properties of the system. This is particularly crucial in the context of orthopedic implants, where mechanical properties play a pivotal role.

To provide further support for the biocompatible properties of the μ C system and to demonstrate the efficacy of bacteria killing via AuNR-generated heat, it would be necessary to utilize cells, particularly immune cells. In the event of incomplete elimination of bacteria, bacterial escape or toxin leakage, cell death and immune cell activation would occur indicating insufficient killing properties.

The scope of the study may be expanded through the investigation of varying laser power densities at different irradiation time periods. Such investigations would be essential to be able to utilize the developed μ C system in medical-related fields.

6.2 Adhesion Mediated Engulfment and Killing of Bacteria by Synthetic Vesicles

In order to successfully achieve an effective, synthetic engulfment system that closely mimics phagocytotic systems, further biocompatibility tests of the gp37- and AuNR-decorated GUVs are necessary to make the system applicable for medical applications. Once evidence of the system's overall biocompatibility has been provided, it will be necessary to design a specifically adjusted experiment to examine single bacteria cell engulfment by the GUVs captured at all stages and in real-time. A comprehensive examination of the engulfment process would facilitate a more thorough understanding of the general process of adhesion-mediated engulfment. Furthermore, such an examination would allow for the optimization of the system to achieve high levels of engulfment and killing efficiency, as well as excellent stability properties.

Following the successful demonstration of the concept, further investigation is necessary to ascertain the specificity of the gp37-decorated GUVs towards the targeted bacteria type and their specific adhesion and engulfment. In order to achieve this objective, it is necessary to conduct experiments with gp37-decorated GUVs in a mixture of different bacteria types, with the adhesion behavior being analyzed. The system's functionality could be expanded through the use of a variety of bacteriophage-derived adhesion proteins that target different types of bacteria with a high degree of specificity.

Bacteriophages not only possess bacteria-specific adhesion proteins but also target-specific endolysins. These enzymes are capable of killing bacteria by degrading the major components of their cell membrane.^{201, 202} Incorporating endolysins and adhesion proteins

into the GUV membrane would facilitate target-specific adhesion, engulfment, and highly specific killing. Consequently, the integration of AuNRs within the lipid membrane would facilitate the implementation of a multifaceted killing mechanism. This mechanism would combine a light-triggered, unspecific mechanism that kills via heat with a contact-triggered, target-specific mechanism that kills via enzymatic degradation. The combination of these engulfing and killing mechanisms would render this artificial phagocytotic system even more powerful for a variety of applications, including flushing solutions.

Appendix

Chapter 7

7 Appendix

7.1 Supporting Information

7.1.1 Modular Porous Polymer-Based Microcapsule System

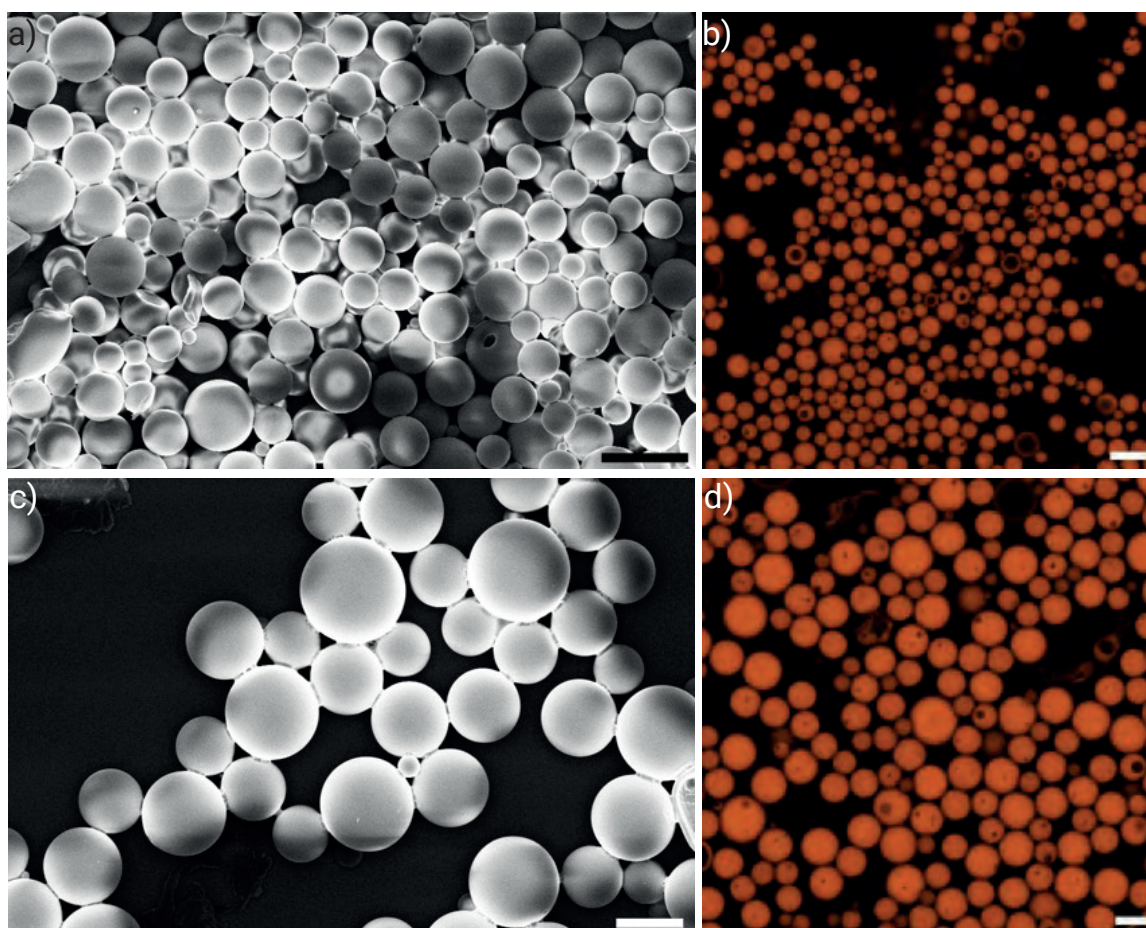
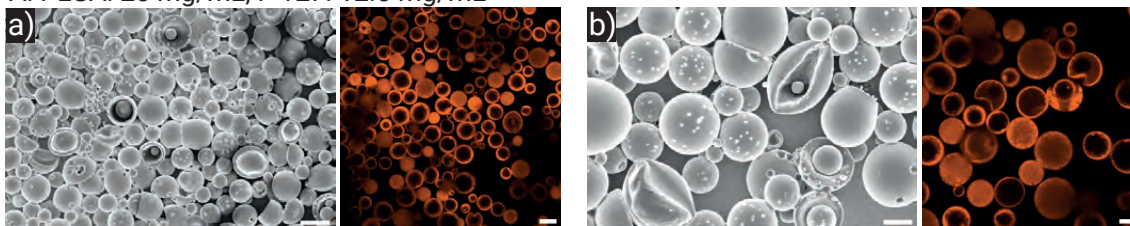


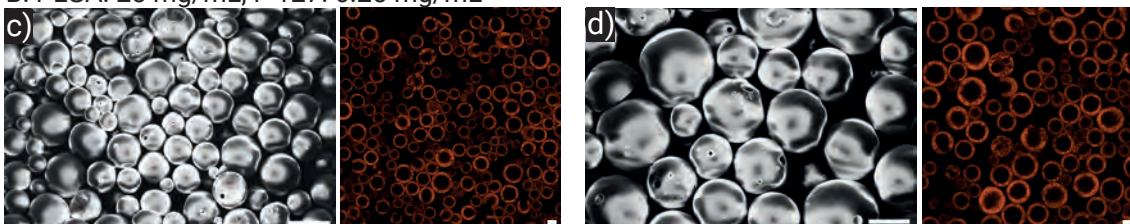
Figure 7-1: Representative SEM (a and c) and CLSM (b and d) images of solid PLGA μ Cs at elevated solvent levels and a PLGA concentration of 12.5 g/L in the oil phase. DCM/PLGA phase was fluorescently labeled by Nile red (orange). Scale bars: a) and b): 20 μ m, c) and d): 10 μ m.

Pluronic: F-127

A: PLGA: 25 mg/mL, F-127: 12.5 mg/mL



B: PLGA: 25 mg/mL, F-127: 6.25 mg/mL



C: PLGA: 12.5 mg/mL, F-127: 6.25 mg/mL

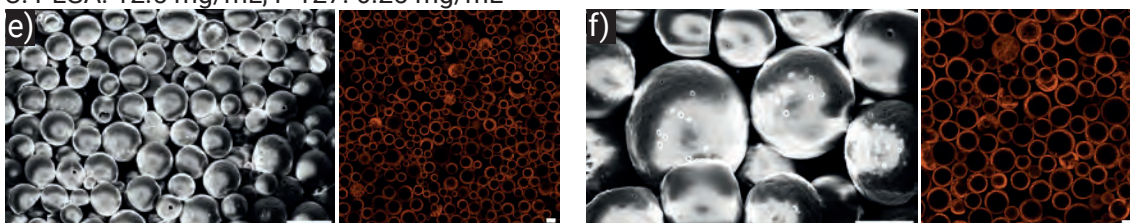
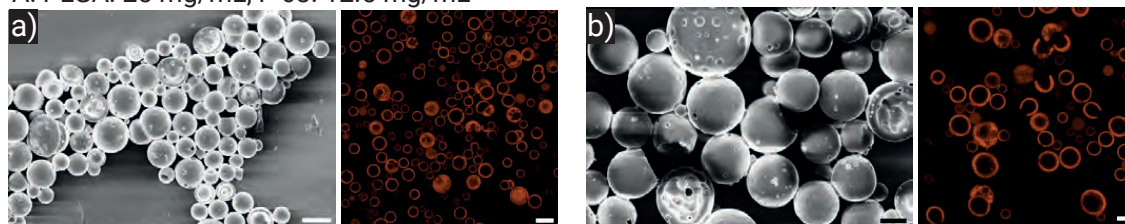


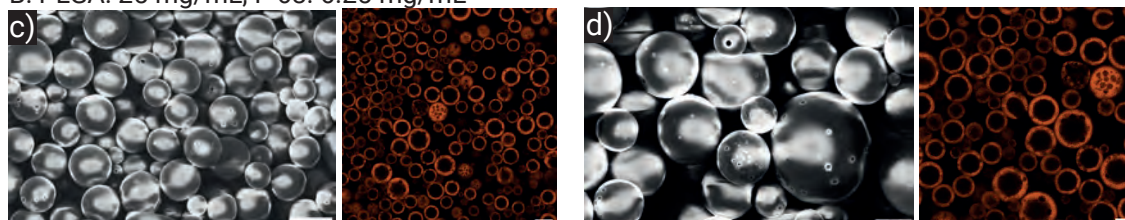
Figure 7-2: Representative SEM and CLSM images of μ Cs produced with different concentrations of PLGA and Pluronic® F-127 as porogen. A: PLGA: 25 g/L, F-127: 12.5 g/L, B: PLGA: 25 g/L, F-127: 6.25 g/L, C: PLGA: 12.5 g/L, F-127: 6.25 g/L. HFE-7500 was used as core-forming agent for all samples. DCM/PLGA phase was fluorescently labeled by Nile red (orange). Scale bars: a), c) and e): 20 μ m, b), d) and f): 10 μ m.

Pluronic: F-68

A: PLGA: 25 mg/mL, F-68: 12.5 mg/mL



B: PLGA: 25 mg/mL, F-68: 6.25 mg/mL



C: PLGA: 12.5 mg/mL, F-68: 6.25 mg/mL

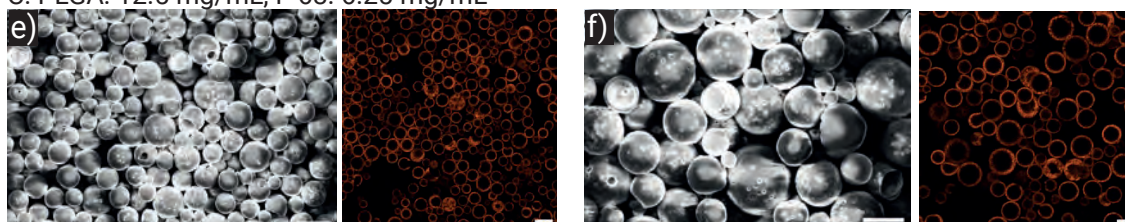
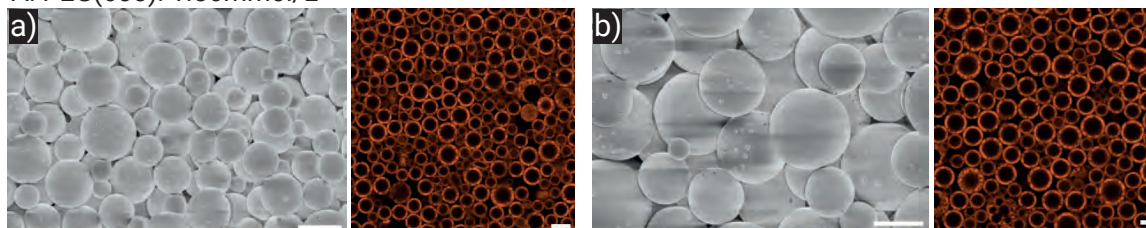


Figure 7-3: Representative SEM and CLSM images of μ Cs produced with different concentrations of PLGA and Pluronic® F-68 as porogen. A: PLGA: 25 g/L, F-68: 12.5 g/L, B: PLGA: 25 g/L, F-68: 6.25 g/L, C: PLGA: 12.5 g/L, F-68: 6.25 g/L. HFE-7500 was used as core-forming agent for all samples. DCM/PLGA phase was fluorescently labeled by Nile red (orange). Scale bars: a), c) and e): 20 μ m, b), d) and f): 10 μ m.

PEG, $M = 600$ g/mol

A: PEG(600): 1.56mmol/L



B: PEG(600): 3.13mmol/L

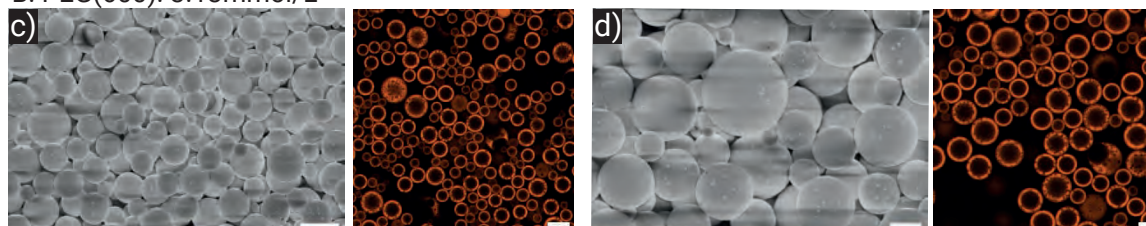
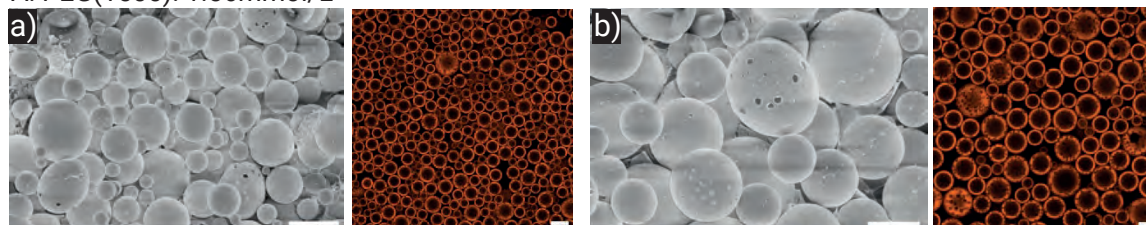


Figure 7-4: Representative SEM and CLSM images of μ Cs produced with PEG₆₀₀ ($M = 600$ g/mol) as porogen. Two different concentrations were tested: A: 1.56mmol/L and B: 3.13 mmol/L. Concentration of PLGA (25 g/L) and HFE-7500 (0.025 μ L/mL) was kept constant. Nile red was used in the oil phase to fluorescently label the PLGA/DCM phase (orange). Scale bar: a and c: 20 μ m, b and d: 10 μ m.

PEG, $M = 1500$ g/mol

A: PEG(1500): 1.56mmol/L



B: PEG(1500): 3.13mmol/L

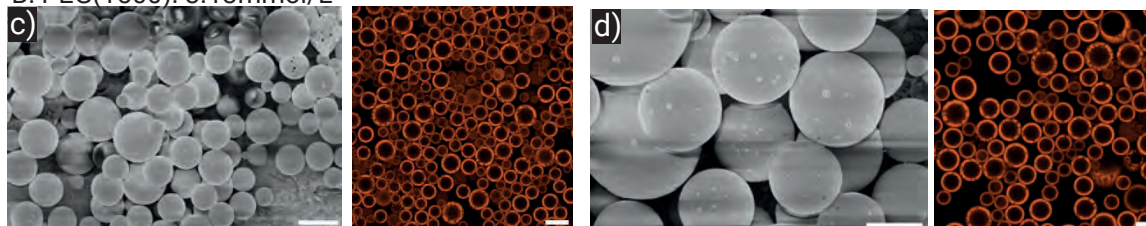
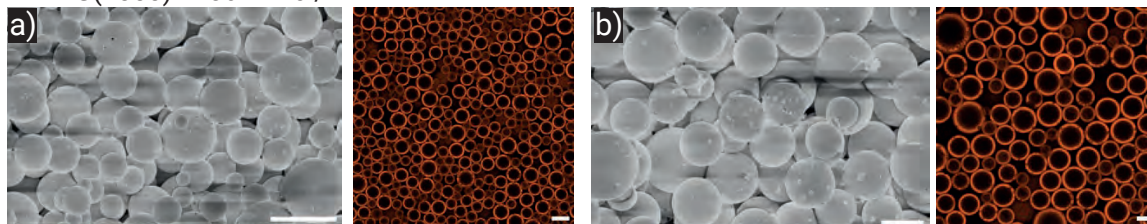


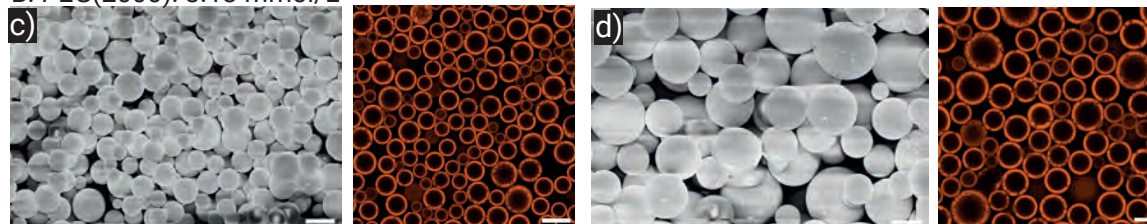
Figure 7-5: Representative SEM and CLSM images of μ Cs produced with PEG₁₅₀₀ ($M = 1,500$ g/mol) as porogen. Two different concentrations were tested: A: 1.56 mmol/L and B: 3.13 mmol/L. Concentration of PLGA (25 g/L) and HFE-7500 (0.025 μ L/mL) was kept constant. Nile red was used in the oil phase to fluorescently label the PLGA/DCM phase (orange). Scale bar: a and c: 20 μ m, b and d: 10 μ m.

PEG, $M = 2000$ g/mol

A: PEG(2000): 1.56 mmol/L



B: PEG(2000): 3.13 mmol/L



C: PEG(2000): 6.25 mmol/L

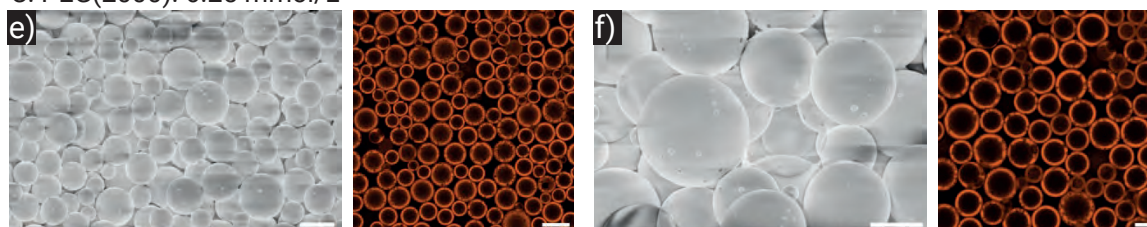
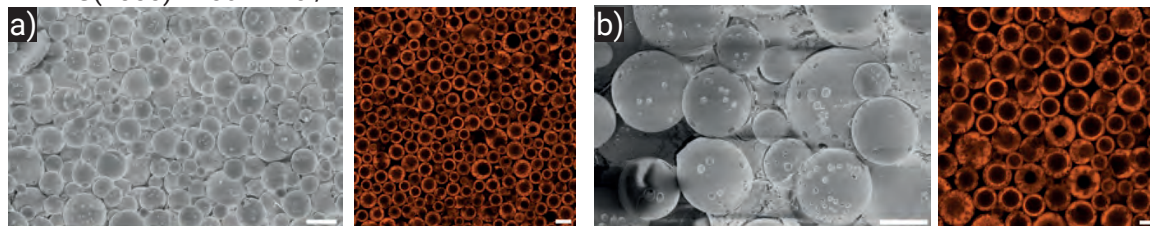


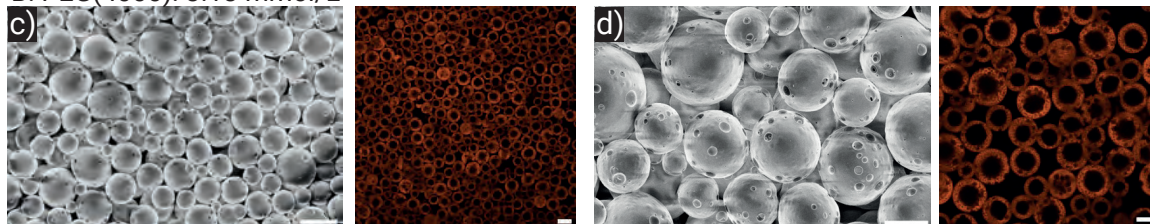
Figure 7-6: Representative SEM and CLSM images of μ Cs produced with PEG₂₀₀₀ ($M = 2,000$ g/mol) as porogen. Three different concentrations were tested: A: 1.56 mmol/L and B: 3.13 mmol/L and C: 6.25 mmol/L. Concentration of PLGA (25 g/L) and HFE-7500 (0.025 μ L/mL) was kept constant. Nile red was used in the oil phase to fluorescently label the PLGA/DCM phase (orange). Scale bar: a, c and e: 20 μ m, b, d and f: 10 μ m.

PEG, $M = 4000$ g/mol

A: PEG(4000): 1.56 mmol/L



B: PEG(4000): 3.13 mmol/L



C: PEG(4000): 6.25 mmol/L

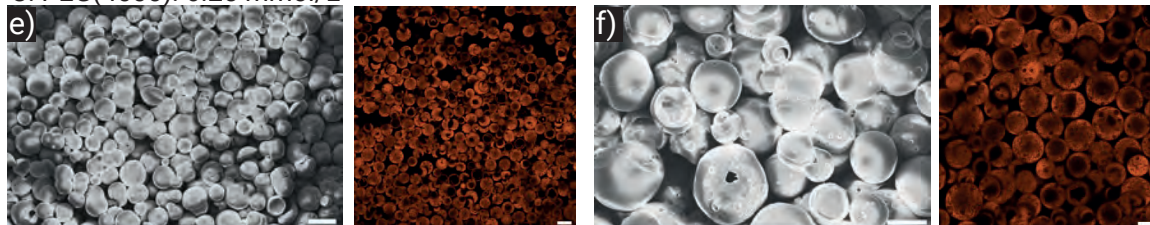


Figure 7-7: Representative SEM and CLSM images of μ Cs produced with PEG₄₀₀₀ ($M = 4,000$ g/mol) as porogen. Three different concentrations were tested: A: 1.56 mmol/L and B: 3.13 mmol/L and C: 6.25 mmol/L. Concentration of PLGA (25 g/L) and HFE-7500 (0.025 μ L/mL) was kept constant. Nile red was used in the oil phase to fluorescently label the PLGA/DCM phase (orange). Scale bar: a, c and e: 20 μ m, b, d and f: 10 μ m.

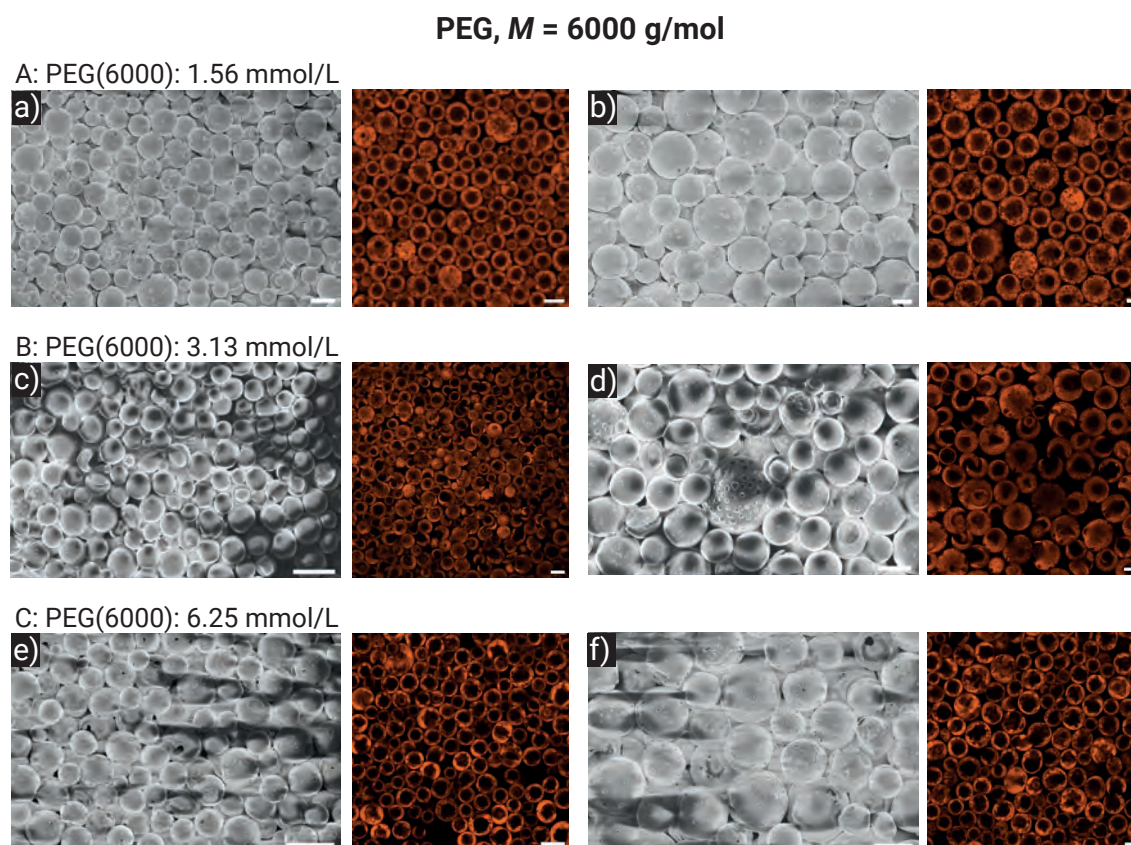
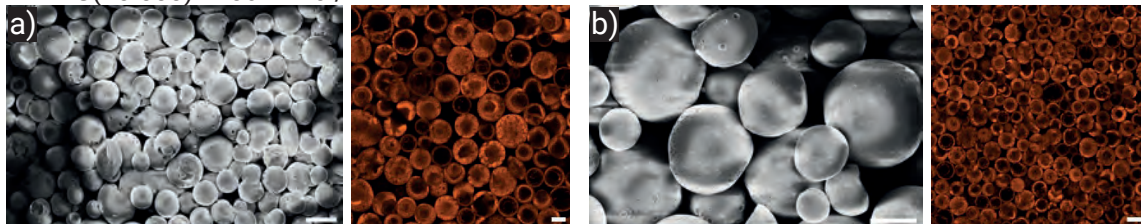


Figure 7-8: Representative SEM and CLSM images of μ Cs produced with PEG₆₀₀₀ ($M = 6,000$ g/mol) as porogen. Three different concentrations were tested: A: 1.56 mmol/L and B: 3.13 mmol/L and C: 6.25 mmol/L. Concentration of PLGA (25 g/L) and HFE-7500 (0.025 μ L/mL) was kept constant. Nile red was used in the oil phase to fluorescently label the PLGA/DCM phase (orange). Scale bar: a, c and e: 20 μ m, b, d and f: 10 μ m.

PEG, $M = 10\,000$ g/mol

A: PEG(10.000): 1.56 mmol/L



B: PEG(10.000): 3.13 mmol/L

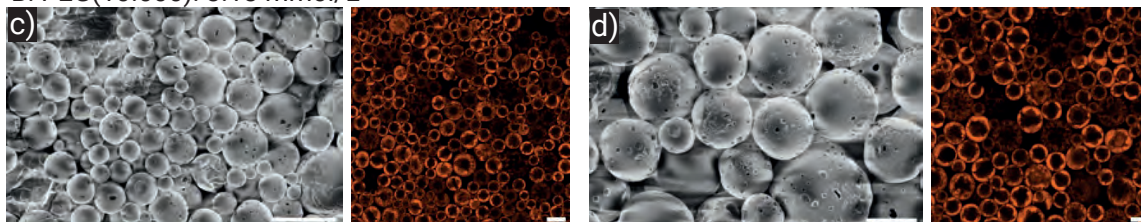


Figure 7-9: Representative SEM and CLSM images of μ Cs produced with PEG₁₀₀₀₀ ($M = 10,000$ g/mol) as porogen. Two different concentrations were tested: A: 1.56 mmol/L and B: 3.13 mmol/L. Concentration of PLGA (25 g/L) and HFE-7500 (0.025 μ L/mL) was kept constant. Nile red was used in the oil phase to fluorescently label the PLGA/DCM phase (orange). Scale bar: a and c: 20 μ m, b and d: 10 μ m.

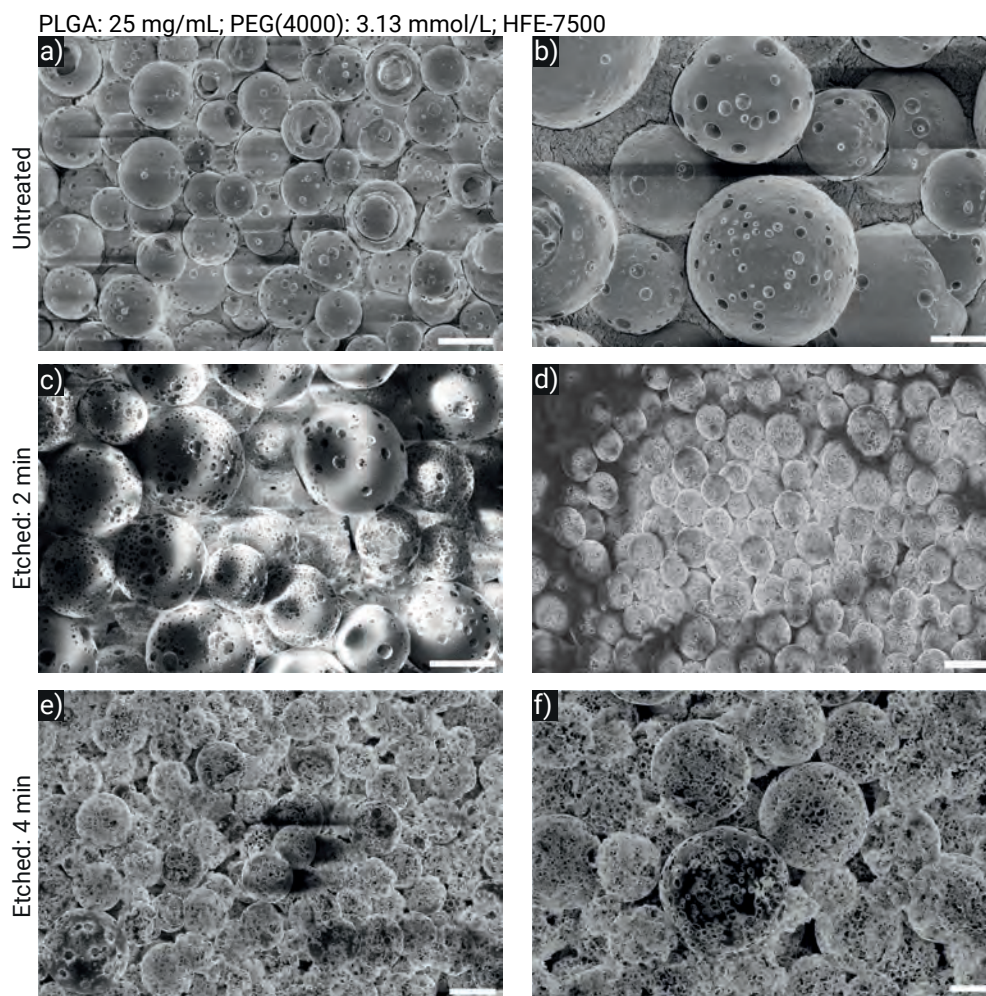


Figure 7-10: Effect of post-production etching procedure on μC porosity. Representative SEM images of untreated μC s produced (a and b) with PEG₄₀₀₀ as porogen, μC s etched for 2 min (c and d) and 4 min (e and f). Scale bars: a), c) and e): 20 μm , b), d) and f): 10 μm .

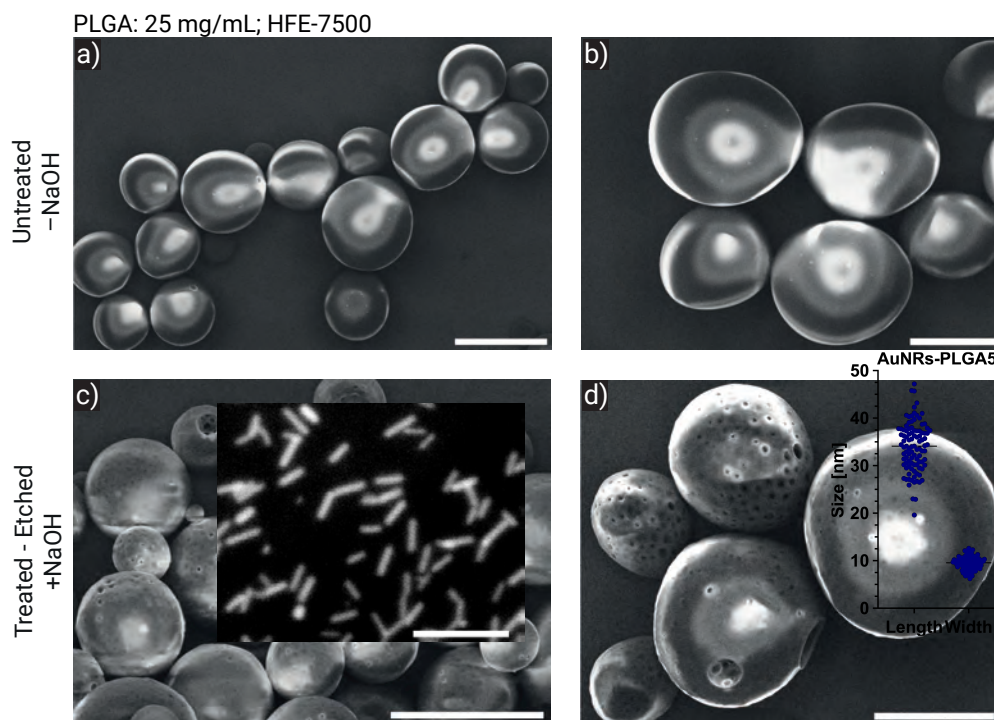


Figure 7-11: Effect of post-production etching NaOH-treatment on μ Cs without porogen. Untreated μ Cs (a and b) were treated for 2 min with an aqueous NaOH solution (1.25%, (w/v), c and d) and subsequently analyzed by SEM. Surface roughness and porosity were increased after treatment (c and d). Scale bars: a) and c): 20 μ m, b) and d): 10 μ m.

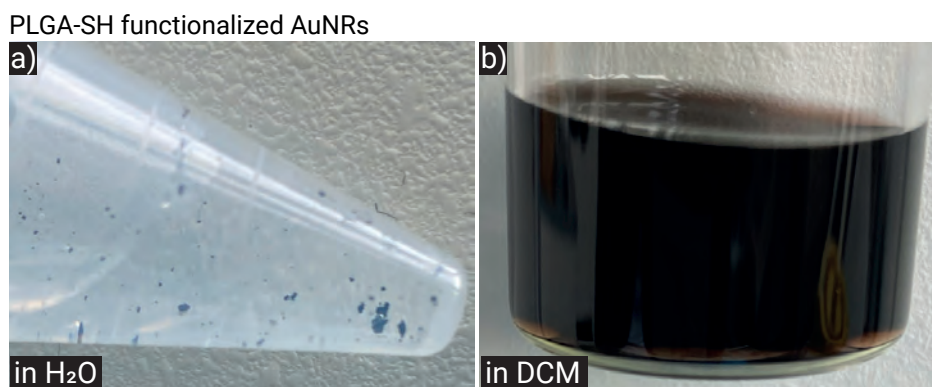


Figure 7-12: Comparison of re-dispersing PLGA-SH functionalized AuNRs in H₂O (a) versus DCM (b).

7.1.2 Synthetic Vesicles

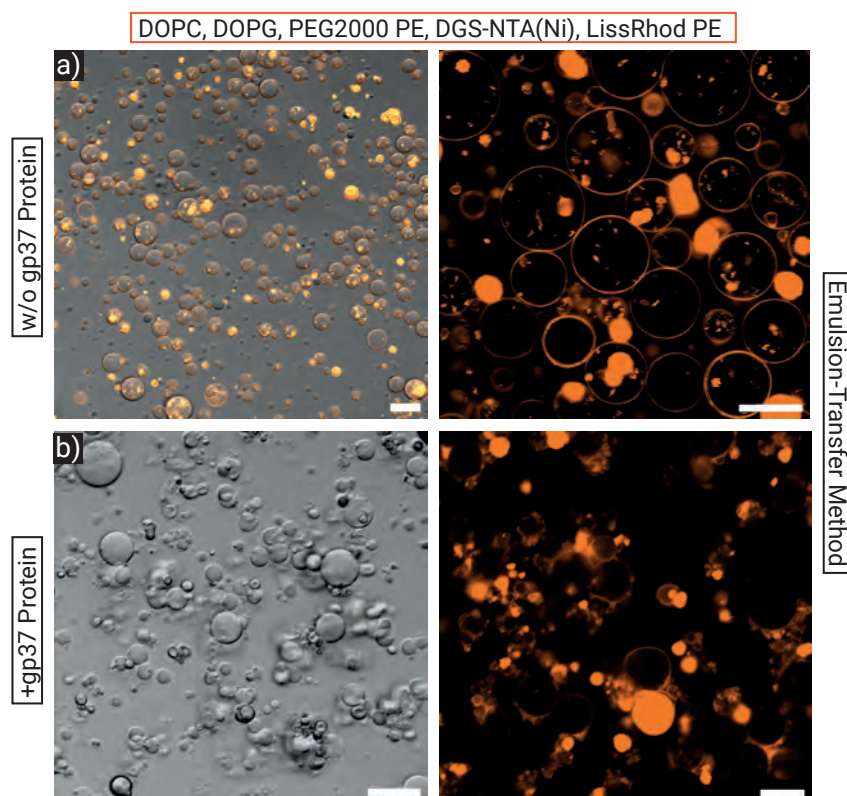


Figure 7-13: CLSM images of fluorescently labeled GUVs (formed via emulsion-transfer method) before (a-b) and after (c-d) the addition of His-gp37 (250 nM). Scale bar: a) and c): 20 μm , b) and d): 10 μm .

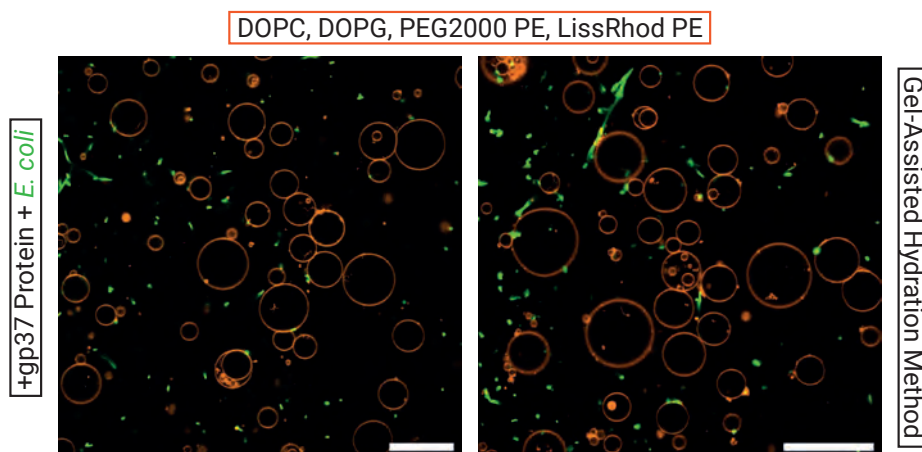


Figure 7-14: CLSM micrographs of fluorescently labeled GUVs (orange) mixed with adhesion protein His-gp37 (250 nM) and *E. coli* (green). No anchor lipids were integrated into the GUVs, formed via the gel-assisted hydration method. This resulted in the absence of specific bacteria binding to the GUVs. Scale bars: 50 μm .

7.2 Publications

Articles

- 1) Conzelmann, N. F.; Benimeli Borràs, A.; Muduli, S.; Schramm, A.; Jeschenko, P. M.; Platzman, I.; Spatz, J. P., *Modular Porous Polymer-Based Microcapsules for Trapping and Near-Infrared Light-Triggered Killing of Bacteria via Gold Nanorods*. ACS Applied Nano Materials **2024**. DOI: 10.1021/acsnm.4c03636.
- 2) Conzelmann, N. F.; Gelmroth A.-K.; Schramm, A.; Platzman, I.; Spatz, J. P. *Adhesion Mediated Engulfment and Killing of Bacteria by Synthetic Vesicles*, manuscript in preparation.

Presentations

- 1) Conzelmann, N. F.; Luo, R.; Pashapour, S.; Platzman, I.; Spatz, J. P., *Poröse, polymerbasierte Mikrokapseln als Bakterienfallen*, Conference ProMatLeben, online, **2021**.
- 2) Conzelmann, N. F.; Platzman, I.; Spatz, J. P., Gleiche, M.; Tenbusch, J.; Rahimzadeh, M.; Möller, M.; Andreeva, T.; Krastev, R.; Kemkemer, R.; Bargon, R.; Weik, T.; Merckle, C.; Henke, M.; *Erforschung räumlich getrennter „on demand“ multifunktionaler Polymerkompartimente für Anwendungen im Bereich antibakterieller und einheilungsfördernder Implantatbeschichtungen*, Conference ProMatLeben, Frankfurt am Main, Germany, **2022**.
- 3) Conzelmann, N. F.; Platzman, I.; Spatz, J. P., *Design of Porous Polymer-Based Microcapsules for Antibacterial Applications*, SynCell, Minneapolis, USA, **2023**.

Posters

- 1) Conzelmann, N. F.; Luo, R.; Pashapour, S.; Platzman, I.; Spatz, J. P., *Poröse, polymerbasierte Mikrokapseln als Bakterienfallen*, Conference ProMatLeben, online, **2021**.

7.3 Bibliography

- (1) Murray, P. R.; Rosenthal, K. S.; Pfaller, M. A. *Medical microbiology*; Elsevier Health Sciences, **2015**.
- (2) Gupta, A.; Gupta, R.; Singh, R. L. Microbes and Environment. In *Principles and Applications of Environmental Biotechnology for a Sustainable Future*, 2017; pp 43-84.
- (3) Bruslind, L. *General microbiology*; Oregon State University, **2019**.
- (4) Doetsch, R. N.; Cook, T. M. *Introduction to bacteria and their ecobiology*; Springer Science & Business Media, **2012**.
- (5) Silhavy, T. J.; Kahne, D.; Walker, S. The bacterial cell envelope. *Cold Spring Harb. Perspect. Biol.* **2010**, *2* (5), a000414. DOI: 10.1101/cshperspect.a000414.
- (6) Palma, V.; Gutierrez, M. S.; Vargas, O.; Parthasarathy, R.; Navarrete, P. Methods to Evaluate Bacterial Motility and Its Role in Bacterial-Host Interactions. *Microorganisms* **2022**, *10* (3). DOI: 10.3390/microorganisms10030563.
- (7) Kim, M. J.; Breuer, K. S. Enhanced diffusion due to motile bacteria. *Phys. Fluids* **2004**, *16* (9), L78-L81. DOI: 10.1063/1.1787527.
- (8) Samad, T.; Billings, N.; Birjiniuk, A.; Crouzier, T.; Doyle, P. S.; Ribbeck, K. Swimming bacteria promote dispersal of non-motile staphylococcal species. *The ISME Journal* **2017**, *11* (8), 1933-1937. DOI: 10.1038/ismej.2017.23.
- (9) Davin-Regli, A.; Lavigne, J. P.; Pagès, J. M. Enterobacter spp.: Update on Taxonomy, Clinical Aspects, and Emerging Antimicrobial Resistance. *Clin. Microbiol. Rev.* **2019**, *32* (4). DOI: 10.1128/cmr.00002-19.
- (10) Ramos, Y.; Rocha, J.; Hael, A. L.; van Gestel, J.; Vlamakis, H.; Cywes-Bentley, C.; Cubillos-Ruiz, J. R.; Pier, G. B.; Gilmore, M. S.; Kolter, R.; et al. PolyGlcNAc-containing exopolymers enable surface penetration by non-motile *Enterococcus faecalis*. *PLoS Pathog.* **2019**, *15* (2), e1007571. DOI: 10.1371/journal.ppat.1007571.
- (11) Ashurst, J. V.; Dawson, A. Klebsiella Pneumonia. In *StatPearls*, StatPearls Publishing, 2024.
- (12) Howard, A.; O'Donoghue, M.; Feeney, A.; Sleator, R. D. *Acinetobacter baumannii*: an emerging opportunistic pathogen. *Virulence* **2012**, *3* (3), 243-250. DOI: 10.4161/viru.19700.

- (13) Zhao, A.; Sun, J.; Liu, Y. Understanding bacterial biofilms: From definition to treatment strategies. *Front Cell Infect Microbiol* **2023**, *13*, 1137947. DOI: 10.3389/fcimb.2023.1137947.
- (14) Rather, M. A.; Gupta, K.; Mandal, M. Microbial biofilm: formation, architecture, antibiotic resistance, and control strategies. *Braz. J. Microbiol.* **2021**, *52* (4), 1701-1718. DOI: 10.1007/s42770-021-00624-x.
- (15) Berger, I.; Loewy, Z. G. Antimicrobial Resistance and Novel Alternative Approaches to Conventional Antibiotics. *Bacteria* **2024**, *3* (3), 171-182. DOI: 10.3390/bacteria3030012.
- (16) Collaborators, A. R. Global burden of bacterial antimicrobial resistance in 2019: a systematic analysis. *Lancet* **2022**, *399* (10325), 629-655. DOI: 10.1016/S0140-6736(21)02724-0.
- (17) Mancuso, G.; Midiri, A.; Gerace, E.; Biondo, C. Bacterial Antibiotic Resistance: The Most Critical Pathogens. *Pathogens* **2021**, *10* (10). DOI: 10.3390/pathogens10101310.
- (18) Kariuki, S. Global burden of antimicrobial resistance and forecasts to 2050. *Lancet* **2024**, *404* (10459), 1172-1173. DOI: 10.1016/S0140-6736(24)01885-3.
- (19) Russell, A. D. Antibiotic and biocide resistance in bacteria: Introduction. *J. Appl. Microbiol.* **2002**, *92* (s1), 1S-3S. DOI: 10.1046/j.1365-2672.92.5s1.14.x.
- (20) Cao, Y.; Naseri, M.; He, Y.; Xu, C.; Walsh, L. J.; Ziora, Z. M. Non-antibiotic antimicrobial agents to combat biofilm-forming bacteria. *Journal of Global Antimicrobial Resistance* **2020**, *21*, 445-451. DOI: 10.1016/j.jgar.2019.11.012.
- (21) Sarkar, T.; Chetia, M.; Chatterjee, S. Antimicrobial Peptides and Proteins: From Nature's Reservoir to the Laboratory and Beyond. *Front Chem* **2021**, *9*, 691532. DOI: 10.3389/fchem.2021.691532.
- (22) Ranveer, S. A.; Dasriya, V.; Ahmad, M. F.; Dhillon, H. S.; Samtiya, M.; Shama, E.; Anand, T.; Dhewa, T.; Chaudhary, V.; Chaudhary, P.; et al. Positive and negative aspects of bacteriophages and their immense role in the food chain. *NPJ Sci Food* **2024**, *8* (1), 1. DOI: 10.1038/s41538-023-00245-8.
- (23) Brives, C.; Pourraz, J. Phage therapy as a potential solution in the fight against AMR: obstacles and possible futures. *Palgrave Communications* **2020**, *6* (1). DOI: 10.1057/s41599-020-0478-4.

-
- (24) Sanz-Gaitero, M.; Seoane-Blanco, M.; van Raaij, M. J. Structure and Function of Bacteriophages. In *Bacteriophages: Biology, Technology, Therapy*, Harper, D. R., Abedon, S. T., Burrowes, B. H., McConville, M. L. Eds.; Springer International Publishing, 2021; pp 19-91.
- (25) Kasman, L. M.; Porter, L. D. Bacteriophages. In *StatPearls*, StatPearls Publishing, 2024.
- (26) Schmelcher, M.; Donovan, D. M.; Loessner, M. J. Bacteriophage endolysins as novel antimicrobials. *Future Microbiol.* **2012**, *7* (10), 1147-1171. DOI: 10.2217/fmb.12.97.
- (27) Lin, D. M.; Koskella, B.; Lin, H. C. Phage therapy: An alternative to antibiotics in the age of multi-drug resistance. *World J. Gastrointest. Pharmacol. Ther.* **2017**, *8* (3), 162-173. DOI: 10.4292/wjgpt.v8.i3.162.
- (28) Bartual, S. G.; Garcia-Doval, C.; Alonso, J.; Schoehn, G.; van Raaij, M. J. Two-chaperone assisted soluble expression and purification of the bacteriophage T4 long tail fibre protein gp37. *Protein Expr. Purif.* **2010**, *70* (1), 116-121. DOI: 10.1016/j.pep.2009.11.005.
- (29) Brzozowska, E.; Lesniewski, A.; Sek, S.; Wieneke, R.; Tampe, R.; Gorska, S.; Jonsson-Niedziolka, M.; Niedziolka-Jonsson, J. Interactions of bacteriophage T4 adhesin with selected lipopolysaccharides studied using atomic force microscopy. *Sci. Rep.* **2018**, *8* (1), 10935. DOI: 10.1038/s41598-018-29383-w.
- (30) Islam, M.; Fokine, A.; Mahalingam, M.; Zhang, Z.; Garcia-Doval, C.; van Raaij, M.; Rossmann, M.; Rao, V. Molecular anatomy of the receptor binding module of a bacteriophage long tail fiber. *PLoS Pathog.* **2019**, *15*, e1008193. DOI: 10.1371/journal.ppat.1008193.
- (31) Bonilla-Gameros, L.; Chevallier, P.; Sarkissian, A.; Mantovani, D. Silver-based antibacterial strategies for healthcare-associated infections: Processes, challenges, and regulations. An integrated review. *Nanomedicine* **2020**, *24*, 102142. DOI: 10.1016/j.nano.2019.102142.
- (32) Cloutier, M.; Mantovani, D.; Rosei, F. Antibacterial Coatings: Challenges, Perspectives, and Opportunities. *Trends Biotechnol.* **2015**, *33* (11), 637-652. DOI: 10.1016/j.tibtech.2015.09.002.
- (33) Ul Haq, I.; Khan, T. A.; Krukiewicz, K. Etiology, pathology, and host-impaired immunity in medical implant-associated infections. *J Infect Public Health* **2024**, *17* (2), 189-203. DOI: 10.1016/j.jiph.2023.11.024.

- (34) Oliva, A.; Miele, M. C.; Al Ismail, D.; Di Timoteo, F.; De Angelis, M.; Rosa, L.; Cutone, A.; Venditti, M.; Mascellino, M. T.; Valenti, P.; et al. Challenges in the Microbiological Diagnosis of Implant-Associated Infections: A Summary of the Current Knowledge. *Front. Microbiol.* **2021**, *12*, 750460. DOI: 10.3389/fmicb.2021.750460.
- (35) Maimaiti, Z.; Li, Z.; Xu, C.; Fu, J.; Hao, L. B.; Chen, J. Y.; Chai, W. Host Immune Regulation in Implant-Associated Infection (IAI): What Does the Current Evidence Provide Us to Prevent or Treat IAI? *Bioengineering (Basel)* **2023**, *10* (3). DOI: 10.3390/bioengineering10030356.
- (36) Ates, B.; Koytepe, S.; Balcioglu, S.; Ulu, A.; Gurses, C. Biomedical applications of hybrid polymer composite materials. In *Hybrid Polymer Composite Materials*, Thakur, V. K., Thakur, M. K., Pappu, A. Eds.; Woodhead Publishing, 2017; pp 343-408.
- (37) Kandi, V.; Vadakedath, S. Implant-Associated Infections: A Review of the Safety of Cardiac Implants. *Cureus* **2020**, *12* (12), e12267. DOI: 10.7759/cureus.12267.
- (38) Israelachvili, J. N. *Intermolecular and Surface Forces*; Elsevier, **2011**. DOI: 10.1016/b978-0-12-391927-4.10003-9.
- (39) Morhardt, D. R.; Mauney, J. R.; Estrada, C. R. Role of Biomaterials in Surgery. In *Encyclopedia of Tissue Engineering and Regenerative Medicine*, Reis, R. L. Ed.; Academic Press, 2019; pp 315-330.
- (40) Bergmann, C. P.; Stumpf, A. Biomaterials. In *Dental Ceramics: Microstructure, Properties and Degradation*, Bergmann, C., Stumpf, A. Eds.; Springer Berlin Heidelberg, 2013; pp 9-13.
- (41) Ratner, B. D.; Bryant, S. J. Biomaterials: where we have been and where we are going. *Annu. Rev. Biomed. Eng.* **2004**, *6*, 41-75. DOI: 10.1146/annurev.bioeng.6.040803.140027.
- (42) Kaur, R.; Liu, S. Antibacterial surface design – Contact kill. *Prog. Surf. Sci.* **2016**, *91* (3), 136-153. DOI: 10.1016/j.progsurf.2016.09.001.
- (43) Olmo, J. A.-D.; Ruiz-Rubio, L.; Pérez-Alvarez, L.; Sáez-Martínez, V.; Vilas-Vilela, J. L. Antibacterial Coatings for Improving the Performance of Biomaterials. *Coatings* **2020**, *10* (2). DOI: 10.3390/coatings10020139.

-
- (44) Liu, Y.; Xiao, Y.; Cao, Y.; Guo, Z.; Li, F.; Wang, L. Construction of Chitosan-Based Hydrogel Incorporated with Antimonene Nanosheets for Rapid Capture and Elimination of Bacteria. *Adv. Funct. Mater.* **2020**, *30* (35). DOI: 10.1002/adfm.202003196.
- (45) Dsouza, A.; Constantinidou, C.; Arvanitis, T. N.; Haddleton, D. M.; Charmet, J.; Hand, R. A. Multifunctional Composite Hydrogels for Bacterial Capture, Growth/Elimination, and Sensing Applications. *ACS Appl. Mater. Interfaces.* **2022**, *14* (42), 47323-47344. DOI: 10.1021/acsami.2c08582.
- (46) Huang, K.; Liu, W.; Wei, W.; Zhao, Y.; Zhuang, P.; Wang, X.; Wang, Y.; Hu, Y.; Dai, H. Photothermal Hydrogel Encapsulating Intelligently Bacteria-Capturing Bio-MOF for Infectious Wound Healing. *ACS Nano* **2022**, *16* (11), 19491-19508. DOI: 10.1021/acsnano.2c09593.
- (47) Avila-Sierra, A.; Moreno, J. A.; Goode, K.; Zhu, T.; Fryer, P. J.; Taylor, A.; Zhang, Z. J. Effects of structural and chemical properties of surface coatings on the adsorption characteristics of proteins. *Surf. Coat. Technol.* **2023**, *452*. DOI: 10.1016/j.surfcoat.2022.129054.
- (48) Zhang, Z.; Wagner, V. E. E. *Antimicrobial Coatings and Modifications on Medical Devices*; Springer International Publishing, **2017**. DOI: 10.1007/978-3-319-57494-3.
- (49) Akay, S.; Yagmur, A. Recent Advances in Antibacterial Coatings to Combat Orthopedic Implant-Associated Infections. *Molecules* **2024**, *29* (5). DOI: 10.3390/molecules29051172.
- (50) Yang, X.; Zhang, W.; Qin, X.; Cui, M.; Guo, Y.; Wang, T.; Wang, K.; Shi, Z.; Zhang, C.; Li, W.; et al. Recent Progress on Bioinspired Antibacterial Surfaces for Biomedical Application. *Biomimetics (Basel)* **2022**, *7* (3). DOI: 10.3390/biomimetics7030088.
- (51) Li, Y.; Li, B.; Guo, X.; Wang, H.; Cheng, L. Applications of quaternary ammonium compounds in the prevention and treatment of oral diseases: State-of-the-art and future directions. *J. Dent.* **2023**, *137*, 104678. DOI: 10.1016/j.jdent.2023.104678.
- (52) Arnold, W. A.; Blum, A.; Branyan, J.; Bruton, T. A.; Carignan, C. C.; Cortopassi, G.; Datta, S.; DeWitt, J.; Doherty, A. C.; Halden, R. U.; et al. Quaternary Ammonium Compounds: A Chemical Class of Emerging Concern. *Environ Sci Technol* **2023**, *57* (20), 7645-7665. DOI: 10.1021/acs.est.2c08244.

- (53) Inacio, A. S.; Costa, G. N.; Domingues, N. S.; Santos, M. S.; Moreno, A. J.; Vaz, W. L.; Vieira, O. V. Mitochondrial dysfunction is the focus of quaternary ammonium surfactant toxicity to mammalian epithelial cells. *Antimicrob Agents Chemother* **2013**, *57* (6), 2631-2639. DOI: 10.1128/AAC.02437-12.
- (54) Peyneau, M.; Zeller, M.; Paulet, V.; Noel, B.; Damiens, M. H.; Szely, N.; Natsch, A.; Pallardy, M.; Chollet-Martin, S.; de Chaisemartin, L.; et al. Quaternary ammoniums activate human dendritic cells and induce a specific T-cell response in vitro. *Allergol Int* **2025**, *74* (1), 105-114. DOI: 10.1016/j.alit.2024.07.003.
- (55) Sanchez-Lopez, E.; Gomes, D.; Esteruelas, G.; Bonilla, L.; Lopez-Machado, A. L.; Galindo, R.; Cano, A.; Espina, M.; Ettcheto, M.; Camins, A.; et al. Metal-Based Nanoparticles as Antimicrobial Agents: An Overview. *Nanomaterials (Basel)* **2020**, *10* (2). DOI: 10.3390/nano10020292.
- (56) Katti, D. S.; Robinson, K. W.; Ko, F. K.; Laurencin, C. T. Bioresorbable nanofiber-based systems for wound healing and drug delivery: optimization of fabrication parameters. *J. Biomed. Mater. Res. B Appl. Biomater.* **2004**, *70* (2), 286-296. DOI: 10.1002/jbm.b.30041.
- (57) Schnieders, J.; Gbureck, U.; Thull, R.; Kissel, T. Controlled release of gentamicin from calcium phosphate-poly(lactic acid-co-glycolic acid) composite bone cement. *Biomaterials* **2006**, *27* (23), 4239-4249. DOI: 10.1016/j.biomaterials.2006.03.032.
- (58) Arif, M. A review on copper nanoparticles loaded in smart microgels. *Materials Today Communications* **2023**, *36*. DOI: 10.1016/j.mtcomm.2023.106580.
- (59) de Almeida Campos, L. A.; de Souza, J. B.; de Queiroz Macedo, H. L. R.; Borges, J. C.; de Oliveira, D. N.; Cavalcanti, I. M. F. Synthesis of polymeric nanoparticles by double emulsion and pH-driven: encapsulation of antibiotics and natural products for combating *Escherichia coli* infections. *Appl Microbiol Biotechnol* **2024**, *108* (1), 351. DOI: 10.1007/s00253-024-13114-5.
- (60) Jain, R. A. The manufacturing techniques of various drug loaded biodegradable poly(lactide-co-glycolide) (PLGA) devices. *Biomaterials* **2000**, *21* (23), 2475-2490. DOI: 10.1016/s0142-9612(00)00115-0.
- (61) Gasparini, G.; Kosvintsev, S. R.; Stillwell, M. T.; Holdich, R. G. Preparation and characterization of PLGA particles for subcutaneous controlled drug release by membrane emulsification. *Colloids Surf., B* **2008**, *61* (2), 199-207. DOI: 10.1016/j.colsurfb.2007.08.011.

-
- (62) He, X.; Yuan, Z.; Kao, W.; Miller, D.; Li, S. K.; Park, Y. C. Size-Exclusive Nanoporous Biodegradable PLGA Capsules for Drug Delivery Implants and In Vivo Stability in the Posterior Segment. *ACS Appl. Bio Mater.* **2020**, *3* (3), 1722-1729. DOI: 10.1021/acsabm.0c00027.
- (63) Lu, Y.; Cheng, D.; Niu, B.; Wang, X.; Wu, X.; Wang, A. Properties of Poly (Lactic-co-Glycolic Acid) and Progress of Poly (Lactic-co-Glycolic Acid)-Based Biodegradable Materials in Biomedical Research. *Pharmaceuticals (Basel)* **2023**, *16* (3). DOI: 10.3390/ph16030454.
- (64) Shi, X.; Sun, L.; Jiang, J.; Zhang, X.; Ding, W.; Gan, Z. Biodegradable polymeric microcarriers with controllable porous structure for tissue engineering. *Macromol. Biosci.* **2009**, *9* (12), 1211-1218. DOI: 10.1002/mabi.200900224.
- (65) Felix Lanao, R. P.; Jonker, A. M.; Wolke, J. G.; Jansen, J. A.; van Hest, J. C.; Leeuwenburgh, S. C. Physicochemical properties and applications of poly(lactic-co-glycolic acid) for use in bone regeneration. *Tissue Eng Part B Rev* **2013**, *19* (4), 380-390. DOI: 10.1089/ten.TEB.2012.0443.
- (66) Netti, P. A.; Biondi, M.; Frigione, M. Experimental Studies and Modeling of the Degradation Process of Poly(Lactic-co-Glycolic Acid) Microspheres for Sustained Protein Release. *Polymers (Basel)* **2020**, *12* (9). DOI: 10.3390/polym12092042.
- (67) Gentile, P.; Chiono, V.; Carmagnola, I.; Hatton, P. V. An overview of poly(lactic-co-glycolic) acid (PLGA)-based biomaterials for bone tissue engineering. *Int. J. Mol. Sci.* **2014**, *15* (3), 3640-3659. DOI: 10.3390/ijms15033640.
- (68) Kapoor, D. N.; Bhatia, A.; Kaur, R.; Sharma, R.; Kaur, G.; Dhawan, S. PLGA: a unique polymer for drug delivery. *Ther. Deliv.* **2015**, *6* (1), 41-58.
- (69) Makadia, H. K.; Siegel, S. J. Poly Lactic-co-Glycolic Acid (PLGA) as Biodegradable Controlled Drug Delivery Carrier. *Polymers (Basel)* **2011**, *3* (3), 1377-1397. DOI: 10.3390/polym3031377.
- (70) Butreddy, A.; Gaddam, R. P.; Kommineni, N.; Dudhipala, N.; Voshavar, C. PLGA/PLA-Based Long-Acting Injectable Depot Microspheres in Clinical Use: Production and Characterization Overview for Protein/Peptide Delivery. *Int. J. Mol. Sci.* **2021**, *22* (16), 8884. DOI: 10.3390/ijms22168884.
- (71) Pitto-Barry, A.; Barry, N. P. E. Pluronic® block-copolymers in medicine: from chemical and biological versatility to rationalisation and clinical advances. *Polymer Chemistry* **2014**, *5* (10), 3291-3297. DOI: 10.1039/c4py00039k.

- (72) Kim, H. K.; Chung, H. J.; Park, T. G. Biodegradable polymeric microspheres with "open/closed" pores for sustained release of human growth hormone. *Journal of Controlled Release* **2006**, *112* (2), 167-174. DOI: 10.1016/j.jconrel.2006.02.004.
- (73) de Freitas, C. F.; de Araujo Santos, J.; Pellosi, D. S.; Caetano, W.; Batistela, V. R.; Muniz, E. C. Recent advances of Pluronic-based copolymers functionalization in biomedical applications. *Biomater Adv* **2023**, *151*, 213484. DOI: 10.1016/j.bioadv.2023.213484.
- (74) Kim, H.; Park, H.; Lee, J.; Kim, T. H.; Lee, E. S.; Oh, K. T.; Lee, K. C.; Youn, Y. S. Highly porous large poly(lactic-co-glycolic acid) microspheres adsorbed with palmityl-acylated exendin-4 as a long-acting inhalation system for treating diabetes. *Biomaterials* **2011**, *32* (6), 1685-1693. DOI: 10.1016/j.biomaterials.2010.10.045.
- (75) Knop, K.; Hoogenboom, R.; Fischer, D.; Schubert, U. S. Poly(ethylene glycol) in drug delivery: pros and cons as well as potential alternatives. *Angew Chem Int Ed Engl* **2010**, *49* (36), 6288-6308. DOI: 10.1002/anie.200902672.
- (76) D'Souza A, A.; Shegokar, R. Polyethylene glycol (PEG): a versatile polymer for pharmaceutical applications. *Expert Opin Drug Deliv* **2016**, *13* (9), 1257-1275. DOI: 10.1080/17425247.2016.1182485.
- (77) Liu, G.; Li, Y.; Yang, L.; Wei, Y.; Wang, X.; Wang, Z.; Tao, L. Cytotoxicity study of polyethylene glycol derivatives. *RSC Advances* **2017**, *7* (30), 18252-18259. DOI: 10.1039/c7ra00861a.
- (78) Harris, J. M. E. *Poly(Ethylene Glycol) Chemistry: Biotechnical and Biomedical Applications*; Springer Science & Business Media, **1992**.
- (79) Badiger, M. V.; McNeill, M. E.; Graham, N. B. Porogens in the preparation of microporous hydrogels based on poly(ethylene oxides). *Biomaterials* **1993**, *14* (14), 1059-1063. DOI: 10.1016/0142-9612(93)90206-h.
- (80) Lin, Y.-C.; Tseng, H.-H.; Wang, D. K. Uncovering the effects of PEG porogen molecular weight and concentration on ultrafiltration membrane properties and protein purification performance. *J. Membr. Sci.* **2021**, *616*, 118729. DOI: 10.1016/j.memsci.2020.118729.
- (81) Mansour, F. R.; Waheed, S.; Paull, B.; Maya, F. Porogens and porogen selection in the preparation of porous polymer monoliths. *J. Sep. Sci.* **2020**, *43* (1), 56-69. DOI: 10.1002/jssc.201900876.

-
- (82) Thananukul, K.; Kaewsaneha, C.; Opaprakasit, P.; Lebaz, N.; Errachid, A.; Elaissari, A. Smart gating porous particles as new carriers for drug delivery. *Adv Drug Deliv Rev* **2021**, *174*, 425-446. DOI: 10.1016/j.addr.2021.04.023.
- (83) Kim, D.-Y.; Jin, S. H.; Jeong, S.-G.; Lee, B.; Kang, K.-K.; Lee, C.-S. Microfluidic preparation of monodisperse polymeric microspheres coated with silica nanoparticles. *Sci. Rep.* **2018**, *8* (1), 8525. DOI: 10.1038/s41598-018-26829-z.
- (84) Amanatchi, N.; Bihi, I.; Briet, M.; Stichelmans, J.; Malsche, W. D.; Hellemans, K. H. Advanced microfluidic techniques for in situ PLGA microparticle formation: A dynamic solvent extraction approach. *Colloids Surf., A* **2024**, *701*, 134885. DOI: 10.1016/j.colsurfa.2024.134885.
- (85) Mao, X.; Wang, M.; Jin, S.; Rao, J.; Deng, R.; Zhu, J. Monodispersed polymer particles with tunable surface structures: Droplet microfluidic-assisted fabrication and biomedical applications. *J. Polym. Sci.* **2022**, *60* (11), 1653-1669. DOI: 10.1002/pol.20210909.
- (86) Astete, C. E.; Sabliov, C. M. Synthesis and characterization of PLGA nanoparticles. *J. Biomater. Sci. Polym. Ed.* **2006**, *17* (3), 247-289. DOI: 10.1163/156856206775997322.
- (87) Operti, M. C.; Bernhardt, A.; Grimm, S.; Engel, A.; Figdor, C. G.; Tagit, O. PLGA-based nanomedicines manufacturing: Technologies overview and challenges in industrial scale-up. *Int. J. Pharm.* **2021**, *605*, 120807. DOI: 10.1016/j.ijpharm.2021.120807.
- (88) Krishnaswamy, K.; Orsat, V. Sustainable Delivery Systems Through Green Nanotechnology. In *Nano- and Microscale Drug Delivery Systems*, 2017; pp 17-32.
- (89) Al Jahdaly, B. A.; Elsadek, M. F.; Ahmed, B. M.; Farahat, M. F.; Taher, M. M.; Khalil, A. M. Outstanding Graphene Quantum Dots from Carbon Source for Biomedical and Corrosion Inhibition Applications: A Review. *Sustainability* **2021**, *13* (4). DOI: 10.3390/su13042127.
- (90) Cohen-Sela, E.; Chorny, M.; Koroukhov, N.; Danenberg, H. D.; Golomb, G. A new double emulsion solvent diffusion technique for encapsulating hydrophilic molecules in PLGA nanoparticles. *J. Control. Release* **2009**, *133* (2), 90-95. DOI: 10.1016/j.jconrel.2008.09.073.

- (91) Hernández-Giottonini, K. Y.; Rodríguez-Córdova, R. J.; Gutiérrez-Valenzuela, C. A.; Peñuñuri-Miranda, O.; Zavala-Rivera, P.; Guerrero-Germán, P.; Lucero-Acuña, A. PLGA nanoparticle preparations by emulsification and nanoprecipitation techniques: effects of formulation parameters. *RSC Advances* **2020**, *10* (8), 4218-4231. DOI: 10.1039/c9ra10857b.
- (92) Ramli, R. A. Hollow polymer particles: a review. *RSC Advances* **2017**, *7* (83), 52632-52650. DOI: 10.1039/c7ra10358a.
- (93) Zhang, Z.; Deng, J.; Sui, J.; Yu, L.; Wan, M.; Wei, Y. Hollow Microstructured Polyaniline Prepared Using Cuprous Oxide Crystals as Templates. *Macromolecular Chemistry and Physics* **2006**, *207* (8), 763-769. DOI: 10.1002/macp.200600007.
- (94) Jang, J.; Ha, H. Fabrication of Hollow Polystyrene Nanospheres in Microemulsion Polymerization Using Triblock Copolymers. *Langmuir* **2002**, *18* (14), 5613-5618. DOI: 10.1021/la0257283.
- (95) Wong, M. S.; Cha, J. N.; Choi, K.-S.; Deming, T. J.; Stucky, G. D. Assembly of Nanoparticles into Hollow Spheres Using Block Copolypeptides. *Nano Lett.* **2002**, *2* (6), 583-587. DOI: 10.1021/nl020244c.
- (96) Salvador-Morales, C.; Brahmhatt, B.; Marquez-Miranda, V.; Araya-Duran, I.; Canan, J.; Gonzalez-Nilo, F.; Vilos, C.; Cebral, J.; Mut, F.; Lohner, R.; et al. Mechanistic Studies on the Self-Assembly of PLGA Patchy Particles and Their Potential Applications in Biomedical Imaging. *Langmuir* **2016**, *32* (31), 7929-7942. DOI: 10.1021/acs.langmuir.6b02177.
- (97) Narayan, P.; Marchant, D.; Wheatley, M. A. Optimization of spray drying by factorial design for production of hollow microspheres for ultrasound imaging. *J Biomed Mater Res* **2001**, *56* (3), 333-341. DOI: 10.1002/1097-4636(20010905)56:3<333::aid-jbm1101>3.0.co;2-k.
- (98) Iqbal, M.; Zafar, N.; Fessi, H.; Elaissari, A. Double emulsion solvent evaporation techniques used for drug encapsulation. *Int. J. Pharm.* **2015**, *496* (2), 173-190. DOI: 10.1016/j.ijpharm.2015.10.057.
- (99) Stucki, M.; Loepfe, M.; Stark, W. J. Porous Polymer Membranes by Hard Templating – A Review. *Adv. Eng. Mater.* **2017**, *20* (1). DOI: 10.1002/adem.201700611.
- (100) Li, X.; Bai, C.; Qiao, Y.; Wang, X.; Yang, K.; Colombo, P. Preparation, properties and applications of fly ash-based porous geopolymers: A review. *Journal of Cleaner Production* **2022**, *359*. DOI: 10.1016/j.jclepro.2022.132043.

-
- (101) Eriksson, V.; Edegran, S.; Croy, M.; Evenas, L.; Andersson Trojer, M. A unified thermodynamic and kinetic approach for prediction of microcapsule morphologies. *J. Colloid Interface Sci.* **2024**, *662*, 572-582. DOI: 10.1016/j.jcis.2024.01.191.
- (102) Bozzuto, G.; Molinari, A. Liposomes as nanomedical devices. *Int J Nanomedicine* **2015**, *10*, 975-999. DOI: 10.2147/IJN.S68861.
- (103) Jesorka, A.; Orwar, O. Liposomes: technologies and analytical applications. *Annu. Rev. Anal. Chem. (Palo Alto Calif.)* **2008**, *1*, 801-832. DOI: 10.1146/annurev.anchem.1.031207.112747.
- (104) Rideau, E.; Dimova, R.; Schwille, P.; Wurm, F. R.; Landfester, K. Liposomes and polymersomes: a comparative review towards cell mimicking. *Chem. Soc. Rev.* **2018**, *47* (23), 8572-8610. DOI: 10.1039/c8cs00162f.
- (105) Gopfrich, K.; Haller, B.; Staufer, O.; Dreher, Y.; Mersdorf, U.; Platzman, I.; Spatz, J. P. One-Pot Assembly of Complex Giant Unilamellar Vesicle-Based Synthetic Cells. *ACS Synth. Biol.* **2019**, *8* (5), 937-947. DOI: 10.1021/acssynbio.9b00034.
- (106) Lu, Y.; Allegri, G.; Huskens, J. Vesicle-based artificial cells: materials, construction methods and applications. *Mater Horiz* **2022**, *9* (3), 892-907. DOI: 10.1039/d1mh01431e.
- (107) Patil, Y. P.; Jadhav, S. Novel methods for liposome preparation. *Chem Phys Lipids* **2014**, *177*, 8-18. DOI: 10.1016/j.chemphyslip.2013.10.011.
- (108) Weiss, M.; Frohnmayer, J. P.; Benk, L. T.; Haller, B.; Janiesch, J. W.; Heitkamp, T.; Borsch, M.; Lira, R. B.; Dimova, R.; Lipowsky, R.; et al. Sequential bottom-up assembly of mechanically stabilized synthetic cells by microfluidics. *Nature Materials* **2018**, *17* (1), 89-96. DOI: 10.1038/nmat5005.
- (109) Meinel, A.; Trankle, B.; Romer, W.; Rohrbach, A. Induced phagocytic particle uptake into a giant unilamellar vesicle. *Soft Matter* **2014**, *10* (20), 3667-3678. DOI: 10.1039/c3sm52964a.
- (110) Sharma, V.; Marques, C. M.; Stocco, A. Driven Engulfment of Janus Particles by Giant Vesicles in and out of Thermal Equilibrium. *Nanomaterials (Basel)* **2022**, *12* (9). DOI: 10.3390/nano12091434.
- (111) Bahrami, A.; Bahrami, A. H. Cooperative engulfment of nanoparticles by membranes and vesicles. *New Journal of Physics* **2024**, *26* (10). DOI: 10.1088/1367-2630/ad80b9.

- (112) Agudo-Canalejo, J.; Lipowsky, R. Critical Particle Sizes for the Engulfment of Nanoparticles by Membranes and Vesicles with Bilayer Asymmetry. *ACS Nano* **2015**, *9* (4), 3704–3720. DOI: 10.1021/acsnano.5b01285.
- (113) van der Wel, C.; Vahid, A.; Saric, A.; Idema, T.; Heinrich, D.; Kraft, D. J. Lipid membrane-mediated attraction between curvature inducing objects. *Sci. Rep.* **2016**, *6*, 32825. DOI: 10.1038/srep32825.
- (114) Azadbakht, A.; Meadowcroft, B.; Varkevisser, T.; Saric, A.; Kraft, D. J. Wrapping Pathways of Anisotropic Dumbbell Particles by Giant Unilamellar Vesicles. *Nano Lett.* **2023**, *23* (10), 4267-4273. DOI: 10.1021/acs.nanolett.3c00375.
- (115) Dimova, R.; Marques, C. *The giant vesicle book*; CRC Press, **2019**.
- (116) Strobl, F. G.; Seitz, F.; Westerhausen, C.; Reller, A.; Torrano, A. A.; Brauchle, C.; Wixforth, A.; Schneider, M. F. Intake of silica nanoparticles by giant lipid vesicles: influence of particle size and thermodynamic membrane state. *Beilstein J Nanotechnol* **2014**, *5*, 2468-2478. DOI: 10.3762/bjnano.5.256.
- (117) Kostina, N. Y.; Rahimi, K.; Xiao, Q.; Haraszti, T.; Dedisch, S.; Spatz, J. P.; Schwaneberg, U.; Klein, M. L.; Percec, V.; Moller, M.; et al. Membrane-Mimetic Dendrimersomes Engulf Living Bacteria via Endocytosis. *Nano Lett.* **2019**, *19* (8), 5732-5738. DOI: 10.1021/acs.nanolett.9b02349.
- (118) Lin, C. M.; Li, C. S.; Sheng, Y. J.; Wu, D. T.; Tsao, H. K. Size-dependent properties of small unilamellar vesicles formed by model lipids. *Langmuir* **2012**, *28* (1), 689-700. DOI: 10.1021/la203755v.
- (119) Zheng, J.; Cheng, X.; Zhang, H.; Bai, X.; Ai, R.; Shao, L.; Wang, J. Gold Nanorods: The Most Versatile Plasmonic Nanoparticles. *Chem Rev* **2021**, *121* (21), 13342-13453. DOI: 10.1021/acs.chemrev.1c00422.
- (120) Huang, X.; Neretina, S.; El-Sayed, M. A. Gold nanorods: from synthesis and properties to biological and biomedical applications. *Adv. Mater.* **2009**, *21* (48), 4880-4910. DOI: 10.1002/adma.200802789.
- (121) Cao, J.; Sun, T.; Grattan, K. T. V. Gold nanorod-based localized surface plasmon resonance biosensors: A review. *Sens. Actuators B Chem.* **2014**, *195*, 332-351. DOI: 10.1016/j.snb.2014.01.056.
- (122) Cui, X.; Ruan, Q.; Zhuo, X.; Xia, X.; Hu, J.; Fu, R.; Li, Y.; Wang, J.; Xu, H. Photothermal Nanomaterials: A Powerful Light-to-Heat Converter. *Chem Rev* **2023**, *123* (11), 6891-6952. DOI: 10.1021/acs.chemrev.3c00159.

-
- (123) Rayavarapu, R. G.; Petersen, W.; Hartsuiker, L.; Chin, P.; Janssen, H.; van Leeuwen, F. W.; Otto, C.; Manohar, S.; van Leeuwen, T. G. In vitro toxicity studies of polymer-coated gold nanorods. *Nanotechnology* **2010**, *21* (14), 145101. DOI: 10.1088/0957-4484/21/14/145101.
- (124) Jia, Y. P.; Shi, K.; Liao, J. F.; Peng, J. R.; Hao, Y.; Qu, Y.; Chen, L. J.; Liu, L.; Yuan, X.; Qian, Z. Y.; et al. Effects of Cetyltrimethylammonium Bromide on the Toxicity of Gold Nanorods Both In Vitro and In Vivo: Molecular Origin of Cytotoxicity and Inflammation. *Small Methods* **2020**, *4* (3). DOI: 10.1002/smt.201900799.
- (125) He, J.; Unser, S.; Bruzas, I.; Cary, R.; Shi, Z.; Mehra, R.; Aron, K.; Sagle, L. The facile removal of CTAB from the surface of gold nanorods. *Colloids Surf., B* **2018**, *163*, 140-145. DOI: 10.1016/j.colsurfb.2017.12.019.
- (126) Connor, E. E.; Mwamuka, J.; Gole, A.; Murphy, C. J.; Wyatt, M. D. Gold nanoparticles are taken up by human cells but do not cause acute cytotoxicity. *Small* **2005**, *1* (3), 325-327. DOI: 10.1002/sml.200400093.
- (127) Niidome, T.; Yamagata, M.; Okamoto, Y.; Akiyama, Y.; Takahashi, H.; Kawano, T.; Katayama, Y.; Niidome, Y. PEG-modified gold nanorods with a stealth character for in vivo applications. *Journal of Controlled Release* **2006**, *114* (3), 343-347. DOI: 10.1016/j.jconrel.2006.06.017.
- (128) Zhang, Z.; Lin, M. Fast loading of PEG-SH on CTAB-protected gold nanorods. *RSC Advances* **2014**, *4* (34). DOI: 10.1039/c3ra48061e.
- (129) Xu, X.; Ding, Y.; Hadianamrei, R.; Lv, S.; You, R.; Pan, F.; Zhang, P.; Wang, N.; Zhao, X. Antimicrobial peptide functionalized gold nanorods combining near-infrared photothermal therapy for effective wound healing. *Colloids Surf., B* **2022**, *220*, 112887. DOI: 10.1016/j.colsurfb.2022.112887.
- (130) Su, C.; Huang, K.; Li, H.-H.; Lu, Y.-G.; Zheng, D.-L.; Taglietti, A. Antibacterial Properties of Functionalized Gold Nanoparticles and Their Application in Oral Biology. *Journal of Nanomaterials* **2020**, *2020*, 1-13. DOI: 10.1155/2020/5616379.
- (131) Qiao, Z.; Yao, Y.; Song, S.; Yin, M.; Yang, M.; Yan, D.; Yang, L.; Luo, J. Gold nanorods with surface charge-switchable activities for enhanced photothermal killing of bacteria and eradication of biofilm. *J Mater Chem B* **2020**, *8* (15), 3138-3149. DOI: 10.1039/d0tb00298d.

- (132) Mutalik, C.; Saukani, M.; Khafid, M.; Krisnawati, D. I.; Widodo; Darmayanti, R.; Puspitasari, B.; Cheng, T. M.; Kuo, T. R. Gold-Based Nanostructures for Antibacterial Application. *Int. J. Mol. Sci.* **2023**, *24* (12). DOI: 10.3390/ijms241210006.
- (133) Al-Bakri, A. G.; Mahmoud, N. N. Photothermal-Induced Antibacterial Activity of Gold Nanorods Loaded into Polymeric Hydrogel against *Pseudomonas aeruginosa* Biofilm. *Molecules* **2019**, *24* (14). DOI: 10.3390/molecules24142661.
- (134) Ramasamy, M.; Zhu, Y.; Paik, U.; Yi, D. K. Synthesis and anti-bacterial activity of AuNRs–PS–MNPs. *Mater. Lett.* **2014**, *137*, 479-482. DOI: 10.1016/j.matlet.2014.09.059.
- (135) Gupta, R.; Sharma, S. Role of alternatives to antibiotics in mitigating the antimicrobial resistance crisis. *Indian J. Med. Res.* **2022**, *156* (3), 464-477. DOI: 10.4103/ijmr.IJMR_3514_20.
- (136) Luo, R.; Venkatraman, S. S.; Neu, B. Layer-by-Layer Polyelectrolyte–Polyester Hybrid Microcapsules for Encapsulation and Delivery of Hydrophobic Drugs. *Biomacromolecules* **2013**, *14* (7), 2262-2271. DOI: 10.1021/bm4003915.
- (137) Mbalaha, Z. S.; Edwards, P. R.; Birch, D. J. S.; Chen, Y. Synthesis of Small Gold Nanorods and Their Subsequent Functionalization with Hairpin Single Stranded DNA. *ACS Omega* **2019**, *4* (9), 13740-13746. DOI: 10.1021/acsomega.9b01200.
- (138) Hu, Z. J.; Hou, S.; Ji, Y. L.; Wen, T.; Liu, W. Q.; Zhang, H.; Shi, X. W.; Yan, J.; Wu, X. C. Fast characterization of gold nanorods ensemble by correlating its structure with optical extinction spectral features. *AIP Adv.* **2014**, *4* (11), 117137. DOI: 10.1063/1.4903163.
- (139) Weinberger, A.; Tsai, F. C.; Koenderink, G. H.; Schmidt, T. F.; Itri, R.; Meier, W.; Schmatko, T.; Schroder, A.; Marques, C. Gel-assisted formation of giant unilamellar vesicles. *Biophys. J.* **2013**, *105* (1), 154-164. DOI: 10.1016/j.bpj.2013.05.024.
- (140) Lagreca, E.; Onesto, V.; Di Natale, C.; La Manna, S.; Netti, P. A.; Vecchione, R. Recent advances in the formulation of PLGA microparticles for controlled drug delivery. *Progress in Biomaterials* **2020**, *9* (4), 153-174. DOI: 10.1007/s40204-020-00139-y.
- (141) Ding, X.; Wang, A.; Tong, W.; Xu, F. J. Biodegradable Antibacterial Polymeric Nanosystems: A New Hope to Cope with Multidrug-Resistant Bacteria. *Small* **2019**, *15* (20), e1900999. DOI: 10.1002/sml.201900999.

-
- (142) Shakya, A. K.; Al-Sulaibi, M.; Naik, R. R.; Nsairat, H.; Suboh, S.; Abulaila, A. Review on PLGA Polymer Based Nanoparticles with Antimicrobial Properties and Their Application in Various Medical Conditions or Infections. *Polymers (Basel)* **2023**, *15* (17). DOI: 10.3390/polym15173597.
- (143) Rezvantalab, S.; Drude, N. I.; Moraveji, M. K.; Guvener, N.; Koons, E. K.; Shi, Y.; Lammers, T.; Kiessling, F. PLGA-Based Nanoparticles in Cancer Treatment. *Front. Pharmacol.* **2018**, *9*, 1260. DOI: 10.3389/fphar.2018.01260.
- (144) Yang, J.; Lee, C.-H.; Park, J.; Seo, S.; Lim, E.-K.; Song, Y. J.; Suh, J.-S.; Yoon, H.-G.; Huh, Y.-M.; Haam, S. Antibody conjugated magnetic PLGA nanoparticles for diagnosis and treatment of breast cancer. *J. Mater. Chem.* **2007**, *17* (26). DOI: 10.1039/b702538f.
- (145) Emami, F.; Mostafavi Yazdi, S. J.; Na, D. H. Poly(lactic acid)/poly(lactic-co-glycolic acid) particulate carriers for pulmonary drug delivery. *Journal of Pharmaceutical Investigation* **2019**, *49* (4), 427-442. DOI: 10.1007/s40005-019-00443-1.
- (146) Yang, Y.; Bajaj, N.; Xu, P.; Ohn, K.; Tsifansky, M. D.; Yeo, Y. Development of highly porous large PLGA microparticles for pulmonary drug delivery. *Biomaterials* **2009**, *30* (10), 1947-1953. DOI: 10.1016/j.biomaterials.2008.12.044.
- (147) Levin, P. A.; Angert, E. R. Small but Mighty: Cell Size and Bacteria. *Cold Spring Harb. Perspect. Biol.* **2015**, *7* (7), a019216. DOI: 10.1101/cshperspect.a019216.
- (148) Yahav, G.; Pawar, S.; Lipovsky, A.; Gupta, A.; Gedanken, A.; Duadi, H.; Fixler, D. Probing Polarity and pH Sensitivity of Carbon Dots in Escherichia coli through Time-Resolved Fluorescence Analyses. *Nanomaterials* **2023**, *13* (14), 2068. DOI: 10.3390/nano13142068.
- (149) Amoyav, B.; Benny, O. Microfluidic Based Fabrication and Characterization of Highly Porous Polymeric Microspheres. *Polymers (Basel)* **2019**, *11* (3), 419. DOI: 10.3390/polym11030419.
- (150) Alkholief, M.; Kalam, M. A.; Anwer, M. K.; Alshamsan, A. Effect of Solvents, Stabilizers and the Concentration of Stabilizers on the Physical Properties of Poly(d,l-lactide-co-glycolide) Nanoparticles: Encapsulation, In Vitro Release of Indomethacin and Cytotoxicity against HepG2-Cell. *Pharmaceutics* **2022**, *14* (4). DOI: 10.3390/pharmaceutics14040870.

- (151) Song, K. C.; Lee, H. S.; Choung, I. Y.; Cho, K. I.; Ahn, Y.; Choi, E. J. The effect of type of organic phase solvents on the particle size of poly(d,l-lactide-co-glycolide) nanoparticles. *Colloids Surf., A* **2006**, *276* (1-3), 162-167. DOI: 10.1016/j.colsurfa.2005.10.064.
- (152) Ramchandani, M.; Pankaskie, M.; Robinson, D. The influence of manufacturing procedure on the degradation of poly(lactide-co-glycolide) 8515 and 5050 implants. *Journal of Controlled Release* **1997**, *43* (2-3), 161–173. DOI: 10.1016/s0168-3659(96)01481-2.
- (153) *Pure Organic Liquids*; Springer-Verlag, **2002**. DOI: 10.1007/b68240.
- (154) Company, M. C. 3M(TM) NOVEC(TM)7500 ENGINEERED FLUID. 11.00 ed.; Company, M. C., Ed.; 2021.
- (155) Riess, J. G. Oxygen Carriers (“Blood Substitutes”)Raison d’Etre, Chemistry, and Some PhysiologyBlut ist ein ganz besondrer Saft. *Chem. Rev.* **2001**, *101* (9), 2797-2920. DOI: 10.1021/cr970143c.
- (156) Lee, L. L.; Niknafs, N.; Hancocks, R. D.; Norton, I. T. Emulsification: Mechanistic understanding. *Trends in Food Science & Technology* **2013**, *31* (1), 72-78. DOI: 10.1016/j.tifs.2012.08.006.
- (157) Xu, J.; Zhang, S.; Machado, A.; Lecommandoux, S.; Sandre, O.; Gu, F.; Colin, A. Controllable Microfluidic Production of Drug-Loaded PLGA Nanoparticles Using Partially Water-Miscible Mixed Solvent Microdroplets as a Precursor. *Sci. Rep.* **2017**, *7* (1), 4794. DOI: 10.1038/s41598-017-05184-5.
- (158) Lam, S.-M.; Kee, M.-W.; Sin, J.-C. Influence of PVP surfactant on the morphology and properties of ZnO micro/nanoflowers for dye mixtures and textile wastewater degradation. *Materials Chemistry and Physics* **2018**, *212*, 35-43. DOI: 10.1016/j.matchemphys.2018.03.002.
- (159) Jin, L.; Yang, Y.-Z.; Fan, J.-F.; Xu, B.-S. Effect of Surfactant Polyvinyl Pyrrolidone on the Properties of Microporous Carbon Nanospheres Reinforced Magnesium Matrix Composites. *Nanomaterials* **2020**, *10* (11), 2281. DOI: 10.3390/nano10112281.
- (160) Dunphy, D. R.; Sheth, P. H.; Garcia, F. L.; Brinker, C. J. Enlarged Pore Size in Mesoporous Silica Films Templated by Pluronic F127: Use of Poloxamer Mixtures and Increased Template/SiO₂ Ratios in Materials Synthesized by Evaporation-Induced Self-Assembly. *Chem. Mater.* **2014**, *27* (1), 75–84. DOI: 10.1021/cm5031624.

-
- (161) Ni, R.; Muenster, U.; Zhao, J.; Zhang, L.; Becker-Pelster, E. M.; Rosenbruch, M.; Mao, S. Exploring polyvinylpyrrolidone in the engineering of large porous PLGA microparticles via single emulsion method with tunable sustained release in the lung: In vitro and in vivo characterization. *Journal of Controlled Release* **2017**, *249*, 11-22. DOI: 10.1016/j.jconrel.2017.01.023.
- (162) Kamranfar, P.; Jamialahmadi, M. Effect of surfactant micelle shape transition on the microemulsion viscosity and its application in enhanced oil recovery processes. *J. Mol. Liq.* **2014**, *198*, 286-291. DOI: 10.1016/j.molliq.2014.07.009.
- (163) Xu, Z.; Li, J.; Zhou, H.; Jiang, X.; Yang, C.; Wang, F.; Pan, Y.; Li, N.; Li, X.; Shi, L.; et al. Morphological and swelling behavior of cellulose nanofiber (CNF)/poly(vinyl alcohol) (PVA) hydrogels: poly(ethylene glycol) (PEG) as porogen. *RSC Advances* **2016**, *6* (49), 43626–43633. DOI: 10.1039/c6ra03620a.
- (164) Ma, Y.; Shi, F.; Ma, J.; Wu, M.; Zhang, J.; Gao, C. Effect of PEG additive on the morphology and performance of polysulfone ultrafiltration membranes. *Desalination* **2011**, *272* (1-3), 51-58. DOI: 10.1016/j.desal.2010.12.054.
- (165) Wang, C.; He, C.; Tong, Z.; Liu, X.; Ren, B.; Zeng, F. Combination of adsorption by porous CaCO₃ microparticles and encapsulation by polyelectrolyte multilayer films for sustained drug delivery. *Int. J. Pharm.* **2006**, *308* (1-2), 160-167. DOI: 10.1016/j.ijpharm.2005.11.004.
- (166) Luo, R.; Neu, B.; Venkatraman, S. S. Surface functionalization of nanoparticles to control cell interactions and drug release. *Small* **2012**, *8* (16), 2585-2594. DOI: 10.1002/smll.201200398.
- (167) Qutachi, O.; Vetsch, J. R.; Gill, D.; Cox, H.; Scurr, D. J.; Hofmann, S.; Muller, R.; Quirk, R. A.; Shakesheff, K. M.; Rahman, C. V. Injectable and porous PLGA microspheres that form highly porous scaffolds at body temperature. *Acta Biomater.* **2014**, *10* (12), 5090-5098. DOI: 10.1016/j.actbio.2014.08.015.
- (168) Houchin, M. L.; Topp, E. M. Chemical degradation of peptides and proteins in PLGA: a review of reactions and mechanisms. *J. Pharm. Sci.* **2008**, *97* (7), 2395-2404. DOI: 10.1002/jps.21176.
- (169) Nomura, T.; Routh, A. F. Benign preparation of aqueous core poly lactic-co-glycolic acid (PLGA) microcapsules. *J. Colloid Interface Sci.* **2018**, *513*, 1-9. DOI: 10.1016/j.jcis.2017.11.007.

- (170) Miörner, H.; Johansson, G.; Kronvall, G. Lipoteichoic acid is the major cell wall component responsible for surface hydrophobicity of group A streptococci. *Infect. Immun.* **1983**, *39* (1), 336-343. DOI: 10.1128/iai.39.1.336-343.1983.
- (171) Sonohara, R.; Muramatsu, N.; Ohshima, H.; Kondo, T. Difference in surface properties between *Escherichia coli* and *Staphylococcus aureus* as revealed by electrophoretic mobility measurements. *Biophys. Chem.* **1995**, *55* (3), 273–277. DOI: 10.1016/0301-4622(95)00004-h.
- (172) Zhang, M.; Xue, M.; Xiao, Z.; Liu, W.; Jiang, N.; Meng, Y.; Fan, Y.; Liu, X.; Zhou, Y. *Staphylococcus sciuri* causes disease and pathological changes in hybrid sturgeon *acipenser baerii* × *acipenser schrencki*. *Front. cell. infect. microbiol.* **2022**, *12*, 1029692. DOI: 10.3389/fcimb.2022.1029692.
- (173) Wilhelm, M. J.; Sharifian Gh, M.; Wu, T.; Li, Y.; Chang, C. M.; Ma, J.; Dai, H. L. Determination of bacterial surface charge density via saturation of adsorbed ions. *Biophys. J.* **2021**, *120* (12), 2461-2470. DOI: 10.1016/j.bpj.2021.04.018.
- (174) Mahmut, Z.; Zhang, C.; Ruan, F.; Shi, N.; Zhang, X.; Wang, Y.; Zheng, X.; Tang, Z.; Dong, B.; Gao, D.; et al. Medical Applications and Advancement of Near Infrared Photosensitive Indocyanine Green Molecules. *Molecules* **2023**, *28* (16), 6085. DOI: 10.3390/molecules28166085.
- (175) Sakudo, A. Near-infrared spectroscopy for medical applications: Current status and future perspectives. *Clin. Chim. Acta* **2016**, *455*, 181-188. DOI: 10.1016/j.cca.2016.02.009.
- (176) Burrows, N. D.; Lin, W.; Hinman, J. G.; Dennison, J. M.; Vartanian, A. M.; Abadeer, N. S.; Grzincic, E. M.; Jacob, L. M.; Li, J.; Murphy, C. J. Surface Chemistry of Gold Nanorods. *Langmuir* **2016**, *32* (39), 9905-9921. DOI: 10.1021/acs.langmuir.6b02706.
- (177) Xue, Y.; Li, X.; Li, H.; Zhang, W. Quantifying thiol–gold interactions towards the efficient strength control. *Nature Communications* **2014**, *5* (1). DOI: 10.1038/ncomms5348.
- (178) Marques, S. S.; Ramos, II; Silva, C.; Barreiros, L.; Domingues, M. R.; Segundo, M. A. Lab-on-Valve Automated and Miniaturized Assessment of Nanoparticle Concentration Based on Light-Scattering. *Anal. Chem.* **2023**, *95* (10), 4619-4626. DOI: 10.1021/acs.analchem.2c04631.

-
- (179) Valkai, S.; Liszi, J.; Szalai, I. Temperature dependence of the refractive index for three chloromethane liquids at 514.5 nm and 632.8 nm wavelengths. *J. Chem. Thermodyn.* **1998**, *30* (7), 825-832. DOI: 10.1006/jcht.1998.0349.
- (180) Kekicheff, P.; Spalla, O. Refractive Index of Thin Aqueous Films Confined between Two Hydrophobic Surfaces. *Langmuir* **1994**, *10* (5), 1584-1591. DOI: 10.1021/la00017a043.
- (181) Daimon, M.; Masumura, A. Measurement of the refractive index of distilled water from the near-infrared region to the ultraviolet region. *Appl. Opt.* **2007**, *46* (18), 3811. DOI: 10.1364/ao.46.003811.
- (182) Deng, Y.; Wang, L.; Chen, Y.; Long, Y. Optimization of staining with SYTO 9:propidium iodide interplay, kinetics and impact on *Brevibacillus brevis*. *Biotechniques* **2020**, *69* (2), 88-98. DOI: 10.2144/btn-2020-0036.
- (183) Migliario, M.; Sabbatini, M.; Mortellaro, C.; Reno, F. Near infrared low-level laser therapy and cell proliferation: The emerging role of redox sensitive signal transduction pathways. *J. Biophotonics* **2018**, *11* (11), e201800025. DOI: 10.1002/jbio.201800025.
- (184) Chung, H.; Dai, T.; Sharma, S. K.; Huang, Y. Y.; Carroll, J. D.; Hamblin, M. R. The nuts and bolts of low-level laser (light) therapy. *Ann. Biomed. Eng.* **2012**, *40* (2), 516-533. DOI: 10.1007/s10439-011-0454-7.
- (185) Dai, S.; Tang, X.; Zhang, N.; Li, H.; He, C.; Han, Y.; Wang, Y. Lipid Giant Vesicles Engulf Living Bacteria Triggered by Minor Enhancement in Membrane Fluidity. *Nano Lett.* **2023**, *23* (1), 371-379. DOI: 10.1021/acs.nanolett.2c03475.
- (186) Liu, H.; Hu, Z.; Li, M.; Yang, Y.; Lu, S.; Rao, X. Therapeutic potential of bacteriophage endolysins for infections caused by Gram-positive bacteria. *J. Biomed. Sci.* **2023**, *30* (1), 29. DOI: 10.1186/s12929-023-00919-1.
- (187) Bruzzese, A.; Gil, C.; Dalton, J. A. R.; Giraldo, J. Structural insights into positive and negative allosteric regulation of a G protein-coupled receptor through protein-lipid interactions. *Sci. Rep.* **2018**, *8* (1), 4456. DOI: 10.1038/s41598-018-22735-6.
- (188) Waite, K. A.; Vance, D. E. Dimethylethanolamine does not prevent liver failure in phosphatidylethanolamine N-methyltransferase-deficient mice fed a choline-deficient diet. *Biochimica et Biophysica Acta (BBA) - Molecular and Cell Biology of Lipids* **2004**, *1636* (2), 175-182. DOI: 10.1016/j.bbalip.2003.10.014.
- (189) Ali, O.; Szabó, A. Review of Eukaryote Cellular Membrane Lipid Composition, with Special Attention to the Fatty Acids. *Int. J. Mol. Sci.* **2023**, *24* (21), 15693.

- (190) Pramanik, S.; Steinkühler, J.; Dimova, R.; Spatz, J.; Lipowsky, R. Binding of His-tagged fluorophores to lipid bilayers and giant vesicles. *Soft Matter* **2022**, *18* (34), 6372-6383. DOI: 10.1101/2022.02.01.478643.
- (191) Summonte, S.; Racaniello, G. F.; Lopedota, A.; Denora, N.; Bernkop-Schnurch, A. Thiolated polymeric hydrogels for biomedical application: Cross-linking mechanisms. *J. Control. Release* **2021**, *330*, 470-482. DOI: 10.1016/j.jconrel.2020.12.037.
- (192) Abdelrasoul, G. N.; Magrassi, R.; Dante, S.; d'Amora, M.; d'Abbusco, M. S.; Pellegrino, T.; Diaspro, A. PEGylated gold nanorods as optical trackers for biomedical applications: an in vivo and in vitro comparative study. *Nanotechnology* **2016**, *27* (25), 255101. DOI: 10.1088/0957-4484/27/25/255101.
- (193) Bhattacharya, S.; Halder, S. Interactions between cholesterol and lipids in bilayer membranes. Role of lipid headgroup and hydrocarbon chain-backbone linkage. *Biochimica et Biophysica Acta (BBA) - Biomembranes* **2000**, *1467* (1), 39-53. DOI: 10.1016/S0005-2736(00)00196-6.
- (194) Rosenberg, M.; Azevedo, N. F.; Ivask, A. Propidium iodide staining underestimates viability of adherent bacterial cells. *Sci. Rep.* **2019**, *9* (1), 6483. DOI: 10.1038/s41598-019-42906-3.
- (195) Lu, Z.; Mahony, A. K.; Arnold, W. A.; Marshall, C. W.; McNamara, P. J. Quaternary ammonia compounds in disinfectant products: evaluating the potential for promoting antibiotic resistance and disrupting wastewater treatment plant performance. *Environmental Science: Advances* **2024**, *3* (2), 208-226. DOI: 10.1039/d3va00063j.
- (196) Adler, J.; Hazelbauer, G. L.; Dahl, M. M. Chemotaxis toward sugars in *Escherichia coli*. *J. Bacteriol.* **1973**, *115* (3), 824-847. DOI: 10.1128/jb.115.3.824-847.1973.
- (197) Yang, Y.; A, M. P.; Höfler, C.; Poschet, G.; Wirtz, M.; Hell, R.; Sourjik, V. Relation between chemotaxis and consumption of amino acids in bacteria. *Mol. Microbiol.* **2015**, *96* (6), 1272-1282. DOI: 10.1111/mmi.13006.
- (198) Long, Z.; Quaipe, B.; Salman, H.; Oltvai, Z. N. Cell-cell communication enhances bacterial chemotaxis toward external attractants. *Sci. Rep.* **2017**, *7* (1), 12855. DOI: 10.1038/s41598-017-13183-9.
- (199) Webre, D. J.; Wolanin, P. M.; Stock, J. B. Bacterial chemotaxis. *Current Biology*, **2003**, *13* (2), R47-R49. DOI: 10.1016/s0960-9822(02)01424-0.

-
- (200) Jain, R.; Faith, N. G.; Milkowski, A.; Nelson, K.; Busche, D.; Lynn, D. M.; Czuprynski, C. J.; Abbott, N. L. Using Chemoattractants to Lure Bacteria to Contact-Killing Surfaces. *Angew. Chem. Int. Ed.* **2016**, *55* (19), 5698-5702. DOI: 10.1002/anie.201510813.
- (201) Fischetti, V. A. Bacteriophage endolysins: a novel anti-infective to control Gram-positive pathogens. *Int. J. Med. Microbiol.* **2010**, *300* (6), 357-362. DOI: 10.1016/j.ijmm.2010.04.002.
- (202) Khan, F. M.; Chen, J.-H.; Zhang, R.; Liu, B. A comprehensive review of the applications of bacteriophage-derived endolysins for foodborne bacterial pathogens and food safety: recent advances, challenges, and future perspective. *Front. Microbiol.* **2023**, *14*. DOI: 10.3389/fmicb.2023.1259210.

**Eidesstattliche Versicherung gemäß § 8 der Promotionsordnung für die
Gesamtfakultät für Mathematik, Ingenieur- und Naturwissenschaften der
Universität Heidelberg**

1. Bei der eingereichten Dissertation zu dem Thema „**Bottom-Up Assembly of Modular Systems for Trapping and Near-Infrared Light-Triggered Killing of Bacteria**“ handelt es sich um meine eigenständig erbrachte Leistung.
2. Ich habe nur die angegebenen Quellen und Hilfsmittel benutzt und mich keiner unzulässigen Hilfe Dritter bedient. Insbesondere habe ich wörtlich oder sinngemäß aus anderen Werken übernommene Inhalte als solche kenntlich gemacht
3. Die Arbeit oder Teile davon habe ich bislang nicht an einer Hochschule des In- oder Auslands als Bestandteil einer Prüfungs- oder Qualifikationsleistung vorgelegt.
4. Die Richtigkeit der vorstehenden Erklärungen bestätige ich.
5. Bedeutung der eidesstattlichen Versicherung und die strafrechtlichen Folgen einer unrichtigen oder unvollständigen eidesstattlichen Versicherung sind mir bekannt.

Ich versichere an Eides statt, dass ich nach bestem Wissen die reine Wahrheit erkläre und nichts verschwiegen habe.

Ort und Datum

Unterschrift